Microbial iron cycling in permafrost peatlands affected by global warming

Impact on carbon mobilization and greenhouse gas emissions

Dissertation

der Mathematisch-Naturwissenschaftlichen Fakultät

der Eberhard Karls Universität Tübingen

zur Erlangung des Grades eines

Doktors der Naturwissenschaften

(Dr. rer. nat.)

vorgelegt von

M. Sc. Monique Sézanne Patzner

aus Konstanz

Tübingen

2021

Gedruckt mit Genehmigung der Mathematisch-Naturwissenschaftlichen Fakultät der Eberhard Karls Universität Tübingen.

Tag der mündlichen Qualifikation:	21.10.2021
Dekan:	Prof. Dr. Thilo Stehle
1. Berichterstatter:	Prof. Dr. Andreas Kappler
2. Berichterstatterin:	Prof. Dr. Britta Planer-Friedrich
3. Berichterstatterin:	Prof. Dr. Ruth Varner

Table of Contents


GEOMICROBIOLOGY – ABISKO – TUEBINGEN – IRON FROST

“The strength of the team is each individual member.
The strength of each member is the team.”
Phil Jackson

Summary

Northern Hemisphere peatlands store vast amounts of carbon, particularly in permafrost regions where low temperatures inhibited organic matter decomposition since the last glacial ice age. With high latitudes warming faster than anywhere else on the planet, there is urgent concern about the impact of permafrost thaw on the stability of this carbon sink.

It has been shown that iron(III) (oxyhydr)oxides can trap organic carbon in soils, underlain by intact permafrost, which may limit carbon mobilization and thus its degradation. Therefore, it is considered as a so-called rusty carbon sink. However, controls on the stability of iron-carbon associations in permafrost peatlands and their response to warming temperatures are poorly understood. Only little is known about the microbial iron cycle in permafrost peatlands and how it is impacted by global warming. Its consequences for carbon mobilization and ultimately greenhouse gas emissions such as carbon dioxide and methane prevail unexplored.

Aiming to fill these knowledge gaps, we characterized the dynamic interactions between iron and carbon in a subarctic thawing permafrost peatland (Stordalen mire) in Abisko, Northern Sweden. Here, in the discontinuous permafrost zone, oxic palsa mounds with ice-rich cores are rapidly collapsing into acidic bogs before they ultimately transform into ice-free fen-type wetlands.

We show that reactive Fe minerals such as iron(III) (oxyhydr)oxides bind significant quantities of organic carbon (up to 20% of total organic carbon) in areas of intact permafrost. However, these iron-carbon associations are not stable during permafrost thaw. Iron(III)-reducing bacteria, such as e.g. *Geobacter* spp., reductively dissolve iron(III) (oxyhydr)oxides coupled to carbon oxidation, and release aqueous iron (iron(II)) and the previously iron-bound, aliphatic-like organic carbon that becomes mobilized. The microbially driven iron(III) reduction thus directly contributes to greenhouse gas emissions such as carbon dioxide by iron(III) reduction coupled to carbon oxidation and indirectly by releasing bioavailable organic carbon which then can become further metabolized to carbon dioxide and/or methane by the present microbial community.

Iron(III)-reducing bacteria increase in abundance soon after thaw initiates, as it results in increased water saturation and expanding reducing conditions. The loss of the rusty carbon sink in permafrost soils coincides with the highest measured dissolved organic carbon (535.75±133.74 mg C/L) and highly bioavailable acetate concentrations (61.7±42.6 mg C/L)

along a permafrost thaw gradient, a significant increase in the abundance of methanogens and methanotrophs, and with increasing fluxes of the greenhouse gases carbon dioxide and methane.

We found that permafrost thaw also increases the abundance of iron(II)-oxidizing microorganisms, such as *Gallionella* spp. and *Sideroxydans* spp. This suggests that post-thaw iron cycling and interlinked greenhouse gas emissions are highly dynamic, and that the measured iron redox state is a result of the net balance between reductive and oxidative processes. Indeed, seasonal re-precipitation of iron(III) (oxyhydr)oxides was observed in the active layer of partially-thawed bog areas. Ultimately, iron(II)-oxidizing microorganisms can not sustain or reform the rusty carbon sink after complete permafrost thaw in fully-thawed fen-type wetlands.

This work has greatly expanded our understanding of microbe-mineral interactions in permafrost peatlands. It reveals an important and previously overlooked role of iron-cycling microorganisms in the release of iron mineral-associated organic carbon and its impact on greenhouse gas emissions of thawing permafrost peatlands – one of Earth's most rapidly changing ecosystems.

Zusammenfassung

Moore auf der Nordhalbkugel speichern große Mengen an Kohlenstoff, insbesondere in Permafrostgebieten, in denen niedrige Temperaturen die Zersetzung von organischem Material seit der letzten Eiszeit hemmen. Da sich hohe Breiten deutlich schneller erwärmen als andere Bereiche des Planeten Erde, besteht Grund zur Besorgnis über die Auswirkung des Auftauens von Permafrost auf die Stabilität dieser Kohlenstoffsenke.

Es wurde bereits gezeigt, dass Eisenminerale, sogenannte Eisen(III) (oxyhydr)oxide, organischen Kohlenstoff in der aktiven Auftauschicht von Permafrostböden binden können. Dies hat zur Folge, dass die Mobilisierung von Kohlenstoff und damit dessen Verfügbarkeit und Abbau für Mikroorganismen eingeschränkt ist. Dieser Mechanismus wird deshalb auch als „rostige Kohlenstoffsenke“ bezeichnet. Prozesse, die die Stabilität dieser Eisen-Kohlenstoffverbindungen in Mooren von Permafrostgebieten beeinflussen und Auswirkungen der steigenden Temperaturen auf diese Kohlenstoffsenke sind bisher kaum untersucht. Über den mikrobiellen Eisenzyklus in solchen auftauenden Permafrost-Mooren und wie dieser von der globalen Erwärmung beeinflusst wird, ist nur sehr wenig bekannt. Insbesondere die Folgen für die Kohlenstoffmobilisierung und letztendlich die daraus resultierenden Treibhausgasemissionen wie Kohlenstoffdioxid und Methan bleiben unerforscht.

Um diese Wissenslücke zu schließen, haben wir die dynamischen Wechselwirkungen zwischen Eisen und Kohlenstoff in einem subarktischen, auftauenden Permafrost-Moor (Stordalen) in Abisko in Nordschweden charakterisiert. Hier, in der diskontinuierlichen Permafrostzone, kollabieren oxische (Sauerstoff-reiche) Bodenhügel mit eisreichen Kernen (sogenannte Palsahügel) in saure Moore, bevor sie sich schließlich in eisfreie Moorfeuchtgebiete verwandeln.

Wir zeigen, dass reaktive Eisenminerale wie Eisen(III)(oxyhydr)oxide in Gebieten mit intaktem Permafrost signifikante Mengen an organischem Kohlenstoff (bis zu 20% des gesamten organischen Kohlenstoffs) binden können. Diese Eisen-Kohlenstoff-Assoziationen sind jedoch während des Auftauens des Permafrosts nicht stabil. Eisen(III)-reduzierende Bakterien, wie beispielsweise *Geobacter* sp., lösen Eisen(III) (oxyhydr)oxide, gekoppelt an Kohlenstoffoxidation, reduktiv auf und setzen so wässriges Eisen (Eisen(II)) und den zuvor gebundenen organischen Kohlenstoff frei. Eisen(II) und organischer Kohlenstoff werden in das Porenwasser der aktiven Bodenschicht mobilisiert. Die mikrobielle Eisen(III)reduktion

gekoppelt an Kohlenstoffoxidation trägt daher direkt zu Treibhausgasen wie Kohlenstoffdioxid bei und indirekt bei der Freisetzung von bioverfügbarem Kohlenstoff, der anschließend von der präsenten mikrobiellen Gemeinschaft weiter zu Kohlenstoffdioxid und Methan metabolisiert werden kann.

Die Eisen-reduzierenden Bakterien nehmen kurz nach Beginn des Auftauens als Reaktion auf eine erhöhte Wassersättigung und daraus resultierende reduzierte Bedingungen stark in ihrer Anzahl zu. Die Auflösung von Eisenmineralen im Moment des Palsa-Kollapses führt zur Freisetzung von wässrigem Eisen und vorherigem Eisenmineral-assoziiertem organischen Kohlenstoff in das umgebene Porenwasser. Der Verlust dieser rostigen Kohlenstoffsenke in Permafrostböden fällt mit den höchsten gemessenen Konzentrationen an gelöstem organischen Kohlenstoff (535,7g ± 133,74 mg C/L) und höchstbioverfügbarem Acetate (61,7 ± 42,6 mg C/L) entlang eines Auftaugradienten, einer signifikanten Zunahme in der Anzahl von Methan-bildender Mikroorganismen (Methanogene) und Methan-verwendeten Mikroorganismen (Methanotrophe) und einem signifikanten Anstieg der Treibhausgase Kohlenstoffdioxid und Methan zusammen.

Mit dem Auftauen der Permafrostböden nimmt auch die Anzahl der Eisen(II)-oxidierenden Mikroorganismen (Eisen-bildner) wie *Gallionella* sp. und *Sideroxydans* sp. stark zu. Dies deutet darauf hin, dass der mikrobielle Eisenkreislauf nach dem Auftauen der Permafrostböden und die damit verbundenen Treibhausgasemissionen sehr dynamisch sein können. Der gemessene Eisen-Redox-Zustand (Eisen(II) oder Eisen(III)) ist daher ein Ergebnis des Nettogleichgewichts zwischen reduktiven und oxidativen mikrobiellen Eisenprozessen. In der Tat wurde eine saisonale Wiederausfällung von Eisen(III) (oxyhydr)oxiden, aufgrund sich veränderter Redoxbedingungen während der aufgetauten Sommermonate in der aktiven Schicht von teilweise aufgetauten Moorböden, beobachtet. Jedoch können diese Bakterien den Verlust dieser rostigen Kohlenstoffsenke mit vollständigem Auftauen der Böden und Ausbreiten der Feuchtgebiete nicht verhindern.

Diese Arbeit hat unser Verständnis der Wechselwirkungen zwischen Mikroben und Mineralen in Permafrost-Mooren erheblich erweitert. Es zeigt sich eine wichtige und bisher übersehene Rolle der eisenmetabolisierenden Mikroorganismen in der Freisetzung von mineralgebundenem organischen Kohlenstoff und in der Freisetzung von Treibhausgasen in auftauenden Permafrost-Mooren – einem der sich am schnellsten verändernden Ökosysteme der Erde.

Chapter 1: Introduction

Besides vegetation and the ocean, permafrost is one of the world's largest carbon (C) sinks, storing twice as much carbon as the atmosphere[1]. Low soil temperatures locked this substantial carbon pool away for thousands of years. However, due to anthropogenically driven climate change, the permafrost zone is warming across the globe[2], leading to permafrost thaw. Thawing permafrost is known to mobilize concerning amounts of carbon which potentially could end up into the atmosphere, leading to a strong positive feedback that may amplify climate warming. Yet, the magnitude of greenhouse gas (GHG) emissions such as methane (CH_4) and carbon dioxide (CO_2) from thawing permafrost areas remains uncertain. This knowledge gap can be explained by the complex range of physical, chemical, and biological changes driven by permafrost thawing that affect not only these permafrost areas, but also wider ecosystems. There is a strong need to better understand what happens to permafrost regions and broader ecosystems as permafrost thaws to determine the net effect on the global carbon cycle. Piercing together carbon sources and sinks in these complex permafrost environments is important to understand its overall climate impact[3]. One such carbon source or sink could be the interactions of iron (Fe) to carbon in thawing permafrost peatlands.

Microbial iron and carbon cycling in permafrost-affected soils

Iron exists in two environmentally relevant redox states: (1) as reduced Fe(II), which is easily soluble at neutral pH, and (2) as oxidized Fe(III), which is poorly soluble at neutral pH and usually precipitates as Fe(III) (oxyhydr)oxide minerals[4]. Organic carbon (OC) can interact with both Fe species, Fe(II) and Fe(III), for example by sorption to or co-precipitation with Fe minerals, or by direct chelation and complexation[5-7]. Such interactions of OC to Fe, specifically to Fe(III) (oxyhydr)oxides, have been shown to be protected by soil structural conditions (such as aggregation formation, macroscale shifts in fluid paths). As a result, carbon bound to Fe is immobilized and thus less accessible to decomposing microorganisms in respective soil environments[8,9]. Further, oxygen (O_2) diffusion in these Fe-OC associations is hindered, which additionally favors carbon preservation over its decomposition[8,9] and ultimately results in a so-called rusty carbon sink[10]. Therefore, the precipitation and dissolution of Fe minerals in response to changing redox conditions could be a key factor in controlling OC stabilization in permafrost-affected soils.

Numerous abiotic processes can lead to Fe redox transformations from Fe(II) to Fe(III) or vice versa, such as for example Fe(II) oxidation by O_2, Fe(III) photoreduction, and Fe(III) reduction by sulfide or reduced natural organic matter (Figure 1). Abiotic oxidation of dissolved Fe(II) by O_2 produces hydroxyl radicals (·OH) that can degrade organic carbon further to low molecular weight organic molecules and CO_2[11-13]. The extent to which Fe-promoted radical formation degrades organic matter in permafrost environments has not been established; however, this process may produce as much CO_2 as microbial respiration in Arctic surface waters[12]. At the same time, microbial Fe(II) oxidation and Fe(III) reduction takes place[4]. At neutral pH, microaerophilic Fe(II)-oxidizing bacteria use O_2 as electron acceptor for Fe(II) oxidation[4]. Under anoxic conditions, Fe(II) can be oxidized coupled to either nitrate reduction or photosynthesis[14,15]. Fe(III)-reducing bacteria reduce Fe(III) to Fe(II) coupled to organic carbon or H_2 oxidation during anaerobic respiration, and thereby provide Fe(II) as an electron donor for Fe(II)-oxidizing bacteria.

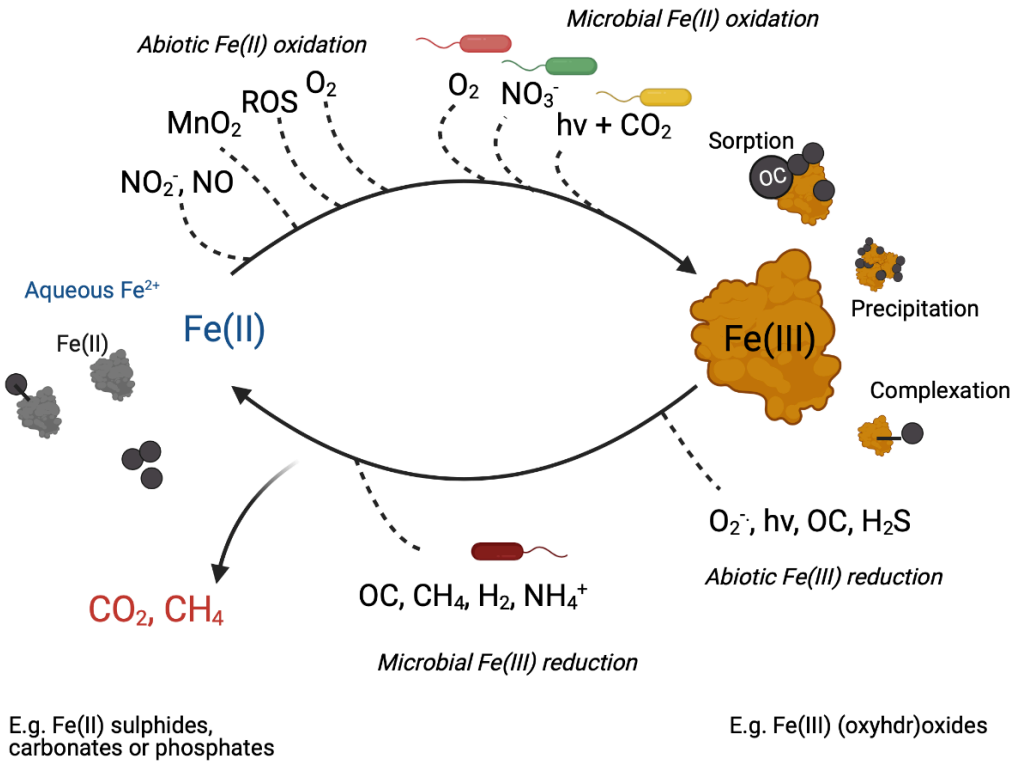

Figure 1. Iron cycling linked to the carbon cycle. *Fe(II) can abiotically be oxidized by reactive nitrogen species such as nitrite (NO_2^-) or nitric oxide (NO), manganese oxides (MnO_2), reactive oxygen species (ROS) and O_2. Fe(II) can microbially be oxidized by microaerophilic Fe(II)-oxidizers using oxygen (O_2) as electron acceptor (purple bacterium), by nitrate-reducing Fe(II)-oxidizers using nitrate (NO_3^-) as electron acceptor (green bacterium), as well as by phototrophic Fe(II)-oxidizers using carbon dioxide (CO_2) as electron acceptor and light (hv) as energy source (yellow bacterium). Fe(III) can abiotically be reduced by superoxide ($O_2^{-\cdot}$), by light (usually when Fe(III) is organically complexed), by organic carbon (OC) and sulphide (H_2S). Fe(III) can microbially be reduced by Fe(III)-reducing bacteria (red bacterium) using OC), methane (CH_4), dihydrogen (H_2) or ammonium (NH_4^+). Iron oxidation promotes OC trapping whilst reduction promotes mineral dissolution and C release. Fe(III) reduction competes with methanogenesis but can promote methanotrophy. Not pictured is the effect of pH which is altered by Fe mineral transformation and influences methane production due to physiological constrains.*

Little is known about the microbial iron carbon cycle in permafrost environments. On the one hand, cold temperatures and slightly acidic pH in permafrost-affected soils, such as for example in arctic peatlands, allow Fe(II)-oxidizing bacteria to compete more effectively with abiotic Fe(II) oxidation. Emerson *et al.*[16] demonstrated microaerophilic Fe(II)-oxidizing bacteria

such as *Lepthothrix sp.* and *Gallionella sp*. to grow in microbial mats in the arctic tundra at the North Slope of Alaska. On the other hand, high dissolved organic carbon (DOC) concentrations and pervasive anoxia promote a higher activity and growth of Fe(III)-reducing bacteria. Fe(III) reduction, normally thought of as a dissimilatory process, could also be coupled to fermentative metabolisms in arctic permafrost-affected peatlands, as described previously for an acidic fen[17]. Fe(II) from Fe(III) reduction can be stabilized against oxidation by complexation with organic compounds, which inhibits re-oxidation even under high O_2 concentrations[18]. To date, the microbial key players of Fe(III) reduction in permafrost environments were only poorly investigated. Only Lipson *et al.*[19] found evidence for the presence of the Fe(III)-reducing bacterium *Rhodoferax ferrireducens* in the organic layer of artic peat soils across a drained thaw lake basin.

The microbial iron and carbon cycles are linked by numerous processes with the ability to either increase or decrease net methane emissions. Fe(III)-reducing and methanogenic microorganisms compete for the same electron donor (Fe(III)). Fe(III) reduction is more thermodynamically favorable than methanogenesis, and thus, conditions more suitable to Fe(III) reducers have the potential to inhibit methanogenesis[20]. However, Fe(III) reduction (e.g. coupled to OC oxidation (see equation 1)) can also consume protons and lead to an increase in pH, which is more favorable for the growth and activity of methanogens.

Equation 1 I

$$4FeOOH + CH_2CHOHCOO^- + \mathbf{7H^+} \rightarrow 4Fe^{2+} + CH_3COO^- + HCO_3^- + 6\ H_2O$$

Despite their potential for competition for electron donors, there is evidence that Fe(III)-reducing and methanogenic microorganisms often co-exist[21]. Additionally, Fe(III) reduction can also be directly coupled to the metabolism of methanogens and methanotrophs. For instance, methanotrophic microorganisms can couple the anaerobic oxidation of CH_4 to Fe(III) reduction and thus lead to a net drop in CH_4 emissions[22] (see equation 2), but also acetoclastic methanogens can use Fe(III) reduction to maximize their energy conservation by metabolizing acetate, and thereby augment the production of CH_4[23].

Equation 2 I

$$8Fe(OH)_3 + CH_4 + 15H^+ \rightarrow 8\ Fe^{2+} + HCO^{3-} + 21H_2O$$

Furthermore, the release of previously Fe-associated C after reductive dissolution of Fe minerals by Fe(III)-reducing bacteria could increase the decomposition of organic carbon and emissions of GHG by the present active microbial community like fermenters and heterotrophs. Mineral-associated OC (MAOC) has been proposed to be mainly comprised of low molecular weight compounds of microbial (as for example microbial polysaccharides, amino sugars and muramic acid) and plant origin[6,24-27] with low activation energies, favoring its assimilation by microbes and plants[5,28,29]. Thus, the release of MAOC through permafrost thaw is considered as a key driver of the composition of arctic surface waters, which ultimately controls bacterial respiration[30,31].

The complex balance of the listed processes that either suppress or promote greenhouse gas emissions such as CO_2 and CH_4, highlights the need of a fundamental understanding of the microbial Fe metabolisms and its microbial interactions with methanotrophs and methanogens in thawing permafrost environments. Ultimately, the bioavailability of Fe-OC associations is crucial for identifying it as a potential carbon source or sink.

Influence of Fe on OC stabilization in permafrost environments

Several studies already stated that iron oxides have the potential to increase OC storage in intact permafrost soils by hindering microbial degradation and thus increasing mineral stabilization of OC (Figure 2).

In permafrost-affected soils from the East Siberian Arctic, Gentsch *et al.*[32,33] found organic matter to be strongly associated with minerals via sorption to clay sized particles and coprecipitation with metals such as poorly crystalline iron oxides. Their data showed that mineral-associated organic carbon was the dominating organic matter fraction (54±15% of the total OC) in the active layer and upper permafrost in cryoturbated soils across the Siberian Arctic[33].

Mu *et al.*[34] determined the amount of soil OC (SOC) associated with reactive Fe phases in permafrost regions of the Qinghai-Tibetan Plateau (QTP). They found that iron-bound organic carbon represented 19.5±12.3% of the total SOC pool and concluded that approximately 20% of SOC could be preserved by the rusty carbon sink in permafrost regions of the QTP[34].

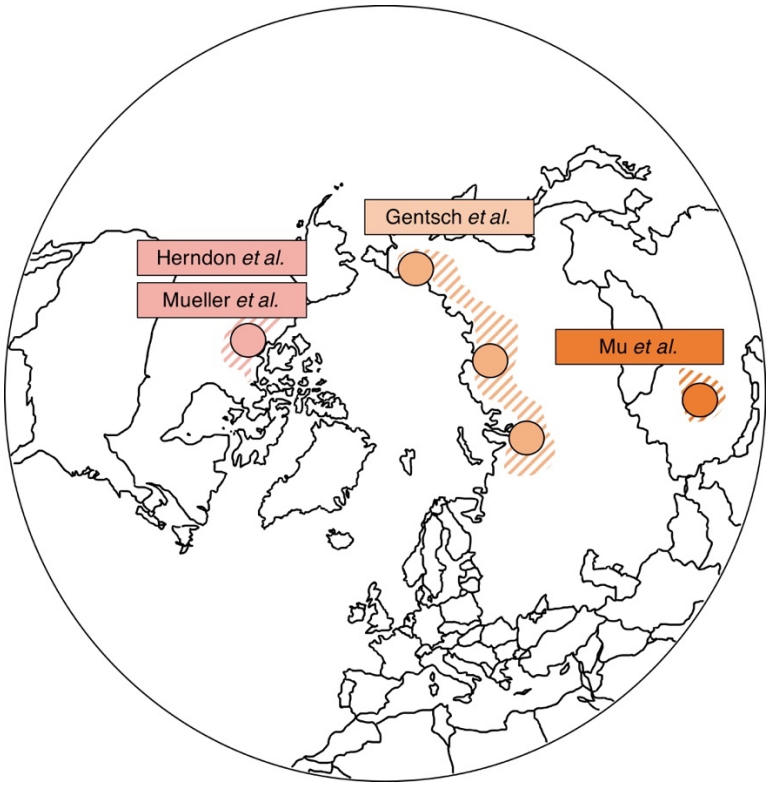

Figure 2. Examples of iron (Fe)-organic carbon (OC) associations found in different permafrost environments. *The listed studies represent examples of known literature and the figure is not aiming for completeness. It shows the widespread abundance of Fe-OC associations in permafrost environments.*

Recently, Mueller *et al.*[35] found close associations between Fe and organic carbon in a cross section from a permafrost layer of a Cryosol from Northern Alaska. They estimated that around 28% of the total OC in the active layer and upper permafrost of drained thaw lake basins on the Arctic coastal plain were mineral-associated. Hobara *et al.*[36,37] estimated that mineral-associated OC is comprised of 30-55% of total OC stored in the active layer in acidic soils from arctic tundra and boreal forest ecosystems. They observed that concentrations of mineral-associated OC were positively correlated with Al- and Fe-bearing minerals[36,37]. Herndon *et al.*[38] described organic horizons in an active layer of the arctic tundra on the North Slope of Alaska that was enriched in (poorly) crystalline Fe(III)(oxyhydr)oxides derived from the upward translocation of dissolved Fe(II) and Fe(III) containing mineral horizons. Their data suggested that iron oxides may inhibit organic carbon degradation by binding low-molecular weight organic compounds, stabilizing soil aggregates, and forming thick coatings around particulate organic matter[38].

The authors clearly state the need of future predictions of iron-induced carbon storage in thawing arctic tundra under changing redox conditions[38,39]. So far the majority of studies focused on still intact permafrost and not on Fe-OC associations during permafrost collapse.

Climate-induced permafrost thaw and resulting biogeochemical shifts

Arctic air temperatures show a 2.5 to 3 times higher increasing trend than the global average due to climate change[40]. By the end of the century, an increase in temperatures of ~3-9°C is projected for Arctic regions[40].

Along with these large air temperature changes, permafrost temperatures have increased, with the highest rise in shallow permafrost[41], leading to an increasing thickness[42] and variability[43] of the active layer and an amplified extent and duration of thaw of long-frozen ground ice and permafrost soils[44]. Multiple lines of evidence suggest that the Arctic hydrological cycle is intensifying due to warming, resulting in increases in all fluxes, including precipitation, runoff and evapotranspiration (ET)[45]. The processes triggered by permafrost thaw coupled to changes in precipitation and drainage are expected to lead to greater fluctuations in water levels and redox conditions in arctic wetlands. Elberling *et al.*[46], for example, reported a decline in precipitation and an increase in ET in wetlands of Northeast Greenland which resulted in an increasing occurrence and frequency of drought events. Moreover, rain events in summer still occur and could even increase in intensity, causing increasing fluctuations in redox conditions as soils drain and (re)flood[46].

Soil warming drives microbial decomposition of previously frozen soil organic carbon and thus highly effects the release of GHG emissions from thawing permafrost environments[1]. The magnitude of GHG emissions strongly depends on redox conditions that control ecosystem C storage[47]. Under oxic conditions, organic matter is quickly consumed by aerobic respiration producing CO_2. In contrast, under anoxic conditions, anaerobic respiration leads to slower production of CO_2, but also of CH_4[48-51]. Not only the carbon cycle is heavily influenced by redox conditions, but also therewith connected biogeochemical cycles, such as the nutrient (nitrogen and phosphorous), sulfur, and iron cycles. Little is known about the response of these cycles to changing redox conditions in permafrost-affected ecosystems with Arctic warming.

A large manipulation experiment provided first insights in the complex net of processes driven by shifts in redox conditions. Within a drained thaw lake basin on the Arctic coastal plain, water tables were either lowered (drained), raised (flooded), or remained unaltered (control setup)[52]. Unfortunately, the effects of soil drainage could not be assessed due to similar water table heights in drained and control areas. However, their results suggested that flooding increased thaw depth and an increase in CO_2 production[52]. The short-term effects of the water table manipulation on CH_4 fluxes were more complex and non-linear. Flooding additionally led to

decreases in dissolved O_2 and an increase in dissolved Fe(II) and phosphate[53], probably caused by mineral dissolution[54]. On the one hand, conditions in flooded permafrost soils could promote Fe(III) mineral dissolution and as a result release previously Fe-associated OC. On the other hand, drainage of previously frozen soils could inhibit Fe(III) reduction, promote Fe(II) oxidation and result in the formation of Fe(III) (oxyhydr)oxides sequestering OC. How climate-induced permafrost thaw will affect the so-called rusty carbon sink by varying redox conditions remains unknown.

Permafrost peatland, Stordalen mire (Abisko), as a model system

In order to better understand the link of the microbial iron to the carbon cycle and ultimately the role of Fe transformations on C degradation and GHG emissions during permafrost thaw, a permafrost peatland in northern Sweden was used as a model field site. Stordalen mire (68.20°N, 19.03°E; 351 m above sea level) is a 15 ha large actively degrading permafrost peatland in the discontinuous permafrost zone located 10 km east of Abisko, Sweden. Average temperatures at Stordalen exceeding the 0°C threshold in the year 2000[55] caused permafrost thaw and a great heterogeneity in the landscape from desiccating palsa (underlain by intact permafrost) (Figure 3) to ombrotrophic bog (intermediately thawed) and waterlogged minerotrophic fen-type wetlands (fully thawed)[56]. Over the past 40 years, palsa regions at Stordalen collapsed, declined, and resulted in an increase in bog and fen areas due to permafrost thaw[57] (Figure 4).

Figure 3. Desiccating palsa, underlain by intact permafrost, at Stordalen mire, permafrost peatland in Northern Sweden.

Along this thaw gradient, an increase in reduced conditions due to waterlogging was observed resulting in anaerobic carbon decomposition and increasing CH_4 production[56,58]. Increased thaw correlated with a shift from hydrogenotrophic to partly acetolactic methanogenesis[58]. The methanotrophic community is diverse and shows strong spatial heterogeneity, but highest methane oxidation in anoxic depths of the bog[59]. Dissolved organic matter composition shifted

toward lower molecular weight compounds with lower aromaticity, lower organic oxygen content, and more abundant microbially produced compounds[60]. These changes are accompanied by a strong correlation with vegetation changes, particularly the presence or absence of Sphagnum moss[60]. Additionally, the pH changes from 4.1 in the bog to more than 5.8 in the fen[60].

Figure 4. Collapsing palsa, resulting in waterlogged conditions and increasing bog and fen areas at Stordalen mire.

Stordalen mire has been the site of pioneering studies on permafrost thaw over more than 4 decades including fundamental parameters such as short- and long-term soil and air temperature trends, rainfall, and snowfall as well as hydrological data[61]. Today, high resolution measurements are recorded for air humidity, temperature, groundwater level, CO_2/CH_4 emissions, precipitation, snow depth, soil moisture and temperature, heat flux and surface temperature as well as ingoing/outgoing solar, terrestrial, and photosynthetically active radiation. This context data is required to capture the heterogeneity, the changing redox conditions and ultimately to be able to characterize and identify the unaddressed microbial processes of the iron and the carbon cycle along a thaw gradient in permafrost peatlands.

References

1 Schuur, E. A. G. *et al.* Climate change and the permafrost carbon feedback. *Nature* **520**, 171-179 (2015).

2 Biskaborn, B. K., Smith, S.L., Noetzi, J. *et al.* Permafrost is warming at a global scale. *Nat Commun* **10**, 264 (2019).

3 When permafrost thaws. *Nat Geosci* **13**, 765 (2020).

4 Kappler, A., Bryce, C., Mansor, M., Lueder, U., Byrne, J.M., Swanner, E. An evolving view on biogeochemical cycling of iron. *Nature Reviews Microbiology* (2021).

5 Kleber, M. *et al.* Mineral-Organic Associations: Formation, Properties, and Relevance in Soil Environments. *Adv Agron* **130**, 1-140 (2015).

6 Kogel-Knabner, I. *et al.* Organo-mineral associations in temperate soils: Integrating biology, mineralogy, and organic matter chemistry. *J Plant Nutr Soil Sc* **171**, 61-82 (2008).

7 Wagai, R. & Mayer, L. M. Sorptive stabilization of organic matter in soils by hydrous iron oxides. *Geochim Cosmochim Ac* **71**, 25-35 (2007).

8 Asano, M. & Wagai, R. Evidence of aggregate hierarchy at micro- to submicron scales in an allophanic Andisol. *Geoderma* **216**, 62-74 (2014).

9 Totsche, K. U. *et al.* Microaggregates in soils. *J Plant Nutr Soil Sc* **181**, 104-136 (2018).

10 Eglinton, T. I. GEOCHEMISTRY A rusty carbon sink. *Nature* **483**, 165-166 (2012).

11 Hall, S. J. & Silver, W. L. Iron oxidation stimulates organic matter decomposition in humid tropical forest soils. *Global Change Biol* **19**, 2804-2813 (2013).

12 Page, S. E. *et al.* Dark Formation of Hydroxyl Radical in Arctic Soil and Surface Waters. *Environ Sci Technol* **47**, 12860-12867 (2013).

13 Trusiak, A., Treibergs, L. A., Kling, G. W. & Cory, R. M. The role of iron and reactive oxygen species in the production of CO2 in arctic soil waters. *Geochim Cosmochim Ac* **224**, 80-95 (2018).

14 Widdel, F. *et al.* Ferrous iron oxidation by anoxygenic phototrphic bacteria. *Nature* **362**, 834-836 (1993).

15 Straub, K. L., Benz, M., Schink, B., Widdel, F. Anaerobic, nitrate-dependent microbial oxidation of ferrous iron. *Appl Environ Microbiol* **62**, 1458-1460 (1996).

16 Emerson, D., Scott, J.J., Benes, J., Bowden, W.B. Microbial iron oxidation in the Arctic tundra and its implications for biogeochemical cycling *Appl Environ Microbiol* **81**, 8066-8075 (2015).

17 Reiche, M., Torburg, G., Küsel, K. Competition of Fe(III) reduction and methanogenesis in an acidic fen. *FEMS Microbioly Ecol* **65**, 88-101 (2008).

18 Wan, X. *et al*. Complexation and reduction of iron by phenolic substances: Implications for transport of dissolved Fe from peatlands to aquatic ecosystems and global iron cycling. *Chem Geol* **498**, 128-138 (2018).

19 Lipson, D. A., Jha, M., Raab, T. K. & Oechel, W. C. Reduction of iron (III) and humic substances plays a major role in anaerobic respiration in an Arctic peat soil. *J Geophys Res-Biogeo* **115**, G00I06 (2010).

20 Van Bodegom, P. M., Scholten, J. C. M, Stams, A. J. M. Direct inhibition of methanogenesis by ferric iron. *FEMS Microbiol Ecol* **49**, 261-268 (2004).

21 Wagner, R., Zona, D., Oechel, W., Lipson, D. Microbial community structure and soil pH correspond to methane production in Arctic Alaska

soils. *Method Enzymol* **19**, 3398-3410 (2017).

22 Ettwig, K. F. *et al*. Archaea catalyze iron-dependent anaerobic oxidation of methane. *P Natl Acad Sci USA* 201609534 (2016).

23 Prakash, D., Chauhan, S. S., Ferry, J. G. Life on the thermodynamic edge : Respiratory growth of an acetotrophic methanogen. *Science Advances* **5**, 1-7 (2019).

24 Baldock, J. A., Skjemstad, J.O. Role of soil matrix and minerals in protecting natural organic materials against biological attack. *Org Geochem* **31**, 697-710 (2000).

25 Christensen, B. T. Physical fractionation of soil and structural and functional complexity in organic matter turnover. *Eur J Soil Sci* **52**, 345-353 (2001).

26 Sanderman, J., Maddern, T. & Baldock, J. Similar composition but differential stability of mineral retained organic matter across four classes of clay minerals. *Biogeochemistry* **121**, 409-424 (2014).

27 Six, J. *et al.* Sources and composition of soil organic matter fractions between and within soil aggregates. *Eur J Soil Sci* **52**, 607-618 (2001).

28 Jilling, A. *et al.* Minerals in the rhizosphere: overlooked mediators of soil nitrogen availability to plants and microbes. *Biogeochemistry* **139**, 103-122 (2018).

29 Williams, E. K., Fogel, M. L., Berhe, A. A. & Plante, A. F. Distinct bioenergetic signatures in particulate versus mineral-associated soil organic matter. *Geoderma* **330**, 107-116 (2018).

30 Crump, B., Kling, G., Bahr, M., Hobbie, J. Bacterioplankton community shifts in arctic lake corrleate with seasonal changes in organic matter sources. . *Appl Environ Microbiol* **69**, 2253-2268 (2003).

31 Judd, K. E., Crump, B. C., Kling, G. W. Variation in dissolved organic matter controls bacterial production and community composition. *Ecology* **87**, 2068-2079 (2006).

32 Gentsch, N. *et al.* Properties and bioavailability of particulate and mineral-associated organic matter in Arctic permafrost soils, Lower Kolyma Region, Russia. *Eur J Soil Sci* **66**, 722-734 (2015).

33 Gentsch, N. *et al.* Storage and transformation of organic matter fractions in cryoturbated permafrost soils across the Siberian Arctic. *Biogeosciences* **12**, 4525-4542 (2015).

34 Mu, C. C. *et al.* Soil organic carbon stabilization by iron in permafrost regions of the Qinghai-Tibet Plateau. *Geophys Res Lett* **43**, 10286-10294 (2016).

35 Mueller, C. W. *et al.* Microscale soil structures foster organic matter stabilization in permafrost soils. *Geoderma* **293**, 44-53 (2017).

36 Hobara, S., Kushida, K., Kim, Y., Koba, K., Lee, B.-Y., Ae, N. Relationships among pH, minerals, and carbon in soils from tundra to boreal forest across Alaska. *Ecosystems* **19**, 1092-1103 (2016).

37 Hobara, S., Koba, K., Ae, N., Giblin, A.E., Kushida, K., Shaver, G.R. Geochemical influences on solubility of soil organic carbon in Arctic tundra ecosystems. *Soil Sci Soc Am J* **77**, 473 (2013).

38 Herndon, E. *et al.* Influence of iron redox cycling on organo-mineral associations in Arctic tundra soil. *Geochim Cosmochim Ac* **207**, 210-231 (2017).

39 Herndon, E., Kinsman-Costello, Godsey, S. Biogeochemical cycling of redox-sensitive elements in permafrost-affected ecosystems. In Biogeochemical cycles: Ecological drivers and envrionmental impact, editor: Dontsova, K., Balogh-Brunstad, Z., Le Roux, G. of *the American Geophysical Union and John Wiley & Sons, Inc.* (2020) 9781119413301.

40 Stocker, T., Qin, D., Plattner, G.-K., Tignor, M., Allen, S., Boschung, J., et al. (Eds.). Climate Change 2013: The physical science basis. Contribution of Working Group I to the Fifth Assessment Report of the Intergovernmental Panel on Climate Change. *Cambridge, UK; New York, NY: Cambridge University Press* (2013).

41 Osterkamp, T. E. Characteristics of the recent warming of permafrost in Alaska. *J Geophys Res-Biogeo* F02S02 (2007).

42 Romanovsky, V. E., Osterkamp, T. E. Effects of unfrozen water on heat and mass transport processes in the active layer and permafrost. *Permafrost Periglac* **11**, 219-239 (2000).

43 Harris, C., Arenson, L.U., Christiansen, H. H., Etzelmüller, B., Frauenfelder, R., Gruber, S., *et al*. Permafrost and climate in Europe: Monitoring and modelling thermal, geomorphological and geotechnical responses. *Earth-Science Reviews* **92**, 117-171 (2009).

44 Sjöberg, Y., Frampton, A., Lyon, S.W., . Using stream- flow characteristics to explore permafrost thawing in northern Swedish catchments. *Hydrogeology Journal* **21**, 121-131 (2013).

45 Rawlins, M. A., Steele, M., Holland, M.M., Adam, J.C., Cherry, J.E., Francis, J.A. et al. . Analysis of the Arctic system for freshwater cycle intensification: Observations and expec- tations. *Journal of Climate* **23**, 5715-5737 (2010).

46 Elberling, B., Christiansen, H. H. & Hansen, B. U. High nitrous oxide production from thawing permafrost (vol 3, pg 332, 2010). *Nat Geosci* **3**, 506-506 (2010).

47 Herndon, E. M. *et al.* Geochemical drivers of organic matter decomposition in arctic tundra soils. *Biogeochemistry* **126**, 397-414 (2015).

48 Roy Chowdhury, T., Herndon, E.M., Phelps, T.J., Elias, D.A., Gu, B., Liang, L. et al. Stoichiometry and tempera- ture sensitivity of methanogenesis and CO2 production from saturated polygonal tundra in Barrow, Alaska. *Global Change Biol* **21**, 722-737 (2015).

49 Schädel, C., Bader, M. K.-F., Schuur, E. A. G., Biasi, C., Bracho, R., Capek, P. *et al*. Potential carbon emissions dominated by carbon dioxide from thawed permafrost soils. *Nature Climate Change* **6**, 950-953 (2016).

50 Schädel, C., Schuur, E. A. G., Bracho, R., Elberling, B., Knoblauch, C., Lee, H. *et al.* Circumpolar assessment of permafrost C quality and its vulnerability over time using long-term incubation data. *Global Change Biol* **20**, 641-652 (2014).

51 Treat, C. C., Natali, S.M., Ernakovich, J., Iversen, C.M., Lupascu, M., McGuire, A.D., *et al*. A pan-Arctic synthesis of CH4 and CO2 production from anoxic soil incubations. *21* **7**, 2787-2803 (2015).

52 Zona, D. *et al.* Methane fluxes during the initiation of a large-scale water table manipulation experiment in the Alaskan Arctic tundra. *Global Biogeochem Cy* **23**, GB2013 (2009).

53 Lipson, D. A., Zona, D., Raab, T. K., Bozzolo, F., Mauritz, M., Oechel, W. C. Water-table height and microtopogra- phy control biogeochemical cycling in an Arctic coastal tundra ecosystem. . *Biogeosciences* **9**, 577-591 (2012).

54 Kinsman-Costello, L. E., O'Brien, J., Hamilton, S.K. Re-flooding a historically drained wetland leads to rapid sed- iment phosphorus release. *Ecosystems* **17**, 641-656 (2014).

55 Callaghan, T. V. *et al.* A new climate era in the sub-Arctic: Accelerating climate changes and multiple

impacts. *Geophys Res Lett* **37**, L14705 (2010).

56 Johansson, T. *et al.* Decadal vegetation changes in a northern peatland, greenhouse gas fluxes and net radiative forcing. *Global Change Biol* **12**, 2352-2369 (2006).

57 Malmer, N., Johansson, T., Olsrud, M., Christensen, T. R. Vegetation, climatic changes and net carbon sequestration in a North-Scandinavian subarctic mire over 30 years. *Global Change Biol* **11**, 1895-1909 (2005).

58 McCalley, C. K. *et al.* Methane dynamics regulated by microbial community response to permafrost thaw. *Nature* **514**, 478-481 (2014).

59 Singelton, C. M., McCalley, C. K., Woodcroft, B. J., Boyd, J. A., Evans, P. N., Hodgkins, S. B., Chanton, J. P., Frolking, S., Crill, P. M., Saleska, S. R., Rich, V. I., Tyson, G. W. . Methanotrophy across a natural permafrost thaw environment *The ISME Journal* **12**, 2544-2558 (2018).

60 Hodgkins, S. B. *et al.* Changes in peat chemistry associated with permafrost thaw increase greenhouse gas production. *P Natl Acad Sci USA* **111**, 5819-5824 (2014).

61 Olefeldt, D. & Roulet, N. T. Effects of permafrost and hydrology on the composition and transport of dissolved organic carbon in a subarctic peatland complex. *J Geophys Res-Biogeo* **117**, G01005 (2012).

Open questions and objectives of this study

Multiple lines of evidence show that significant amounts of organic carbon could be bound to iron minerals in intact permafrost regions, however, it remains unknown if this so-called rusty carbon sink preserves organic carbon during and after permafrost thaw. A fundamental understanding of the role of the microbial iron cycle, influencing carbon mobilization and decomposition in permafrost soils, and its response to permafrost thaw is lacking. Iron mineral dissolution during permafrost thaw has been overlooked as a potential source of dissolved organic carbon in permafrost regions. It is unknown to what extent the rusty carbon sink is destabilized with permafrost thaw and what influence released, previously iron mineral-associated organic carbon could have on future greenhouse gas emissions of thawing permafrost environments.

These questions can not be answered by one environmental discipline alone, but requires a complex and cross-disciplinary approach combining various fields such as biogeochemistry, microbiology, hydrology and climatology. The presented work in this thesis addresses the above-described questions by the use of a model habitat for permafrost environments in transition – Stordalen mire, a thawing permafrost peatland in Northern Sweden. Aimed at improving our understanding of the microbial iron cycle in permafrost peatlands affected by global warming and its impact on carbon mobilization and greenhouse gas emissions, the specific objectives of this study are:

- To determine to which extent the formation and dissolution of iron minerals contribute to soil organic carbon persistence in permafrost peatlands and how this so-called rusty carbon sink responds to changing redox conditions associated with permafrost thaw and seasonal fluctuations in runoff and soil moisture (**Chapters 2, 3 and 4**).

- To determine the identity, quality and bioavailability of organic carbon associated with iron minerals with continuous permafrost thaw (**Chapters 2 and 3**).

- To identify, quantify, and isolate iron(II)-oxidizing and iron(III)-reducing microorganisms involved in formation and dissolution of organic carbon-binding iron minerals with permafrost thaw (**Chapters 2, 3 and 4**).

Open questions and objectives of this study

- To determine the interplay of iron-cycling microorganisms with methanotrophic and methanogenic microorganisms during permafrost thaw (**Chapter 2**).

- To quantify the extent to which the formation and dissolution of iron minerals, and thus carbon release and increased bioavailability, influences greenhouse gas emissions such as CO_2 and CH_4 with permafrost thaw (**Chapters 2, 3 and 4**).

- To determine to which extent this so-called rusty carbon sink can preserve organic carbon in other dynamically thawing permafrost environments (**Chapter 5**).

Chapter 2 – Personal contribution

The original hypothesis was formulated by myself, Dr. C. Bryce and Prof. Dr. A. Kappler. Together with Dr. C. Bryce and Prof. Dr. A. Kappler, I designed the project, interpreted the data and wrote the manuscript. Dr. C. Bryce, M. Malusova and I collected the samples. I gathered the data presented in the main text. Supporting information from the 2017 campaign was collected by V. Nikeleit, M. Malusova, M. Baur and Dr. C. Bryce. Prof. Dr. T. Borch conducted the synchrotron analysis and contributed to the data analysis and interpretation. I collected, analyzed and interpreted the nanoSIMS data together with Dr. C. Hoeschen and Prof. Dr. C. W. Mueller. Dr. J. M. Byrne and I conducted the SEM analyses. Prof. Dr. T. Scholten contributed to project design and data interpretation. Further, Dr. H. Miller helped with EXAFS analysis. Dr. E. Stopelli conducted the ICP-MS measurements.

Chapter 2

Iron mineral dissolution releases iron and associated organic carbon during permafrost thaw

Monique S. Patzner[1], Carsten W. Mueller[2,3], Miroslava Malusova[1], Moritz Baur[1], Verena Nikeleit[1], Thomas Scholten[4], Carmen Hoeschen[2], James M. Byrne[1], Thomas Borch[5], Andreas Kappler[1] & Casey Bryce[1,6]

[1] Geomicrobiology, Center for Applied Geosciences, University of Tuebingen, Tuebingen, Germany.

[2] Chair of Soil Science, Technical University Muenchen, Freising, Germany.

[3] Department of Geosciences and Natural Resource Management, University of Copenhagen, Denmark.

[4] Chair of Soil Science and Geomorphology, University of Tuebingen, Germany.

[5] Department of Soil & Crop Sciences and Department of Chemistry, Colorado State University, Fort Collins, US.

[6] School of Earth Sciences, University of Bristol, Bristol, UK.

Published in: *Nature Communications*

Abstract

It has been shown that reactive soil minerals, specifically iron(III) (oxyhydr)oxides, can trap organic carbon in soils overlying intact permafrost, and may limit carbon mobilization and degradation as it is observed in other environments. However, the use of iron(III)-bearing minerals as terminal electron acceptors in permafrost environments, and thus their stability and capacity to prevent carbon mobilization during permafrost thaw, is poorly understood. We have followed the dynamic interactions between iron and carbon using a space-for-time approach across a thaw gradient in Abisko (Sweden), where wetlands are expanding rapidly due to permafrost thaw. We show through bulk (selective extractions, EXAFS) and nanoscale analysis (correlative SEM and nanoSIMS) that organic carbon is bound to reactive Fe primarily in the transition between organic and mineral horizons in palsa underlain by intact permafrost (41.8±10.8 mg carbon per g soil, 9.9 to 14.8% of total soil organic carbon). During permafrost thaw, water-logging and O_2 limitation lead to reducing conditions and an increase in abundance of Fe(III)-reducing bacteria which favor mineral dissolution and drive mobilization of both iron and carbon along the thaw gradient. By providing a terminal electron acceptor, this rusty carbon sink is effectively destroyed along the thaw gradient and cannot prevent carbon release with thaw.

Introduction

The release of vast amounts of organic carbon during thawing of high-latitude permafrost is an emerging issue of global concern. Yet, the extent of greenhouse gas emissions from permafrost thawing remains unpredictable due to knowledge gaps related to controls on the fate of carbon in permafrost soils[1]. The mobility, lability and bioavailability of organic carbon is determined by a number of inter-connected physico-biogeochemical parameters and processes. One such parameter is the presence of reactive iron minerals (defined here as iron minerals that are reductively dissolved by the chemical reductant sodium dithionite, e.g. ferrihydrite or goethite), which are known to stabilize organic carbon by sorption and co-precipitation[2-5]. Fe-bound carbon can be protected by soil structural conditions (such as aggregate formation, macro-scale shifts in fluid flow paths), thus be less accessible to decomposer organisms[6,7]. At the same time, oxygen (O_2) diffusion is hindered further favoring soil organic matter preservation rather than decomposition[6,7]. Thus, Fe-C associations are thought to significantly influence long-term carbon storage in numerous environments[5,8-10].

Several studies already identified poorly crystalline Fe organic matter associations in the field or produced them in the lab, and demonstrated that they are resistant to microbial or chemical reduction[11-13]. The inventory of reactive iron minerals in humid climates is highly dynamic as they precipitate and dissolve in response to changing redox conditions. Mineral soil slurry incubations previously showed organic matter protection by iron only under static oxic conditions[14]. However, iron(III) mineral reduction and dissolution under oxygen limitation led to anaerobic mineralization of dissolved organic matter and soil organic matter by 74% and 32-41%, respectively[14]. When mineral dissolution occurs, iron and carbon mobilization, increased carbon lability/bioavailability, and increased gaseous carbon loss as CO_2 and CH_4 follow (catalyzed by heterotrophic and methanogenic microorganisms)[15-19]. The extent to which the formation and dissolution of reactive Fe phases contribute to soil organic matter persistence in redox-dynamic permafrost soils remains unknown. Despite the importance of iron minerals for carbon storage, we have little understanding of the presence of this so called rusty carbon sink in organic-rich permafrost peatlands and even less knowledge of how it will respond to changing redox conditions associated with permafrost thaw.

In order to address this knowledge gap, we examined peatland soils collected along a thaw gradient at Stordalen mire (Abisko, Sweden). For this study, three thaw stages were defined, based on possible shifts in vegetation and hydrology, as has been done previously[20-23], and

known changes in microbial ecology[24,25] (Fig. 1, Supplementary Figure 1). These are: (1) desiccating palsa underlain by permafrost, (2) intermediately thawed bog, and (3) fully-thawed fen. Desiccating palsa sites are mainly dry and oxic[21]. As the permafrost thaws, the raised, dry ombrotophic palsas collapse, causing enlargement of semiwet and wet ombrotrophic bog areas with continuously frozen soil underneath[21,22]. With continued thawing, the bog areas decrease and minerotrophic fen areas expand with complete water saturation and thus even more reducing conditions than in the bog[20-22,26]. To be able to use a space for time-approach, the habitats are ordered following a temporal succession of apparent time since onset of thaw, as has been done by Hodgkins *et al.*[21].

We collected cores from locations deemed to be most representative of the three thaw stages and analyzed iron-carbon associations in three different layers within the cores defined by geochemical stratification, as has been done previously[27]. Cores were split into (1) organic horizon, (2) transition zone, interface between the two soil horizons, which can be locally very sharply defined (3-5 cm), but also reach over 20 cm layer thickness[27], and (3) mineral horizon (Supplementary Figure 1). We analyzed the solid phase by selective extractions to determine different iron phases such as reactive iron (dithionite citrate extractable), poorly crystalline iron (hydroxylamine HCl), colloidal and OM-chelated iron (sodium pyrophosphate), and more crystalline iron phases such as poorly reactive sheet silicate Fe or FeS species (6M HCl). The selective extractions were simultaneously used to determine iron-bound carbon by measurement of DOC in the sodium dithionite citrate and sodium pyrophosphate extractions. Extended X-ray absorption fine structure (EXAFS) analysis was performed to support extraction data and further determine the presence of phases such as Fe-containing clays which were not extracted by the selective dissolutions. Correlative scanning electron microscopy (SEM) and nanoscale secondary ion mass spectrometry (nanoSIMS) were used to visualize iron-carbon associations in the fine fraction of the different soil layers. This was complemented by geochemical analysis of the porewater to determine potential electron acceptors and donors, and to track iron and carbon release from the solid into the liquid phase. Additionally, Fe(III)-reducing bacteria which are the driving force behind iron mineral reduction under anoxic conditions were quantified by a growth-dependent approach. We found that reactive Fe can bind organic carbon primarily in palsa soils underlain by intact permafrost. Water-logging and O_2 limitation during permafrost thaw lead to reducing conditions and an increasing abundance of Fe(III)-reducing bacteria. By using the reactive Fe as terminal electron acceptor, they favor mineral dissolution and drive mobilization of both iron and carbon

along the thaw gradient. Thus, the rusty carbon sink is destroyed and cannot preserve organic carbon from carbon mineralization with permafrost thaw.

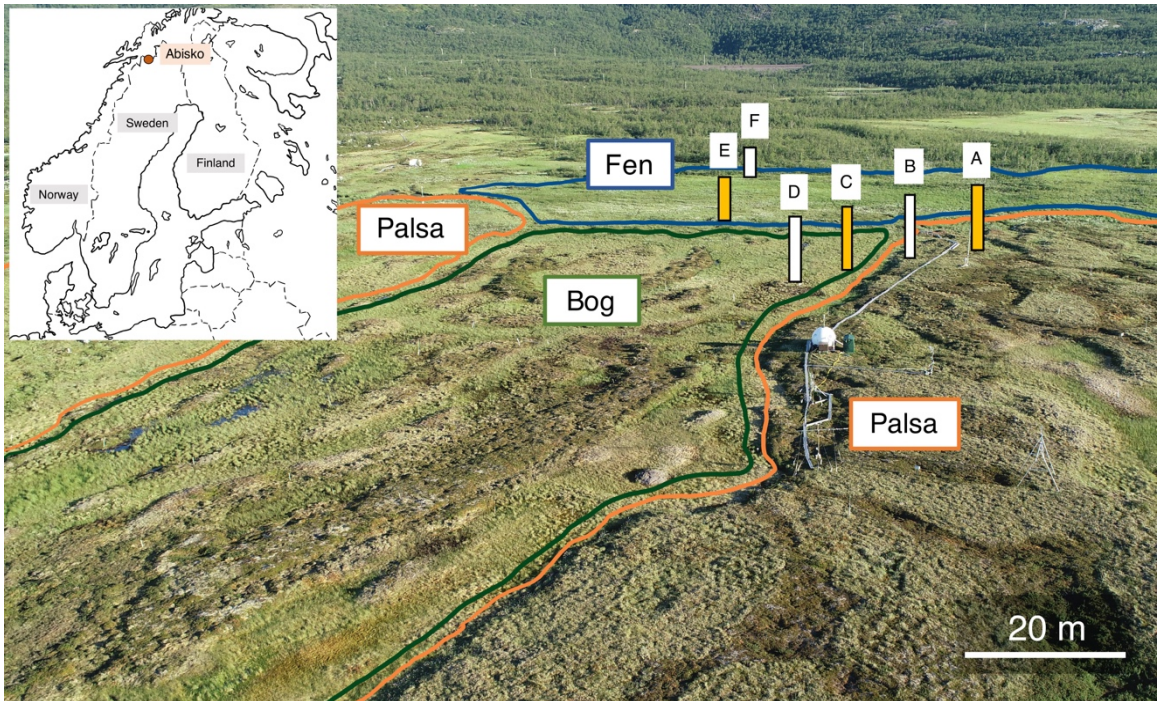

Figure 1. Field site Stordalen mire close to Abisko in the North of Sweden. *The three main thaw stages are (1) palsa (marked in orange), (2) bog (in green) and (3) fen (in blue). The positions of the three cores analyzed in detail within 3-4 days of collection in 2018, which represent all three thaw stages, are shown in yellow. Additional cores (shown in white) were taken in 2018 and analyzed after 7 months of incubation at 4°C (Supplementary Figures 1 and 3). Data for further replicates, taken in 2017 and 2019, is provided in the SI (Supplementary Figures 1-5).*

Material and Methods

Site description and sample collection

Stordalen Mire is a peatland 10 km southeast of Abisko in northern Sweden (68 22′ N, 19 03′ E)[50] which is underlain by quartz-feldspar-rich sedimentary rock (Geological Survey of Sweden). The study site is within the discontinuous permafrost region of northern Scandinavia and consists of three distinct sub-habitats which are common to northern wetlands: (1) a well-drained palsa underlain by permafrost, dominated by ericaceous and woody plants, (2) a bog with variable water table depth and some active thawing, dominated by *Sphagnum* spp. mosses, and (3) a fully-thawed and inundated fen, dominated by sedges such as *Eriophorum angustifolium*[21,22]. Dissolved O_2 decreases with increasing water table depth in bog areas from 150 ± 40 μM dissolved O_2 at 10 cm depth to 20 ± 10 μM at 20 cm depth. In the fen, dissolved O_2 at 10 cm depth is 20 ± 10 μM and 10 μM at 20 cm depth [26]. Growing season mean soil temperature at 10 cm depth below surface varies along the thaw gradient, from 6.2 ± 0.2 °C in palsa to 7.2 ± 0.3°C in bog, and to 7.6 ± 0.3 °C in the fen[51]. In this study, the three sub-habitats were ordered following a temporal succession of apparent time from palsa, to bog and fen, a space for time-approach, as has been done before[21] following the classification of Johansson *et al.* (2006)[22]. This approach is limited in that (1) permafrost thaw progression through these three thaw stages is not necessarily linear[21], (2) intermediate thaw stages (e.g. collapsed palsa) are not accounted for, and (3) it does not fully capture the heterogeneity of the landscape. However, this approach provides the best available estimate of how palsa mires will evolve with progressive climate change and thus has been applied widely at this site. The palsa and bog areas are underlain by permafrost with a thickness of 10-20 m[52]. The active layer, depending on the surface topography, ranges from 0.5-1 m thickness at maximum thaw[52,53]. These three thaw stages cover ~98% of the mire's non-lake surface[21]. A thaw-dependent shift in these habitats was observed from 1970 to 2000 during which palsa regions collapsed and bog and fen areas increased by 17%[20]. At the same time, an increase in average annual temperature by 2.5°C between 1913 and 2006 was measured, resulting in an annual mean temperature >0°C during the recent decades[54]. The total precipitation also increased during this period of time to an annual average of 306 mm[54]. The expansion of wetlands after permafrost melt is a widespread characteristic of peatlands affected by permafrost thawing[55-58] and the successional shift from palsa to bog and fen areas has been documented in other northern peatlands[57-60].

In July 2018, cores were taken in duplicates along a gently collapsing thaw gradient from palsa to bog and fen (Supplementary Figure 1). Stordalen mire is a protected area with other

ongoing field research, thus the extent of coring is strictly limited due to the risk of accelerating permafrost thaw and/or disturbance to other long-term measurements, especially at sensitive sites like erosion fronts. However, extensive context data ([https://polar.se/en/research-in-abisko/research-data/]) from the Abisko scientific community is available which ensures representative field sampling of a heterogeneous permafrost area, with cores taken following a transect along the direction of hydrological flow from palsa to bog and fen as described by Olefeldt and Roulet (2012)[28]. Given the restrictions in place, it was only possible to collect six cores per each thaw stage over three field campaigns (2017, 2018 and 2019) (Supplementary Figures 1-5). A Humax corer of 50 cm length and 3-cm-diameter with inner core liners was used. The inner liners were washed three times with 80% ethanol, six times with sterile MilliQ water and sealed with sterilized butyl rubber stoppers until coring. Butyl rubber stoppers were boiled three times in deionized water and sterilized at 121°C for 20 min in an autoclave. Sharp edges were cut into the end of the coring device to help cut the peat layer. A hammer was used to further sample the active layer. Hammering caused slight compaction of the cores, mainly in the organic horizon. Therefore, the recorded depths are not completely comparable to the initial soil profiles. Thus, the data is presented by the different soil layers (organic horizon, transition zone and mineral horizon) and depth intervals are still reported to illustrate that the dataset represents the active layer depth along the thaw gradient. Stocks (mg/cm^2) were calculated considering compaction and compared to the content (mg/g) (Supplementary Figure 9). In the palsa and bog area, cores were taken until the depth of the ground ice. Layers at the bottom of the core which contained predominantly ice were excluded from further analyses. Therefore, the soil investigated in this study represented the seasonally thawed active layer at Stordalen mire, ranging from 30 to 49 cm. The cores were stored vertically at 4°C in the dark. Three cores representing desiccating palsa, bog and fen were processed within 3-4 days (Supplementary Figure 6). Due to detailed analysis of the first core set (Palsa A, Bog C and Fen E), additional cores (Palsa B, Bog D and Fen F) from each thaw stage were analyzed after storage for 7 months at 4°C in the dark, which is not ideal, but still could be used to determine if preservation of the carbon by reactive iron was stable over longer time periods (Supplementary Figures 1 and 3). The long-term stored core Palsa B still showed higher abundance of reactive iron-associated organic carbon than Bog D and Fen F, but less than Palsa A which could be due to natural variability, long-term storage or because it was taken closer to the collapsing edge (Supplementary Figures 1 and 3). In 2019, an additional three cores (1 per thaw stage) (Palsa a, Bog c and Fen e) were collected and analyzed under same conditions and with the same methods as Palsa A, Bog C and Fen E from 2018. The cores taken in 2018 and 2019 were compared to triplicate cores previously collected in

September 2017 at each thaw stage with a Pürckhauer corer and processed directly after sampling, to show that the trends are representative for the whole mire (Supplementary Figures 1, 4 and 5). The organic horizon of the bog and fen replicate cores could not be sampled with the Pürckhauer corer. The palsa cores captured the whole active layer profile. The replicate cores showed the same trends of 6 M HCl extractable iron. Readily extractable Fe (defined by 0.5 M HCl extractable iron) showed similar trends to the sodium dithionite citrate or hydroxylamine HCl extraction for all three thaw stages (Supplementary Figure 4). The same trend of total organic carbon along the thaw gradient was observed (Supplementary Figure 5).

Porewater sampling and analysis

The cores were kept in a vertical position during transfer into an anoxic glovebox (100% N_2). Three different sections were identified by texture and color changes: (1) an organic horizon on top, (2) a middle transition zone between the organic-rich and mineral-rich layer and (3) a mineral horizon at the bottom (Supplementary Figure 1). Rhizon porewater samplers (Rhizosphere research products, Netherlands) with a porous sampling area of 5 cm and 0.15 μm pore size were used to extract porewater from three different depths, resulting in one sample representing each organic horizon, transition zone and mineral horizon. The extracted porewater was analyzed for dissolved Fe (total and Fe(II)), organic carbon (DOC) and fatty acids. For total Fe and Fe(II), the supernatant was acidified in 1 M HCl and quantified spectrophotometrically in triplicate with the ferrozine assay[61]. Dissolved OC was quantified in triplicate with a total organic carbon analyzer (High TOC II, Elementar, Elementar Analysensysteme GmbH, Germany). For the DOC analysis, the calibration curves were $r^2 > 0.999$ and the standard deviations of the triplicate analysis were <2%. Inorganic carbon was removed by acidifying the samples with 2 M HCl prior analysis. High performance liquid chromatography (HPLC; class VP with refractive index detector [RID] 10A and photo-diode array detector SPD-M10A VP detectors; Shimadzu, Japan) was used to determine the fatty acid concentrations.

Core splitting

The soil cores were removed from their liners under a N_2 atmosphere. Each core was sectioned into an organic horizon of varying thickness (4-10 cm), a transition zone (3-5 cm) and mineral horizon (4-10 cm) (Supplementary Figure 1), following Ryden *et al.* (1980)[27]. The transition zone represents the boundary between organic and mineral horizon and was

additionally defined due to distinct geochemical conditions in the porewater analysis in the middle of the active layer near the boundary between organic and mineral horizon. Calculated bulk densities as a function of soil organic matter following Bockheim *et al.* (2003)[62] were consistent with other studies conducted at Stordalen mire[27] (Palsa A: organic horizon: 0.03±0.01 g/cm^3, transition zone: 0.08±0.02 g/cm^3, mineral horizon: 0.84±0.26 g/cm^3; Bog C: organic horizon 0.08±0.01 g/cm^3, transition zone 1.29±0.04 g/cm^3 and mineral horizon 1.74±0.01 g/cm^3, Fen E: organic horizon 0.21±0.02 g/cm^3, transition zone 1.97±0.2 g/cm^3 and mineral horizon 1.72±0.01 g/cm^3). Sub-samples were homogenized and weighed into 10 mL glass vials and kept frozen at -20°C prior to subsequent analysis.

Selective extractions

The soil layers were subjected to several chemical extractions to quantify the different iron phases. The soils were kept frozen prior to analysis, then dried at 20°C under anoxic conditions until no further weight loss was observed (1 day). Prior to use, all glassware was washed with 1 M HCl for 10 min, flushed three times with deionized water and once with MilliQ water. Afterwards glassware was sterilized at 180°C in the oven for 4.5 hours. 0.3 g dry soil was weighed into a 10 mL glass vial with 6.25 mL extractant and N_2 headspace. Following the extraction, as detailed below, all samples were centrifuged at room temperature for 10 min at 5300 g. After centrifugation the supernatant was decanted into another 10 mL glass vial. Each extraction was performed in duplicates for each layer. Throughout the extraction, samples were kept in the dark under anoxic conditions (N_2 atmosphere). The extracts were analyzed for Fe and DOC as described above. Additionally, the samples were acidified in 1% (v/v) HNO_3 and analyzed in duplicates by MP-AES (microwave plasma atomic emission spectroscopy)/ICP-MS (inductively coupled plasma mass spectrometry). To get the total iron (Fe), phosphorous (P) and sulphur (S) concentrations, the extracts were analyzed using ICP-MS. To further obtain aluminum (Al) concentrations and a cross-check of the total Fe concentrations, the MP-AES was used for analysis (Supplementary Figure 10). The illustrated iron values throughout the whole study represent the iron values obtained by the ferrozine assay (for differences in iron concentrations through the different analysis see Supplementary Figure 12). Due to dark color of the extracts which can disturb the spectrophotometric measurement during ferrozine complexation, the absorbance of blanks (sample diluted in 1 M HCl or hydroxylamine-HCl) was measured and later subtracted to avoid overestimation of iron concentrations. At the same time, samples and standards are heavily diluted in 1 M HCl and hydroxylamine-HCl (1:1000 and 1:10,000) before spectrophotometric quantification. Given

these high levels of dilution, no matrix effects of the extractant solution remains. For the ferrozine assay, the calibration curves were $r^2 > 0.999$, and the standard deviations of the triplicate analyses were <1%. For the ICP-MS, the calibration curves were $r^2 > 0.999$, and the standard deviations of the triplicate analyses were <5%. For the MP-AES, the calibration curves were $r^2 > 0.993$ and the standard deviations of the triplicate analysis were <10%. The results of all Fe analysis (ferrozine assay, MP-AES/ICP-MS analysis) show all the same trends with depth and along the thaw gradient (Supplementary Figure 12). For additional extractant specific experimental parameters see below.

6 M HCl

To extract more crystalline iron phases of the soil layers, such as poorly reactive sheet silicate Fe or FeS species, dried samples were subjected to 6 M HCl extraction at 70°C for 24 h[63-65].

Sodium pyrophosphate

The sodium pyrophosphate extraction was performed following Coward *et al*. (2017)[8] at pH 10 to determine the colloidal or OM-chelated iron and bound organic carbon (Supplementary Figures 7 and 8).

Hydroxylamine-HCl

To extract the short ranged ordered (SRO) Fe oxides, an acidic hydroxylamine-HCl (pH <2) extraction was carried out under the same conditions as the sodium pyrophosphate extraction[8].

Dithionite-citrate

Extractions were conducted using a solution of 0.27 M trisodium citrate, 0.11 M sodium bicarbonate and 0.1 M sodium dithionite (total ionic strength: 1.85 M), as previously described[5] (see also Supplementary Method 1). This extraction was used to also quantify the reactive iron minerals but in particular the organic molecules binding to it (released during iron mineral dissolution). Instead of heating to 80°C as described by Lalonde *et al*. (2012)[5], the dithionite-citrate extraction was performed under the same conditions as the sodium pyrophosphate and hydroxylamine-HCl extraction (on a rolling shaker at room temperature for 16 h) for better comparison between the different extractions and to prevent carbon alteration during heating (see also Supplementary Method 1, Supplementary Figures 7 and 8), following previous studies[8,66,67]. The citrate addition as a metal ion complexing agent was necessary to avoid under-estimation of iron and organic carbon as a result of complexation or mineral precipitation during extraction (Supplementary Method 1). Without citrate addition, we obtained 64±3% less iron and 57±28% less carbon after sodium dithionite reductive dissolution. As described in Lalonde *et al.* (2012)[5], we also used a 1.85 M sodium chloride/0.11 M sodium bicarbonate

extraction as a control experiment under the same conditions (same solid:solution ratio, temperature, time, ionic strength) to distinguish between organic carbon (OC) which is readily desorbed and organic carbon which is released by the reduction of iron(III) minerals (Supplementary Figures 7 and 8). To determine the DOC background concentrations caused by the trisodium citrate, blanks (trisodium citrate sodium bicarbonate solution) were analyzed during each measurement. The background concentration was later subtracted from the total DOC value, as well as the DOC concentration of the control experiment (sodium chloride sodium bicarbonate solution), resulting in the OC which is released by the reduction of reactive iron (Supplementary Table 1). Microbial activity during and after the dithionite-citrate extraction and trisodium citrate sodium bicarbonate extraction can be excluded due to high salt content (ionic strength of 1.85 M). Rath *et al.*[68] previously showed that salinity exerts a strong inhibitory effect on a range of microbial processes in soil and that acute toxic effects occurred immediately (within 2h).

TOC analysis

To quantify the total organic carbon (TOC) (Fig. 4, Supplementary Table 1, Supplementary Figures 2, 3 and 5), soil samples from each layer were dried at 60°C until the weight remained constant. The dry soils were then ground and acidified with 16% HCl to remove the inorganic carbon. After washing with deionized water and subsequent drying, the TOC content was analyzed by an Elementar vario El (Elementar Analysensysteme GmbH, Germany). The TOC content goes in line with previously reported values [69-71]. For the TOC analysis, the calibration curves were $r^2 > 0.998$ and the standard deviations of the triplicate analysis were <1%.

EXAFS analysis

Samples were dried under an N_2 atmosphere and stored anoxically in a glove box prior to analysis. Sample were then sealed in plastic multi-sample holders with Kapton polyimide tape and kept anoxic until they were transferred to a sample mount at the beamline. The sample holder was in a cryostat during analysis to limit beam damage and to prevent oxidation of Fe(II).

Fe K-edge X-ray absorption spectroscopic analyses were conducted at Beamline 11–2 at the Stanford Synchrotron Radiation Light source (SSRL) in Menlo Park, CA. The Si(220) phi = 0° monochromator was used, and beam size of 1 mm vertical and 10 mm horizontal. EXAFS fluorescence spectra were collected with the PIPS detector simultaneously with the

transmission spectrum of Fe foil, which was used for internal energy calibrations. Multiple scans (3-4) per sample were acquired as necessary to achieve satisfactory data quality. Scans were calibrated to 7112 eV (the first inflection point of Fe(0), and then averaged over 3 or 4 scans using SixPack software. They were deglitched at 7250 and 7600 eV, and then normalized with the E0 value, determined by finding the inflection point of the first derivative of each sample. A set of Fe reference compounds was used to perform linear combination fitting (LCF) of EXAFS spectra in SixPack from chi values of 2 to 12 with an x-weight of 3. Non-negative fits were performed. Reference compounds were chosen based on prior knowledge of the sample including, for example, criteria such as elemental composition (determined by element composition of in the soil extracts), site characteristics (e.g. redox conditions, pH), and principal component analysis (PCA). PCA determines the number of distinct species in series of spectra. All contributions below 5 wt% were eliminated since we have previously determined that the limit of detection for mixed Fe species is around 5 wt% [29,72]. We determined the best least square fitting based on fitting parameters such as the reduced chi^2 (X^2) and R-factor values. The best fits were reference samples such as natural nontronite and ferrosmectite (referred to as Fe clays) obtained from the Clay Mineral Society, Fe(II)-citrate and Fe(III)-citrate (referred to as Fe(II)-OM and Fe(III)-OM) which were prepared and analyzed as described in Daugherty *et al*. (2017)[73], mackinawite (referred to as FeS) which was prepared and analyzed as described in Troyer *et al*. (2014)[74] and 2-line ferrihydrite (referred to as poorly crystalline Fe), prepared and analyzed as described in Borch *et al*. (2007)[75], (Fig. 3).

Correlative SEM and nanoSIMS

The two end-members, palsa and fen, were analyzed using SEM and nanoSIMS (Fig. 4, Supplementary Figure 11) using only the free particles of the fine fraction of the transition zone and the mineral horizon. As described by Kopittke *et al*. (2018)[76] and Keiluweit *et al.* (2012)[77], subsamples of each layer (1 mg) were dispersed in 10 mL of anoxic deionized water and gently shaken to obtain the free organo-mineral particles from the fine fraction of the soil. 100 μl of the suspension was placed onto a silica wafer and dried under an N_2 atmosphere. The samples were sputter-coated with 12 nm platinum (Pt) using a Bal-Tec SCD005 sputter coater. To characterize the organo-mineral particles of the fine fraction by size and crystallinity and identify representative particles, a field emission scanning electron microscope (FE-SEM; Jeol JSM-6500F), equipped with secondary electron detector, was used prior to nanoSIMS analysis. The acceleration voltage was set to 5 kV, with a working distance of 10 mm.

The nanoSIMS analysis were performed at the Cameca nanoSIMS 50L of the Chair of Soil Science (TU München, Germany). Prior to the measurements, the samples were additionally coated with Au/Pd layer (~30 nm) to avoid charging during the analysis. The Cs^+ primary ion beam was used with a primary ion impact energy of 16 keV. Prior to the final measurement, any potential contaminants and the Au/Pd coating layer were sputtered away at 50 x 50 μm with a high primary beam current (pre-sputtering). To enhance the secondary ion yields, Cs^+ ions were implanted into the sample during this pre-sputtering process. The primary beam (~1.2 pA) was focused at a lateral resolution ~100 nm and scanned over the sample with $^{12}C^-$, $^{16}O^-$, $^{12}C^{14}N^-$, $^{31}P^-$, $^{32}S^-$, $^{27}Al^{16}O^-$ and $^{56}Fe^{16}O^-$ secondary ions collected using electron multipliers. To compensate for any charging of the non-conductive mineral particles, the electron flood gun was used. All analyses were performed in imaging mode. For every layer, four representative spots were analyzed to obtain a reliable data basis for the spatial distribution of $^{12}C^-$ and $^{56}Fe^{16}O^-$. Ion images of 30 x 30 μm field of view, 30 planes with a dwell time of 1 ms/pixel, 256 pixels x 256 pixels were recorded. The estimated depth resolution with 16 keV Cs^+ ions was 10 nm.

Finally, the nanoSIMS images were analyzed using the Open MIMS Image plugin available within ImageJ (available free-of-charge at [https:// imagej.nih.gov/ij/]. All presented images were corrected for the electron multiplier dead time (44 ns), as well as drift corrected, and the planes accumulated. A median filter was applied on all images.

Most-probable-number (MPN) counts

A growth-dependent approach, Most-probable number (MPN) counts (Fig. 2), was performed on the soil samples from the different depths of the cores in seven replicates. This is a useful way to quantify Fe(III)-metabolizing bacteria as there is a lack of specificity in the potential genes used for Fe(III) reduction and has the strength of directly showing that the microorganisms are capable of reducing Fe(III). The three soil layers (organic horizon, transition zone and mineral horizon) were homogenized and used for preparing a dilution series. Each tube of the dilution series contained 9 ml of anoxic freshwater media. 5 mM sodium acetate, 5 mM sodium lactate and 5 mM 2-line ferrihydrite (chemically synthesized as previously described[78]) were added as amendments to the anoxic media (0.6 g/L KH_2PO_4, 0.3 g/L NH_4Cl, 0.025 g/L $MgSO_4$ x 7 H_20, 0.4 g/L $MgCl_2$ x 6 H_20, $CaCl_2$ x 2 H_20, 22 mM $NaHCO_3$, 1 mL/L trace element according to Widdel *et al.* (1983)[79], 1 mL/L vitamin solution after Widdel & Pfennig (1981)[80] and 1 mL/L selenite/tungstate solution according to Widdel (1980)[81]) before preparing the dilution series. The headspace in the dilution series was N_2:CO_2 (90:10). To the

first tube of a dilution series, 1 g of soil was added, and a 10 x dilution series up to a dilution of 10^{-12} was prepared, as has been previously done with sediments by Laufer *et al*. (2016)[82]. MPN enumerations of Fe(III)-metabolizing bacteria were set up in 96-well plates with 7 replicates for each dilution[78,83]. To each well, 900 μl of the media was added, and then 100 μl of the respective dilution of the soil was added. Each dilution was inoculated into 7 wells, while 1 well served as a sterile control and remained uninoculated (no dilution of soil added, only anoxic media with lactate, acetate and ferrihydrite amendments)[82]. For anoxic incubation, the Anaerocult system (Merck, Germany) was used, together with an O2 indicator stick (Merck, Germany). Incubation was done for 8 weeks at 20°C in the dark. Generally, anoxic MPN deep-well plates were evaluated visually for positive growth, as reduced-black Fe(II) minerals formed were easily detectable, meanwhile the control stayed rusty-orange[82]. To calculate the cell numbers (cells/g soil) from the positive MPN wells, all positive wells per dilution were counted and the most probable number was calculated using the software program KLEE, applying confidence limits of Cornish and Fisher (1938)[84] and the bias correction after Salama (1978)[85,86]. Further isolation of Fe(III)-reducing bacteria was performed with same media and supplies via multiple round of dilution to extinction. DNA was extracted of the further isolated culture (after 7 transfers) using the UltraClean® Microbial DNA Isolation Kit (MO BIO Labratories, Carlsbad, CA, US). 16S rRNA gene fragments were amplified using the 341F (CCTACGGGAGGCAGCAG) and 907R (CCGTCAATTCCTTTRAGTTT) primer pair[87] and resulting amplicons were sent for Sanger sequencing (Eurofins GATC biotech, Konstanz, Germany). Sequence results were analyzed using nucleotide BLAST (Basic Local Alignment Search Tool) to identify the closest relative.

Results and Discussion

Thaw increases aqueous Fe^{2+} and dissolved organic carbon

Along the thaw gradient, the aqueous Fe^{2+} in the porewater increased from average concentrations of 0.02±0.01 mM in the palsa to up to 1.6±0.3 mM in the fen transition zone (Fig. 2). This correlates with an increase in average dissolved organic carbon (DOC) from 19.7±0.8 mg/L in the palsa to 102.1±14.1 mg/L in the fen area. In the bog porewater, acetate (0.6±0.1 mM) was measurable in the transition zone and mineral horizon, whereas lactate (0.8±0.02 mM) was only found in the transition zone. (Fig. 2). At the fen site, lactate and acetate were detected throughout the depth profile (0.2±0.1 mM). An additional peak in acetate (2.3±0.01 mM), propionate (0.8±0.02 mM) and butyrate (0.2±0.01 mM) was observed in the transition zone of the fen (Fig. 2). The appearance of butyrate and propionate in the fen porewater could be an indicator for ongoing microbial processes such as fermentation and methanogenesis in the more water-logged and thus more reduced fen soils. This is in line with observations from previous studies that highest methane emissions occur in the fen[24]. Our porewater data along the thaw gradient clearly shows an increase in aqueous Fe^{2+} and more labile organic carbon. It also highlights unique biogeochemical processes in the transition zone leading to the consumption or accumulation of fatty acids in this layer. The presence of more labile organic carbon in the porewater is consistent with previous work[21]. The palsa to bog catchment was described previously to have no other extrinsic sources of Fe or DOC[28]. The fen catchment however is hydrologically influenced by palsa to bog flow and by surrounding surface water bodies (ponds, river and lake)[28]. Analysis of this surface water showed average DOC concentrations of 24.87 ± 6.68 mg/L and average aqueous Fe^{2+} concentrations of 0.02 ± 0.02 mg/L. Thus, these extrinsic surface water sources cannot explain the high Fe and DOC measured in the fen.

The abundance of Fe(III)-reducing bacteria increases with thaw

The trend in increasing aqueous Fe^{2+} and DOC concentrations observed across the thaw gradient goes hand in hand with a significant increase in abundance of Fe(III)-reducing bacteria in the organic horizon from palsa to fen (unpaired t-test, N=7, α=0.05, p=0.0001) and a significant increase in the transition zone from palsa to fen (unpaired t-test, N=7, α=0.05, p=0.0001). In the mineral horizon at all three thaw stages no difference in abundance of Fe(III)-reducing cells was observed ($2x10^3$ cells per g soil). In the palsa organic horizon, $2.4x10^2$ cells per g soil were found, in comparison to $2.6x10^4$ cells per g soil in the organic horizon in the fen. In the transition zone of palsa, $2.4x10^3$ cells per g soil were determined. Whereas, in the

fen transition zone the highest abundance of Fe(III)-reducing bacteria with $3.1x10^5$ cells per g soil was observed. The abundance of Fe(III)-reducing bacteria was determined via growth and Fe(III) reduction by Most Probable Numbers (MPNs). Further isolation efforts from the fen yielded a microorganism with 99% similarity on the 16S rRNA level to *Cupriavidus metallidurans* (Proteobacteria). The isolate was able to reduce ferrihydrite to Fe(II) whilst simultaneously consuming lactate and producing acetate (Supplementary Figure 6). It did not utilize acetate. Fe-associated organic carbon could further enhance or lower reduction rates of ferrihydrite (depending on the OC:Fe ratios), but is unlikely to prevent mineral dissolution[29]. *Cupravidus metallidurans* strains are known to be extremely metabolically flexible and can utilize lactate fermentation under anoxic conditions[30]. They are also highly tolerant of toxic metals[30]. Although Fe(III) reduction is usually thought of as a dissimilatory process, in some peatlands, Fe(III) reduction coupled to fermentative metabolisms have been observed to be more common[31]. This could be one explanation for the acetate peak in the fen transition zone and increasing Fe(II) concentrations in the fen. Woodcroft *et al.* (2018)[25] describes evidence of lactate fermentation along this thaw gradient and found Proteobacteria as one of primary lactate metabolizers in the fen. Our growth-dependent quantification is suggestive of increased microbially-driven Fe(III) mineral dissolution along the thaw gradient (Fig. 2).

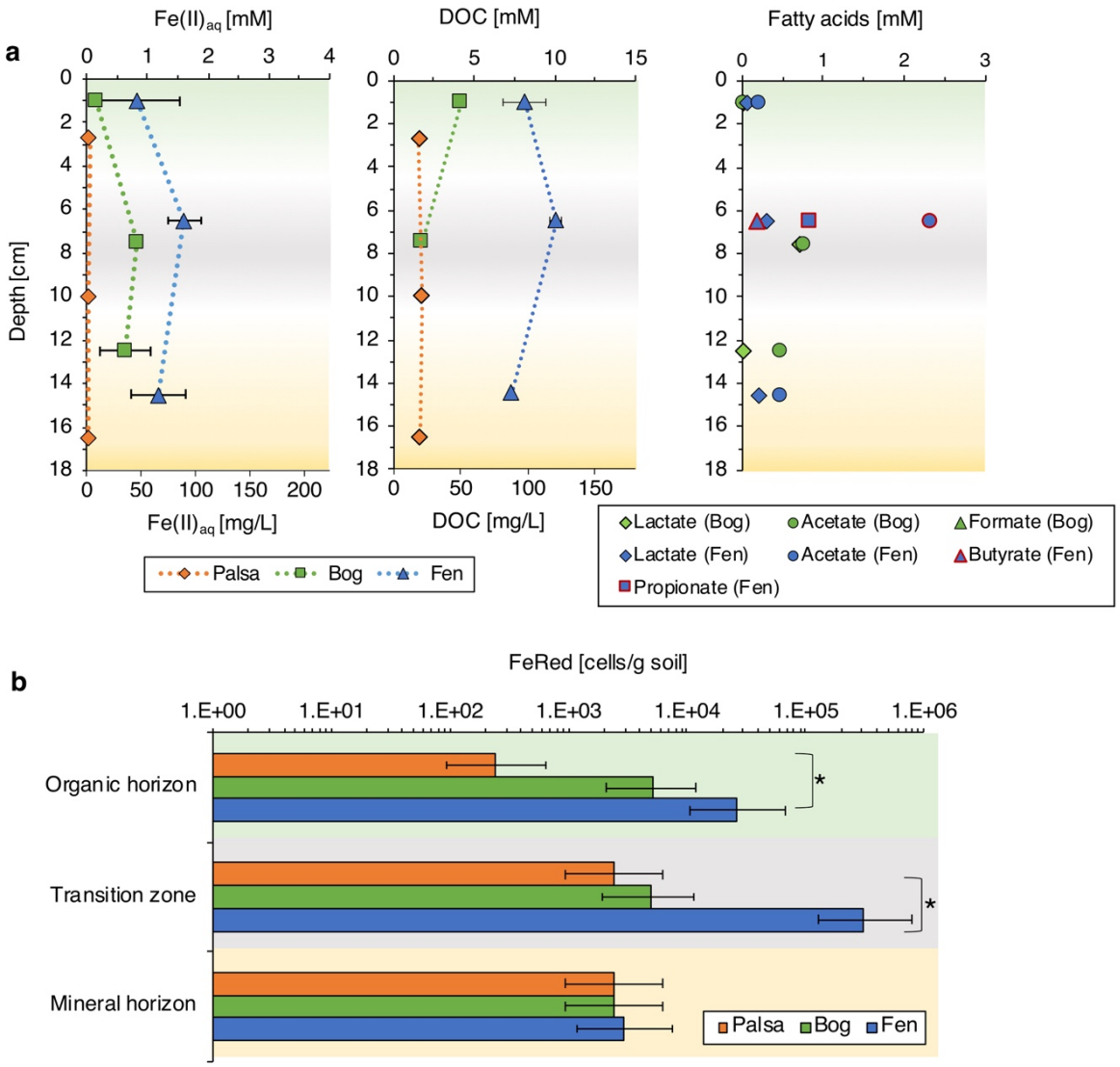

Figure 2. Increasing iron and dissolved organic carbon concentrations accompanied by an increase in abundance of Fe(III)-reducing bacteria along the permafrost thaw gradient. *a, Porewater geochemical analysis of the cores Palsa A, Bog C and Fen E and b, most probable number quantifications of Fe(III)-reducing bacteria (FeRed) in the solid phase of the cores Palsa A, Bog C and Fen E along the thaw gradient. Red marks the high acetate concentrations in the fen, in comparison to the bog, and the additional fatty acids butyrate and propionate, only detected in the fen. The error bars of the porewater data represent triplicate measurements. The error bars of the most probable number estimations of Fe(III)-reducers represent 7 replicate analyses and indicate lower and upper limits of the 95% confidence intervals. * marks significant difference between FeRed in palsa and fen, organic horizon and transition zone (unpaired t-test, N=7, α = 0.05, p = 0.0001). The green background marks the organic horizon, grey the transition zone, and yellow the mineral horizon. The backgrounds*

for the porewater geochemistry are shaded due to the fact that this represents three cores, one core per thaw stage, with different horizon depths.

Reactive iron minerals are dissolved along the thaw gradient

In order to determine whether the observed increases in DOC were related to increased Fe(III) mineral reduction and dissolution, we quantified the amount of organic carbon associated with the reactive iron minerals along the thaw gradient by applying the citrate-dithionite iron reduction method[5,32,33]. This method simultaneously dissolves all reactive solid iron phases and releases the organic carbon associated with these minerals into solution. The extraction is performed at circumneutral pH to prevent hydrolysis of organic matter as well as its protonation and re-adsorption onto the remaining solid phases and thus its precipitation. A control experiment was conducted at the same pH with equivalent ionic strength (sodium chloride instead of the reducing agent sodium dithionite). The organic carbon which is released in this control is not associated with the reactive iron minerals and was therefore subtracted from the amount of carbon released from the dithionite-citrate extractions as previously described[5] (Supplementary Table 1). Well-known issues with these extractions and a discussion of how we have overcome these are included in the Supplementary Information (Supplementary Method 1, Supplementary Figures 7 and 8). Additionally, we performed a sodium hydroxylamine-hydrochloric acid (HCl) extraction (pH<2) to target the poorly crystalline iron minerals, a sodium pyrophosphate extraction (pH 10) to extract colloidal or OM-chelated iron, and a 6M HCl extraction to obtain more crystalline iron phases of the soil layers (referred to as mg Fe(tot) per g) (Fig. 3). It should be noted that the total amount of iron per dry weight in the layers is different along the thaw gradient due to different redox-driven biogeochemical cycles in the three different thaw stages resulting in loss of total soil organic carbon and thus in an increasing abundance of the mineral material present in the active layer (Supplementary Figures 1-4 for spatial and horizontal variance in replicate cores). Stocks (mg/cm^2) were calculated, but due to slight compaction, mainly for the organic horizons, not reported in the main text (Supplementary Figure 9). In the following, only the data from cores Palsa A, Bog C and Fen E are discussed (Fig. 1, Fig. 3 and Fig. 4), but observed trends are supported by further analyses conducted on cores analyzed in the same manner, but collected in 2019 (Palsa a, Bog c and Fen e) (Supplementary Figure 2), as well as cores collected at the same time as Palsa A, Bog C and Fen E in 2018 but stored for a longer period (Palsa B, Bog D, Fen F) (Supplementary Figure 3). We also observed similar trends in triplicate cores from each thaw stage, collected in 2017 and analyzed with different but comparable methods (Supplementary Figure 4 and 5). The collected cores capture the three thaw stages over three

years (2017, 2018 and 2019) (Supplementary Figure 1) and show that the trends of Fe and organic carbon along the thaw gradient are robust.

In the transition zone of the palsa, the reducible iron mineral fraction was 72.9 to 93.9% of the total extractable iron (2.6±0.6 to 8.44 mg reactive Fe per g soil in comparison to 3.5±0.1 to 9.0±0.3 mg Fe(tot) per g soil) (Fig. 3, Supplementary Table 1). We suggest that this is driven by Fe(III) reduction in deeper layers leading to mobilization of Fe^{2+}_{aq}. This can be subsequently re-oxidized close to the interface between the organic horizon and mineral horizon by O_2 which diffuses from the surface. Oxidation will result in precipitation as Fe(III) oxyhydroxide minerals at this transition, as has been previously suggested for boreal peat soils[34]. The amount of reactive iron minerals in the transition zone then decreased to 11.1% of the total extractable iron in the bog (2.1±0.1 mg reactive Fe per g soil in comparison to 18.7±0.7 mg Fe(tot) per g soil) and to 18.3% of the extractable iron in the fen (2.6±0.03 mg reactive Fe per g soil in comparison to 14.5±0.2 mg Fe(tot) per g soil) (Fig. 3, Supplementary Table 1). In the mineral horizons along the thaw gradient, a loss of the reactive iron minerals was also observed, likely due to more reduced conditions favoring Fe(III) mineral reduction at deeper depths. Reactive iron in the palsa mineral layer was 10.0 to 36.6% of the total extractable iron (3.2±0.2 to 1.4±0.2 mg reactive Fe per g soil in comparison to 8.7±0.3 to 13.5±0.2 mg Fe(tot) per g soil) and declined to 7.5% of the total extractable iron in the bog (0.9±0.1 mg reactive Fe per g soil in comparison to 11.7±0.8 mg Fe(tot) per g soil) and 9.0 to 10.7% of the total iron in the fen (1.8±0.04 to 1.7±0.04 mg reactive Fe per g soil in comparison to 16.3±0.4 to 19.01±0.25 mg Fe(tot) per g soil) (Fig. 3, Supplementary Table 1). This loss of reactive iron in the transition zone and mineral horizon was also confirmed by the hydroxylamine-HCl extraction and iron speciation by EXAFS (Fig. 3). The abundance of colloidal and/or OM-complexed iron (defined as sodium pyrophosphate extractable iron) also decreased along the thaw gradient, giving way to an increasing relative atom percent-based abundance of Fe-bearing clays (Fig. 3). This observation is consistent with increasing aluminum concentrations in the extracts (Supplementary Figure 10). The iron content in the organic layer increased from almost no iron in the palsa (0.2±0.02 mg Fe(tot) per g soil, all poorly crystalline) to 4.7±0.01 mg Fe(tot) per g soil (with 43.4% of the total extractable iron being reactive iron) in the organic layer of the fen (Fig. 3). This might again be driven by Fe(III) reduction in deeper layers leading to mobilization of Fe^{2+}_{aq}, which might precipitate now close to the water table.

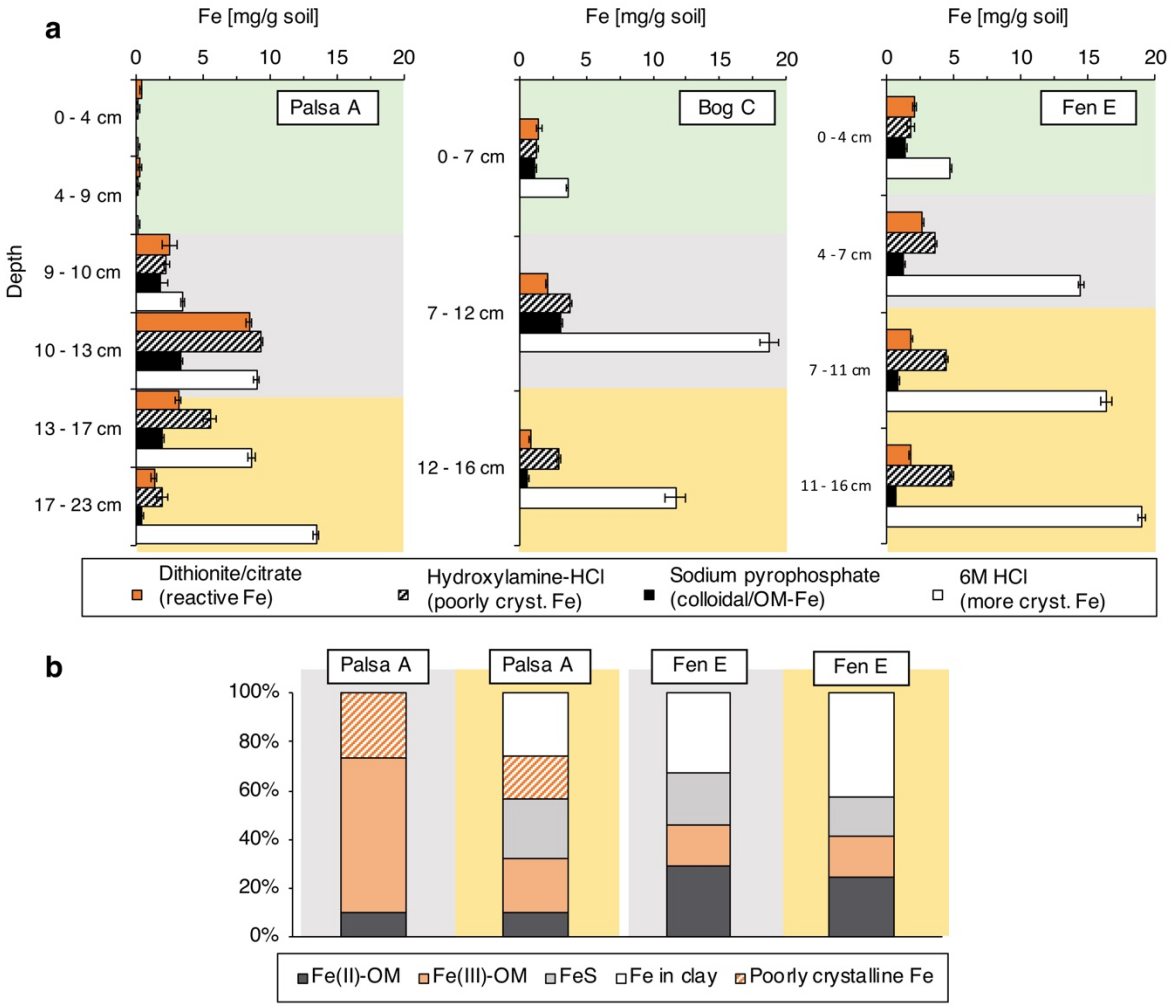

Figure 3. Reactive Fe along the permafrost thaw gradient. Fe speciation was determined along the thaw gradient by a, selective extractions and b, extended X-ray absorption fine structure (EXAFS). *The reactive iron mineral fraction [mg iron (Fe) per g soil] was quantified in the different layers, control corrected by a sodium chloride bicarbonate extraction with the same ionic strength and pH (Supplementary Table 1), and compared to the more crystalline Fe (6M HCl extractable Fe, referred to mg Fe(tot) per g soil in the text) and to the colloidal and/or organic matter (OM)-chelated Fe. Please note the differences in the scale of y-axis due to variable thickness of each soil layer along the thaw gradient. The green background marks the organic horizon, grey the transition zone, and yellow the mineral horizon. Error bars of all extractions represent duplicate extractions of each layer per thaw stage, except for the dithionite citrate extractable iron which represents a combined standard deviation of sodium chloride bicarbonate extractable iron and dithionite/citrate extractable iron (not control corrected). EXAFS results of the transition zone and the mineral horizon of the two-end members palsa and fen show loss of the poorly crystalline Fe (reference probe: 2-line ferrihydrite), the decrease in OM-chelated Fe (reference probes: Fe(II)-citrate and Fe(III)-citrate), the increase of Fe in clays (reference probes: natural nontronite and ferrosmectite)*

and Fe sulfur species (reference probe: mackinawite) with depth and along the thaw gradient. Absolute values are reported in Supplementary Table 1.

Dissolution of reactive iron minerals releases associated organic carbon

With the dissolution of reactive iron minerals along the thaw gradient, the mineral-associated carbon was mobilized. Organic carbon bound to the reactive iron phases is primarily found in the transition zone and the mineral horizon of the palsa, as well as in the transition zone of the bog (Fig. 4, Supplementary Table 1). 9.9 to 14.8% of the total organic carbon (31.0±0.7 to 52.5±0.1 mg organic carbon bound to reactive Fe per g soil) was released by reductive dissolution of reactive iron minerals in the palsa transition (Fig. 4, Supplementary Table 1). In the palsa mineral horizon, 18.7 to 20.1% of the total organic carbon (13.6±0.42 mg organic carbon bound to reactive Fe per g soil in comparison to 72.7±0.29 to 136.1±0.2 mg total soil organic carbon per g soil) was released. In the transition zone of the bog, 39.4% of the total organic carbon (22.7±8.6 mg organic carbon bound to reactive Fe per g soil in comparison to 57.5±0.4 mg total soil organic carbon per g soil) was associated with iron minerals (Fig. 4, Supplementary Table 1). However, it should be noted that the total amount of carbon was less in these samples (57.5±0.4 mg total soil organic carbon per g soil) when compared to the palsa transition zone (312.1±0.3 to 354.7±0.04 mg total soil organic carbon per g soil) due to total carbon loss along the thaw gradient. Highest total amounts of carbon bound by the reactive iron were therefore found in the palsa transition zone with an average of 41.8±10.8 mg per g soil. This is also supported by the strong spatial association of C with Fe minerals in the fine fraction of this transition zone observed by nanoSIMS analysis (Fig. 4, Supplementary Figure 11), as has been also previously shown for intact permafrost soils[35]. The maximum mass ratio of organic carbon to iron of 0.22, based on the maximal sorption capacity of reactive iron oxides for natural organic matter[4,36], as has been previously done to further characterize Fe-C associations in such systems[37,38], was exceeded for reactive Fe-associated organic carbon:reactive Fe, determined via the sodium dithionite citrate extraction, in the bulk palsa soil layers (organic/transition/mineral), in the bulk bog organic horizon and in the bulk bog transition zone (8.59±3.0 OC:Fe (wt:wt)) (Supplementary Table 1). This suggests co-precipitation and/or chelation of organic compounds also in the bulk sample which can generate structures with OC:Fe ratios above 0.22, as shown in other studies[4]. Existence of such structures is consistent with our high sodium pyrophosphate extractable iron values.

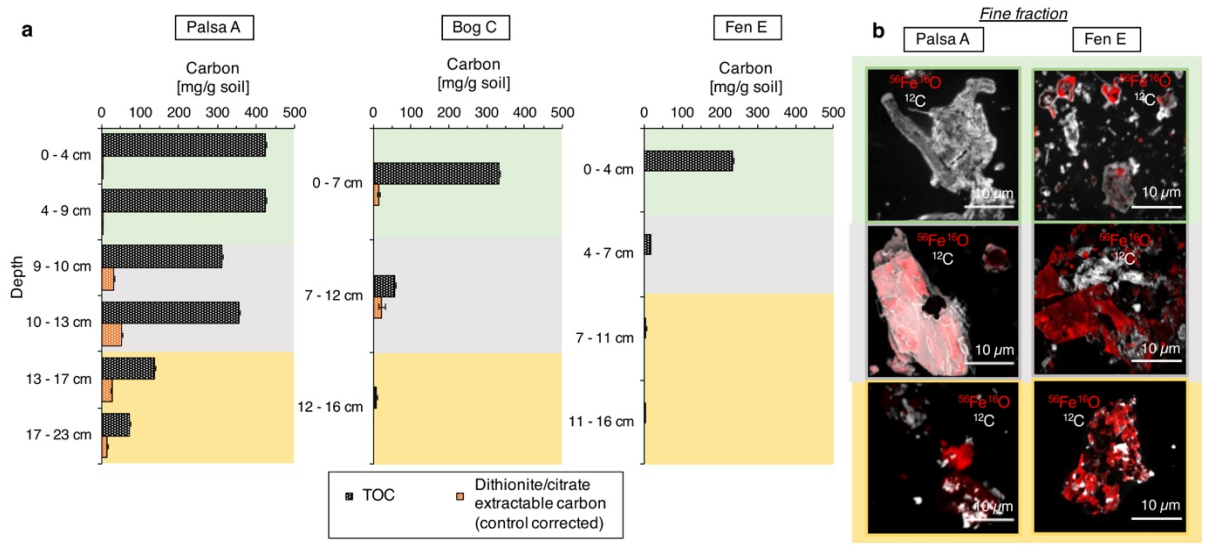

Figure 4. Reactive Fe bound organic carbon along the permafrost thaw gradient. *Iron (Fe) carbon (C) associations were determined along the thaw gradient by bulk (b) and fine fraction analysis (a). a, Carbon bound by reactive iron minerals along the thaw gradient. The carbon which dislodged from the soil during the reductive dissolution of reactive iron oxides (orange) is shown in comparison to the total organic carbon determined via combustion (black grids, labelled as total organic carbon (TOC)). Dithionite-citrate extractable carbon is control-corrected by subtracting the measured dissolved organic carbon (DOC) content of a citrate solution and the measured DOC value from the sodium chloride (NaCl) control experiment. The NaCl control (same ionic strength and same pH as the sodium dithionite citrate extraction) shows negligible carbon release (Supplementary Table 1). Errors of the TOC indicate the range of duplicate analyses of each layer in each thaw stage. Errors of the dithionite/citrate extractable carbon (control corrected) represent a combined standard deviation of sodium chloride bicarbonate extractable OC, citrate blank and dithionite/citrate extractable OC (not control corrected). b, High spatial resolution analysis of iron-carbon associations by nanoSIMS along the thaw gradient (two end-members palsa (left) and fen (right)). The strong spatial association of carbon (C) to iron (Fe) (III) minerals could only be observed in the palsa transition zone. The other fine fractions showed organic-free iron minerals. For the two end-members palsa and fen, four particles of the fine fractions of each layer were analyzed by nanoSIMS, all showing the same spatial distribution of Fe and C as shown by these six representatives (see also Supplementary Figure 11). The green background marks the organic horizon (b, upper images), grey the transition zone (b, middle images), and yellow the mineral horizon (b, lower images).*

Implications for stability of Fe-associated carbon in thawing permafrost peatlands

Carbon binding to reactive iron minerals in the palsa area is consistent with previous observations in permafrost regions of the Qinghai-Tibet Plateau[33] where Fe associated organic carbon represents, on average, 19.5±12.3% of the total soil organic carbon pool in the upper 30 cm of permafrost soils throughout the year. Assuming a carbon pool of 191.29 x 10^{15} g carbon in the active layer (0-30 cm depth)[39] in northern permafrost regions, we suggest that 13.39 x 10^{15} to 38.26 x 10^{15} g carbon could potentially be bound to reactive iron in permafrost soils. The lower estimate assumes, based on our data, an average of 7% of total organic carbon is bound to reactive iron in active layers underlain by intact permafrost (Supplementary Table 1, average mg C bound to reactive Fe per g soil in comparison to average mg TOC per g soil in %). The higher estimate assumes a maximum of 20% of total organic carbon is bound to reactive iron, based on our data (Supplementary Table 1) and Mu *et al.* (2016)[33]. This Fe-bound carbon stock is equivalent to approximately 2-5% of the amount of carbon which is currently present in the atmosphere which is equivalent to between 2 and 5 times the amount of carbon released yearly through anthropogenic fossil fuel emissions. Fisher *et al*. (2020) even showed evidence for only partial dissolution of the Fe phases and associated organic carbon by the dithionite-citrate approach, indicating that carbon sequestration by Fe minerals is likely to be more significant than currently estimated[40]. However, this estimate does not account for carbon sequestration by biomass in the fen or deeper layers. Stock calculations show a higher Fe-associated OC fraction in mineral horizon than in the palsa transition zone which could indicate that OC sequestration by reactive Fe minerals is likely to be more significant in deeper layers than currently estimated (Supplementary Figure 9). It is therefore crucial to further determine the amount of iron in deeper layers, the amount of carbon bound to reactive iron minerals in numerous permafrost environments, and the lability/bioavailability of this carbon following its release.

Our space for time-approach reveals, for the first time, how we may expect the dynamics of this rusty carbon sink to respond to progressive climate change. This study suggests that, as soon as the conditions in permafrost peatlands become water-logged, the reactive iron minerals are reduced, probably by Fe(III)-reducing bacteria, and dissolved iron and associated organic carbon are released into the surrounding porewater. As has been stated previously, reactive Fe phases require their own physiochemical protection in order to contribute to organic matter persistence[14] and the presence of organic matter itself can both increase or decrease the stability of Fe(III) minerals depending on the geochemical conditions. High C/Fe

ratios, shown to enhance the extent of bioreduction compared to pure reactive iron mineral phases[29], could be one explanation as to why the reactive Fe phases present in these soils were not resistant to mineral dissolution with permafrost thaw. High C/Fe ratios were thought to enhance reduction rates[29] due to the function of carbon as electron shuttle[41], its role as a strong ligand for Fe complexation[42], or its importance for particle aggregation[43]. Additionally, co-association of aluminum and iron with organic matter could have further made this rusty carbon sink more susceptible to reductive dissolution[44]. On the other hand, reduction-resistant surface coatings, embedding in a composite aggregate structure [6,13], or higher Fe mineral crystallinity[45] could prevent mineral dissolution.

Chen *et al*. (2020)[14] showed the formation of more crystalline Fe phases under O_2 fluctuations and suggested a substantial loss of co-precipitated organic matter under repeated redox fluctuations with a remaining Fe-bound fraction of organic matter resistant to reductive dissolution. In the bog thaw stage, redox fluctuations may have led to a core Fe-MAOM structure[14] (Fe mineral associated organic matter) but constant reducing conditions in the fen caused a complete loss of Fe-bound carbon in the solid phase.

It should be kept in mind that it is not only the released carbon that can directly contribute to greenhouse gas emissions. The reduction of Fe(III) itself will also contribute to CO_2 emissions since it is directly coupled to the oxidation and mineralization of organic carbon. On the other hand, since Fe(III) reduction is more thermodynamically favorable, conditions more suitable for Fe(III)-reducers can also inhibit methanogenesis[46]. However, Fe(III) reduction consumes protons and leads to an increase in pH which can make conditions more favorable for methanogens[47]. Along the thaw gradient, an increase in pH and an increasing abundance of methanogens has been reported[24]. Acetotrophic methanogens can use Fe(III) reduction to maximize energy conservation from metabolism of acetate[48]. Shifts in CH_4 production pathway from CO_2 to acetate cleavage along the thaw gradient was previously described[21,24]. At the same time, anaerobic oxidation of methane by methanotrophs can also be coupled to Fe(III) reduction. An increase in methane oxidation rates along the thaw gradient has been shown by Perryman *et al.* (2020)[26]. Our data clearly show that reactive Fe phases serve as an important and overlooked, terminal electron acceptor along the thaw gradient and thus could exert a significant control on net methane emissions.

Furthermore, the released aqueous Fe^{2+} could be complexed by organic carbon[10] along the thaw gradient, inhibiting re-oxidation even when oxygen concentrations are high. The peatland at Stordalen mire could be a significant source of bioavailable iron to surrounding lakes and rivers, as has been shown at other permafrost environments[49]. It has also been shown that Fe(III) minerals can act as sieves for DOM by selectively trapping terrestrially derived OM (enriched in aromatic moieties) on mineral surfaces at redox interfaces[10]. More work is needed to elucidate the chemical nature of associated organic carbon to determine its lability, but our data suggest that direct chelation or co-precipitation of Fe-C structures play an essential role in carbon protection.

In order to better predict future greenhouse gas emissions from thawing permafrost soils and improve the accuracy of existing climate models, it is therefore crucial to further determine Fe(III) reduction rates, its direct contribution to CO_2 emissions from peatland mires and its competition with other microbial processes, such as e.g. methanogenesis or methanotrophy.

Acknowledgements

The authors would like to acknowledge the Abisko Research Station (Abisko, Sweden) for their support during sampling missions. We thank H. Miller (Colorado State University, Fort Collins, United States) for her assistance with EXAFS analysis, G. Harrington and J. Lugmeier (Munich, Germany) for nanoSIMS analysis and E. Stopelli (Zuerich, Switzerland) for ICP-MS measurements. This work was supported by the University of Tübingen (Programme for the Promotion of Junior Researchers grant to C.B) and by the German Academic Scholarship Foundation (scholarship to M.P). Use of the Stanford Synchrotron Radiation Lightsource, SLAC National Accelerator Laboratory, is supported by the U.S. Department of Energy, Office of Science, Office of Basic Energy Sciences under Contract No. DE-AC02-76SF00515.

References

1 Estop-Aragones, C. *et al.* Limited release of previously-frozen C and increased new peat formation after thaw in permafrost peatlands. *Soil Biol Biochem* **118**, 115-129 (2018).

2 Kleber, M. *et al.* Mineral-Organic Associations: Formation, Properties, and Relevance in Soil Environments. *Adv Agron* **130**, 1-140 (2015).

3 Kogel-Knabner, I. *et al.* Organo-mineral associations in temperate soils: Integrating biology, mineralogy, and organic matter chemistry. *J Plant Nutr Soil Sc* **171**, 61-82 (2008).

4 Wagai, R. & Mayer, L. M. Sorptive stabilization of organic matter in soils by hydrous iron oxides. *Geochim Cosmochim Ac* **71**, 25-35 (2007).

5 Lalonde, K., Mucci, A., Ouellet, A. & Gelinas, Y. Preservation of organic matter in sediments promoted by iron. *Nature* **483**, 198-200 (2012).

6 Asano, M. & Wagai, R. Evidence of aggregate hierarchy at micro- to submicron scales in an allophanic Andisol. *Geoderma* **216**, 62-74 (2014).

7 Totsche, K. U. *et al.* Microaggregates in soils. *J Plant Nutr Soil Sc* **181**, 104-136 (2018).

8 Coward, E. K., Thompson, A. T. & Plante, A. F. Iron-mediated mineralogical control of organic matter accumulation in tropical soils. *Geoderma* **306**, 206-216 (2017).

9 Kleber, M., Mikutta, R., Torn, M. S. & Jahn, R. Poorly crystalline mineral phases protect organic matter in acid subsoil horizons. *Eur J Soil Sci* **56**, 717-725 (2005).

10 Riedel, T., Zak, D., Biester, H. & Dittmar, T. Iron traps terrestrially derived dissolved organic matter at redox interfaces. *P Natl Acad Sci USA* **110**, 10101-10105 (2013).

11 Eusterhues, K. *et al.* Reduction of ferrihydrite with adsorbed and coprecipitated organic matter: microbial reduction by Geobacter bremensis vs. abiotic reduction by Na-dithionite. *Biogeosciences* **11**, 4953-4966 (2014).

12 Henneberry, Y. K., Kraus, T. E. C., Nico, P. S. & Horwath, W. R. Structural stability of coprecipitated natural organic matter and ferric iron under reducing conditions. *Org Geochem* **48**, 81-89 (2012).

13 Coward, E. K., Thompson, A. & Plante, A. F. Contrasting Fe speciation in two humid forest soils: Insight into organomineral associations in redox-active environments. *Geochim Cosmochim Ac* **238**, 68-84 (2018).

14 Chen, C., Hall, S. J., Coward, E. & Thompson, A. Iron-mediated organic matter decomposition in humid soils can counteract protection. *Nat Commun* **11**, 2255 (2020).

15 Herndon, E. M. *et al.* Pathways of anaerobic organic matter decomposition in tundra soils from Barrow, Alaska. *J Geophys Res-Biogeo* **120**, 2345-2359 (2015).

16 Lipson, D. A., Jha, M., Raab, T. K. & Oechel, W. C. Reduction of iron (III) and humic substances plays a major role in anaerobic respiration in an Arctic peat soil. *J Geophys Res-Biogeo* **115**, G00I06 (2010).

17 Olefeldt, D., Turetsky, M. R., Crill, P. M. & McGuire, A. D. Environmental and physical controls on northern terrestrial methane emissions across permafrost zones. *Global Change Biol* **19**, 589-603 (2013).

18 Turetsky, M. R. *et al.* Short-term response of methane fluxes and methanogen activity to water table and soil warming manipulations in

an Alaskan peatland. *J Geophys Res-Biogeo* **113**, G000496 (2008).

19 Zona, D. *et al.* Methane fluxes during the initiation of a large-scale water table manipulation experiment in the Alaskan Arctic tundra. *Global Biogeochem Cy* **23**, GB2013 (2009).

20 Malmer, N., Johansson, T., Olsrud, M. & Christensen, T. R. Vegetation, climatic changes and net carbon sequestration in a North-Scandinavian subarctic mire over 30 years. *Global Change Biol* **11**, 1895-1909 (2005).

21 Hodgkins, S. B. *et al.* Changes in peat chemistry associated with permafrost thaw increase greenhouse gas production. *P Natl Acad Sci USA* **111**, 5819-5824 (2014).

22 Johansson, T. *et al.* Decadal vegetation changes in a northern peatland, greenhouse gas fluxes and net radiative forcing. *Global Change Biol* **12**, 2352-2369 (2006).

23 Swindles, G. T. *et al.* The long-term fate of permafrost peatlands under rapid climate warming. *Sci Rep* **5**, 17951 (2015).

24 McCalley, C. K. *et al.* Methane dynamics regulated by microbial community response to permafrost thaw. *Nature* **514**, 478-481, doi:10.1038/nature13798 (2014).

25 Woodcroft, B. J. *et al*. Genome-centric view of carbon processing in thawing permafrost. *Nature* **560**, 49-54 (2018).

26 Perryman, C. R. *et al*. Thaw Transitions and Redox Conditions Drive Methane Oxidation in a Permafrost Peatland. *J Geophys Res-Biogeo* **125**, G005526 (2020).

27 Rydén, B. E., Fors, L & Kostov, L. Physical properties of the tundra soil-water system at Stordalen, Abisko. *Ecol Bull* **30**, 27-54 (1980).

28 Olefeldt, D. & Roulet, N. T. Effects of permafrost and hydrology on the composition and transport of dissolved organic carbon in a subarctic peatland complex. *J Geophys Res-Biogeo* **117**, G01005 (2012).

29 Shimizu, M. *et al.* Dissimilatory Reduction and Transformation of Ferrihydrite-Humic Acid Coprecipitates. *Environ Sci Technol* **47**, 13375-13384 (2013).

30 Janssen, P. J. *et al.* The complete genome sequence of Cupriavidus metallidurans strain CH34, a master survivalist in harsh and anthropogenic environments. *PLoS One* **5**, e10433 (2010).

31 Reiche, M., Torburg, G. & Küsel, K. Competition of Fe(III) reduction and methanogenesis in an acidic fen. *FEMS Microbiol Ecol* **65**, 88-101 (2008).

32 Mehra, O. P. & Jackson, M. L. Iron oxide removal from soils and clays by a dithionite-citrate system buffered with sodium bicarbonate. *Clays Clay Min.* **7**, 317-327 (1958).

33 Mu, C. C. *et al.* Soil organic carbon stabilization by iron in permafrost regions of the Qinghai-Tibet Plateau. *Geophys Res Lett* **43**, 10286-10294 (2016).

34 Herndon, E. M. *et al*. Iron (oxyhydr)oxides serve as phosphate traps in tundra and boreal peat soils. *J Geophys Res-Biogeo* **124**, G004776 (2019).

35 Sowers, T. D. *et al*. Spatially-resolved organomineral interactions across a permafrost chronosequence. *Environ Sci Technol* **54**, 2951-2960 (2020).

36 Kaiser, K. & Guggenberger, G. Sorptive stabilization of organic matter by microporous goethite: sorption into small pores vs. surface complexation. *Eur J Soil Sci* **58**, 45-59 (2007).

37 Herndon, E. M. *et al*. Influence of iron redox cycling on organo-mineral associations in Arctic tundra soil. *Geochim Cosmochim Ac* **207**, 210-231 (2017).

38 Mu, C. C. *et al*. Organic carbon stabilized by iron during slump

deformation on the Qinghai-Tibetan Plateau. *Catena* **187**, 104282 (2020).

39 Tarnocai, C. *et al.* Soil organic carbon pools in the northern circumpolar permafrost region. *Global Biogeochem Cy* **23**, GB2023 (2009).

40 Fisher, B. J., Moore, O. W., Faust, J. C. & Peacock, C. L. Experimental evaluation of the extractability of iron bound organic carbon in sediments as a function of carboxyl content. *Chem Geol* **556**, 119853-119853 (2020).

41 Roden, E. E. *et al.* Extracellular electron transfer through microbial reduction of solid-phase humic substances. *Nat Geosci* **3**, 417-421 (2010).

42 Jones, A. M., Collins, R. N., Rose, J. & Waite, T. D. The effect of silica and natural organic matter on the Fe(II)-catalysed transformation and reactivity of Fe(III) minerals. *Geochim Cosmochim Ac* **73**, 4409-4422 (2009).

43 Amstaetter, K., Borch, T. & Kappler, A. Influence of humic acid imposed changes of ferrihydrite aggregation on microbial Fe(III) reduction. *Geochim Cosmochim Ac* **85**, 326-341 (2012).

44 Masue-Slowey, Y., Loeppert, R. H. & Fendorf, S. Alteration of ferrihydrite reductive dissolution and transformation by adsorbed As and structural Al: Implications for As retention. *Geochim Cosmochim Ac* **75**, 870-886 (2011).

45 Hall, S. J., Berhe, A. A. & Thompson, A. Order from disorder: do soil organic matter composition and turnover co-vary with iron phase crystallinity? *Biogeochemistry* **140**, 93-110 (2018).

46 Van Bodegom, P. M., Scholten, J. C. M. & Stams, A. J. M. Direct inhibition of methanogenesis by ferric iron. *FEMS Microbiol Ecol* **49**, 261-268 (2004).

47 Wagner, R., Zona, D., Oechel, W. & Lipson, D. Microbial community structure and soil pH correspond to methane production in Arctic Alaska soils. *Method Enzymol* **19**, 3398-3410 (2017).

48 Prakash, D., Chauhan, S. S. & Ferry, J. G. Life on the thermodynamic edge : Respiratory growth of an acetotrophic methanogen. *Sci Adv* **5**, eaaw9059 (2019).

49 Pokrovsky, O. S., Manasypov, R. M., Loiko, S. V. & Shirokova, L. S. Organic and organo-mineral colloids in discontinuous permafrost zone. *Geochim Cosmochim Ac* **188**, 1-20 (2016).

50 Mondav, R. *et al.* Discovery of a novel methanogen prevalent in thawing permafrost. *Nat Commun* **5**, 3212 (2014).

51 Malhotra, A. & Roulet, N. T. Environmental correlates of peatland carbon fluxes in a thawing landscape: do transitional thaw stages matter? *Biogeosciences* **12**, 3119-3130 (2015).

52 Akerman, H. J. & Johansson, M. Thawing permafrost and thicker active layers in sub-arctic Sweden. *Permafrost Periglac* **19**, 279-292 (2008).

53 Klaminder, J., Yoo, K., Rydberg, J. & Giesler, R. An explorative study of mercury export from a thawing palsa mire. *J Geophys Res-Biogeo* **113**, G000776 (2008).

54 Callaghan, T. V. *et al.* A new climate era in the sub-Arctic: Accelerating climate changes and multiple impacts. *Geophys Res Lett* **37**, L14705 (2010).

55 Jorgenson, M. T., Racine, C. H., Walters, J. C. & Osterkamp, T. E. Permafrost degradation and ecological changes associated with a warming climate in central Alaska. *Climatic Change* **48**, 551-579 (2001).

56 O'Donnell, J. A. *et al.* The Effects of Permafrost Thaw on Soil

Hydrologic, Thermal, and Carbon Dynamics in an Alaskan Peatland. *Ecosystems* **15**, 213-229 (2012).

57 Payette, S., Delwaide, A., Caccianiga, M. & Beauchemin, M. Accelerated thawing of subarctic peatland permafrost over the last 50 years. *Geophys Res Lett* **31**, GL020358 (2004).

58 Vitt, D. H., Halsey, L. A. & Zoltai, S. C. The changing landscape of Canada's western boreal forest: the current dynamics of permafrost. *Can J Forest Res* **30**, 283-287 (2000).

59 Quinton, W. L., Hayashi, M. & Chasmer, L. E. Permafrost-thaw-induced land-cover change in the Canadian subarctic: implications for water resources. *Hydrol Process* **25**, 152-158 (2011).

60 Zoltai, S. C. Cyclic Development of Permafrost in the Peatlands of Northwestern Alberta, Canada. *Arctic Alpine Res* **25**, 240-246 (1993).

61 Stookey, L. L. Ferrozine - a New Spectrophotometric Reagent for Iron. *Anal Chem* **42**, 779-781 (1970).

62 Bockheim, J. G., Hinkel, K. M. & Nelson, F. E. Predicting carbon storage in tundra soils of arctic Alaska. *Soil Sci Soc Am J* **67**, 948-950 (2003).

63 Aller, R. C., Mackin, J. E. & Cox, R. T. Diagenesis of Fe and S in Amazon Inner Shelf Muds - Apparent Dominance of Fe Reduction and Implications for the Genesis of Ironstones. *Cont Shelf Res* **6**, 263-289 (1986).

64 Poulton, S. W. & Canfield, D. E. Development of a sequential extraction procedure for iron: implications for iron partitioning in continentally derived particulates. *Chem Geol* **214**, 209-221 (2005).

65 Heron, G., Crouzet, C., Bourg, A. C. M. & Christensen, T. H. Speciation of Fe(Ii) and Fe(Iii) in Contaminated Aquifer Sediments Using Chemical-Extraction Techniques. *Environ Sci Technol* **28**, 1698-1705 (1994).

66 Loeppert, R. H. & Inskeep, W. Iron. In: Sparks, D.L., Page, A.L, Helmke, P.A., Loeppert, R.H., Soltanpour, P.N., Tabatabai, M.A., Johnston, C.T., Summer, M.E. (1996).

67 Holmgren, G. G. A Rapid Citrate-Dithionite Extractable Iron Procedure. *Soil Sci Soc Am Pro* **31**, 210-211 (1967).

68 Rath, K. M., Maheshwari, A., Bengtson, P. & Rousk, J. Comparative toxicities of salts on microbial processes in soil *Appl Environ Microbiol* **82**, 2012-2020 (2012).

69 Lupascu, M., Wadham, J. L., Hornibrook, E. R. C. & Pancost, R. D. Temperature Sensitivity of Methane Production in the Permafrost Active Layer at Stordalen, Sweden: a Comparison with Non-permafrost Northern Wetlands. *Arct Antarct Alp Res* **44**, 469-482 (2012).

70 Siewert, M. B. High-resolution digital mapping of soil organic carbon in permafrost terrain using machine learning: a case study in a sub-Arctic peatland environment. *Biogeosciences* **15**, 1663-1682 (2018).

71 Hugelius, G. *et al*. Estimated stocks of circumpolar permafrost carbon with quantified uncertainty ranges and identified data gaps. *Biogeosciences* **11**, 6573-6593 (2014).

72 Hansel, C. M. *et al.* Secondary mineralization pathways induced by dissimilatory iron reduction of ferrihydrite under advective flow. *Geochim Cosmochim Ac* **67**, 2977-2992 (2003).

73 Daugherty, E. E., Gilbert, B., Nico, P. S. & Borch, T. Complexation and Redox Buffering of Iron(II) by Dissolved Organic Matter. *Environ Sci Technol* **51**, 11096-11104 (2017).

74 Troyer, L. D., Tang, Y. & Borch, T. Simultaneous reduction of arsenic(V) and uranium(VI) by mackinawite: role of uranyl arsenate precipitate formation. *Environ Sci Technol* **48**, 14326-14334 (2014).

75 Borch, T., Masue, Y., Kukkadapu, R. K. & Fendorf, S. Phosphate imposed limitations on biological reduction and alteration of ferrihydrite. *Environ Sci Technol* **41**, 166-172 (2007).

76 Kopittke, P. M. *et al.* Nitrogen-rich microbial products provide new organo-mineral associations for the stabilization of soil organic matter. *Global Change Biol* **24**, 1762-1770 (2018).

77 Keiluweit, M. *et al.* Nano-scale investigation of the association of microbial nitrogen residues with iron (hydr)oxides in a forest soil O-horizon. *Geochim Cosmochim Ac* **95**, 213-226 (2012).

78 Straub, K. L., Kappler, A. & Schink, B. Enrichment and isolation of ferric-iron- and humic-acid-reducing bacteria. *Method Enzymol* **397**, 58-77 (2005).

79 Widdel, F., Kohring, G. W. & Mayer, F. Studies on Dissimilatory Sulfate-Reducing Bacteria That Decompose Fatty-Acids .3. Characterization of the Filamentous Gliding Desulfonema-Limicola Gen-Nov Sp-Nov, and Desulfonema-Magnum Sp-Nov. *Arch Microbiol* **134**, 286-294 (1983).

80 Widdel, F. & Pfennig, N. Studies on Dissimilatory Sulfate-Reducing Bacteria That Decompose Fatty-Acids .1. Isolation of New Sulfate-Reducing Bacteria Enriched with Acetate from Saline Environments - Description of Desulfobacter-Postgatei Gen-Nov, Sp-Nov. *Arch Microbiol* **129**, 395-400 (1981).

81 Widdel, F. Anaerobic degradation of fatty acids and benzoic acid by newly isolated species sulphate-reducing bacteria. *Dissertation, Universität Göttingen, FRG* (1980).

82 Laufer, K. *et al.* Coexistence of Microaerophilic, Nitrate Reducing, and Phototrophic Fe(II) Oxidizers and Fe(III) Reducers in Coastal Marine Sediment (vol 82, pg 1433, 2016). *Appl Environ Microbiol* **82**, 3694-3694 (2016).

83 Melton, E. D., Rudolph, A., Behrens, S., Schmidt, C. & Kappler, A. Influence of Nutrient Concentrations on MPN Quantification and Enrichment of Nitrate-Reducing Fe(II)-Oxidizing and Fe(III)-Reducing Bacteria from Littoral Freshwater Lake Sediments. *Geomicrobiol J* **31**, 788-801 (2014).

84 Cornish, E. A. & Fisher, R. A. Moments and cumulants in the specification of distributions. *Revue de l'Institut International de Statistique/Rev. Int. Stat. Inst. 5* **4**, 307-320 (1938).

85 Klee, A. J. A Computer-Program for the Determination of Most Probable Number and Its Confidence-Limits. *J Microbiol Meth* **18**, 91-98 (1993).

86 Salama, I. A., Koch, G. G. & Tolley, H. D. On the estimation of the most probable number in a serial dilution technique. *Commun. Stat. - Theory Methods* **A7**, 1267-1281 (1978).

87 Muyzer, G., de Waal, E. C. & Uitterlinden, A. G. Profiling of complex microbial populations by denaturing gradient gel electrophoresis analysis of polymerase chain reaction-amplified genes coding for 16S rRNA. *Appl Environ Microbio* **59**, 659-700 (1993).

88 Holmgren, G. G. A Rapid Citrate-Dithionite Extractable Iron Procedure. *Soil Sci Soc Am Pro* **31**, 210-211 (1967).

89 Loeppert, R. H. & Inskeep, W. Iron. In: Sparks, D.L., Page, A.L, Helmke, P.A., Loeppert, R.H., Soltanpour, P.N., Tabatabai, M.A.,

Johnston, C.T., Summer, M.E. (1996).

90 Wagai, R., Mayer, L. M., Kitayama, K. & Shirato, Y. Association of organic matter with iron and aluminum across a range of soils determined via selective dissolution techniques coupled with dissolved nitrogen analysis. *Biogeochemistry* **112**, 95-109 (2013).

91 Ryan, J. N. & Gschwend, P. M. Extraction of iron oxides from sediments using reductive dissolution by titanium(III). *Clays Clay Min* **39**, 509-518 (1991).

Supplementary Information for

Iron mineral dissolution releases iron and associated organic carbon during permafrost thaw

Monique S. Patzner[1], Carsten W. Mueller[2,3], Miroslava Malusova[1], Moritz Baur[1], Verena Nikeleit[1], Thomas Scholten[4], Carmen Hoeschen[2], James M. Byrne[1], Thomas Borch[5], Andreas Kappler[1] & Casey Bryce[1,6]

[1] Geomicrobiology, Center for Applied Geosciences, University of Tuebingen, Tuebingen, Germany.

[2] Chair of Soil Science, Technical University Muenchen, Freising, Germany.

[3] Department of Geosciences and Natural Resource Management, University of Copenhagen, Denmark.

[4] Chair of Soil Science and Geomorphology, University of Tuebingen, Germany.

[5] Department of Soil & Crop Sciences and Department of Chemistry, Colorado State University, Fort Collins, US.

[6] School of Earth Sciences, University of Bristol, Bristol, UK.

Published in: *Nature Communications*

Replication along a thaw gradient

To evaluate the consistency of iron and carbon trends along the thaw gradient, 5 cores per thaw stage were analyzed in total. These include:

(1) Palsa A, Bog C and Fen E in 2018 (discussed in the main text) (1 core per thaw stage)

Cores were taken with a Humax corer and sterile plastic liners in June 2018. This set was immediately split and processed after sampling (3-4 days) (Supplementary Figure 1, a, yellow cores).

(2) Palsa a, Bog c and Fen e in 2019 (1 core per thaw stage)

These cores were taken with a Humax corer in July 2019 (Supplementary Figure 1, a, red). Also, this set of cores was immediately split and processed after sampling and thus is directly comparable to Palsa A, Bog C and Fen E.

(3) Palsa B, Bog D and Fen F in 2018 (1 core per thaw stage)

This set was taken at the same time and same conditions as cores Palsa A, Bog C and Fen E, but stored at 4°C for 7 months and then processed (Supplementary Figure 1, a, white cores).

(4) Triplicate cores in each thaw stage in 2017 (3 cores per thaw stage)

Triplicate cores in each thaw stage were taken with a Pürckhauer corer in September 2017 and immediately processed after sampling (Supplementary Figure 1, a, orange, green and blue cores). The whole depth profile was successfully captured for all palsa triplicate cores. The organic horizon was lost for the bog and the fen triplicate cores during coring, thus are not reported in Supplementary Figure 4 and Supplementary Figure 5. In bog and fen, the transition zones and mineral horizons were successfully sampled, confirming the loss of reactive iron along the thaw gradient at several spots in the permafrost peatland mire.

All cores showed the same trend for total extractable iron, for the poorly crystalline iron and the total carbon along the thaw gradient. However, we did not directly combine these observations in the main text as there was some variation in the sampling and storage methods.

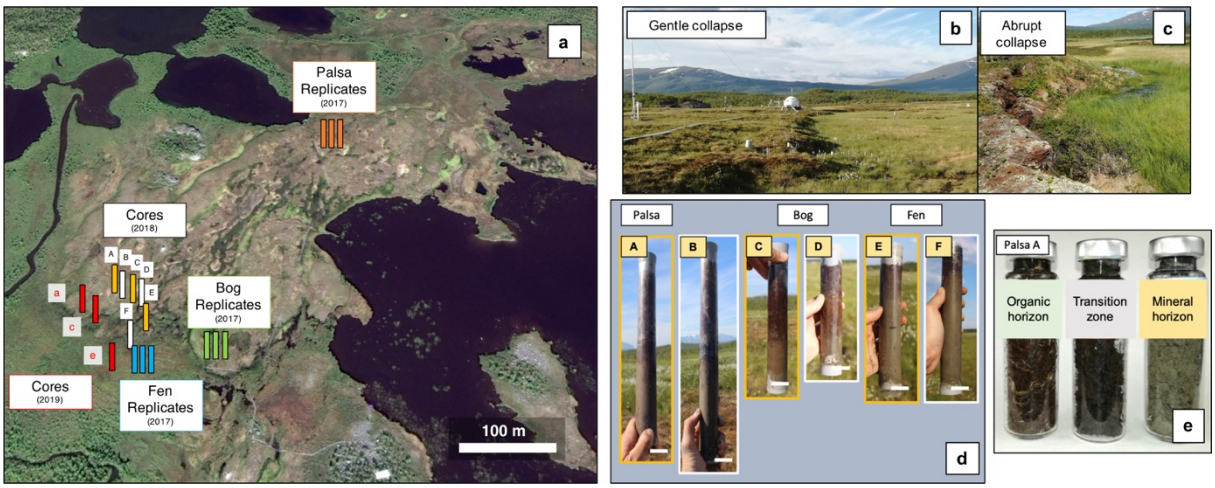

***Supplementary Figure 1. Coring at Stordalen mire, Abisko (Sweden)**. a, Position of cores taken along a thaw gradient at Stordalen mire (Abisko, Sweden). Yellow: Cores were immediately split and processed after sampling (3-4 days). White: Cores were stored at 4°C for 7 months and then processed. Red: Cores were immediately split and processed after sampling in the same manner as the cores in yellow (palsa a (68°21'18.03"N, 19° 2'35.20"E), bog c (68°21'18.02"N, 19° 2'36.53"E) and fen e (68°21'17.24"N, 19° 2'37.44"E)). The data was compared to triplicate cores in each thaw stage (palsa in orange, bog in green and fen in blue). b, Gentle collapse of palsa sites at Stordalen mire (Abisko, Sweden). The sampled thaw gradient represents a gentle collapse of palsa to bog. c, Abrupt collapse of palsa sites at Stordalen mire (Abisko, Sweden). Permafrost thaw does not necessarily progress through all three thaw stages (palsa, bog and fen). d, Cores taken along a thaw gradient. Palsa: Core A (68°21'18.70"N, 19° 2'38.00"E) and core B (68°21'18.50"N, 19° 2'38.80"E) showed the three main layers in the palsa area: (1) organic horizon, (2) transition zone and (3) mineral horizon. The organic layer was dry and oxic. Bog: Core C (68°21'18.60"N, 19° 2'39.20"E) and core D (68°21'18.30"N, 19° 2'40.00"E) clearly showed the division into the three layers: (1) organic horizon, (2) transition zone and (3) mineral horizon. Both cores were completely water saturated. Fen: Core E (68°21'16.80"N, 19° 2'40.30"E) and core F (68°21'17.80"N, 19° 2'41.30"E) also showed the three layers and were water saturated. The cores represent the active layer in July 2018. The scale bar represents 3 cm. e, Example of the subdivision into (1) organic horizon, (2) transition zone and (3) mineral horizon (Palsa A).*

(1) Replicate cores Palsa a, Bog c and Fen e (in 2019)

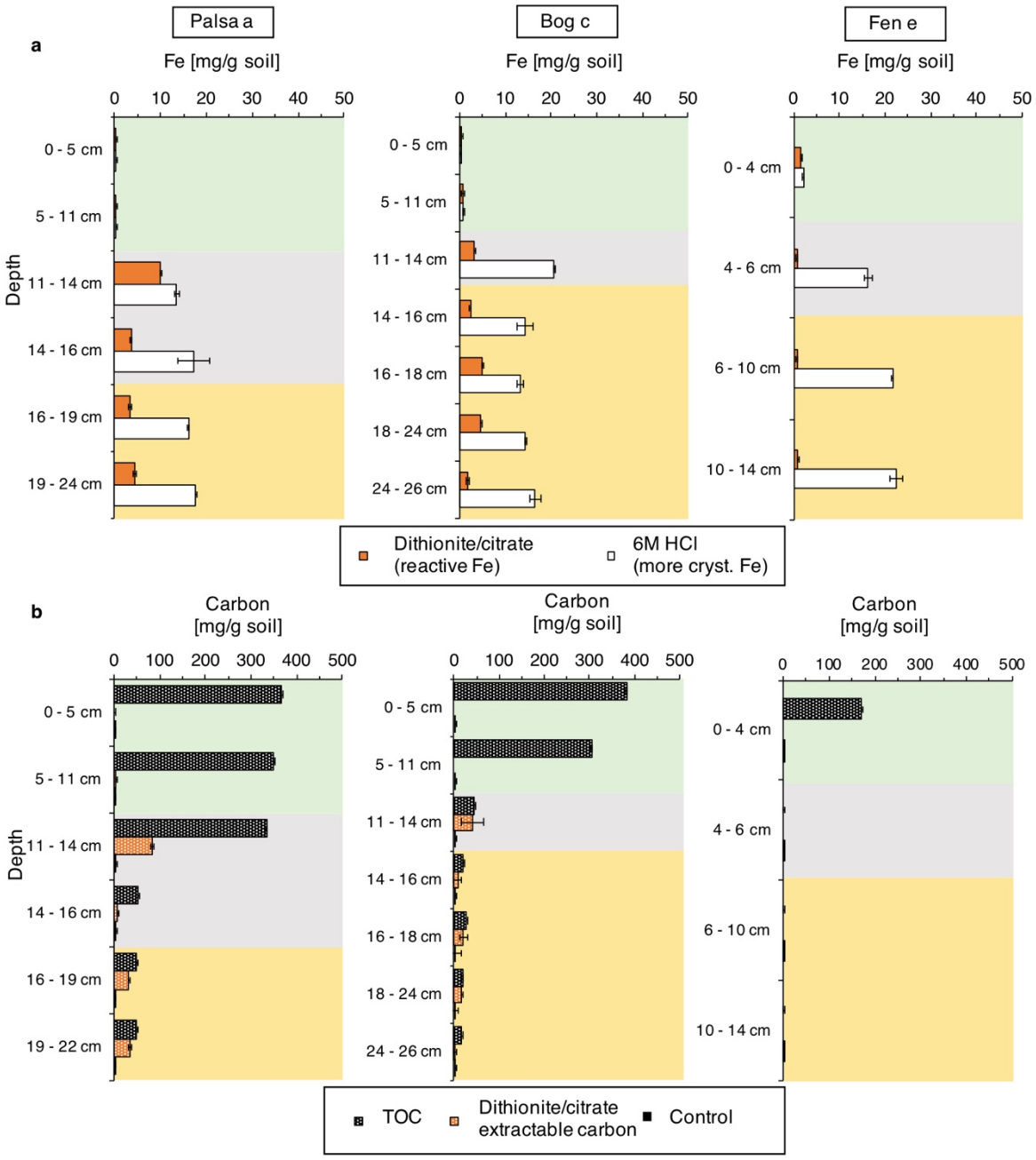

Supplementary Figure 2. Extractions of replicate cores. *a, Iron and b, Carbon concentration of cores Palsa a, Bog c and Fen e. Cores were taken in July 2019, split directly after sampling and immediately processed. The green box marks the organic horizon, grey box the transition zone and yellow box the mineral horizon. Extractable iron was determined via the ferrozine assay. Total organic carbon (TOC) was determined via combustion, whereas the carbon in the dithionite citrate (control corrected) and the control extract (sodium chloride bicarbonate) was determined with the carbon analyzer. Errors of the TOC and 6M hydrochloric acid (HCl) extractable iron indicate the range of duplicate analyses of each layer in each thaw*

stage. Errors of the dithionite/citrate extractable a, iron and b, carbon (control corrected) represent a combined standard deviation of sodium chloride bicarbonate extractable a, iron and b, carbon, b, citrate blank and dithionite/citrate extractable a, iron and b, carbon (not control corrected).

(2) Replicate cores Palsa B, Bog D, Fen F along the thaw gradient (in 2018)

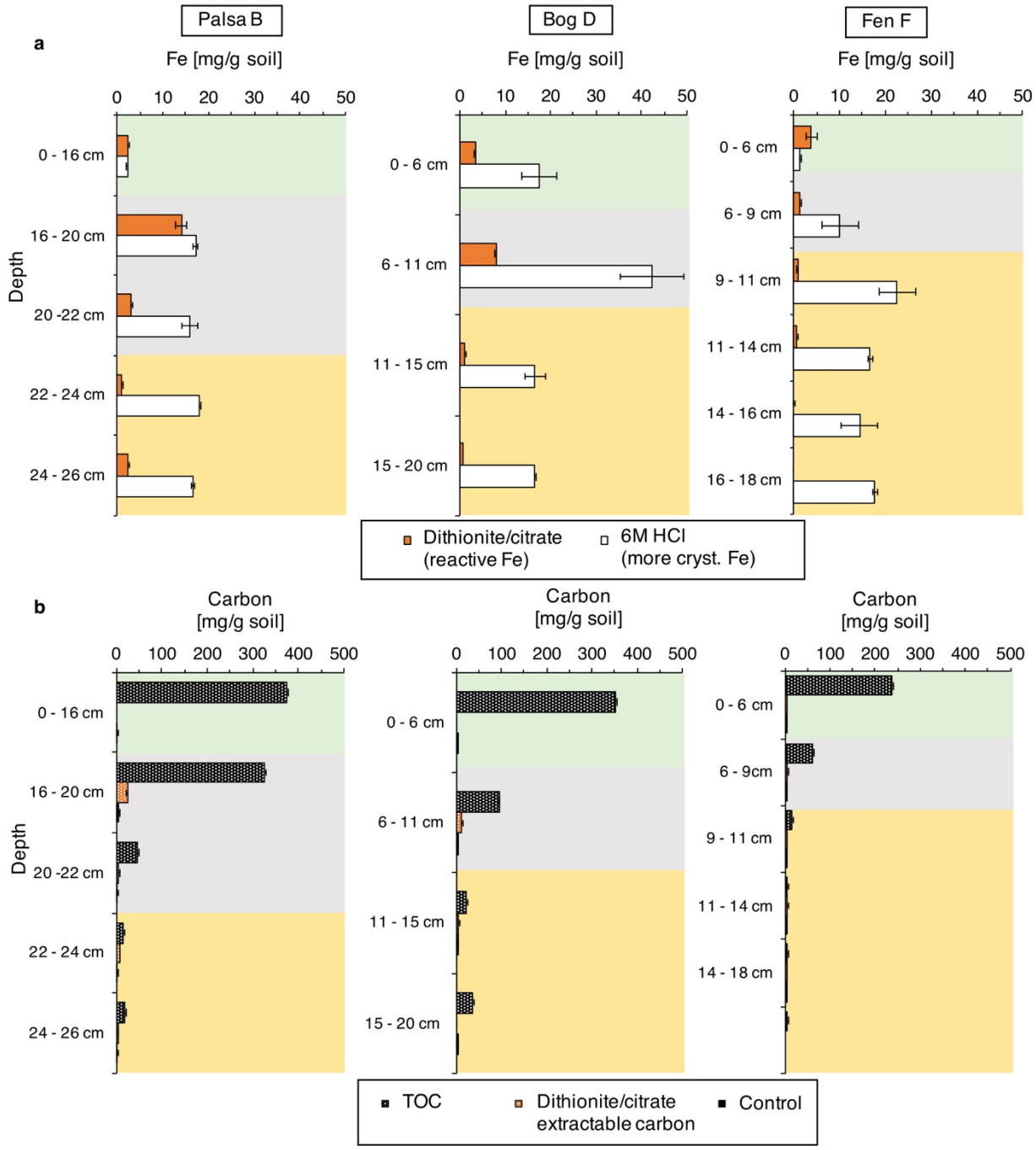

Supplementary Figure 3. Extractions of replicate cores. *a, Iron and b, Carbon concentration of cores Palsa B, Bog D and Fen F. Cores were split after 7 months of incubation at 4°C. The green box marks the organic horizon, grey box the transition zone and yellow box the mineral horizon. Iron in the extracts was determined via the ferrozine assay. Total organic carbon (TOC) was determined via combustion, whereas the carbon in the dithionite citrate (control corrected) and the control extract (sodium chloride bicarbonate) was determined with the carbon analyzer. Errors of the TOC and 6M hydrochloric acid (HCl) extractable iron indicate the range of duplicate analyses of each layer in each thaw stage. Errors of the*

dithionite/citrate extractable a, iron and b, carbon (control corrected) represent a combined standard deviation of sodium chloride bicarbonate extractable a, iron and b, carbon, b, citrate blank and dithionite/citrate extractable a, iron and b, carbon (not control corrected).

(3) Triplicate cores in each thaw stage (iron analysis) (in 2017)

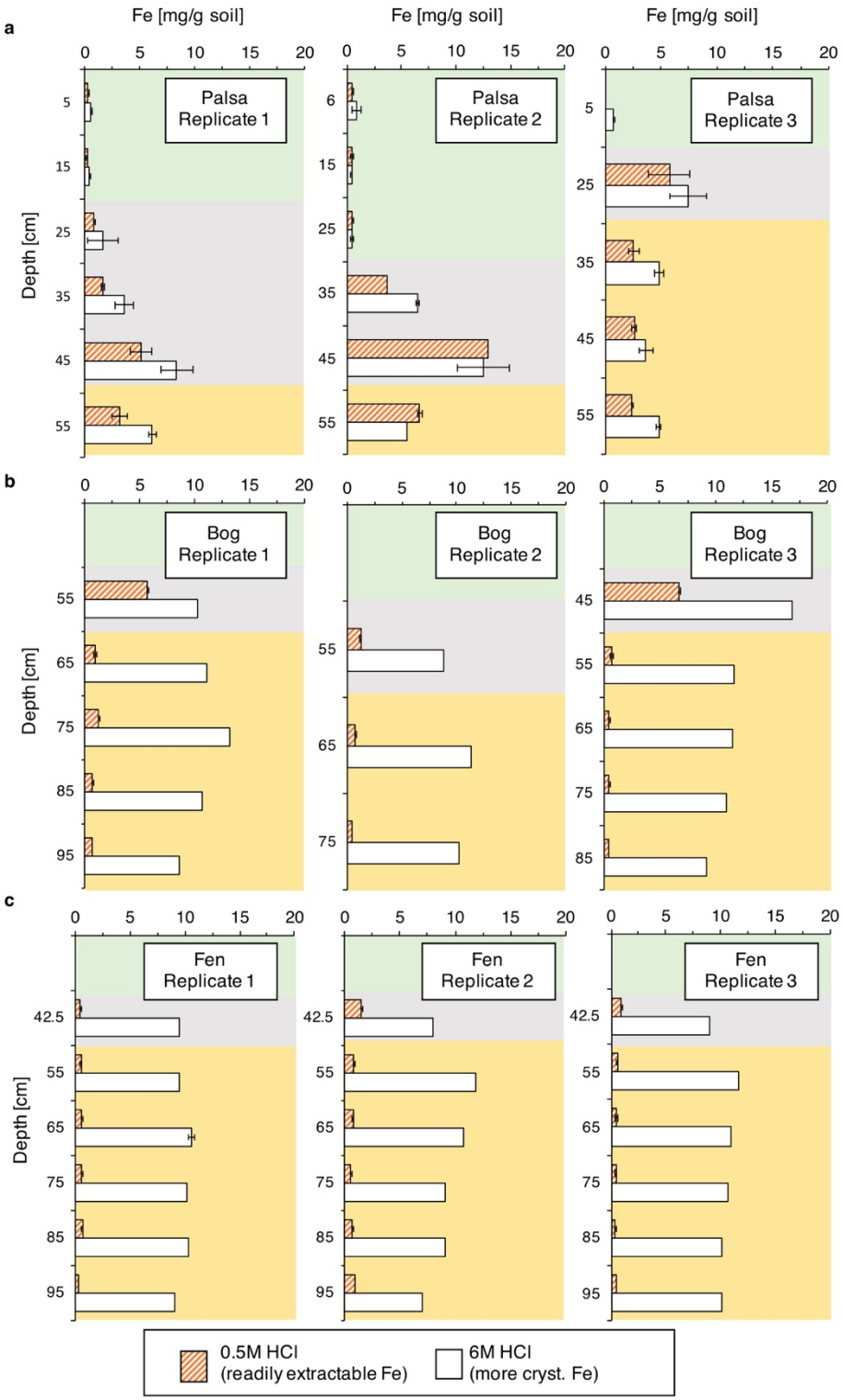

Supplementary Figure 4. Iron extractions of replicate cores taken with a Pürckhauer corer: a, Palsa (68°21'26.56"N, 19° 3'0.19"E), b, Bog (68°21'16.02"N, 19° 2'49.21"E), c, Fen (68°21'17.16"N, 19° 2'36.29"E). *Each core was divided into layers in the field and immediately processed. The organic horizon for the triplicate cores of bog and fen were lost*

during sampling and thus, are not reported in this figure. All replicates represent the active layer in September 2017. The bog and the fen soils were waterlogged. The green box marks the organic horizon, grey box the transition zone and yellow box the mineral horizon. Errors indicate the range of duplicate analyses of each layer in each thaw stage.

(4) Triplicate cores in each thaw stage (carbon analysis)

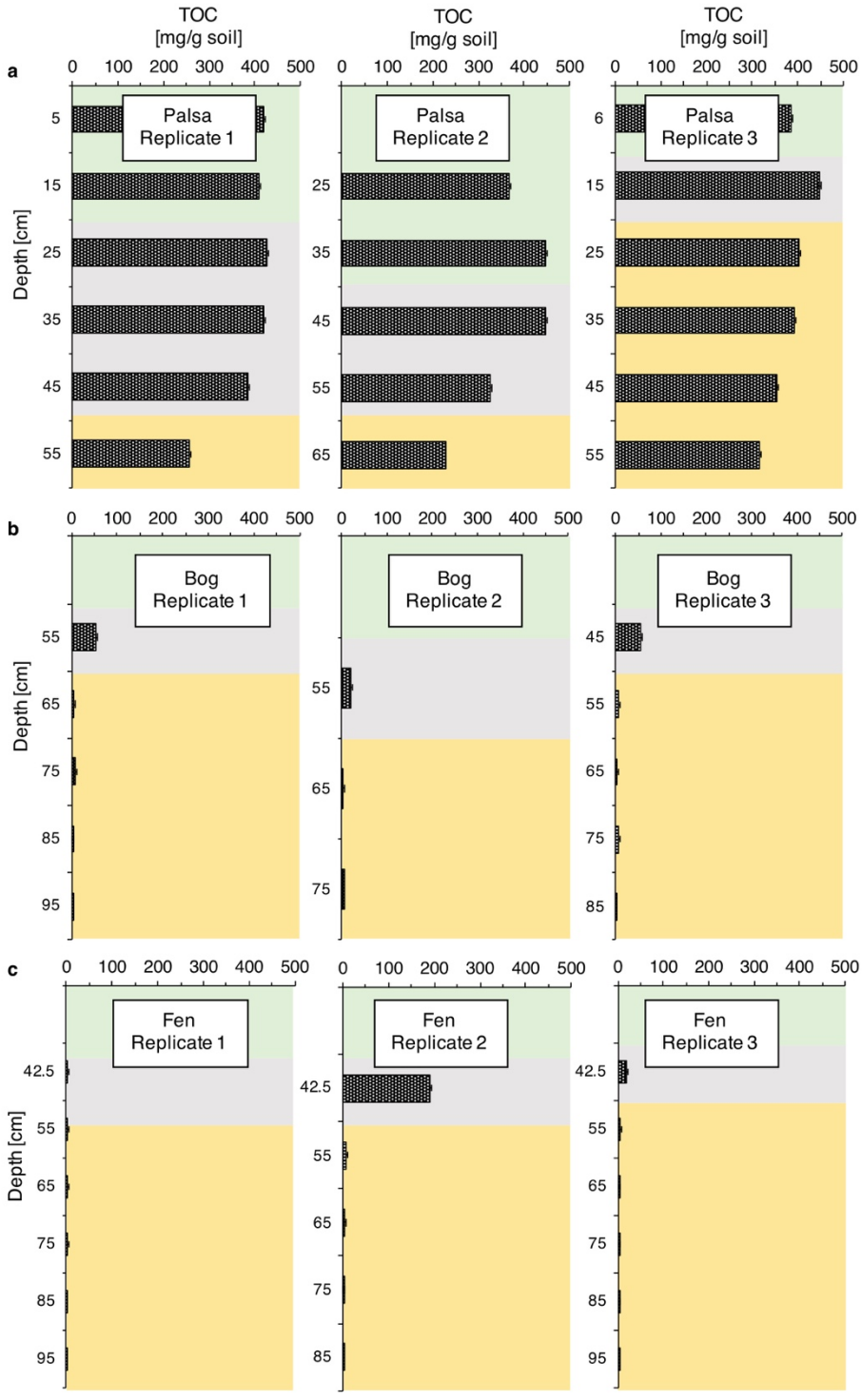

Supplementary Figure 5. TOC of replicate cores taken with a Pürckhauer corer: a, Palsa (68°21'26.56"N, 19° 3'0.19"E), b, Bog (68°21'16.02"N, 19° 2'49.21"E) and c, Fen (68°21'17.16"N, 19° 2'36.29"E). *Each core was divided into layers in the field and immediately processed. The organic horizon for the bog and fen triplicate cores were lost during sampling and thus are not reported in this figure. All replicates represent the active layer in September*

2017. The bog and fen soils were waterlogged. The green box marks the organic horizon, grey box the transition zone and yellow box the mineral horizon. Total organic carbon (TOC) was determined via combustion. Errors indicate the range of duplicate analyses of each layer in each thaw stage.

Fe(III) reduction by a further isolated Fe(III)-reducing bacteria from the fen, consuming lactate and forming acetate

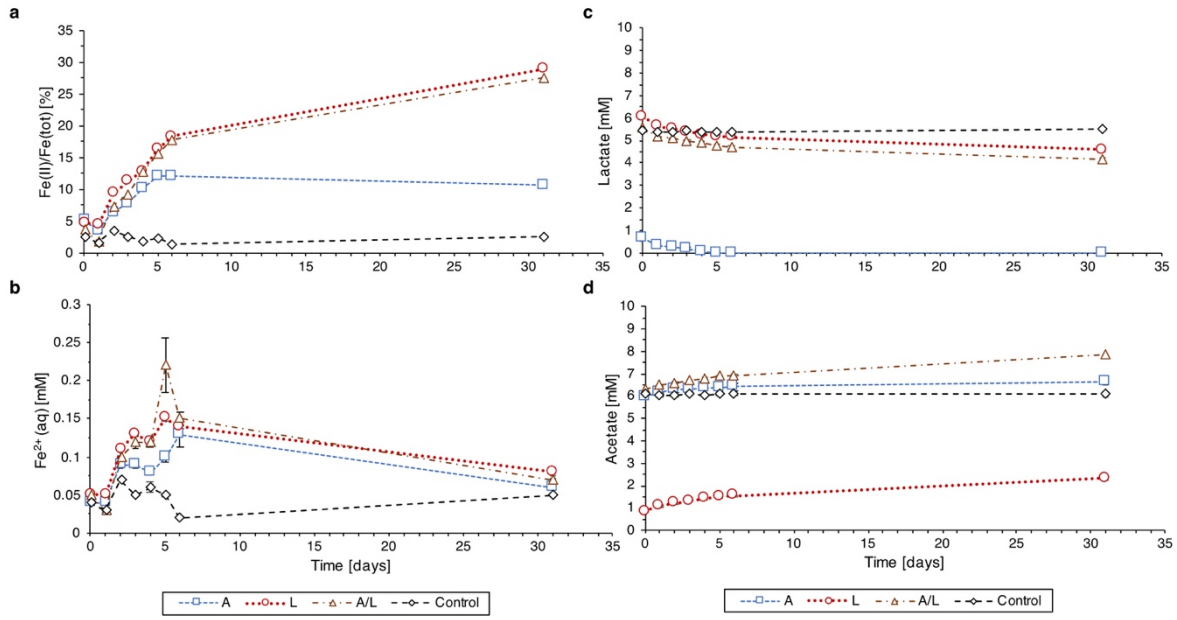

Supplementary Figure 6. Iron (Fe) (III) reduction by the Fe(III) reducer isolate from the fen soil core in four experimental setups: only acetate (A), only lactate (L), both acetate and lactate (A/L) and control (no amendments added). *a, Fe(II) to Fe(tot) ratio in % in the solid phase over time. 100% would mean that all initial present ferrihydrite was reduced to Fe(II). b, Fe(II) released into the liquid phase over time. c, lactate consumption over time. d, acetate formation over time. Note: The culture which was used for inoculum was previously cultivated in medium supplemented with 5 mM acetate and 5 mM lactate. Therefore, approximately 1 mM of both organic acids were transferred together with the bacteria in all setups, leading to minor Fe(III) reduction also in the acetate only setup using the transferred lactate and forming acetate (0.6 mM) due to residual lactate consumption. After, 31 days, 25% of the initial Fe(III) was reduced to Fe(II) in the solid phase in the lactate only (L) and lactate and acetate (A/L) setup. The lactate concentrations decreased, and the acetate concentration increased by 1.5 mM over 31 days in the lactate amended (L) and (A/L) setup. Some Fe^{2+} was first released into the aqueous phase but later re-adsorbed onto iron minerals, resulting in a decrease in the aqueous Fe^{2+}. Error bars represent standard deviations from 3 batch bottles from 0 to 31 days. Each microcosm was measured in triplicates.*

Absolute and % values of organic carbon and reactive iron content reported in the main text

Supplementary Table 1. Absolute and % values of iron and carbon in locations Palsa A, Bog C and Fen E, i.e. the cores reported in the main text. *In most of the layers, the maximum mass ratio of organic carbon (OC) to iron (Fe) (reactive Fe-associated organic carbon:reactive Fe, OC:Fe (wt:wt)) exceeds 0.22, the maximal sorption capacity of reactive iron oxides for natural organic matter[4,36] . Co-precipitation and/or chelation of organic compounds can generate structures with OC:Fe ratios (wt:wt) above 0.22, as shown in other studies[4,36.] Errors of control iron, control carbon, total organic carbon and total extractable iron indicate the range of duplicate analyses of each layer in each thaw stage. Total extractable iron represents the 6M HCl extractable iron (more crystalline Fe phases). Errors of the dithionite/citrate extractable a, iron (reactive Fe, control corrected) and b, carbon (carbon bound to reactive iron, control corrected) represent a combined standard deviation of sodium chloride bicarbonate extractable a, iron and b, carbon, b, citrate blank and dithionite/citrate extractable a, iron and b, carbon (not control corrected).*

	Reactive iron (control corrected)	Reactive iron of total extractable iron	Control iron	C bound to reactive iron (control corrected)	C bound to reactive iron of the total organic carbon	Control carbon	OC:Fe (wt:wt)	Total organic carbon	Total extractable Fe
	mg/g	%	mg/g	mg/g	%	mg/g		mg/g	mg/g
Palsa A									
Organic horizon	0.40 ± 0.11	100.00	0.00 ± 0.00	0.94 ± 0.58	0.22	1.37 ± 0.01	2.35	423 ± 0.00	0.20 ± 0.02
	0.29 ± 0.09	100.00	0.00 ± 0.00	2.16 ± 0.95	0.51	1.65 ± 0.08	7.45	422.91 ± 0.13	0.17 ± 0.00
Transition zone	2.55 ± 0.57	72.86	0.29 ± 0.08	30.99 ± 0.71	9.93	3.13 ± 0.02	12.15	312.11 ± 0.33	3.51 ± 0.08
	8.44 ± 0.21	93.86	0.75 ± 0.11	52.50 ± 0.13	14.80	10.36 ± 0.50	6.22	354.72 ± 0.04	8.99 ± 0.28
Mineral horizon	3.17 ± 0.19	36.58	0.25 ± 0.03	27.39 ± 1.61	20.13	2.88 ± 0.08	8.64	136.11 ± 0.21	8.65 ± 0.28
	1.35 ± 0.21	10.00	0.07 ± 0.06	13.58 ± 0.42	18.67	1.39 ± 0.10	10.06	72.71 ± 0.29	13.48 ± 0.22
Bog C									
Organic horizon	1.48 ± 0.18	40.60	0.73 ± 0.07	16.16 ± 3.91	4.85	3.16 ± 1.67	10.92	333.31 ± 0.05	3.63 ± 0.05
Transition zone	2.08 ± 0.05	11.14	0.41 ± 0.04	22.67 ± 8.60	39.42	1.18 ± 0.21	10.90	57.51 ± 0.38	18.65 ± 0.70
Mineral horizon	0.88 ± 0.06	7.52	0.28 ± 0.04	0.00 ± 0.00	0.00	1.04 ± 0.01	0.00	8.28 ± 0.25	11.69 ± 0.81
Fen E									
Organic horizon	2.03 ± 0.14	43.39	0.75 ± 0.00	0.00 ± 0.00	0.00	1.53 ± 0.00	0.00	234.70 ± 0.83	4.68 ± 0.01
Transition zone	2.64 ± 0.03	18.29	0.37 ± 0.00	0.00 ± 0.00	0.00	1.38 ± 0.18	0.00	16.24 ± 0.18	14.46 ± 0.22
Mineral horizon	1.75 ± 0.04	10.71	0.15 ± 0.00	0.00 ± 0.00	0.00	2.57 ± 0.76	0.00	3.52 ± 0.05	16.34 ± 0.44
	1.70 ± 0.04	8.95	0.19 ± 0.01	0.00 ± 0.00	0.00	1.13 ± 0.17	0.00	4.99 ± 0.10	19.01 ± 0.25

Fe-associated organic carbon: extraction method and controls

The determination of Fe-associated organic carbon has several well-known difficulties which can only be addressed by combining different approaches.

Considerations for the sodium dithionite-citrate extraction:

(1) pH

To prevent hydrolysis of organic matter as well as its protonation and re-adsorption onto sediment particles, which occur under acidic conditions, the sodium dithionite citrate extraction was performed at circumneutral pH (sodium bicarbonate buffered). Therefore, the additional hydroxylamine-HCl extraction (performed below pH 2) can only be a comparison for the sodium dithionite citrate extractable Fe, but not for the sodium dithionite citrate extractable carbon. The control extraction was performed under the same ionic strength (addition of NaCl) and pH (sodium bicarbonate buffered).

(2) Temperature and incubation time

Dithionite citrate bicarbonate extractions have been widely applied in various studies and were previously performed under two different temperatures and incubation times. One is conducted at room temperature at pH 7-8 for 16 hours on a shaker[4,8,88,89,90] and the other conducted at 80°C for 15 minutes[5,32]. Due to the high organic carbon content of the soil samples, the standard approach at room temperature at neutral pH for 16 hours was chosen to avoid alteration of carbon during heating of sample to 80°C, which could further influence the amount of extracted iron. The approach conducted at 80°C is suspected to contribute more to nonselective dissolution[90] in organic-rich samples.

(3) Leaching of carbon which is not associated with iron

The carbon measured in the sodium dithionite citrate extraction was corrected by subtraction of the measured DOC values in a citrate blank and in a control extraction, performed under the same ionic strength and pH. This control extraction determines how much carbon would be leached from the soil without any reduction (see Table S1 and Supplementary Figure 7). The effect of a reducing agent, which potentially reductively transforms certain organic functional groups, is not considered in this control (see point *(4)*).

(4) Dithionite as strong reducing agent

Dithionite is a strong reducing agent which can reductively transform certain organic functional groups and could lead to organic carbon release which is not associated with reactive Fe. Nevertheless, we consider this to be negligible for our extractions as the concentration of sodium dithionite citrate extractable carbon of a horizon containing primarily organic material and no mineral phase (Palsa A, organic horizon) is very low (0.3±0.1 to 0.4±0.1 mg extractable carbon per g soil; see also Supplementary Table 1). Additionally, a sodium pyrophosphate extraction was performed to determine the colloidal/OM-Fe. The sodium pyrophosphate extraction carbon yielded similar concentrations and showed similar trends to the dithionite-citrate extractable carbon across the thaw gradient (Supplementary Figure 7). Variation between the absolute values can occur due to heterogeneity in the samples and the alkaline conditions of the sodium pyrophosphate extraction (pH 10).

(5) Citrate as strong metal complexing agent

Citrate is a strong metal complexing agent that can influence the amount of extractable iron during dithionite extraction. A test-run was performed with the same experimental conditions (same ionic strength and pH), but no citrate addition. Without citrate, we obtained 64±3% less iron and 57±28% less carbon after sodium dithionite reductive dissolution. We therefore concluded, that the metal ion complexing agent citrate is necessary to avoid under-estimation of iron and organic carbon as a result of complexing or mineral precipitation during extraction.

Since extractions have well-known limitations as mentioned above, additional approaches were used and combined to characterize Fe-C associations in the solid phase along the thaw gradient.

Additional approaches used were:

(A) Extended X-ray absorption fine structure (EXAFS) with reference for reactive Fe (ferrihydrite) and references for organic carbon associated with Fe (Fe(II)-citrate) and Fe(III)-citrate)

(B) Nanoscale analysis using correlative SEM and nanoSIMS to show close spatial distribution of iron and carbon

The data set is consistent with an increase in aqueous Fe^{2+} and DOC and an increasing abundance of Fe(III)-reducing bacteria along the thaw gradient.

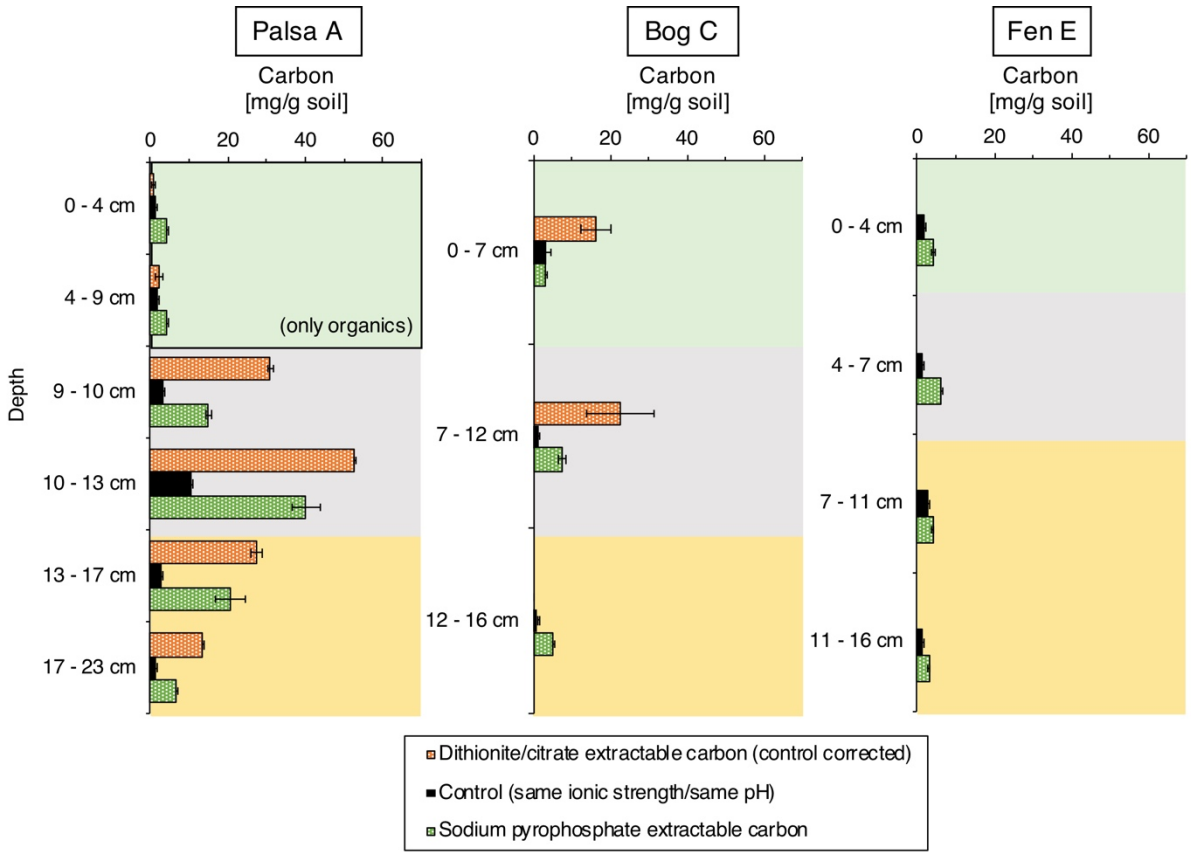

Supplementary Figure 7. Extractable carbon measured using different approaches to address issues with the sodium dithionite citrate extraction. *The sodium dithionite citrate extractable carbon is control corrected (subtraction of citrate blank and extractable carbon of the control extraction with same ionic strength and pH), shown in orange (see also Supplementary Table 1). The control extraction (same ionic strength and pH) is shown in black (see also Supplementary Table 1). The sodium pyrophosphate (pH 10) extractable carbon shows similar amounts and trends with depth and along the thaw gradient, as the control corrected dithionite citrate extractable carbon. Dithionite citrate extractable carbon only from organics (Box, Palsa A, organic horizon) is low, therefore hydrolytic cleavage of organic matter can be ruled out. Errors indicate the range of duplicate analyses of each layer in each thaw stage.*

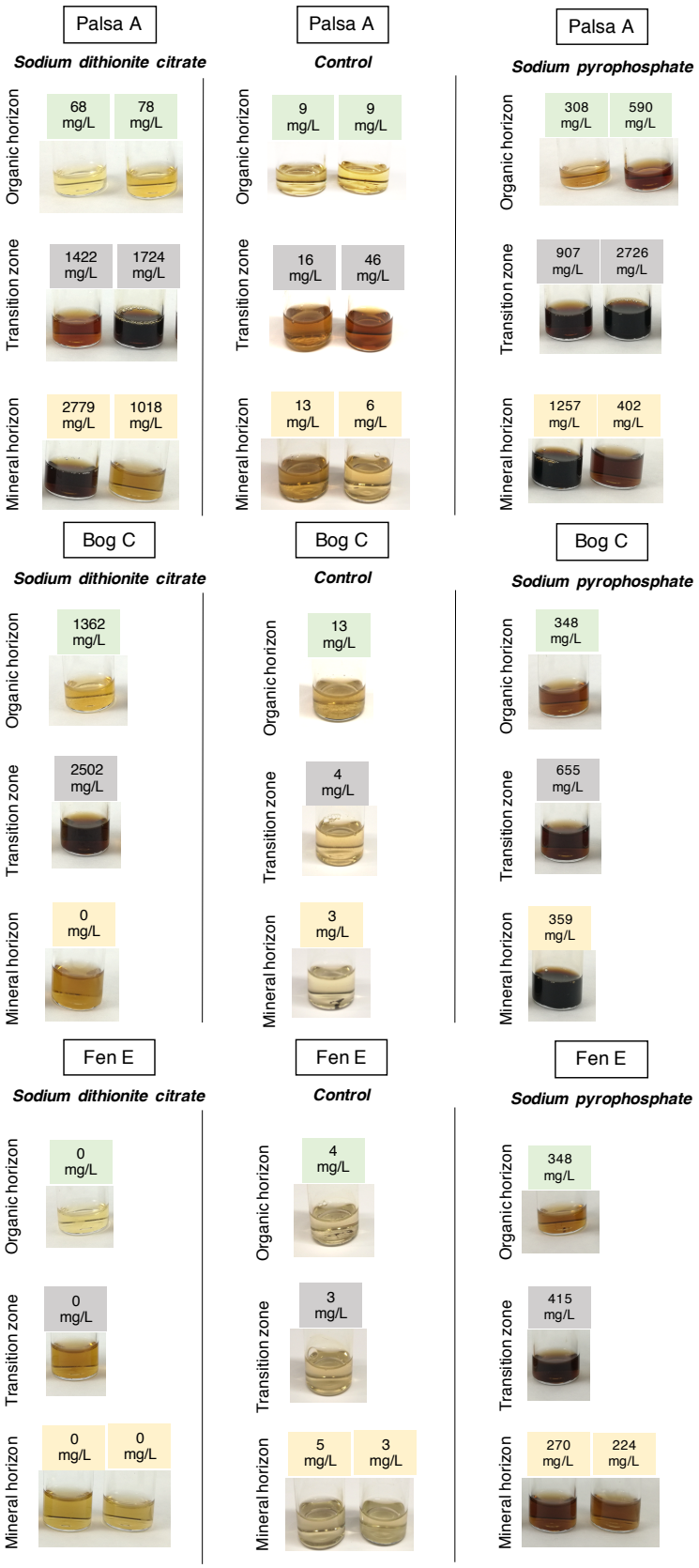

Supplementary Figure 8. Extracts of sodium dithionite, control and sodium pyrophosphate. *Values of sodium dithionite citrate indicate the dissolved organic carbon*

concentrations in the extracts after subtraction of the background of the citrate concentration. The background concentration of the citrate for the analysis Palsa A, Bog C and Fen F was 20.5±0.14g/L. Pictures of the extracts are shown to highlight the loss of the reactive iron phase and carbon associated with it along the thaw gradient, here visible by brown color loss in the sodium dithionite citrate extracts from palsa to fen. The control is shown to demonstrate that there was no carbon leached under same ionic strength and pH. The sodium pyrophosphate extracts support the trends shown by the sodium dithionite citrate extraction. Green marks the organic horizon, grey the transition zone and yellow the mineral horizon.

Calculated stocks (mg/cm^2) versus content (mg/g) of reactive Fe and reactive Fe-associated organic carbon

During coring compaction occurred. Based on the bulk densities, compaction was assumed to have occurred in the palsa organic horizon (0.03±0.01 g/cm^3) and palsa transition zone (0.08±0.02 g/cm^3), but not for the dense palsa mineral horizon (0.84±0.26 g/cm3). For the bog organic horizon (0.08±0.01 g/cm^3) and for fen organic horizon (0.21±0.02 g/cm^3), compaction was assumed but we assume that no compaction occurred in the dense horizons (bog transition zone: 1.29±0.04 g/cm^3, bog mineral horizon: 1.74±0.01 g/cm^3, fen transition zone: 1.97±0.2 g/cm^3, fen mineral horizon: 1.72±0.01 g/cm^3).

Thus, where no compaction was assumed (Supplementary Figure 9), the stock was calculated without compaction consideration i.e. thickness used for the calculation is as reported by depth intervals in the main text:

*Stock = bulk density * content * layer thickness*

with stock in mg/cm^{-2}, bulk density in g cm^{-3}, content in mg g^{-1} and actual layer thickness in the core in cm.

For the horizons where compaction was assumed (Supplementary Figure 9), a compaction factor was calculated from the difference between the actual core depth (as reported in the text) and the core hole (compaction factor for palsa organic horizon and palsa transition zone 2.31, for bog organic horizon 5.00 and for fen organic horizon 8.25). The compaction-corrected stock was calculated as follows:

*Stock = compaction factor * bulk density * content* layer thickness*

with stock in mg/cm^{-2}, bulk density in g cm^{-3}, content in mg g^{-1} and actual layer thickness in the core in cm.

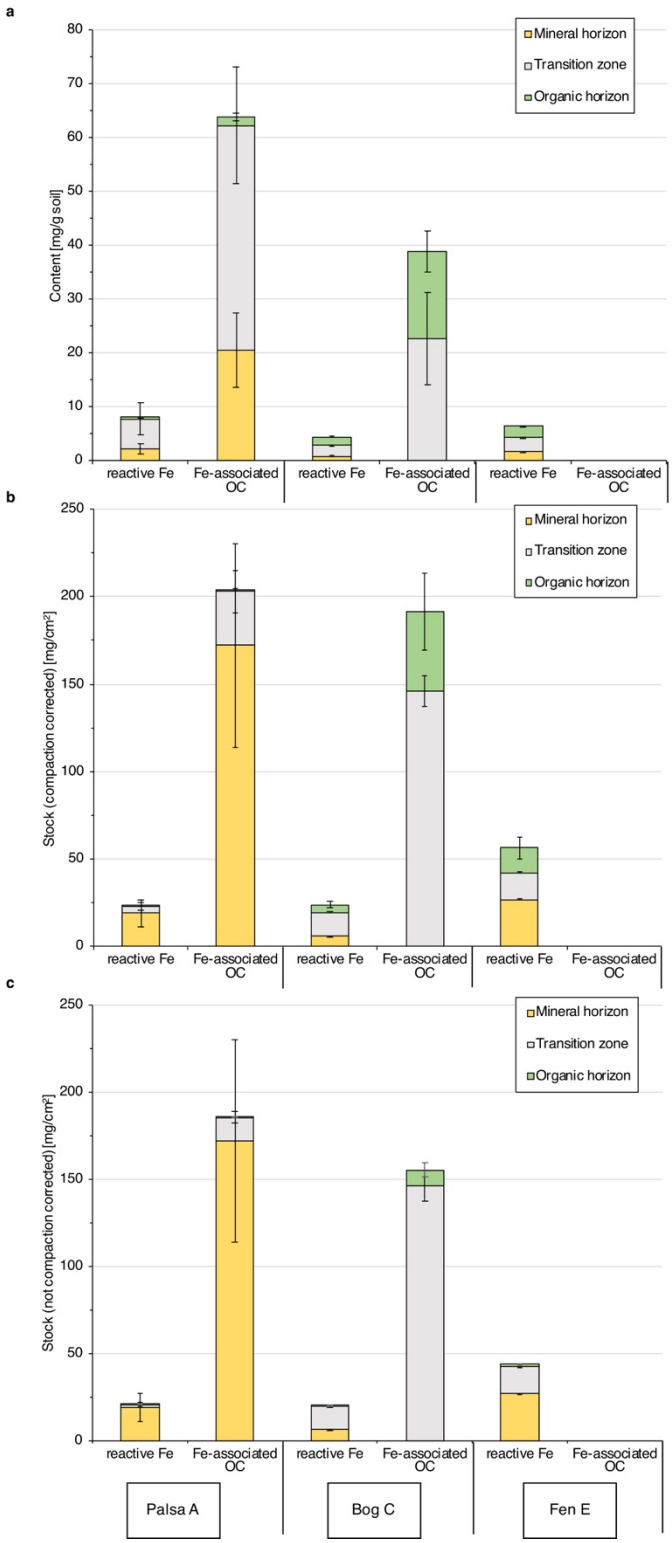

Supplementary Figure 9. Calculated stocks (mg/cm²) versus absolute amounts (mg/g) of reactive iron (Fe) and reactive Fe-associated organic carbon (OC). *a, Averaged absolute amounts of reactive Fe and associated organic carbon in mg per g soil per horizon (green: organic horizon, grey: transition zone, yellow: mineral horizon) for palsa, bog and fen. Error bars represent a combined standard deviation of the absolute values per depth (see*

Table S1) of duplicate extractions per horizons of Palsa A, Bog C and Fen E. b, Calculated average stock of reactive Fe and reactive Fe-associated OC in mg per cm², compaction corrected. Green represents the organic horizon, grey the transition zone and yellow the mineral horizon in Palsa E, Bog C and Fen E. Error bars represent a combined standard deviation of the absolute values, bulk density and compaction per horizons of Palsa A, Bog C and Fen E. c, Calculated average stock of reactive Fe and reactive Fe-associated OC in mg per cm² without assuming compaction. The reported depth intervals in the main text were used to calculate the stock. Green represents the organic horizon, grey the transition zone and yellow the mineral horizon in Palsa E, Bog C and Fen E. Error bars represent a combined standard deviation of the absolute values and the bulk density per horizons of Palsa A, Bog C and Fen E.

Additional elements (P, S and Al) appearing with Fe minerals along the thaw gradient

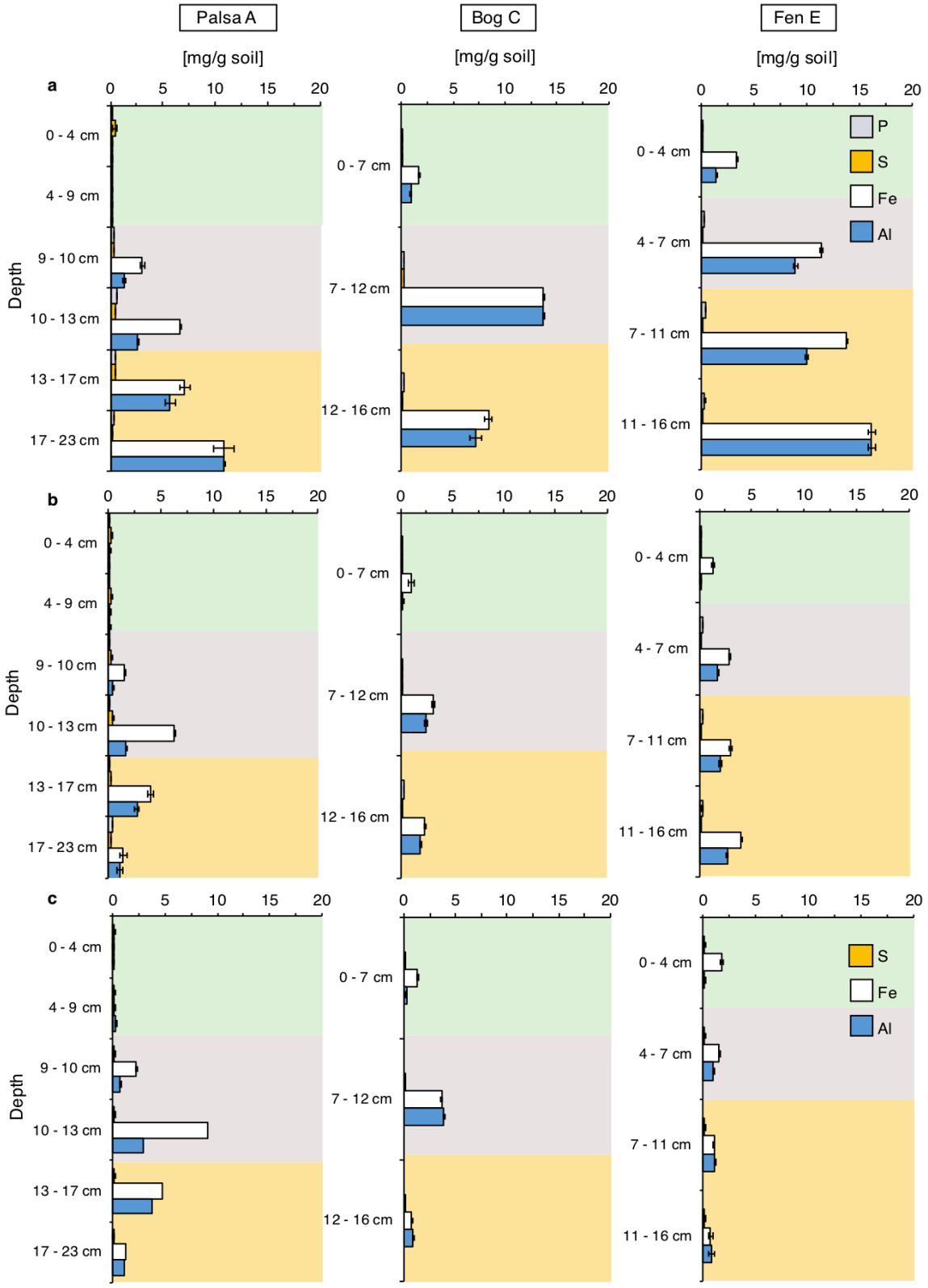

Supplementary Figure 10. Other elements (phosphorous (P), sulphur (S), iron (Fe) and aluminum (Al)) in extracts of Palsa A, Bog C and Fen E. *a, 6M hydrochloric acid (HCl), b, hydroxylamine-HCl and c, sodium pyrophosphate extracted. Fe, P and S concentrations were*

measured with ICP-MS (inductively coupled plasma mass spectrometry). Fe and Al concentrations were analyzed using MP-AES (microwave plasma atomic emission spectroscopy). The illustrated Fe values here are measured by MP-AES. The slightly different Fe concentrations by the different analytical approaches (ferrozine assay, MP-AES and ICP-MS) are shown in Supplementary Figure 4. The green box marks the organic horizon, grey box the transition zone and yellow box the mineral horizon. Errors indicate the range of duplicate analyses of each layer in each thaw stage.

Replication of nanoSIMS analysis (4 representatives per soil layer)

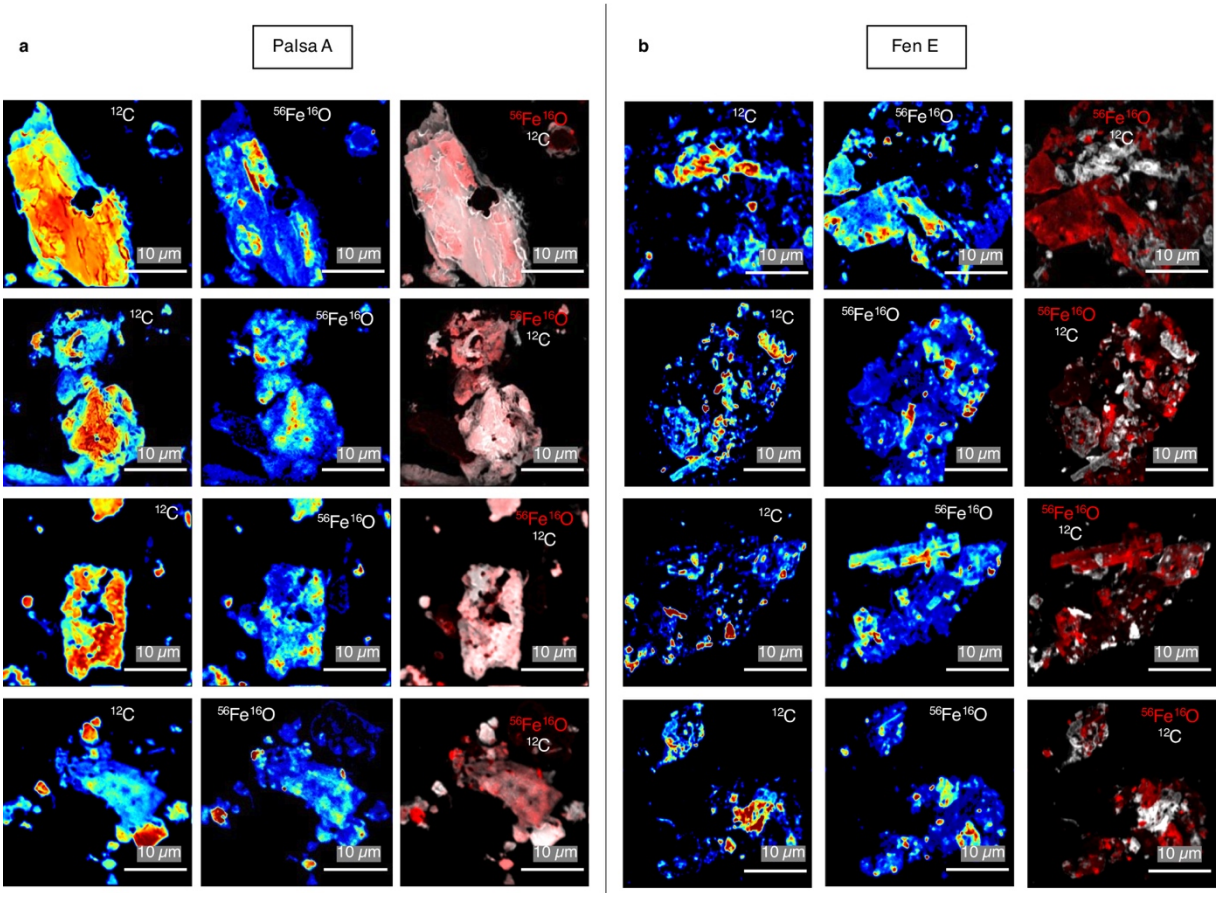

Supplementary Figure 11. Four representative particles of the fine fraction of a, Palsa A and b, Fen E analyzed with nanoSIMS showing a close spatial distribution of Fe and C. *Seven detectors were used during nanoSIMS measurements for ^{12}C, $^{56}Fe^{16}O$, ^{16}O, $^{12}C^{14}N$, ^{31}P, ^{32}S and $^{27}Al^{16}O$. ^{12}C and $^{56}Fe^{16}O$ are shown for four representative fine particles plus ^{12}C and $^{56}Fe^{16}O$ distributions, overlain in a single image on the left.*

Different Fe analysis of the extracts to rule out matrix effects

Different analytical approaches (ferrozine assay, MP-AES, ICP-MS) have been used to determine Fe in the extracts, to rule out matrix effects and to determine additional elements in the extracts (Supplementary Figure 12). ICP-MS was also used to measure sulphur (S) and phosphorous (P) (Supplementary Figure 8). MP-AES was also used to determine aluminum concentrations in the extracts (Al) (Supplementary Figure 8). For the ferrozine assay, the calibration curves were $r^2 > 0.999$, and the standard deviations of the triplicate analyses were <1%. For the ICP-MS, the calibration curves were $r^2 > 0.999$, and the standard deviations of the triplicate analyses were <5%. For the MP-AES, the calibration curves were $r^2 > 0.993$ and the standard deviations of the triplicate analysis were <10%. We are aware of differences between the iron values. However, because the values only vary slightly, the ferrozine values had a higher accuracy (<1%) and sodium dithionite citrate was not measured with ICP-MS and MP-AES due to citric formation after acidification, we decided to use the data from the ferrozine assay.

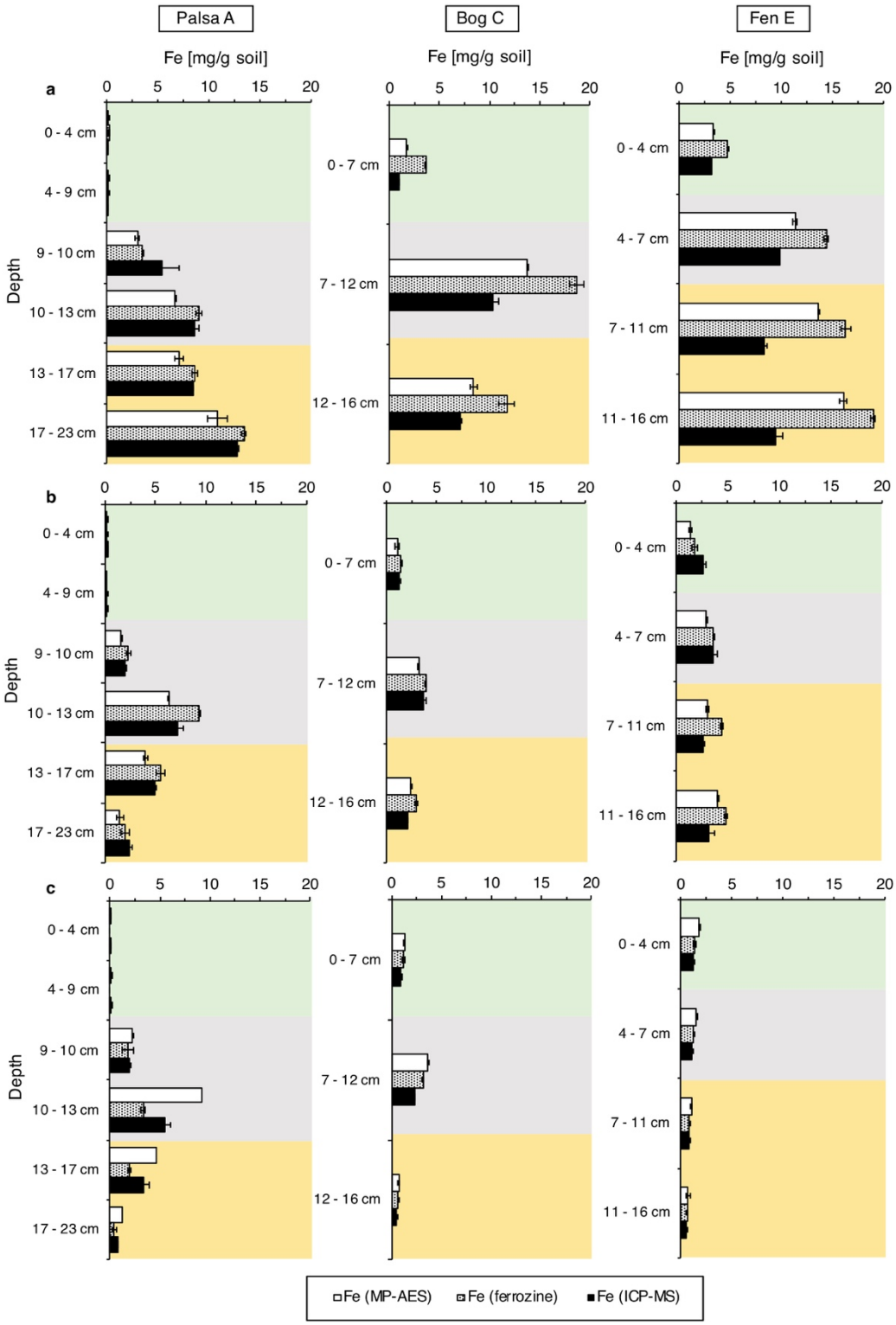

Supplementary Figure 12. Fe analysis by MP-AES (microwave plasma atomic emission spectroscopy), ferrozine and ICP-MS (inductively coupled plasma mass spectrometry) analysis of Palsa A, Bog C and Fen E: a, 6M hydrochloric acid (HCl) extraction, b, hydroxylamine-HCl extraction and c, sodium pyrophosphate extraction. *Due to citric acid formation after acidification, the sodium dithionite citrate extract was not measured with the*

more sensitive MP-AES and ICP-MS instrument. For the 6M HCl and hydroxylamine-HCl extracts, the MP-AES iron values are slightly lower than the ferrozine iron values due to matrix interference during MP-AES measurements of the extracts (HCl). For the sodium pyrophosphate extract, the MP-AES iron values are slightly higher than the ferrozine iron values. This could be explained by the dark color of the extracts which disturb the spectrophotometric measurement during ferrozine complexation. After blank subtraction this can result in lower iron concentrations determined by the ferrozine assay. The ICP-MS iron values are close to the ferrozine values (122±54% similarity), except for one extraction (6M HCl extraction) and two horizons (transition zone and mineral horizon of bog and fen). Errors indicate the range of duplicate analyses of each layer in each thaw stage.

Chapter 3 – Personal contribution

The original hypothesis was formulated by myself, Dr. C. Bryce and Prof. Dr. A. Kappler. Together with the support of Dr. C. Bryce and Prof. Dr. A. Kappler, I designed the project, interpreted the data and wrote the manuscript. Dr. C. Bryce, M. Logan and I collected the samples. I conducted the experiments and gathered the data presented in the main text. M. Logan and Dr. A. McKenna conducted the FT-ICR-MS measurements and contributed to the data interpretation. Prof. Dr. T. Borch and Dr. R. Young contributed to the data analysis and interpretation. Dr. Z. Zhou performed the Mössbauer spectroscopy and helped interpreting the results. H. Joss helped collecting the porewater samples and with data interpretation. With the help of Dr. C. Hoeschen and Prof. Dr. C.W. Mueller, I collected, analyzed and interpreted nanoSIMS data. Dr. D. Straub helped processing the Amplicon sequencing samples and, together with Prof. Dr. S. Kleindienst, with interpretation of the microbial community results. Prof. Dr. T. Scholten contributed to project design and data interpretation.

Chapter 3

Microbial iron(III) reduction during palsa collapse promotes greenhouse gas emissions before complete permafrost thaw

Monique S. Patzner[1], Merritt Logan[2], Amy M. McKenna[3], Robert B. Young[2,4], Zhe Zhou[1,5], Hanna Joss[1], Carsten W. Mueller[6,7], Carmen Hoeschen[6], Thomas Scholten[8], Daniel Straub[9,10], Sara Kleindienst[9], Thomas Borch[2], Andreas Kappler[1,11] & Casey Bryce[1,12]

[1]Geomicrobiology, Center for Applied Geosciences, University of Tuebingen, Schnarrenbergstrasse 94-96, 72076 Tuebingen, Germany.
[2]Department of Soil & Crop Sciences and Department of Chemistry, Colorado State University, 307 University Ave, 80523-1170 Fort Collins, US.
[3]National High Magnetic Field Laboratory, Florida State University, Tallahassee, FL 32310-4005, US.
[4]Chemical Analysis and Instrumentation Laboratory, New Mexico State University, P.O. Box 30001, MSC 3RES, Las Cruces, NM, 88003, US.
[5]Alfred-Wegener-Institute, Helmholtz Centre for Polar and Marine Research, Am Handelshafen 12, 27570 Bremerhaven, Germany
[6]Chair of Soil Science, TUM School of Life Sciences, Technical University of Munich, Emil-Ramann Strasse 2, 85354 Freising, Germany.
[7]Department of Geosciences and Natural Resource Management, University of Copenhagen, Øster Voldgade 10, 1350 Copenhagen, Denmark.
[8]Chair of Soil Science and Geomorphology, Rümelinstraße 19-23, 72070 Tübingen, University of Tuebingen, Germany.
[9]Microbial Ecology, Center for Applied Geosciences, University Tuebingen, Schnarrenbergstrasse 94-96, 72076 Tuebingen, Germany.
[10]Quantitative Biology Center (QBiC), University Tuebingen, Auf der Morgenstelle 10, 72076 Tuebingen, Germany.
[11]Cluster of Excellence: EXC 2124: Controlling Microbes to Fight Infection, Tuebingen, Germany.
[12]School of Earth Sciences, University of Bristol, Wills Memorial Building, Queens Road Bristol BS8 1RJ, UK.

Manuscript submitted for publication to: *Nature Comms Earth & Environment*

Abstract

Reactive iron (Fe) minerals can preserve organic carbon (OC) in soils overlying intact permafrost. With permafrost thaw, reductive dissolution of iron minerals releases Fe and OC into the porewater, potentially increasing the bioavailability of OC for microbial decomposition. However, the stability of this so-called rusty carbon sink, the microbial community driving mineral dissolution, the identity of the iron-associated carbon and the resulting impact on greenhouse gas emissions are unknown. We examined palsa hillslopes, gradients from intact palsa towards collapsing fronts into semi-wet bog in a permafrost peatland in Abisko (Sweden), and analyzed dissolved versus mineral-associated OC (with FT-ICR-MS), solid phase Fe-OC associations (with selective extractions, nanoSIMS and Mössbauer spectroscopy), and microbial community relative abundance and potential activity (with DNA- and RNA-based 16S rRNA (gene) amplicon sequencing). We found that Fe-bound OC in intact palsa soils is comprised of loosely bound more aliphatic and strongly-bound more aromatic OC. Iron mineral dissolution by both fermentative (e.g. by *Clostridium* sp.) and dissimilatory Fe(III)-reduction (e.g. by *Geobacter* sp.) leads to a release of Fe-bound OC into the surrounding porewater along the palsa hillslopes, already before complete permafrost thaw. The increasing bioavailability of dissolved OC (DOC) leads to its further decomposition, an increasing nominal oxidation state of carbon (NOSC), and a peak in bioavailable acetate (61.7±42.6 mg C/L) at the collapsing palsa front. The released aqueous Fe^{2+} is partially re-oxidized by Fe(II)-oxidizing bacteria (presumably by *Gallionella* sp. and *Sideroxydans* sp.) but cannot prevent the overall loss of the rusty carbon sink with palsa collapse. The increasing relative abundance and activity of Fe(III)-reducers is accompanied by an increasing abundance of methanogens (e.g. *Methanobacterium* sp.) and a peak in methane (CH_4) emissions at the collapsing front. Our data suggest that the loss of the rusty carbon sink directly contributes to carbon dioxide (CO_2) by Fe(III) reduction coupled to OC oxidation and indirectly to CH_4 emission by promoting methanogenesis even before complete permafrost thaw.

Introduction

Permafrost regions have experienced an increase in surface air temperatures in recent decades, causing permafrost thaw and promoting active layer deepening, thermokarst formation, and river and coastal erosion[1]. Climate change has enormous consequences for permafrost environments, causing rapid changes in soil conditions (such as thermal and moisture regime, and aeration) with direct consequences for organic (OC) destabilization[2]. Permafrost soils store ~60% of the world's soil OC in 15% of the global soil area[3,4]. This preserved OC will become increasingly exposed to microbial decomposition and thus can be released from the active layer to the atmosphere as greenhouse gases (GHGs) such as carbon dioxide (CO_2) and methane (CH_4)[5], or discharged by drainage[6]. However, the magnitude of the release of this OC depends strongly on a large variety of factors[7], including the soil parent material (e.g. peat forming plant, bedrock) and the ability of soil minerals to protect OC from degradation, which can regulate long-term preservation of OC[8].

Iron (Fe) minerals are known to stabilize organic carbon by sorption/co-precipitation and protect it from degradation by generating OC-Fe associations that are more persistent in soils[9,10, 11-14]. However, by providing a terminal electron acceptor for anaerobic respiration[15,16], Fe can also enhance decomposition. The fate of Fe and associated OC determines Fe-OC aggregate formation and ultimately accessibility for microbial decomposition[16, 17,18]. Reactive Fe-OC associations (defined as the solid Fe phases that are reductively dissolved by sodium dithionite[12,19,20]) have been shown to serve as an effective rusty carbon sink and to preserve OC over geological timescales[12]. Previously, it has been shown that reactive Fe-OC associations can mainly be found in intact permafrost soils[21], but cannot preserve OC with complete permafrost thaw[20]. Transitional processes along permafrost thaw gradients, however, remain rather unstudied. Even though, methane dynamics can strongly differ between end-members and transitional thaw stages[22]. The need to better understand the climate impact of transitional processes in thawing permafrost was stated previously by Shelef *et al.*[23] who emphasize large uncertainty in permafrost carbon stocks (>200%) due to processes at collapsing fronts.

With permafrost thaw, soils become water-logged and oxygen (O_2) limited, as a result more reduced, favoring reductive dissolution of reactive Fe[20]. Fe(III)-reducing microorganisms are able to use the reactive Fe(III) as electron acceptor for anaerobic respiration and, depending on its composition, the associated OC as electron source leading to CO_2 and Fe(II) formation[22]. Thus, Fe(III) reduction directly contributes to CO_2 emissions[24]. Fe(III) reduction may also influence CH_4 emissions in thawing permafrost peatlands. On the one hand, Fe(III)

reduction is thermodynamically more favorable and thus could inhibit methanogenesis[25]. On the other hand, Fe(III) reduction leads to proton consumption which results in an increasing pH that could favor methanogenesis[26]. The complex balance of these processes that either suppress or promote GHG emissions such as CO_2 and CH_4, highlights the need for a fundamental understanding of microbial Fe metabolisms and their interactions with methanotrophs and methanogens, which is currently lacking in permafrost research.

The release of previously Fe-associated OC into surrounding porewater following reductive dissolution could lead to further microbial decomposition of OC and emission of GHGs such as CO_2 and CH_4. Mineral-associated OC (MAOC) has been proposed to be comprised of low molecular weight compounds of microbial (e.g. microbial polysaccharides, amino sugars, muramic acid) and plant origin[14,27-31] with low activation energies of MAOC for degradation by microbes and plants[11,32,33]. Therefore, the release of MAOC with permafrost thaw is considered an important driver of the composition of arctic surface waters and microbial respiration[34,35]. Recent studies described carboxylic-rich[36] and aliphatic Fe-bound OC in forest soils as more resistant during reductive dissolution[37]. In Siberian permafrost soils, hydrophobic, aromatic DOC was preferentially sorbed by shallower, acidic soil horizons and correlated with an increasing abundance of Fe oxides[38]. The identity of Fe-bound OC in permafrost environments, however, still remains unknown.

To understand the direct impact of the loss of this so called rusty carbon sink[39] on net GHG emissions in thawing permafrost peatlands, it is essential to further determine (1) the bioavailability of Fe-bound OC and released OC during permafrost thaw and (2) changes in the present and active microbial community, particularly the Fe(III)-reducing bacteria which are key players in reactive Fe mineral dissolution and their interplay with methanotrophs and methanogens.

We followed the dynamic biogeochemical interactions of Fe-OC associations in the active layer along collapsing palsa hillslopes, where palsas underlain by intact permafrost are collapsing into partially-thawed, semi-wet bogs. Fe-OC associations were characterized in the solid phase using selective extractions, scanning electron microscopy (SEM), nanoscale secondary ion mass spectrometry (nanoSIMS), and Mössbauer spectroscopy, and the effect of palsa collapse on porewater geochemistry and CO_2 and CH_4 fluxes was quantified. Reactive Fe-associated OC and DOC in the porewater along the palsa hillslope were investigated at the molecular-level with Fourier transform ion cyclotron resonance mass spectrometry (FT-ICR-MS), and the present and active microbial community was characterized using DNA- and RNA-based 16S rRNA amplicon gene sequencing.

Material and Methods

Site information

Stordalen Mire (68 22' N, 19 03' E) is a subarctic peatland in northern Sweden underlain by discontinuous permafrost. The mire consists of three distinct sub-habitats: (1) palsa (intact permafrost) with ericaceous and woody plants; (2) ombrotrophic peatland or bog (intermediate thaw) with *Sphagnum spp.*, sedges and shrubs and (3) minerotrophic peatland or fen (fully thawed) with sedges, mainly *Eriophorum spp*[40] (SI, Figure S1). Generally, palsas and bogs are only fed by precipitation and melt water and have more acidic surface waters (pH ~4). Fens are fed by surface water and groundwater, and maintain slightly acidic to alkaline pH[41]. The areal extent of intact palsa across Stordalen mire has declined significantly since 1970 due to progressive warming in the Arctic, while fen habitats have expanded[42]. It is also predicted that the whole mire might be free of permafrost as early as 2050[43,44].

Gas measurements

To measure CO_2 emissions along the palsa hillslope, two eosense instruments (eosFD Forced Diffusion chamber in conjunction with the eosLink-FD software, EOSENSE INC, Dartmouth, Canada) were installed (SI, Figures S1 and S2): (1) at the top of the palsa hillslope (spot: Palsa A) and (2) at the transition to bog (spot: Front). The collar was situated in a flat location and inserted to near full depth. A centimeter of space was left to aid in installation of the eosFD itself as well as collar retrieval. The collar area was cleared of any rocks or debris, larger vegetation was removed or avoided. The eosFD was deployed in the installed collar. The collars were deployed at least 24 hours prior to the start of the eosFD measurement collection to avoid disturbance-related fluxes in the early portion of the data collection. The eosFD samples gases from the atmospheric and soil cavities within the device. Briefly, gas is pulled from the atmospheric cavity to the sensor for 20 seconds to purge the sensor cavity, then sampled every 10 minutes for five samples. Gas is then pulled from the soil cavity for 20 seconds, then pulsed every 10 minutes for five samples. Forced diffusion flux is calculated as follows:

$$(V/A)\,(\partial C/\partial t) = Fs - D\,(\Delta C/L)$$

(volume/surface area scaled rate of change in flux rate equal to the flux from the soil surface (Fs) minus the difference in concentration, ΔC (scaled by both the path length L and the diffusivity of the interface (membrane), D)).

The change in the flux rate over the timespan of the concentration measurements (around 60 seconds) is assumed to be zero (steady state):

$$(V/A)\,(\partial C/\partial t) = 0$$

This assumption results in a linear dependence with the path length and interface (membrane) diffusivity being constant and represented by a single coefficient, G:

$$Fs = G\,\Delta C$$

Further, carbon dioxide and methane emissions along the palsa hillslope were measured in triplicate using plastic chambers sealed with a rubber stopper (SI, Figures S1 and S2), as described previously[45]. The metal frames were pushed into the ground at least 24 hours before the measurements to avoid collecting gas emissions from the soil during installation. Again rocks, debris and larger vegetation was avoided. Deionized water was used in the frames to seal off the chambers from ambient air. Gas chamber samples were collected with a gas-tight syringe (1100TLL 100 mL Gastight, Hamilton, Reno, NV, USA) and directly transferred into evacuated 12 mL exetainer vials[46] until analyzed. The sampling was done every 5 min for a total period of 30 mins in duplicates for palsa and front and in triplicates for bog. All gas samples from the field and standard gases used for calibration were measured with a gas chromatograph (Hewlett Packard, 5890 Series II) equipped with an electron capture detector (^{63}Ni-ECD).

Sample collection

In July 2019, cores were taken along three palsa hillslopes (see SI, Figure S1 and Figure S7), gently collapsing into bog, following the expected hydrological flow described previously[41]. A Humax corer of 50 cm length and 3-cm diameter with inner liners was used to sample the active layer[20]. The cores for mineral analysis were directly split after sampling under 100% N_2 atmosphere in a glove bag and subsamples stored at -20°C until analysis. The cores for microbial community analysis were split directly in the field, immediately frozen with liquid nitrogen and stored at -80°C until further processing. As previously described[20], the cores were split into three soil horizons based on texture and color changes: (1) A peat or organic horizon, followed by (2) a transition zone between the organic-rich and mineral-rich layer and (3) a mineral horizon.

In July and September 2019, porewater samples were collected from 30 and 60 cm depth below the peat surface along the palsa hillslope (8 transects, SI, Figure S1 and Figure S4)

using a luer lock syringe connected to a lysimeter with an effective pore size of 2.5 microns (Simpler Luer-Lock Micro Samplers, Model 1910LL, Soilmoisture Equipment Corp., Santa Barbara, CA). Prior to use, syringes and lysimeters were rinsed 10 times with 50 mL MiliQ water and air dried. Syringe filters (0.22 μm, PES, Merck™ Steritop™, Millipore) were pre-rinsed with 120 mL MilliQ water each to avoid leaching residuals of the filters. The syringes were flushed three times with N_2 and sealed till further use. Syringe filters (0.22 μm) were flushed three times with N_2 and placed into a SCHOTT bottle with N_2 atmosphere till further use. The lysimeters were installed in the soil, pre-flushed by pulling porewater with a syringe and the first 2 mL discharged. Immediately afterwards, the N_2 flushed syringes were unsealed, nitrogen gas pushed out, and then tightly connected to the installed lysimeter. To avoid direct sunlight exposure, syringes were covered with white cotton bags during the time of porewater extraction. After 3-4 hours, the samples were filtered through a 0.22 μm syringe filter into stoppered, N_2 flushed glass vials, wrapped in aluminum foil to avoid any sunlight exposure. The first 1 mL filtrate from each sample was disposed. The samples were stored at 4°C till further analysis.

Selective iron and carbon extractions

To extract reactive Fe and associated OC, selective dissolutions were conducted as described previously[20]. Briefly, a sodium bicarbonate (0.11 M) sodium dithionite (0.27 M) trisodium citrate (0.27 M) solution was used to reductively dissolve reactive Fe and associated organic carbon. As described in Lalonde *et al.*[12], a sodium bicarbonate (0.11 M) sodium chloride (1.85 M) solution was used as a control experiment to distinguish between Fe and OC readily desorbed (leachable OC) and organic carbon associated with reactive Fe and only dissolved during reductive dissolution with dithionite. The citrate background in the extract also needs to be subtracted to receive the reactive Fe-associated OC. Thus, only the control corrected values are discussed:

Reactive Fe

$$= Fe(\text{dithionite citrate}) - Fe(\text{sodium chloride}) \quad (1)$$

Reactive Fe-associated OC

$$= DOC(\text{dithionite citrate}) - DOC(\text{blank citrate}) - DOC(\text{sodium chloride}) \quad (2)$$

For each soil horizon (organic horizon, transition zone, mineral horizon), 0.3 g dry soil was weighed into 10 mL glass vials with 6.25 mL extractant and N_2 headspace. After 16 hours at

room temperature on a rolling shaker, samples were centrifuged at room temperature for 10 min at 5300 g. The supernatant was decanted and further analyzed for total Fe and DOC.

Geochemical analysis

To determine total Fe and Fe(II), porewater or extract was acidified in 1 M HCl and quantified spectrophotometrically in triplicates with the ferrozine assay[47]. DOC was measured in triplicates with a total organic carbon analyzer (High TOC II, Elementar, Elementar Analysensysteme GmbH, Germany). Inorganic carbon was removed by acidification with 2 M HCl addition prior to analysis. High performance liquid chromatography (HPLC; class VP with refractive index detector [RID] 10A and photo-diode array detector SPD-M10A VP detectors; Shimadzu, Japan) was used to determine the fatty acid concentrations. To further quantify other elements in the porewater (i.e. phosphorous and sulfur) the samples were acidified in 1% (v/v) HNO_3 and analyzed in triplicates by inductively coupled plasma mass spectrometry (ICP-MS/MS Agilent 8900). A flow injection analysis (FIA) instrument equipped with a dialysis membrane for removal of Fe to prevent side reactions during measurement (Seal Analytical, Germany) was applied for quantification of NH_4^+, NO_3^- and NO_2^- concentrations.

Correlative SEM and nanoSIMS analysis

The free particles of the fine fraction of each organic horizon, transition zone and mineral horizon in cores Palsa A (referred to intact palsa), Palsa B (referred to more collapsed palsa) and Front (referred to collapsing front) along the palsa hillslope were analyzed using correlative SEM and nanoSIMS, as described previously[20,48,49]. Briefly, subsamples of each layer (1 mg) were dispersed in anoxic deionized water and gently shaken to obtain the free organo-mineral particles. All larger particles and aggregates were allowed to settle. A drop of 100 μl of the suspension was placed on a silica wafer and dried in an anoxic glovebox (N_2 atmosphere). Finally, samples were sputter-coated with ~30 nm Au/Pd conductive layer using a Bal-Tec SCD005 sputter coater (Baltec GmbH, Germany). To characterize the organo-mineral particles of the fine fraction by size and crystallinity and identify representative particles, a field emission scanning electron microscope (FE-SEM; Jeol JSM-6500F), equipped with secondary electron detector, was used prior to nanoSIMS analysis. The acceleration voltage was set to 5 kV, with a working distance of 10 mm. The nanoSIMS analysis were performed at the Cameca nanoSIMS 50L of the Chair of Soil Science (TU München, Germany). As described previously[20], a primary ion beam (~2 pA) was set at a lateral resolution ~100 nm and scanned over the samples with $^{12}C^-$, $^{16}O^-$, $^{12}C^{14}N^-$, $^{31}P^-$, $^{32}S^-$, $^{27}Al^{16}O^-$ and $^{56}Fe^{16}O^-$ secondary ions collected using electron multipliers.

Mössbauer spectroscopy

The soil samples for ^{57}Fe Mössbauer spectroscopy were collected under the protection of 100% N_2. Samples from three thaw stages were measured, including Palsa A, Bog and Fen (both wetland cores obtained by a previous campaign see Patzner *et al.*[20]) of transition zone and mineral horizon (Figure S13 and Table S6). The samples were dried anoxically before loading into a Plexiglass holder. The prepared samples were stored anoxically at -20°C until measurement. Mössbauer spectroscopy was performed in a standard transmission setup (Wissel, Wissenschaftliche Elektronik GmbH), and absorption spectra were collected at 77 and 6 K controlling with a closed-cycle cryostat (SHI-850-I, Janis Research Co). The spectra were calibrated with $\alpha^{57}Fe^0$ foil at 295 K, and fitted using the Voigt Based Fitting (VBF)[50] routine in the Recoil software (University of Ottawa, Canada). Results are shown in the SI, Figure S13 and Table S6.

TOC and TN analysis

As described previously[20], total organic carbon (TOC) and total organic nitrogen (TN) were quantified by an Elementar vario EI (Elementar Analaysysteme, GmbH, Germany). Soil samples were dried at 60°C until no further weight loss was observed. The dried soils were ground and acidified with 16% HCl to remove the inorganic carbon. After washing with deionized water, followed by drying, the TOC and TN content was analyzed. Results of C/N ratios are shown in the SI (Figure S14).

Microbial community analysis

Total RNA and DNA was extracted using the PowerSoil® RNA and DNA isolation kit as described by the manufacturer (MO BIO Laboratories, Carlsbad, CA, USA), with the following modifications: 2-3 g of soil was used from each soil horizon; 10 min bead-beating; centrifugation steps at maximal speed (7000 x g) at 4°C; and longer incubation times at -20°C (1.5 h). RNA and DNA were eluted in 50 μl RNase/DNase-Free water. RNA and DNA concentrations were determined using a Qubit® 2.0 Fluorometer with RNA and DNA HS kits (Life Technologies, Carlsbad, CA, USA). Subsequent DNA digestion and reverse transcription reactions were performed using a Reverse Transcriptase (Invitrogen, Life Technologies) as described previously by Otte *et al.*, 2018[51]. Quantitative PCR (qPCR) specific for the 16S rRNA (gene) of bacteria and archaea was performed as described previously[51]. Microbial 16S rRNA (genes) were amplified using primers 515F and 806R[52]. Quality and quantity of the purified amplicons were determined using agarose gel electrophoresis and Nanodrop (NanoDrop

1000, Thermo Scientific, Waltham, MA, USA). Subsequent library preparation steps (Nextera, Illumina) and sequencing were performed by Microsynth AG (Switzerland) using the 2 × 250 bp MiSeq Reagent Kit v2 on an Illumina MiSeq sequencing system (Illumina, San Diego, CA, USA). From 10,112 to 396,483 (average 113,374) read pairs were generated per sample in three separate sequencing runs on the same MiSeq machine, resulting in total in 8.6 million read pairs. Quality control, reconstruction of 16S rRNA (gene) sequences and taxonomic annotation was performed with nf-core/ampliseq v1.1.2[53,54] with Nextflow v20.10.0[55] using containerized software with singularity v3.4.2[56]. Data from the three sequencing runs were treated initially separately by the pipeline using the option "mulipleSequencingRuns" and ASV tables were merged. Primers were trimmed, and untrimmed sequences were discarded (< 25%, on average 7.7%) with Cutadapt v2.6[57]. Adapter and primer-free sequences were imported into QIIME2 version 2019.10.0[58], processed with DADA2 version 1.10.0[59] to eliminate PhiX contamination, trim reads (before the median quality drops below 35, i.e. position 230 in forward reads and 174 in reverse reads), correct errors, merge read pairs, and remove PCR chimeras; ultimately, in total 9,576 amplicon sequencing variants (ASVs) were obtained across all samples. Alpha rarefaction curves were produced with the QIIME2 diversity alpha-rarefaction plugin, which indicated that the richness of the samples had been fully observed. A Naive Bayes classifier was fitted with 16S rRNA (gene) sequences extracted with the PCR primer sequences from the QIIME compatible, 99%-identity clustered SILVA v132 database[60]. ASVs were classified by taxon using the fitted classifier[61]. 225 ASVs that classified as chloroplasts or mitochondria were removed, totalling to < 7% (average 0.6%) relative abundance per sample, and the remaining 9,351 ASVs had their abundances extracted by feature-table (https://github.com/qiime2/q2-feature-table).

Pathways, i.e. MetaCyc ontology predictions, were inferred with PICRUSt2 version 2.2.0-b (Phylogenetic Investigation of Communities by Reconstruction of Unobserved States)[62] and MinPath (Minimal set of Pathways)[63] using ASVs and their abundance counts. Inferring metabolic pathways from 16S rRNA amplicon sequencing data is certainly not as accurate as measuring genes by shotgun metagenomics, but it yields helpful approximations to support hypotheses driven by additional microbiological and biogeochemical analyses[62].

FT-ICR-MS analysis

Soil extracts and DOM in the porewater were analyzed with FT-ICR MS to identify and monitor compositional changes in the mineral-associated organic carbon fraction and the mobile, DOC fraction. All of the samples were prepared for FT-ICR-MS analysis by solid phase extraction (SPE) under N_2 atmosphere (glove bag) following the procedure described by Dittmar *et al.,*

2008[64] and Li *et al.*, 2016[65] with some modifications. In brief, 1 g, 3 mL Bond Elut PPL cartridges (part#12102148, Aglient Technologies, Santa Clara, CA, USA) were conditioned with 5 mL of HPLC grade methanol (Simga-Aldrich, Rehovot, Israel), followed by 5 mL of 0.01 M HCl. Each sample was acidified to pH ~2.5 and then loaded onto the SPE columns, loading volume was adjusted to load a total of 0.5 mg C based on the TOC content. After sample loading, the SPE cartridges were rinsed with 5 mL of 0.01 M HCl followed by drying with N_2 for 3-5 mins. Finally, the samples were eluted with 1 mL of HPLC grade methanol and stored in airtight amber sample vials wrapped in aluminum foil at 4°C. There was no additional dilution of the samples performed prior to analysis by negative ion electrospray ionization.

The samples were analyzed with a custom-built FT-ICR mass spectrometer, equipped with a 21T superconducting solenoid magnet and a modular software package for data acquisition (Predator)[66]. Sample solution was infused via a microelectrospray source[67] (50 μm i.d. fused silica emitter) at 500 nL/min by a syringe pump. Typical conditions for negative ion formation were: emitter voltage, -3.0 kV; S-lens RF level, 45%; and heated metal capillary temperature, 350 °C. Ions were initially accumulated in an external multipole ion guide (1-5 ms) and released *m/z*-dependently[68]. Ions were excited to *m/z*-dependent radius to maximize the dynamic range and number of observed mass spectral peaks (32-64%)[69], and excitation and detection were performed on the same pair of electrodes[70]. The dynamically harmonized ICR cell in the 21 T FT-ICR is operated with 6 V trapping potential[71,72]. Time-domain transients (100 time-domain acquisitions for all experiments) of 3.1 seconds were acquired with the Predator data station that handled excitation and detection only, initiated by a TTL trigger from the commercial Thermo data station[73]. Mass spectra were phase-corrected[74] and internally calibrated with 10-15 highly abundant homologous series that span the entire molecular weight distribution (~150 to 1300 m/z) based on the "walking" calibration method[75]. Experimentally measured masses were converted from the International Union of Pure and Applied Chemistry (IUPAC) mass scale to the Kendrick mass scale[76] for rapid identification of homologous series for each heteroatom class[77]. Peaks with signal to noise ratios greater than 6 times the noise at the baseline root-mean-square (rms) noise at *m/z* 500 were exported to custom software (PetroOrg©) for additional formula and elemental composition assignment[78]. All assigned formulas were part of a ≥3 peak carbon series and had less than ±0.3 ppm mass error. A LOD of 6 σ was considered sufficient to minimize ionization difference effects between samples, and therefore biasing by large numbers of low abundance peaks. To further identify macro compositional shifts, analysis of differences between samples was performed only on peaks with ≥20% difference in relative abundance. Additionally, modified aromaticity index (ModAI)

was calculated according to Koch&Dittmar[64] and nominal oxidation state of carbon (NOSC) was calculated according to La Rowe&Van Cappellen[79]. Data processing post formula assignment was performed with RStudio utilizing R software (V4.0.3).

Results and Discussion

Greenhouse gas emissions promoted by microbial iron-cycling in thawing permafrost peatlands

In the palsa and at the collapsing front (SI, Figures S1 and S2), net CO_2 emissions were similar on average 1.57±0.27 μmol/m^2/s and slightly decreased in the bog to 1.12±0.51 μmol/m^2/s (Figure 1 a, measured with gas chambers). Replicate analysis of CO_2 concentrations in automatic Eosense gas chambers showed similar CO_2 emissions along the palsa hillslope (SI, Figure S3). Net CH_4 emissions were very low in the palsa (0.003±0.001 μmol/m^2/sec), significantly increased (unpaired *t*-test, $N = 3$, $\alpha = 0.05$, $p = 0.0001$) at the collapsing front to 0.025±0.001 μmol/m^2/s and then slightly decreased in the bog (0.013±0.001 μmol/m^2/s; Figure 1 a). Emission rates of CO_2 and CH_4 in the palsa and the bog at Stordalen mire are in line with previous studies [80-82]. This is the first report of emissions at the collapsing front, where palsa is collapsing into the bog.

Previous work demonstrated that highest reactive Fe and associated OC contents can be found in the soil profile where the organic and mineral horizons meet, which we have termed the “transition zone”[20]. DOC concentrations in the porewater of the transition zone were low in the intact palsa (Palsa A, 57.97±16.49 mg/L). They significantly increased (unpaired *t*-test, $N = 8$, $\alpha = 0.05$, $p = 0.0252$) towards the collapsing front to 207.65±168.16 mg/L in more collapsed palsa (Palsa B). Highest DOC concentrations were found directly at the collapsing front (535.75±131.45 mg/L) and then significantly decreased (unpaired *t*-test, $N = 8$, $\alpha = 0.05$, $p = 0.0009$) in the bog (279.62±113.14 to 206±80.28 mg/L) (Figure 1 b; SI, Figure S1 and Figure S4). The DOC shows the same trend as the aqueous Fe^{2+} concentrations (Figure 1 b). Aqueous Fe^{2+} concentrations in the palsa were lowest along the palsa hillslope (4.47±3.16 to 22.62±30.14 mg/L; Figure 1 b) and significantly increased (unpaired *t*-test, $N = 8$, $\alpha = 0.05$, $p = 0.0001$) at the collapsing front. Highest aqueous Fe^{2+} concentrations were measured at the collapsing front (153.24±40.14 mg/L) and significantly decreased again (unpaired *t*-test, $N = 8$, $\alpha = 0.05$, $p = 0.0064$) at the two measured locations in the bog to 48.86±11.43 and 82.43±47.93 mg/L (Figure 1 b). Other elements such as e.g. dissolved phosphorous also strongly correlated with the aqueous Fe^{2+} pulse at the collapsing front, suggestive for mineral dissolution (see SI, Figure S5 and for deeper mineral horizons see SI, Figures S6).

The release of OC and aqueous Fe^{2+} along the palsa hillslope was accompanied by a significant increase in the relative 16S rRNA gene sequence abundance (DNA-based) of iron-

and methane-cycling microorganisms in the transition zone and mineral horizon from the palsa to the collapsing front (Figure 1 c; SI, Figure S7). Fe(II)-oxidizing bacteria significantly increased (unpaired *t*-test, $N = 9$, $\alpha = 0.05$, $p = 0.0001$ and $p = 0.0076$) from the palsa to the collapsing front from 0.54±0.26 to 2.33±0.33% relative 16S rRNA gene sequence abundance in the transition zone and from 0.92±0.58 to 1.66±0.44% in the mineral horizon. Towards the collapsing front, Fe(III)-reducing bacteria also significantly increased (unpaired *t*-test, $N = 9$, $\alpha = 0.05$, $p = 0.0001$) from 0.41±0.07 to 2.46±0.34% relative 16S rRNA gene sequence abundance in the transition zone and from 0.21±0.05 to 2.42±0.27% in the mineral horizon (Figure 1 c). Methanogens significantly increased along the palsa hillslope (Palsa A to collapsing front; unpaired *t*-test, $N = 9$, $\alpha = 0.05$, $p = 0.0001$) from 0.42±0.37 to 2.83±0.26% relative 16S rRNA gene sequence abundance in the transition zone and from 1.40±1.40 to 11.68±3.12% in the mineral horizon. Methanotrophs significantly increased (unpaired *t*-test, $N = 9$, $\alpha = 0.05$, $p = 0.0001$) from the palsa to the collapsing front from 0.90±0.30 to 1.93±0.09% relative 16S rRNA gene sequence abundance in the transition zone and from 0.58±0.08 to 1.26±0.29% in the mineral horizon (Figure 1 c). Along the palsa hillslope, the relative 16S rRNA gene sequence abundances of iron- and methane-cycling microorganisms were stable in the organic horizon (Figure 1 c). The iron- and methane-cycling microorganisms are described in detail in Figure 3. For estimated absolute abundances of bacteria (DNA-based: $3.23 \times 10^5 – 4.24 \times 10^9$ and RNA-based: $1.44 \times 10^7 – 7.45 \times 10^{10}$ 16S rRNA gene copy numbers per g soil) and archaea (DNA-based: $1.55 \times 10^6 – 1.38 \times 10^9$ and RNA-based: $2.75 \times 10^4 – 5.58 \times 10^7$ 16S rRNA gene copy numbers per g soil) as well as the manually-compiled database used to identify iron- and methane-cycling microorganisms and the whole microbial community see SI (Figures S8 and S9 and Tables S1-S4).

At the same time, highest reactive Fe concentrations (defined as Fe reductively dissolved by sodium dithionite and control corrected by leachable Fe, see Material&Methods) (10.04±0.07 mg reactive Fe per g soil) were found in the transition zone of the most intact palsa soil (Palsa A) (Figure 2 a; for replicate core analysis see SI, Figure S10). Towards the collapsing front, reactive Fe in the transition zone between the organic and mineral horizons significantly decreased (unpaired *t*-test, $N = 9$, $\alpha = 0.05$, $p = 0.0001$) to 3.22±0.06 mg reactive Fe per g soil at the front (Figure 2 a). The amount of reactive Fe-associated OC (OC dissolved after reductive dissolution of reactive Fe minerals by sodium dithionite and control corrected by leachable OC, see Material&Methods) also decreased from the palsa (Palsa A and Palsa B) to the bog in the transition zone (83.69±10.04 and 76.60±16.89 mg Fe-associated OC per g soil in the palsa to 40.88±10.76 mg per g soil in the bog) (Figure 2 a). In the organic horizons along the palsa hillslope, reactive Fe and Fe-associated OC amounts were lowest in the soil

profile with average values of 0.49±0.25 mg reactive Fe per g soil and 2.08±2.47 mg Fe-associated OC per g soil (Figure 2 a). In the mineral horizons from the palsa to the collapsing front, reactive Fe was very stable (average 3.81±0.38 reactive Fe per g soil), whereas Fe-associated OC slightly decreased from 47.21±14.30 mg Fe-associated OC per g soil in the palsa to the collapsing front with 11.60±8.54 mg Fe-associated OC per g soil (Figure 2 a). The highest content of Fe-associated OC was found in the most intact palsa (Palsa A) along the palsa hillslope. This is supported by the strong spatial associations of OC with Fe minerals in the fine fraction observed by nanoSIMS analysis in the transition zone at Palsa A (Figure 2 b; see also replicate analysis of Palsa A, SI, Figures S1, transect 1 and S11-S12). The transition zone and mineral horizons at the collapsing front showed organic-free, co-existing Fe and aluminum (Al), suggestive of Fe-bearing clays (Figure 2 b). This is also supported by Mössbauer spectroscopy (SI, Figure S13 and Table S6) and by previous observations with extended X-ray adsorption fine structure (EXAFS)[20].

Highest reactive Fe and Fe-associated OC were found at the redox boundary between organic horizon and mineral horizon in intact permafrost soils[20,21,83]. It has been shown that these Fe-OC associations are completely lost in the solid phase along a permafrost thaw gradient[20]. Our newest data now reveals that this so called rusty carbon sink is already destabilized during palsa collapse, even before complete permafrost thaw. Lateral flow by runoff of rain and/or melt water[41,84] in the transition zone between organic and mineral hoirzon, caused by bulk density shifts (organic horizon: 0.03±0.01 g/cm^3 and mineral horizon: 0.84±0.26 g/cm^3)[20], favors micro-oxic conditions, as also described for other permafrost hillslopes[85]. These redox conditions promote Fe(III) reduction of reactive Fe minerals coupled to carbon oxidation driven by Fe(III)-reducing bacteria [15,86]. This results in a release of Fe and Fe-associated OC into the surrounding porewater and ultimately contributes to a pulse of aqueous Fe^{2+} and DOC at the collapsing front – where we observed the highest aqueous Fe^{2+} and DOC concentrations along the whole thaw gradient[20].

The release of OC along the palsa hillslope results from multiple co-occurring processes[85]. These include the release of Fe-associated OC, changes in in pH[87], plant community[40], and in microbial degradation of organic matter[88] (SI, Figure S14).

Fe(II)-oxidizers cannot prevent the overall loss of reactive Fe and Fe-associated OC by Fe(II) oxidation to Fe(III) along the palsa hillslope. The released OC, including previously Fe-associated-OC, and the CO_2 subsequently produced, further stimulated methanotrophic and methanogenic microorganisms at the collapsing front. This CO_2 production was at least partially driven by Fe(III) reduction coupled to carbon oxidation based on the increasing

abundance of Fe(III)-reducing bacteria along the palsa hillslope (also suggested for subalpine wetland soils[89]).

Ultimately, the loss of this so called rusty carbon sink contributes to net GHG emissions of CO_2 and CH_4, directly by Fe(III) reduction coupled to carbon oxidation and indirectly by promoting methanotrophy and methanogenesis at the collapsing front.

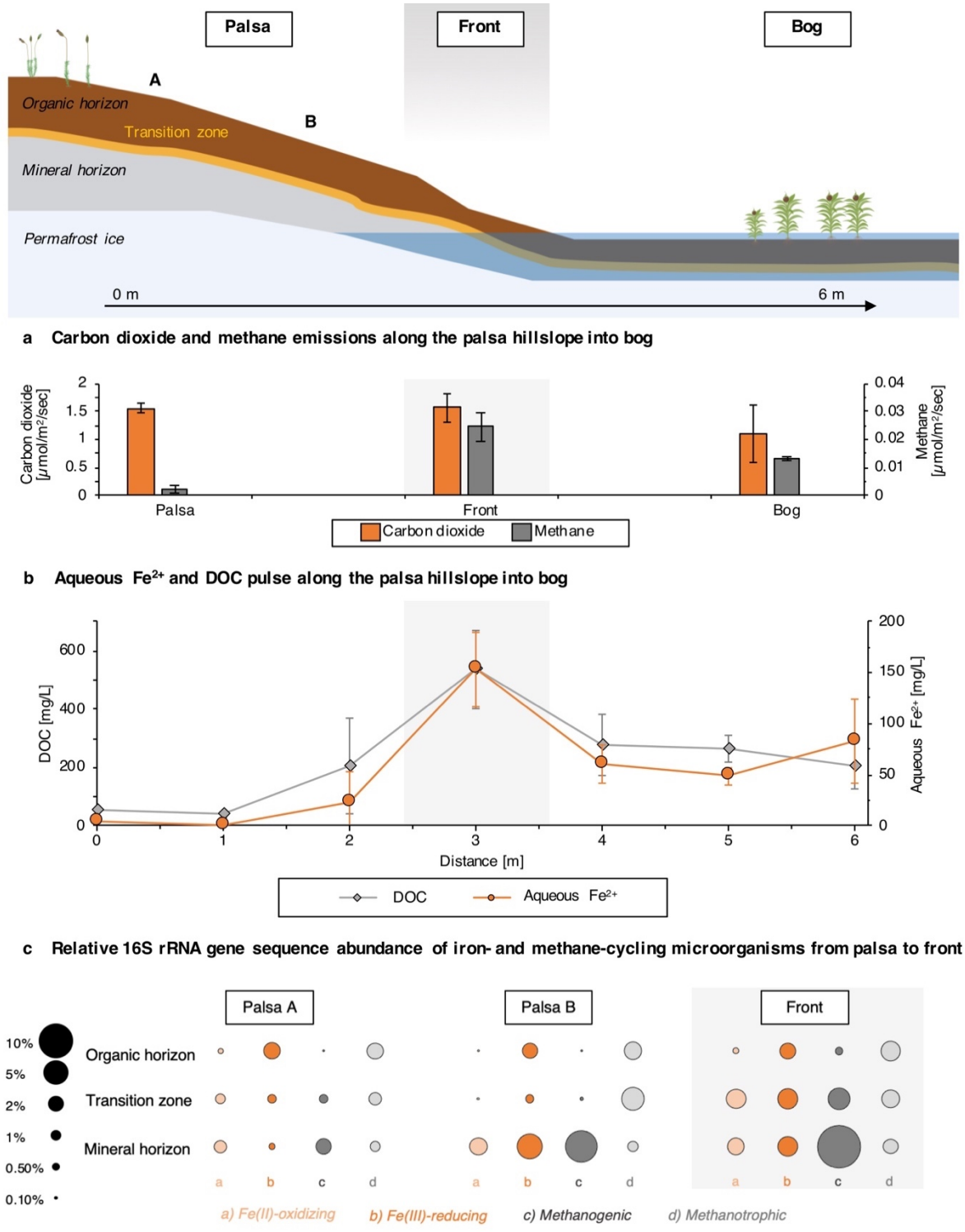

Figure 1. Microbial iron-cycling and carbon release as dissolved organic carbon (DOC), carbon dioxide and methane emissions along a palsa hillslope. *a, Carbon dioxide and methane emissions along the palsa hillslope with highest emissions at the collapsing front. The reported values and error bars represent the average and standard deviation of three days with three times 30 mins in 5 mins sampling intervals in July 2019 (see also SI, Figures*

S1, S2 and for replicate analysis Figure S3). b, Aqueous iron (Fe^{2+}) and DOC pulse along the palsa hillslope at 30 cm depth with highest values at the collapsing front. Reported values and error bars represent the average and standard deviation of eight palsa to bog hillslopes sampled in June/July 2019 (see also SI, Figure S1 and Figures S4-S6). c, Relative 16S rRNA gene abundance of iron- and methane-cycling strains [%] along the palsa hillslope with highest abundances at the collapsing front: a) Fe(II)-oxidzing, b) Fe(III)-reducing, c) methanogenic and d) methanotrophic. For absolute abundance of bacteria based on qPCR analysis specific for 16S rRNA genes and Fe- and methane-cycling microorganisms analyzed in this study (adapted from Otte et al.[51] and Weber et al.[90]) see SI, Figure S8 and Tables S1-S4. Cores were taken in July 2019 (see also SI, Figures S1, transect 1 and 3 and Figure S7-8 and Table S1-S4) in palsa (Palsa A = most intact, Palsa B = close to collapsing front) and at the collapsing front. Reported values and error bars represent the average and standard deviation of triplicate analysis of each soil horizon (organic horizon, transition zone and mineral horizon) along the palsa hillslope.

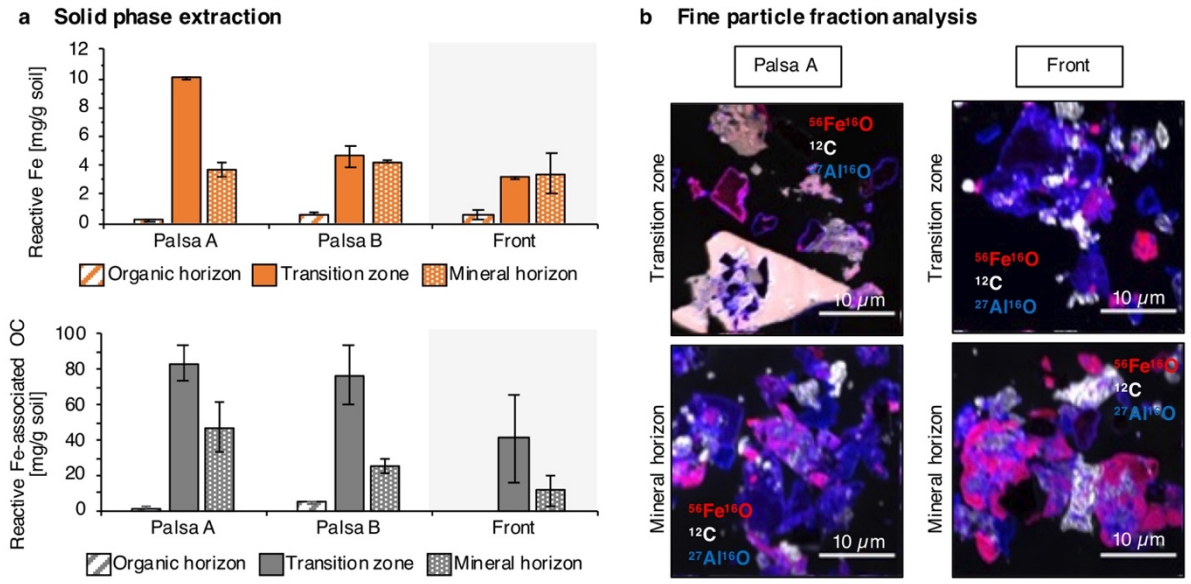

Figure 2. Reactive iron (Fe) and associated organic carbon (OC) from intact palsa to the collapsing front in a, the bulk soil and b, in the fine particle fraction. *a, Reactive Fe and Fe-associated organic carbon in the solid phase decrease from the intact palsa (Palsa A) towards the collapsing front. Reactive Fe values are the average of sodium dithionite citrate duplicate extractions, control corrected by sodium chloride bicarbonate extractable Fe (leachable Fe). Fe-associated OC values are the average of sodium dithionite citrate extractions, control corrected by subtraction of the citrate background and the sodium chloride*

bicarbonate extractable OC (leachable OC) (see Material&Methods). Cores were taken in July 2019 (see also SI, Figures S1, transect 1 and Figure S7-8 and Table S1-S4) in palsa (Palsa A = most intact, Palsa B = close to collapsing front) and at the collapsing front. Error bars of reactive Fe represent a combined standard deviation of sodium chloride bicarbonate extractable Fe and sodium dithionite citrate extractable Fe. Errors of the Fe-associated carbon represent a combined standard deviation of the citrate blank, sodium chloride bicarbonate extractable OC and sodium dithionite citrate extractable OC. For absolute amounts see SI, Table S5 and replicates see SI, Figure S10. b, High spatial resolution analysis of Fe-OC associations by nanoSIMS in the fine fraction of the soil, displayed as $^{12}C^-$ (white), $^{56}Fe^{16}O^-$ (red) and $^{27}Al^{16}O^-$ (blue) overlaid in a composite image. For the two end-members, Palsa A and collapsing front, four particles of the fine fractions of each layer were analyzed by correlative SEM and nanoSIMS, all showing the same spatial distribution of Fe, C and Al as shown by the four representatives (see SI, Figure S11-S12).

Microbial iron- and methane-cycling during palsa collapse

To investigate microbial key plays in the iron- and methane-cycle, we analyzed the microbial community by 16S rRNA gene amplicon sequencing.

Along the palsa hillslope, iron- and methane-cycling microorganisms are increasing in relative abundance, here defined as DNA-based relative 16S rRNA gene abundance, and in potential activity, here defined as RNA-based relative 16S rRNA abundance (Figure 3; for total microbial community and replicate analysis see SI, Figure S9 and S15).

Fe(III)-reducers, driving reactive Fe mineral dissolution and associated OC release, are found in high abundance and potential activity along the palsa hillslope. From Palsa A to the collapsing front, *Geobacter* sp., a classical Fe(III)-reducer[24], significantly increased (unpaired *t*-test, $N = 3$, $\alpha = 0.05$, $p = 0.0001$) in relative abundance from 0 to 1.55±0.30% in the transition zone and to 1.62±0.18% in the mineral horizon and potential activity from 0 to 2.50±0.13% in the transition zone and to 4.75±1.07% in the mineral horizon (Figure 3 a and b). *Clostridium* sp., a fermentative Fe(III)-reducer[53], significantly increased (unpaired *t*-test, $N = 3$, $\alpha = 0.05$, $p = 0.0001$) in their relative abundance from 0 to 0.81±0.02% in the transition zone and 0.76±0.07% in the mineral horizon (Figure 3 a) and in their potential activity from 0 to 2.31±1.15% in the transition zone and to 1.23±0.22% in the mineral horizon (Figure 3 b). *Rhodoferax* sp., known for dissimilatory Fe(III) reduction[52], only appeared to be present (1.98±1.51%) and active (1.62±0.16%) in the mineral horizon of the more collapsed palsa

(Palsa B), close to the collapsing front (Figure 3 a and b). *Myxococcales* sp. showed highest relative abundance from 1.67±0.15% in the intact palsa (Palsa A) to 1.30±0.23% at the collapsing front and potential activity from 9.13±0.08 in the intact palsa to 7.03±2.08% at the collapsing front in the organic horizon (Figure 3 a and b).

This microbial community analysis indicated that the rusty carbon sink is lost by dissimilatory and fermentative Fe(III) reduction. Dissimilatory Fe(III) reduction is conducted along the palsa hillslope by abundant and active Fe(III)-reducing microorganisms such as *Geobacter* sp., *Rhodoferax* sp. and *Myxococcales* sp. (Figure 3; see also absolute abundances in SI, Figure S8 and replicate core analysis SI, Figure S15)[51,90]. *Myxococcales* sp. are not only capable of Fe(III) reduction, but also i.e. polysaccharide and protein digestion[88]. *Geobacter* sp. and *Rhodoferax* sp. represent classical Fe(III)-reducing microorganisms, that are well studied in different environments[24] with *Rhodoferax* sp. also being described at other permafrost sites[15]. Fermentative Fe(III) reduction is probably performed by *Clostridium* sp. who might use, besides the present DOC, also the solid phase reactive Fe-associated OC to reduce reactive Fe (see SI, Figures S11-12).

The abundant and active Fe(III)-reducing bacteria are accompanied by lower relative abundant and probably lower active Fe(II)-oxidizers. *Gallionella* sp. was relative abundant with 0.82±1.16% and potentially active with 1.42±1.92% in the mineral horizon of the more collapsed palsa (Palsa B). *Sideroxydans* sp. significantly increased in their relative abundance from not detected to 1.42±0.21% in the transition zone (unpaired *t*-test, $N = 3$, $\alpha = 0.05$, $p = 0.0003$) and to 1.08±0.34% in the mineral horizon (unpaired *t*-test, $N = 3$, $\alpha = 0.05$, $p = 0.0053$). Other *Gallinoellaceae*, besides *Gallionella* sp. and *Sideroxydans* sp., were equally distributed in their relative abundance along the palsa hillslope from 0.54±0.26% in the transition zone and 0.86±0.55% in the mineral horizon of the intact palsa (Palsa A) to 0.90±0.12% in the transition zone and 0.58±0.09% in the mineral horizon at the collapsing front. The activity of the other *Gallionellaceae* was probably highest at the collapsing front with 0.53±0.24% in the transition zone and 0.35±0.07% in the mineral horizon. The relative abundant and potentially active classical Fe(II)-oxidizing bacteria[51,90] such as *Gallionella* sp., already described in arctic ponds[91], and *Sideroxydans* sp. (Figure 3) cannot sustain or reform the rusty carbon sink during palsa collapse (Figure 2).

The increasing relative 16S rRNA (gene) abundance (DNA- and RNA-based) of classical Fe(III)-reducing bacteria is accompanied by a significant increase (unpaired *t*-test, $N = 3$, $\alpha = 0.05$, $p = 0.0075$) in the relative abundance of methanogenic microorganisms, mainly *Methanobacterium* sp.. *Methanobacterium* sp. significantly increased in their relative

abundance in the transition zone from 0.25±0.24% in the intact palsa (Palsa A) to 2.05±0.14% at the collapsing front and in the mineral horizon from 1.15±1.22% in the intact palsa (Palsa A) to 10.07±2.84% at the collapsing front (Figure 3). Along the palsa hillslope (Palsa A to collapsing front), only a slight increase towards higher activity of *Methanobacterium* sp. was observed in the transition zone from 0 to 0.14±0.05% and in the mineral horizon from 0 to 1.91±0.85 % (Figure 3). Other methanogens belonging to *Bathyarchaeia* also significantly increased in relative abundance along the palsa hillslope from 0.17±0.13% to 0.71±0.12% in the transition zone (unpaired *t*-test, $N = 3$, $\alpha = 0.05$, $p = 0.0061$) and from 0.25±0.18% to 1.45±0.24% in the mineral horizon (unpaired *t*-test, $N = 3$, $\alpha = 0.05$, $p = 0.0023$). Methanotrophs, such as *Roseiarcus* sp. and other *Beijerinckiacaeae* (i.e. *Methylobacterium* sp. or *Methylocystis* sp.) were based on DNA equally relative abundant along the palsa hillslope with highest potential activity in the palsa closest to the collapsing front (Palsa B) with 12.55±0.30%.

Acetate, formed along the palsa hillslope with up to 61.70±42.56 mg C/L (10.33% of the total DOC) at the collapsing front (Figure 4), stimulates Fe(III) reduction coupled to acetate oxidation and leads to CO_2 formation by Fe(III)-reducing bacteria such as *Geobacter* sp., known to metabolize acetate[24]. The potential for reductive acetogenesis from CO_2 by *Bathyarchaeia* was previously suggested[92]. Our MetaCyc ontology predictions showed a high potential for acetoclastic methanogenesis (SI, Figure S16), but only the relative abundance of hydrogenotrophic methanogens such as *Methanobacterium* sp. This could be explained by the higher thermodynamical favorability of Fe(III) reduction coupled to acetate oxidation as compared to acetoclastic methanogenesis. H_2 and CO_2, partially produced by fermentative Fe(III) reduction by e.g. *Clostridium* sp., can be used by hydrogenotrophic methanogens and lead to CH_4 emissions at the collapsing front. The CH_4 is partially turned back to CO_2 by methanotrophs as shown by Perryman *et al.*[22] who described highest methane oxidation rates for palsa at the transition between palsa and bog (here referred as collapsing front).

Our data clearly shows a co-existence of the relative abundant and potentially active microbial iron- and methane-cycling microbial community during palsa collapse, which ultimately cause GHG emissions and effect the balance between CO_2 and CH_4 emissions already before complete permafrost thaw.

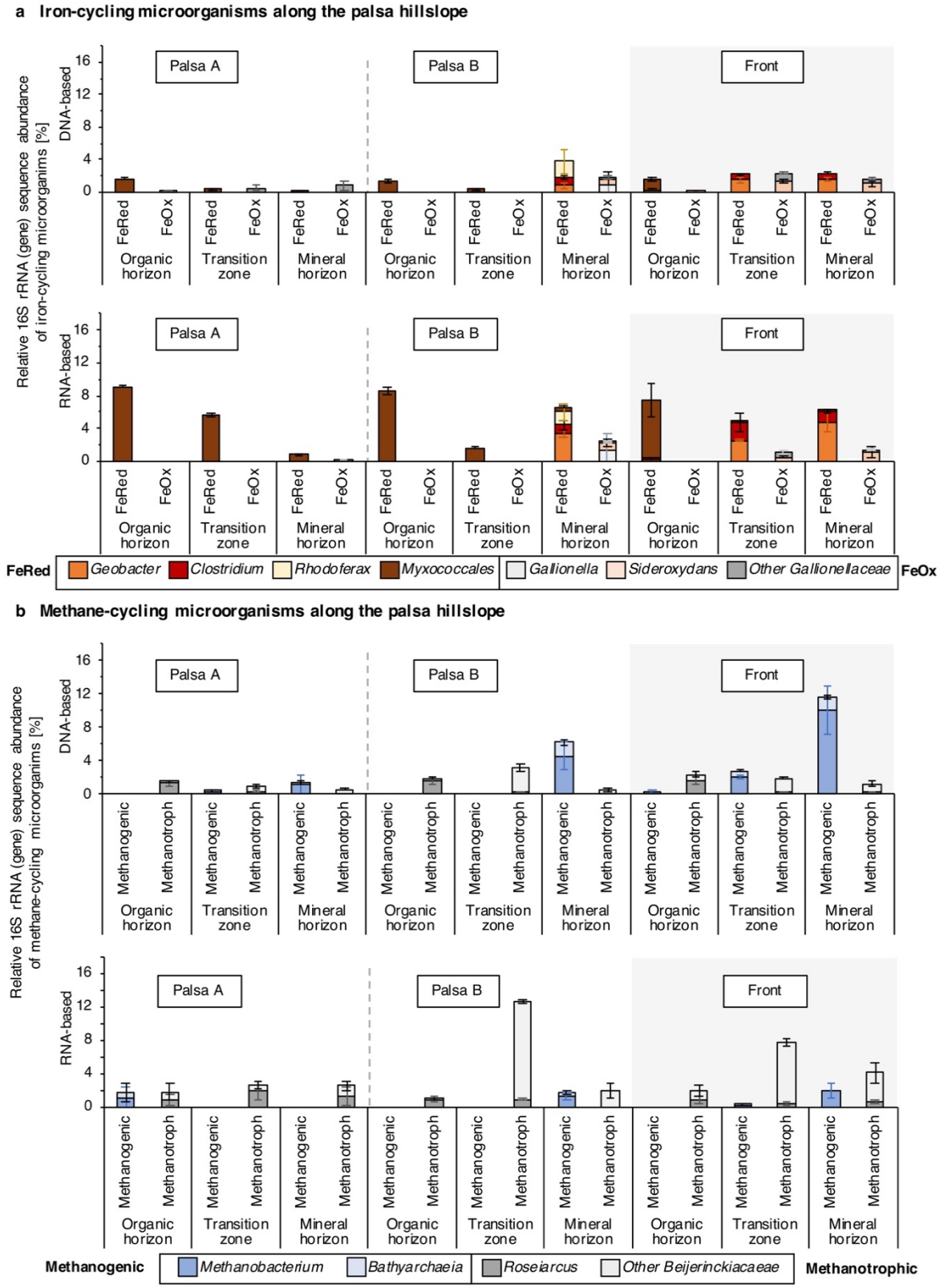

Figure 3. Relative 16S rRNA (gene) abundance of abundant (DNA-based) and likely active (RNA-based) iron (Fe)- and methane-cycling microbial communities along the palsa hillslope (Palsa A, Palsa B, Front). *a, Iron-cycling microorganisms show an increasing*

relative 16S rRNA (gene) abundance (DNA- and RNA-based) [%] along the palsa hillslope with highest abundances in the transition zone and mineral horizon at the collapsing front. b, Methane-cycling microorganisms are increasing in relative 16S rRNA (gene) abundance (DNA- and RNA-based) [%] along the palsa hillslope. For absolute abundance of bacteria and archaea based on qPCR analysis specific for 16S rRNA (genes) (based on DNA and RNA) and Fe- and methane-cycling microorganisms analyzed in this study (adapted from Otte et al.[51] and Weber et al.[90]) see SI, Figure S8 and Tables S1-S4. Reported values and error bars represent the average and standard deviation of triplicate analysis of each soil horizon (organic horizon, transition zone and mineral horizon) along the palsa hillslope (see also SI, Figure S1, transect 3 and Figure S7). Replicate cores show similar relative 16S rRNA (gene) abundance of abundant (DNA-based) and potentially active (RNA-based) Fe- and methane cycling microbial community along the palsa hillslope (SI, Figure 16).

Release of bioavailable iron-associated organic carbon during palsa collapse

The loss of the rusty carbon sink during the palsa collapse contributes to net GHG emissions directly by Fe(III) reduction coupled to carbon oxidation. To investigate if the loss of the rusty carbon sink also directly contributes to net GHG emissions by releasing bioavailable, previously Fe-bound organic carbon into the porewater which then becomes further metabolized by the present microbial community[88] (see also Figure S9), we determined the identity of Fe-bound OC in the solid phase (dithionite extractable OC) and released OC in the porewater. Dithionite did not affect the fate of extractable OC and did not lead to molecular artifact formation (see SI, Table S7).

FT-ICR-MS analyses showed that in the transition zone of the palsa, the reactive Fe-associated OC had a higher relative abundance of aliphatic species (green) than the reactive Fe-associated OC at the collapsing front (Figure 4 a; see SI, Figure S17). This more aliphatic-like fraction could represent amino sugar-like, carbohydrate-like and lignin-like compounds (O/C range: 0.3 to 0.6, H/C range: 1.0 to 1.5) [93,94]. A higher fraction of aromatics (purple) was associated with reactive Fe phases at the collapsing front compared to the organics bound by reactive Fe in the intact palsa (Figure 4 a; see also SI, Figures S14). In general, it should be noted that the amounts (mg/g) of reactive Fe-associated OC are decreasing along the palsa hillslope (see Figure 2 and Table S5). The higher relative abundance of the more aliphatic compounds (green) associated with reactive Fe in the intact palsa soils is lost during reductive dissolution to the surrounding porewater along the palsa hillslope, thus the aliphatic fraction

most likely contributes to the aqueous Fe^{2+} and DOC pulse at the collapsing front (Figure 4 a). Loosely bound OC (salt extractable) appeared in lower quantities and showed less defined, but similar organic fractions as the reactive Fe-associated OC (SI, Figure S18, Table S5 and S7).

Porewater extracted from the same soil interface (transition zone), in where the rusty carbon sink is lost along the palsa hillslope (Figure 1 and 2), contained a higher relative abundance of more aliphatic species and more aromatic species (green) as compared to porewater extracted at the collapsing front (Figure 4 a; see SI, Figures S17 and replicate analysis Figures S19). At the collapsing front, an increased relative abundance of organic molecules, potentially representing tannin-like compounds (O/C range: 0.5 to 0.9, H/C range: 0.5 to 1.4)[93,94], is observed (Figure 4 a; see SI, Figures S17). The more aliphatic and more aromatic species were lower in relative abundance in the DOC at the collapsing front, whereas a higher relative abundance of aromatic species was observed (purple, Figure 4 a). This could indicate decomposition processes that occur in the palsa hillslope porewater that yield smaller organic compounds, uptake by native microbes, assimilation of organic carbon into biomass and/or further metabolism, and ultimately emissions of GHGs by microbial respiration.

Further decomposition of DOC along the palsa hillslope is supported by an increasing nominal oxidation state of carbon (NOSC) of the DOC in the porewater at the transition zone from the palsa towards the collapsing front from 0.12±0.04 to 0.24±0.04 (Figure 4 b). As the DOC becomes more oxidized, the NOSC increases at the collapsing front. This is in line with an increasing average molecular weight (MW) from 591.24±7.70 in palsa to 614.80± 0.40 at the collapsing front (Figure 4 b and SI, Figure S20). NOSC values slightly decreased in the bog to 0.20±0.02 due to the overall loss of organic carbon mainly as CO_2 and, consequently, enrichment of less decomposed and more reduced DOC in the porewater. The double-bond equivalents (DBE, the number of rings plus double bonds to carbon, calculated from the neutral elemental composition[95]), remained rather stable along the palsa hillslope (0.39±0.08). The DBE along the palsa hillslope showed lower values than previously reported for bog and fen[87], indicating that bog and fen DOC is overall more unsaturated compared to DOC released along the palsa hillslope.

The further decomposition of released organic carbon contributes to acetate formation (Figure 4 c) at the collapsing front, probably by pyruvate fermentation, indicated by MetaCyc ontology predictions (SI, Figure S16). Along the palsa hillslope, acetate in the porewater at the transition zone between organic and mineral horizons significantly increased (unpaired *t*-test, $N = 8$, $\alpha = 0.05$, $p = 0.0024$) from 6.24±0.34 mg C/L (3.56% of the total DOC) in the palsa to

61.70±42.56 mg C/L (10.33% of the total DOC) at the collapsing front, the highest acetate concentrations observed across the whole thaw gradient[20]. Further into the bog, the acetate concentrations significantly decreased (unpaired *t*-test, $N = 8$, $\alpha = 0.05$, $p = 0.0085$) from 15.13±6.53 to 6.10±1.44 mg C/L.

Previous studies at Stordalen mire focused on the soil organic carbon, dissolved organic matter composition (DOM) and DOC transport along the thaw gradient. These analyses have highlighted shifts towards faster decomposition from partially-thawed bog to fully-thawed fen with an increasing proportion of carbon released as CH_4 [41,87,96]. Processes occurring at the transition between palsa and bog had not been studied, thus enhanced production of acetate and its promotion of methanogenesis at this transition has been overlooked.

Our data showed that reactive Fe at the redox boundary between organic and mineral horizons can bind aliphatic organic carbon, probably by downward cycling of DOM[97,98] which is released during reductive dissolution into the surrounding porewater. Lower molecular weight compounds, aliphatic compounds or compounds poor in carboxyl functional groups show lower sorption capacities to Fe minerals than higher molecular weight compounds, aromatics, or compounds rich in carboxyl functionalities[98]. This is also supported by the leachable OC extractions (same ionic strength and pH as the sodium dithionite extraction; see SI, Figure S20). Thus, these compounds are not protected from microbial degradation along the palsa hillslope. The previously Fe-associated aliphatic fraction becomes more bioavailable to microorganisms when it is released from mineral associations[98]. This likely contributes to promotion of microbial growth and respiration of DOM during permafrost thaw[97,99-101]. Relative to aromatic compounds, aliphatic compounds are expected to be even more labile to microorganisms [97,100,101], which is supported by the overall loss of this more aliphatic carbon fraction in the porewater at the collapsing front (Figure 4 a) with only minor quantities of aromatic organic molecules remaining preserved by reactive Fe minerals after palsa collapse (Figure 2 and Figure 4 a). Kawahigashi *et al.* showed that aromatic DOC was preferentially retained by mineral horizons in Siberian tundra containing reactive Fe[38].

Our data clearly suggests that the loss of this rusty carbon sink directly contributes to high DOC concentrations along the palsa hillslope and provides a bioavailable organic carbon source that stimulates microbial respiration and promotes GHG emissions.

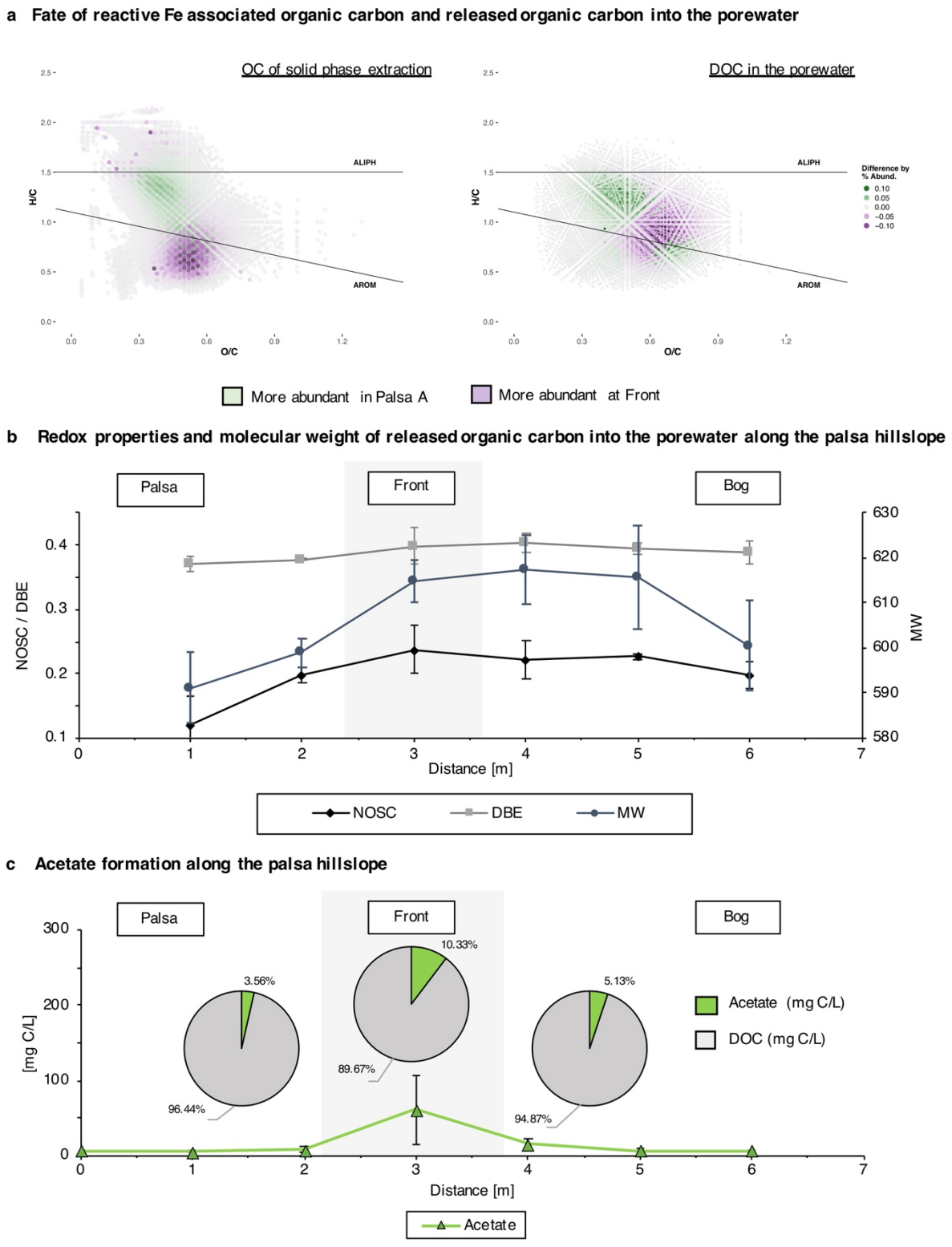

Figure 4. Bioavailability of reactive iron (Fe)-associated organic carbon (OC) released along the palsa hillslope. *a, Composition of reactive Fe-associated OC and released OC into the porewater visualized by van Krevelen diagrams. Fe-bound carbon in palsa soils, underlain by intact permafrost, is comprised of more aliphatic species (class 1, green) and more aromatic species (class 2, purple) and lost with reductive dissolution into the porewater.*

Towards the collapsing front into the bog, the remaining Fe-associated OC fraction is comprised of less bioavailable organic compounds which are likely associated with clay minerals (common in Palsa A, Front and Bog, marked in purple). Dissolved OC, which is only found in Palsa A, is enriched in more aliphatic compounds (green). Towards Front and Bog, only more aromatic species (purple) remain. For replicate analysis and control extractions to determine leachable OC (same ionic strength and pH as the sodium dithionite extraction) see also SI, Figures S17-S20. B, Redox properties and molecular weight of released organic carbon into the porewater along the palsa hillslope. Reported values represent average and error bars the range of duplicate porewater analysis along two palsa hillslopes (see also SI, Figures S17-S20). C, Acetate formation along the palsa hillslope. Following further decomposition of the dissolved OC, highly bioavailable acetate [mg C/L] is formed which then is again used to further reduce present reactive Fe(III) to Fe^{2+} coupled to acetate oxidation and CO_2 formation. Reported values and error bars represent the average and standard deviation of 8 palsa to bog hillslopes, sampled in June/July 2019 (see also SI, Figures S1 and Figure S4).

Implications for the carbon cycle in thawing permafrost peatlands

There is a substantial need to piece together carbon sources and sinks in thawing permafrost environments to better understand and predict the overall climate impact of permafrost thaw[102]. One such carbon sink or source are Fe-OC associations[39], which sequesters organic carbon in intact permafrost soils[21] but releases it with complete permafrost thaw[20]. Our data now showed that the release of the OC from the rusty carbon sink turns the OC into a source of labile DOC (10% acetate), CO_2 and CH_4 even before permafrost soils have completely collapsed. With increasing abrupt thaw, occurring in 20% of the permafrost zone, new active hillslope features are formed[103] and thus could speed up the loss of the rusty carbon sink in currently intact permafrost environments. Newest estimates showed that collapsing fronts will occupy 3% of abrupt thaw terrain by 2300, but could emit one-third of abrupt thaw carbon losses[103]. Ultimately, interlinked processes of iron- and carbon cycling in thawing permafrost environments need to be integrated into existing climate models to better understand and predict GHG emissions of thawing permafrost areas and thus better estimate its overall climate impact. For this, it is crucial to further determine co-occurring Fe(III) reduction rates and CO_2 and CH_4 production rates following Fe mineral dissolution.

Acknowledgments

We are grateful for assistance in field work and sampling by Sara Anthony and the Arctic Research station (Abisko Sweden), especially thankful to Jennie Wikström, Eric Lundin, Niklas Rakos and Alexander Meire. We are thankful to Mette Svenning (Arctic University of Norway, Tromsø, Norway) for providing the gas chambers with the plastic lids. We thank EOSENSE INC, Dartmouth, Canada for getting the chance to use the EOSENSE gas chambers for our research. We thank Miroslava Malusova and Katrin Wunsch for assistance in the lab, Timm Bayer for his help during SEM analysis and Johann Lugmeier for assistance during nanoSIMS analysis. The authors acknowledge infrastructural support by the Deutsche Forschungsgemeinschaft (DFG, German Research Foundation) under Germany's Excellence Strategy, cluster of Excellence EXC2124, project ID 390838134. This work was supported by the University of Tuebingen (Programme for the Promotion of Junior Researchers award to Casey Bryce) and by the German Academic Scholarship Foundation (scholarship to Monique Patzner). S.K is funded by an Emmy-Noether fellowship from the DFG (grant number 326028733). D.S was funded by the Institutional Strategy of the University of Tuebingen (DFG, ZUK63). The National High Magnetic Field Laboratory is supported by the National Science Foundation Divisions of Chemistry and Materials Research through DMR-1644779, Florida State University, and the State of Florida.

References

1 Fountain, A. G., Campbell, J. L., Schurr, E. A. G., Stammerjohn, S. E., Williams, M. W., Ducklow, H. W. The disappearing cryosphere: impacts and ecosystems responses to rapid cryosphere loss. *BioScience* **62**, 405-415 (2012).

2 Ping, C. L., Jastrow, J. D., Jorgenson, M. T., Michaelson, G. J., Shur, Y. L. Permafrost soils and carbon cycling *Soil* **1**, 147-171 (2015).

3 Schuur, E. A. G. *et al.* Climate change and the permafrost carbon feedback. *Nature* **520**, 171-179 (2015).

4 Hugelius, G. *et al.*, Estimated stocks of circumpolar permafrost carbon with quantified uncertainty ranges and identified data gaps. *Biogeosciences* **11**, 6573-6593 (2014).

5 Nowinski, N., Taneva, L., Trumbore, S., Welker, J. Decomposition of old organic matter as a result of deeper active layers in a snow depth manipulation experiment *Oecologia* **163**, 785-792 (2010).

6 Vonk, J. E., Mann, P. J., Davydov, S., Davydova, A., Spencer, R. G. M., Schade, J. High biolability of ancient permafrost carbon upon thaw *Geophys Res Lett* **40**, 2689-2693 (2013).

7 Henkner, J., Scholten, T., Kühn, P. Soil organic carbon stocks in permafrost-affected soils in West Greenland. . *Geoderma* **282**, 147-159 (2016).

8 Hemingway, J. D., Rothman, D. H., Grant, K. E., Rosengard, S. Z., Eglinton, T. I., Derry, L. A., Galy, V. V. Mineral protection regulates long-term global preservation of natural organic carbon. *Nature* **570**, 228-231 (2019).

9 Kleber, M., Mikutta, R., Torn, M. S. & Jahn, R. Poorly crystalline mineral phases protect organic matter in acid subsoil horizons. *Eur J Soil Sci* **56**, 717-725 (2005).

10 Baldock, J. A., Skjemstad, J. O. Role of soil matrix and minerals in protecting natural organic materials against biological attack. . *Org Geochem* **31**, 697-710 (2000).

11 Kleber, M. *et al.* Mineral-Organic Associations: Formation, Properties, and Relevance in Soil Environments. *Adv Agron* **130**, 1-140 (2015).

12 Lalonde, K., Mucci, A., Ouellet, A. & Gelinas, Y. Preservation of organic matter in sediments promoted by iron. *Nature* **483**, 198-200 (2012).

13 Wagai, R., Mayer, L. M., Kitayama, K. & Shirato, Y. Association of organic matter with iron and aluminum across a range of soils determined via selective dissolution techniques coupled with dissolved nitrogen analysis. *Biogeochemistry* **112**, 95-109 (2013).

14 Kogel-Knabner, I. *et al.* Organo-mineral associations in temperate soils: Integrating biology, mineralogy, and organic matter chemistry. *J Plant Nutr Soil Sc* **171**, 61-82 (2008).

15 Lipson, D. A., Jha, M., Raab, T. K. & Oechel, W. C. Reduction of iron (III) and humic substances plays a major role in anaerobic respiration in an Arctic peat soil. *J Geophys Res-Biogeo* **115**, G00I06 (2010).

16 Lovely, D. R. & Phillips, E.J. Novel mode of microbial energy metabolism: organic carbon oxidation coupled to dissimiliatory reduction of iron or mangenese. . *Applied and Environmental Microbiology* **57**, 1536-1540 (1988).

17 Asano, M. & Wagai, R. Evidence of aggregate hierarchy at micro- to submicron scales in an allophanic Andisol. *Geoderma* **216**, 62-74 (2014).

18 Totsche, K. U. *et al.* Microaggregates in soils. *J Plant Nutr Soil Sc* **181**, 104-136 (2018).
19 Coward, E. K., Thompson, A. T. & Plante, A. F. Iron-mediated mineralogical control of organic matter accumulation in tropical soils. *Geoderma* **306**, 206-216 (2017).
20 Patzner, M. S., Mueller, C. W., Malusova, M., Baur, M., Nikeleit, V., Scholten, T., Hoeschen, C., Byrne, J. M., Borch, Thomas, Kappler, A. & C. Bryce Iron mineral dissolution releases iron and associated organic carbon during permafrost thaw. *Nat Commun,* 11, 6329 (2020).
21 Mu, C. C. *et al.* Soil organic carbon stabilization by iron in permafrost regions of the Qinghai-Tibet Plateau. *Geophys Res Lett* **43**, 10286-10294 (2016).
22 Perryman, C. R. *et al.* Thaw Transitions and Redox Conditions Drive Methane Oxidation in a Permafrost Peatland. *J Geophys Res-Biogeo* **125** (2020).
23 Shelef, E., Rowland, J.C., Wilson, C.J., Hilley, G.E., ishra, U., Altmann, G.L., Ping, C.L. Large uncertainity in permafrost carbon stocks due to hillslope soil deposits. *Geophys Res Lett* **44**, 6134-6144 (2017).
24 Kappler, A., Bryce, C., Mansor, M., Lueder, U., Byrne, J.M., Swanner, E. An evolving view on biogeochemical cycling of iron. *Nature Reviews Microbiology* (2021).
25 Van Bodegom, P. M., Scholten, J. C. M. S., Stams, A. J. M. Direct inhibition of methanogenesis by ferric iron. *FEMS Microbiology Ecology* **49**, 261-268 (2004).
26 Wagner, R., Zona, D., Oechel, W., Lipson, D. Microbial community structure and soil pH correspond to methane production in Arctic Alaska soils. *Method Enzymol* **19**, 3398-3410 (2017).
27 Baldock, J. A. & Skjemstad, J. O. Role of the soil matrix and minerals in protecting natural organic materials against biological attack. *Org Geochem* **31**, 697-710 (2000).
28 Christensen, B. T. Physical fractionation of soil and structural and functional complexity in organic matter turnover. *Eur J Soil Sci* **52**, 345-353 (2001).
29 Sanderman, J., Maddern, T. & Baldock, J. Similar composition but differential stability of mineral retained organic matter across four classes of clay minerals. *Biogeochemistry* **121**, 409-424 (2014).
30 Six, J. *et al.* Sources and composition of soil organic matter fractions between and within soil aggregates. *Eur J Soil Sci* **52**, 607-618 (2001).
31 Daugherty, E. E. M., G. A.; Bergstrom, R.; Burton, S.; Pallud, C.; Hubbard, R. M.; Kelly, E. F.; Rhoades, C. C.; Borch, T. Hydrogeomorphic controls on soil carbon composition in two classes of subalpine wetlands. *Biogeochemistry* **145**, 161-175 (2019).
32 Jilling, A. *et al.* Minerals in the rhizosphere: overlooked mediators of soil nitrogen availability to plants and microbes. *Biogeochemistry* **139**, 103-122 (2018).
33 Williams, E. K., Fogel, M. L., Berhe, A. A. & Plante, A. F. Distinct bioenergetic signatures in particulate versus mineral-associated soil organic matter. *Geoderma* **330**, 107-116 (2018).
34 Crump, B., Kling, G., Bahr, M., Hobbie, J. Bacterioplankton community shifts in arctic lake corrleate with seasonal changes in organic matter sources. . *Applied and Environmental Microbiology* **69**, 2253-2268 (2003).
35 Judd, K. E., Crump, B.C., Kling, G.W. Variation in dissolved organic matter controls bacterial production

and community composition. *Ecology* **87**, 2068-2079 (2006).
36 Zhao, Q. *et al.* Iron-bound organic carbon in forest soils: quantification and characterization. *Biogeosciences* **13**, 4777-4788 (2016).
37 Adhikari, D. & Yang, Y. Selective stabilization of aliphatic organic carbon by iron oxide. *Sci Rep* **5**, 11214 (2015).
38 Kawahigashi, M., Kaiser, K., Rodionov, A., Guggenberger, G. Sorption of dissolved organic matter by mineral soils of the Siberian forest tundra. *Global Change Biol* **12**, 1868-1877 (2006).
39 Eglinton, T. I. GEOCHEMISTRY A rusty carbon sink. *Nature* **483**, 165-166 (2012).
40 Johansson, T. *et al.* Decadal vegetation changes in a northern peatland, greenhouse gas fluxes and net radiative forcing. *Global Change Biol* **12**, 2352-2369 (2006).
41 Olefeldt, D. & Roulet, N. T. Effects of permafrost and hydrology on the composition and transport of dissolved organic carbon in a subarctic peatland complex. *J Geophys Res-Biogeo* **117**, G01005 (2012).
42 Malmer, N., Johansson, T., Olsrud, M. & Christensen, T. R. Vegetation, climatic changes and net carbon sequestration in a North-Scandinavian subarctic mire over 30 years. *Global Change Biol* **11**, 1895-1909 (2005).
43 Fronzek, S., Carter, T. R., Raisanen, J., Ruokolainen, L. & Luoto, M. Applying probabilistic projections of climate change with impact models: a case study for sub-arctic palsa mires in Fennoscandia. *Climatic Change* **99**, 515-534 (2010).
44 Parviainen, M. & Luoto, M. Climate envelopes of mire complex types in Fennoscandia. *Geogr Ann A* **89a**, 137-151 (2007).
45 Liebner, S. *et al.* Shifts in methanogenic community composition and methane fluxes along the degradation of discontinuous permafrost. *Front Microbiol* **6**, 356 (2015).
46 Glatzel, S. & Well, R. Evaluation of septum-capped vials for storage of gas samples during air transport. *Environ Monit Assess* **136**, 307-311 (2008).
47 Stookey, L. L. Ferrozine - a New Spectrophotometric Reagent for Iron. *Anal Chem* **42**, 779-781 (1970).
48 Kopittke, P. M. *et al.* Nitrogen-rich microbial products provide new organo-mineral associations for the stabilization of soil organic matter. *Global Change Biol* **24**, 1762-1770 (2018).
49 Keiluweit, M. *et al.* Nano-scale investigation of the association of microbial nitrogen residues with iron (hydr)oxides in a forest soil O-horizon. *Geochim Cosmochim Ac* **95**, 213-226 (2012).
50 Rancourt, D. G., Ping, J. Y. Voigt-based methods for arbitrary-shape static hyperfine parameter distributions in Mössbauer spectroscopy *Nucl. Instrum. Methods Phys. Res. Sect. B* **58**, 85-97 (1991).
51 Otte, J. M. *et al.* The distribution of active iron-cycling bacteria in marine and freshwater sediments is decoupled from geochemical gradients. *Method Enzymol* **20**, 2483-2499 (2018).
52 Caporaso, J. G. *et al.* QIIME allows analysis of high-throughput community sequencing data. *Nat Methods* **7**, 335-336 (2010).
53 Ewels, P. A. *et al.* The nf-core framework for community-curated bioinformatics pipelines. *Nat Biotechnol* **38**, 276-278 (2020).
54 Straub, D. *et al.* Interpretations of environmental microbial community studies are biased by the selected 16S rRNA (gene) amplicon

sequencing pipeline. *Front Microbiol* **11**, 550420 (2020).
55 Di Tommaso, P. *et al.* Nextflow enables reproducible computational workflows. *Nat Biotechnol* **35**, 316-319 (2017).
56 Kurtzer, G. M., Sochat, V. & Bauer, M. W. Singularity: Scientific containers for mobility of compute. *PLoS One* **12**, (2017).
57 Martin, M. Cutadapt removes adapter sequences from high-throughput sequencing reads. *EMBnet journal* **17**, 3 (2011).
58 Bolyen, E. *et al.* Reproducible, interactive, scalable and extensible microbiome data science using QIIME 2. *Nat Biotechnol* **37**, 852-857 (2019).
59 Callahan, B. J. *et al.* DADA2: High-resolution sample inference from Illumina amplicon data. *Nat Methods* **13**, 581-583 (2016).
60 Pruesse, E. *et al.* SILVA: a comprehensive online resource for quality checked and aligned ribosomal RNA sequence data compatible with ARB. *Nucleic Acids Res* **35**, 7188-7196 (2007).
61 Bokulich, N. A. *et al.* Optimizing taxonomic classification of marker-gene amplicon sequences with QIIME 2's q2-feature-classifier plugin. *Microbiome* **6**, 90 (2018).
62 Langille, M. G. I., Zaneveld, J., Caporaso, J.G., McDonald, D., Knights, D., Reyes, J.A., Clemente, J.C., Burkepile, D.E., Vega Thurber, R.L., Knight, R., Beiko, R.G., Huttenhower, C. Predictive functional profiling of microbial communities using 16S rRNA marker gene sequences. *Nat. Biotechnol.* **31**, 814-821 (2013).
63 Ye, Y., Doak, T.G. A Parsimony Approach to Biological Pathway Reconstruction/Inference for Genomes and Metagenomes. *PLoS Comput. Biol.* **5** (2009).
64 Dittmar, T., Koch, B., Hertkorn, N. & Kattner, G. A simple and efficient method for the solid-phase extraction of dissolved organic matter (SPE-DOM) from seawater. *Limnol Oceanogr-Meth* **6**, 230-235 (2008).
65 Li, Y. *et al.* Proposed Guidelines for Solid Phase Extraction of Suwannee River Dissolved Organic Matter. *Anal Chem* **88**, 6680-6688 (2016).
66 Blakney, G. T., Hendrickson, C. L. & Marshall, A. G. Predator data station: A fast data acquisition system for advanced FT-ICR MS experiments. *Int J Mass Spectrom* **306**, 246-252 (2011).
67 Emmett, M. R., White, F. M., Hendrickson, C. L., Shi, S. D.-H. & Marshall, A. G. Application of micro-electrospray liquid chromatography techniques to FT-ICR MS to enable high-sensitivity biological analysis. *J. Am. Soc. Mass Spectrom.* **9**, 333-340 (1998).
68 Kaiser, N. K., Savory, J. J. & Hendrickson, C. L. Controlled ion ejection from an external trap for extended *m/z* range in FT-ICR mass spectrometry. *J. Am. Soc. Mass Spectrom.* **25**, 943-949 (2014).
69 Kaiser, N. K., McKenna, A. M., Savory, J. J., Hendrickson, C. L. & Marshall, A. G. Tailored ion radius distribution for increased dynamic range in FT-ICR mass analysis of complex mixtures. *Anal. Chem.* **85**, 265-272 (2013).
70 Chen, T., Beu, S. C., Kaiser, N. K. & Hendrickson, C. L. Note: Optimized circuit for excitation and detection with one pair of electrodes for improved Fourier transform ion cyclotron resonance mass spectrometry. *Rev. Sci. Instrum.* **85** (2014).
71 Boldin, I. A. & Nikolaev, E. N. Fourier transform ion cyclotron resonance cell with dynamic harmonization of the electric field in the whole volume by shaping of the excitation and detection electrode

assembly. *Rapid Commun. Mass Spectrom.* **25**, 122-126 (2011).

72 Kaiser, N. K., Quinn, J. P., Blakney, G. T., Hendrickson, C. L. & Marshall, A. G. A Novel 9.4 Tesla FT ICR mass spectrometer with improved sensitivity, mass resolution, and mass range. *J. Am. Soc. Mass Spectrom.* **22**, 1343-1351 (2011).

73 Blakney, G. T., Hendrickson, C. L. & Marshall, A. G. Predator data station: A fast data acquisition system for advanced FT-ICR MS experiments. *Int. J. Mass Spectrom.* **306**, 246-252 (2011).

74 Xian, F., Hendrickson, C. L., Blakney, G. T., Beu, S. C. & Marshall, A. G. Automated Broadband Phase Correction of Fourier Transform Ion Cyclotron Resonance Mass Spectra. *Anal Chem* **82**, 8807-8812 (2010).

75 Savory, J. J. *et al.* Parts-Per-Billion Fourier transform ion cyclotron resonance mass measurement accuracy with a "Walking" calibration equation. *Anal. Chem.* **83**, 1732-1736 (2011).

76 Kendrick, E. A mass scale based on CH_2 = 14.0000 for high resolution mass spectrometry of organic compounds. *Anal. Chem.* **35**, 2146-2154 (1963).

77 Hughey, C. A., Hendrickson, C. L., Rodgers, R. P., Marshall, A. G. & Qian, K. N. Kendrick mass defect spectrum: A compact visual analysis for ultrahigh-resolution broadband mass spectra. *Anal Chem* **73**, 4676-4681 (2001).

78 Corilo, Y. E. The Florida State University: Tallahassee, Fl, USA. *PetroOrg* (2012).

79 LaRowe, D. E. & Van Cappellen, P. Degradation of natural organic matter: A thermodynamic analysis. *Geochim Cosmochim Ac* **75**, 2030-2042 (2011).

80 McCalley, C. K. *et al.* Methane dynamics regulated by microbial community response to permafrost thaw. *Nature* **514**, 478-481 (2014).

81 Mondav, R. *et al.* Discovery of a novel methanogen prevalent in thawing permafrost. *Nat Commun* **5**, 3212 (2014).

82 Singelton, C. M., McCalley, C.K., Woodcroft, B.J., Boyd, J.A., Evans, P.N., Hodgkins, S.B., Chanton, J.P., Frolking, S., Crill, P.M., Saleska, S.R., Rich, V.I., Tyson, G.W. . Methanotrophy across a natural permafrost thaw environment *The ISME Journal* **12**, 2544-2558 (2018).

83 Herndon, E. *et al.* Influence of iron redox cycling on organo-mineral associations in Arctic tundra soil. *Geochim Cosmochim Ac* **207**, 210-231 (2017).

84 Tang, J., Yurova, A.Y., Schurgers, G., Miller, P.A., Olin, S., Smith, B., Siewert, M.B., Olefeldt, D., Pilesjö, P., Poska, A. Drivers of dissolved organic carbon export in a subarctic catchment: Importance of microbial decomposition, sorption-desorption, peatland and lateral flow. *Science of the Total Environment,* 260-274 (2018).

85 Lynch, L. M., Machmuller, M.B., Boot, C.M., Covino, T.P., Rithner, C.D., Cotrufo, M.F., Hoyt, D.W., Wallenstein, M.D. Dissolved organic matter chemistry and transport along an Arctic tundra hillslope. *Global Biogeochem Cy* **33**, 47-62 (2019).

86 Lipson, D. A., Raab, T.K., Goria, D., Zlamal, J. . The contribution of Fe(III) and humic acid reduction to ecosystem respiration in drained thaw lake basins of the Arcitc Coastal Plain. *Global Biogeochem Cy* **27**, 399-409 (2013).

87 Hodgkins, S. B. *et al.* Changes in peat chemistry associated with permafrost thaw increase greenhouse gas production. *P Natl Acad Sci USA* **111**, 5819-5824 (2014).

88 Woodcroft, B. J. *et al*. Genome-centric view of carbon processing in thawing permafrost. *Nature* **560**, 49-54 (2018).

89 Pallud, C., Rhoades C. C., Schneider, L., Dwivedi, P., Borch, T. Temperature-induced iron (III) reduction results in decreased dissolved organic carbon export in subalpine wetland soils, Colorado, USA. *Geochim Cosmochim Ac* **280**, 148-160 (2020).

90 Weber, K. A., Achenbach, L.A., Coates, J.D. . Microorganisms pumping iron: anaerobic microbial iron oxidation and reduction. . *Nature Reviews Microbiology* **4**, 752-764 (2006).

91 Emerson, D., Scott, J.J., Benes, J., Bowden, W.B. . Microbial iron oxidation in the Arctic tundra and its implications for biogeochemical cycling *Applied and Environmental Microbiology* **81**, 8066-8075 (2015).

92 Loh, H. Q., Hervé, V., Brune, A. . Metabolic potential for reductive acetogenesis and a novel energy-converting [NiFe] Hydrogenase in Bathyarchaeia from termite guts - a genome-centric analysis. *Front Microbiol,* **11** 635786 (2021).

93 Tfaily, M. M. C., R.K., Tolic, N., Roscioli, K.M., Anderton, C.R., Pasa-Tolic, L. et al. . Advanced solvent based methods for molecular characterization of soil organic matter by high-resolution mass spectrometry. *Anal Chem* **87**, 5026-5215 (2015).

94 Tfaily, M. M., Chu, R.K., Toyoda, J., Tolic, N., Robinson, E.W., Pasa-Tolic, L. et al. Sequential extraction protocol for organic matter from soils and sediments using high resolution mass spectrometry. *Anal Chim Acta* **972**, 54-61 (2017).

95 McLafferty, F. W., Choi, J., Tureček, F. & Turecek, F. *Interpretation Of Mass Spectra*. (University Science Books, 1993).

96 AminiTabrizi, R. *et al.* Controls on soil organic matter degradation and subsequent greenhouse gas emissions across a permafrost thaw gradient in Northern Sweden. *Frontiers in Earth Science* **8**, 557961 (2020).

97 Ward, P. C., Cory, R.M. . Chemical composition of dissolved organic matter draining permafrost soils. *Geochim Cosmochim Ac* **167**, 63-67 (2015).

98 Kaiser, K., Kalbitz, K. . Cycling downwards - dissolved organic matter in soils *Soil Biol Biochem* **52**, 29-32 (2012).

99 Fuchs, G., Boll, M., Heider, J. . Microbial degradation of aromatic compounds - From one strategy to four. *Nat Rev Microbiol* **9**, 803-816 (2011).

100 Abbott, B. W., Larouche, J.R., Jones, J.B., Bowden, W.B., Balser, A.W. Elevated dissolved organic carbon biodegradability from thawing and collapsing permafrost. *J Geophys Res* **119**, 2049-2063 (2014).

101 Mann, P. J., Davydova, A., Zimov, N., Spencer, R. G. M., Davydov, S., Bulygina, E., Zimov, S., Holmes, R.M. Controls on the composition and lability of dissolved organic matter in Siberia's Kolyma River basin. *J Geophys Res,* **117**, G01028 (2012).

102 When permafrost thaws. *Nat Geosci* **13**, 765 (2020).

103 Turetsky, M. R. *et al.* Carbon release through abrupt permafrost thaw. *Nat Geosci* **13**, 138-143 (2020).

Supplementary information for

Microbial iron(III) reduction during palsa collapse promotes greenhouse gas emissions before complete permafrost thaw

Monique S. Patzner[1], Merritt Logan[2], Amy M. McKenna[3], Robert B. Young[2,4], Zhe Zhou[1,5], Hanna Joss[1], Carsten W. Mueller[6,7], Carmen Hoeschen[6], Thomas Scholten[8], Daniel Straub[9,10], Sara Kleindienst[10], Thomas Borch[2], Andreas Kappler[1,11] & Casey Bryce[1,12]

[1]Geomicrobiology, Center for Applied Geosciences, University of Tuebingen, Schnarrenbergstrasse 94-96, 72076 Tuebingen, Germany.

[2]Department of Soil & Crop Sciences and Department of Chemistry, Colorado State University, 307 University Ave, 80523-1170 Fort Collins, US.

[3]National High Magnetic Field Laboratory, Florida State University, Tallahassee, FL 32310-4005, US.

[4]Chemical Analysis and Instrumentation Laboratory, New Mexico State University, P.O. Box 30001, MSC 3RES, Las Cruces, NM, 88003, US.

[5]Alfred-Wegener-Institute, Helmholtz Centre for Polar and Marine Research, Am Handelshafen 12, 27570 Bremerhaven, Germany

[6]Chair of Soil Science, TUM School of Life Sciences, Technical University of Munich, Emil-Ramann Strasse 2, 85354 Freising, Germany.

[7]Department of Geosciences and Natural Resource Management, University of Copenhagen, Øster Voldgade 10, 1350 Copenhagen, Denmark.

[8]Chair of Soil Science and Geomorphology, Rümelinstraße 19-23, 72070 Tübingen, University of Tuebingen, Germany.

[9]Microbial Ecology, Center for Applied Geosciences, University Tuebingen, Schnarrenbergstrasse 94-96, 72076 Tuebingen, Germany.

[10]Quantitative Biology Center (QBiC), University Tuebingen, Auf der Morgenstelle 10, 72076 Tuebingen, Germany.

[11]Cluster of Excellence: EXC 2124: Controlling Microbes to Fight Infection, Tuebingen, Germany.

[12]School of Earth Sciences, University of Bristol, Wills Memorial Building, Queens Road Bristol BS8 1RJ, UK.

Manuscript submitted for publication to: *Nature Comms Earth & Environment*

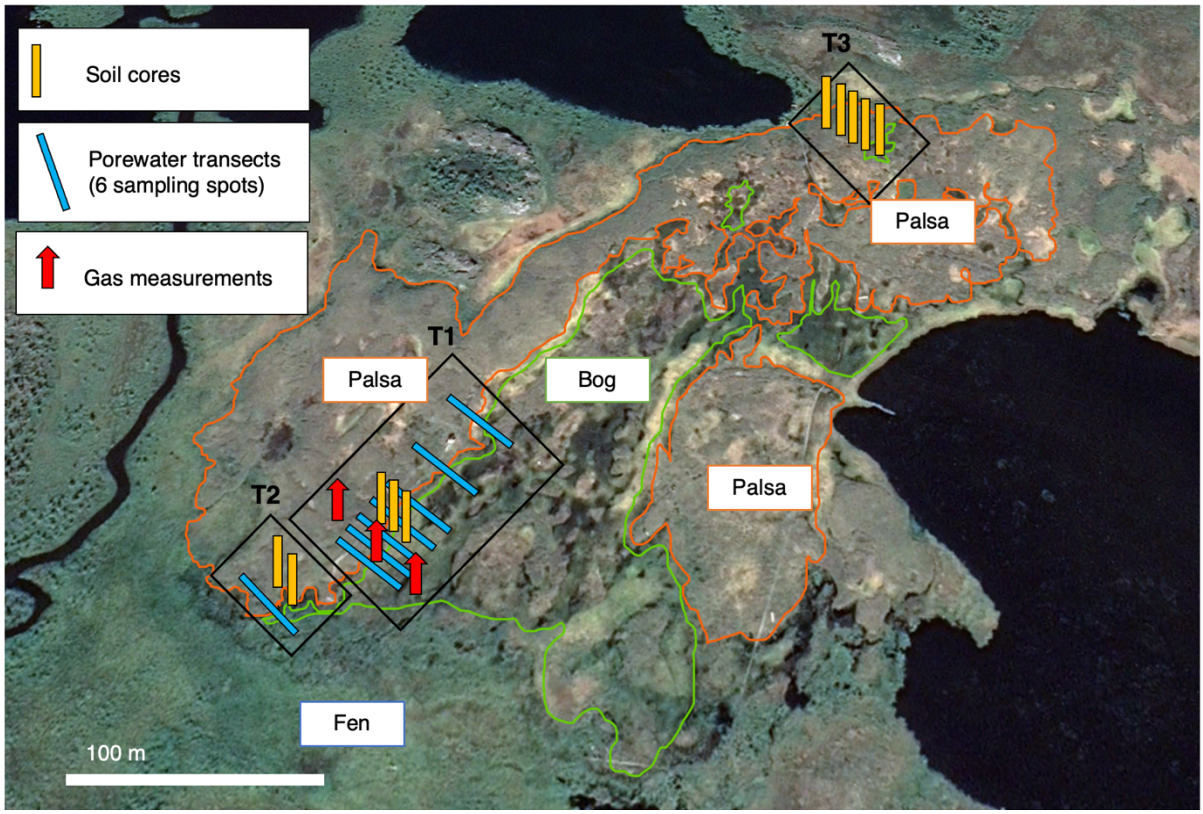

Figure S1. Field site and sample collection. *Soil cores (yellow), porewater samples (blue) and gas samples (red) were taken in three transects (T1, T2 and T3) along palsa hillslopes into bog at Stordalen mire, Abisko (Sweden). Background picture is taken by GoogleEarth in 2019.*

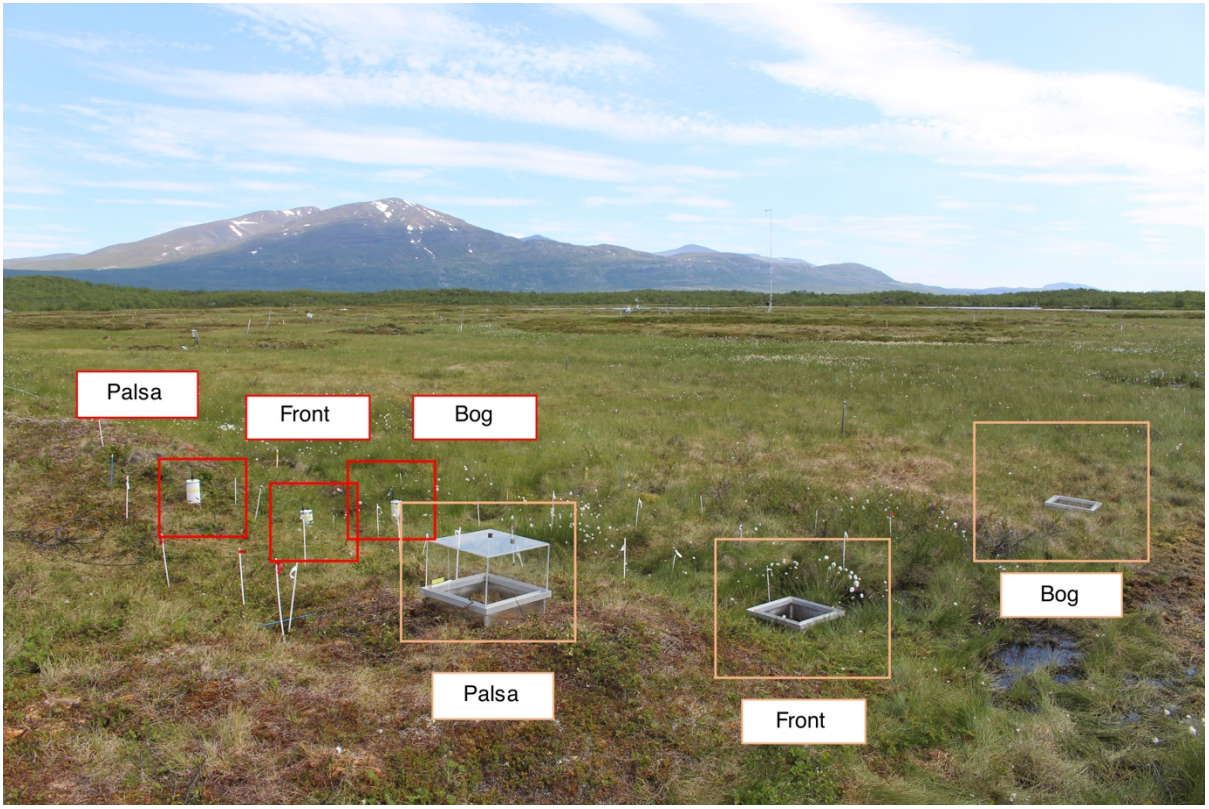

Figure S2. Gas sampling along palsa hillslopes. *In transect 1 (see also Figure S1), Eosense gas chambers (eosFD Forced Diffusion chamber in conjunction with the eosLink-FD software, EOSENSE INC, Dartmouth, Canada) (red) were installed to measure carbon dioxide emissions along the palsa hillslope (68°21'18.70"N, 19° 2'38.00"E). Additional gas chambers with plastic chambers, sealed with a rubber stopper, and metal frames (orange) were installed to obtain replicate carbon dioxide and additionally methane emissions along the palsa hillslope into the bog area.*

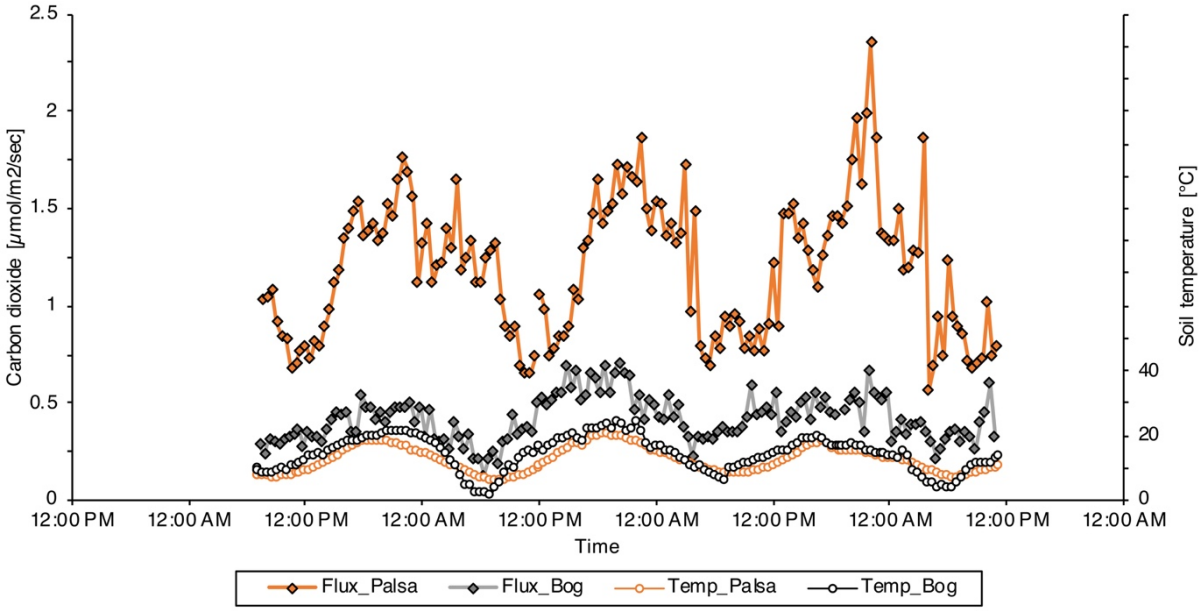

***Figure S3. Carbon dioxide emissions along the palsa hillslope (palsa and bog**). Eosense gas chambers (eosFD Forced Diffusion chamber in conjunction with the eosLink-FD software, EOSENSE INC, Dartmouth, Canada) were installed along the palsa hillslope and analysis performed from the 8th of July to 10th of July 2019. Unfortunately, the second Eosense instrument at the collapsing front (shown in Figure S2) was broken during shipment and thus excluded in the analysis. The carbon dioxide emissions correlate with the surface soil temperature (measured at 5 cm soil depth at palsa and bog), measured by Integrated Carbon Observation System (ICOS) Sweden Abisko – Stordalen[1].*

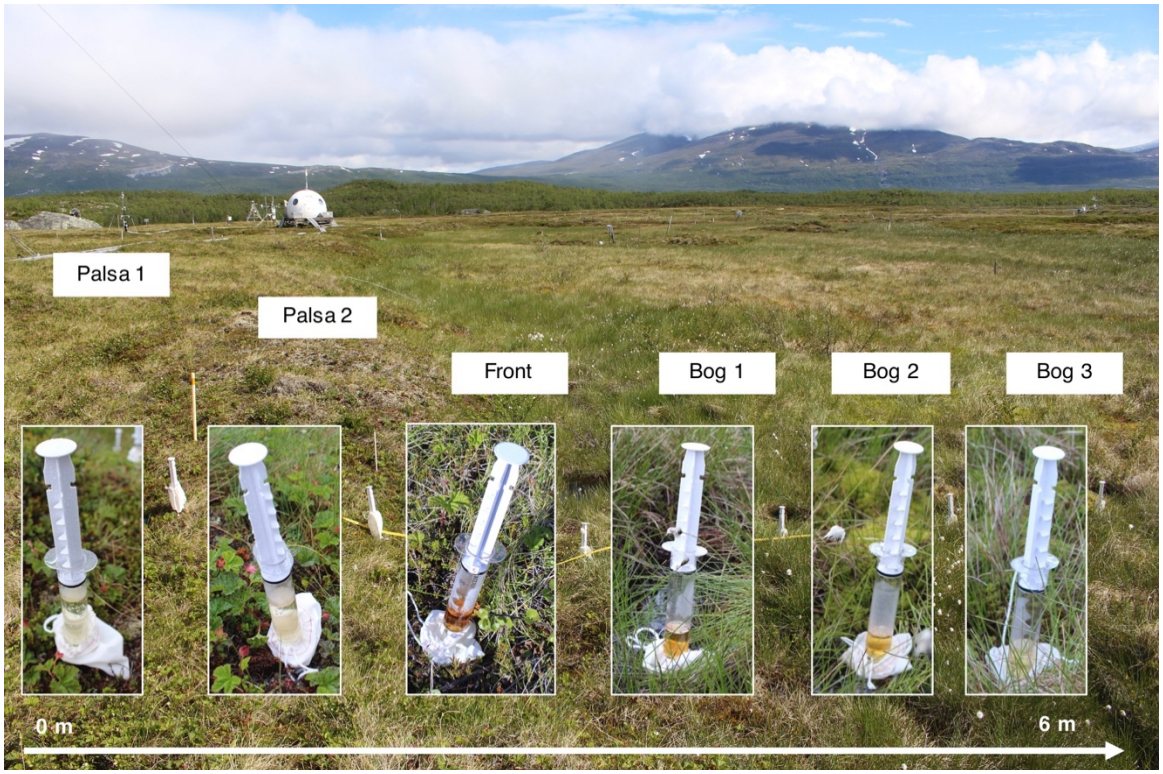

Figure S4. Porewater sampling along palsa hillslopes. *Along eight palsa hillslopes, porewater was extracted with lysimeters at six defined sampling points in July 2019. In transect 1 (shown here, see also Figure S1), lysimeters were installed for 3-4 hours along the palsa hillslope (68°21'18.70"N, 19° 2'38.00"E) at a distance of 1 m in between each other from palsa to bog. The porewater with dark brown, reddish color at the collapsing front represents the sample with the highest aqueous iron and dissolved organic carbon along the palsa hillslope into bog.*

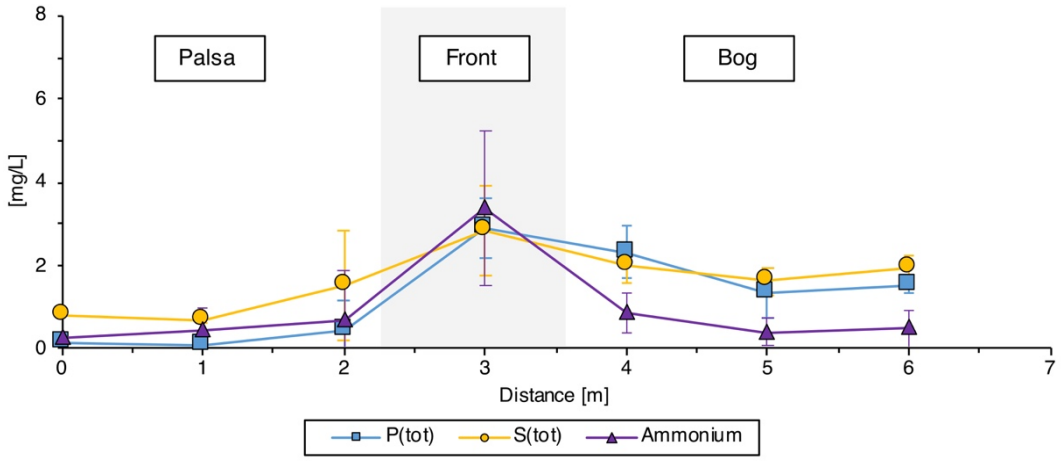

Figure S5. Aqueous total phosphorous (P(tot)), aqueous total sulfur (S(tot)) and ammonium concentrations in the porewater along the palsa hillslope (30 cm depth, transition zone). *Aqueous concentrations are reported in mg/L from palsa (0-2.7 m) to bog (2.7-7 m). Reported values represent the average of six sampling spots for eight palsa hillslopes (0-2.3 m) to collapsing front (2.3-3.6) to bog (3.6-7 m), sampled in June/July (see also SI, Figures S1 and Figure S4). Error bars represent the standard deviation of eight palsa hillslopes (0-2.3 m) to collapsing front (2.3-3.6) to bog (3.6-7 m), sampled in June/July (see also SI, Figure S1).*

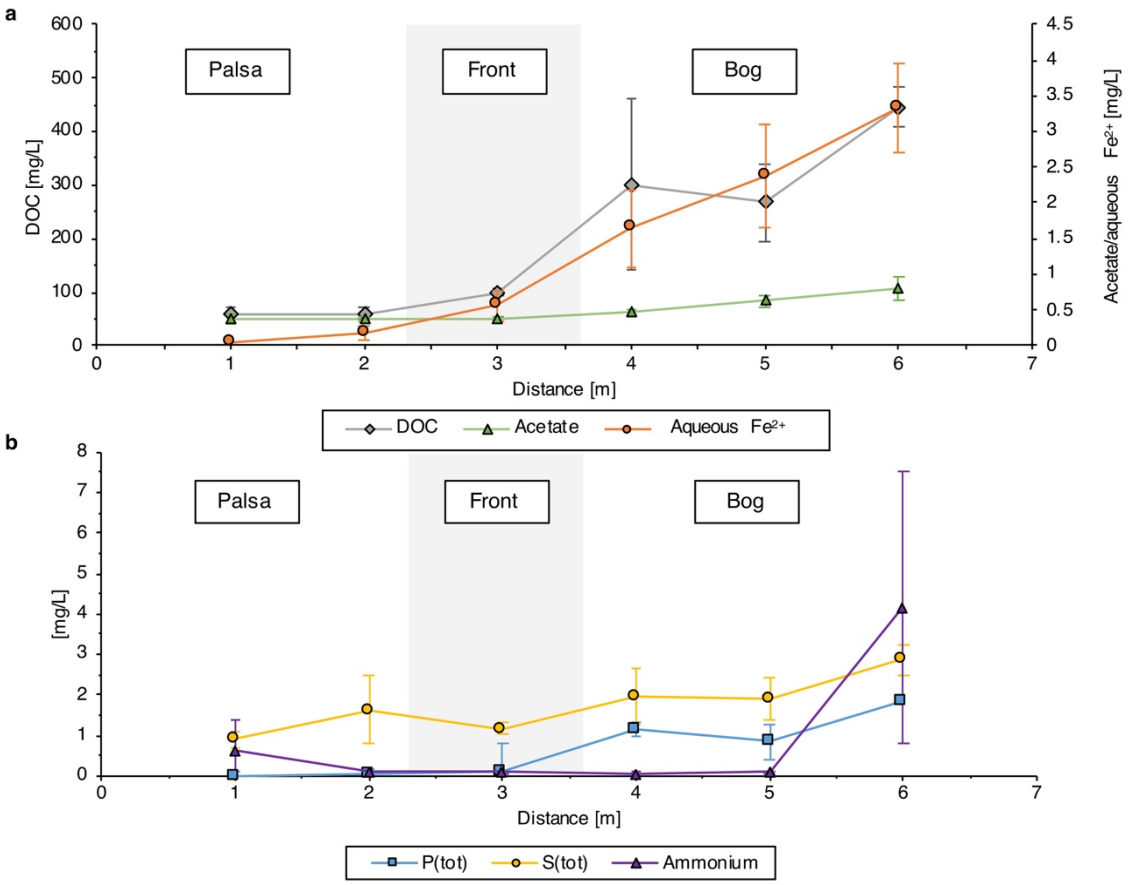

Figure S6. Porewater analysis along the palsa hillslope (60 cm, mineral horizon). *a, Dissolved organic carbon (DOC), acetate and aqueous Fe^{2+} in mg/L and b, aqueous total phosphorous (P(tot)), aqueous total sulfur (S(tot)) and ammonium concentrations along the collapsing palsa hillslope into bog. Reported values represent the average of six sampling spots for eight palsa hillslopes (0-2.3 m) to collapsing front (2.3-3.6) to bog (3.6-7 m), sampled in June/July (see also SI, Figure S1). Error bars represent the standard deviation of eight palsa hillslopes (0-2.3 m) to collapsing front (2.3-3.6) to bog (3.6-7 m), sampled in June/July (see also SI, Figure SI).*

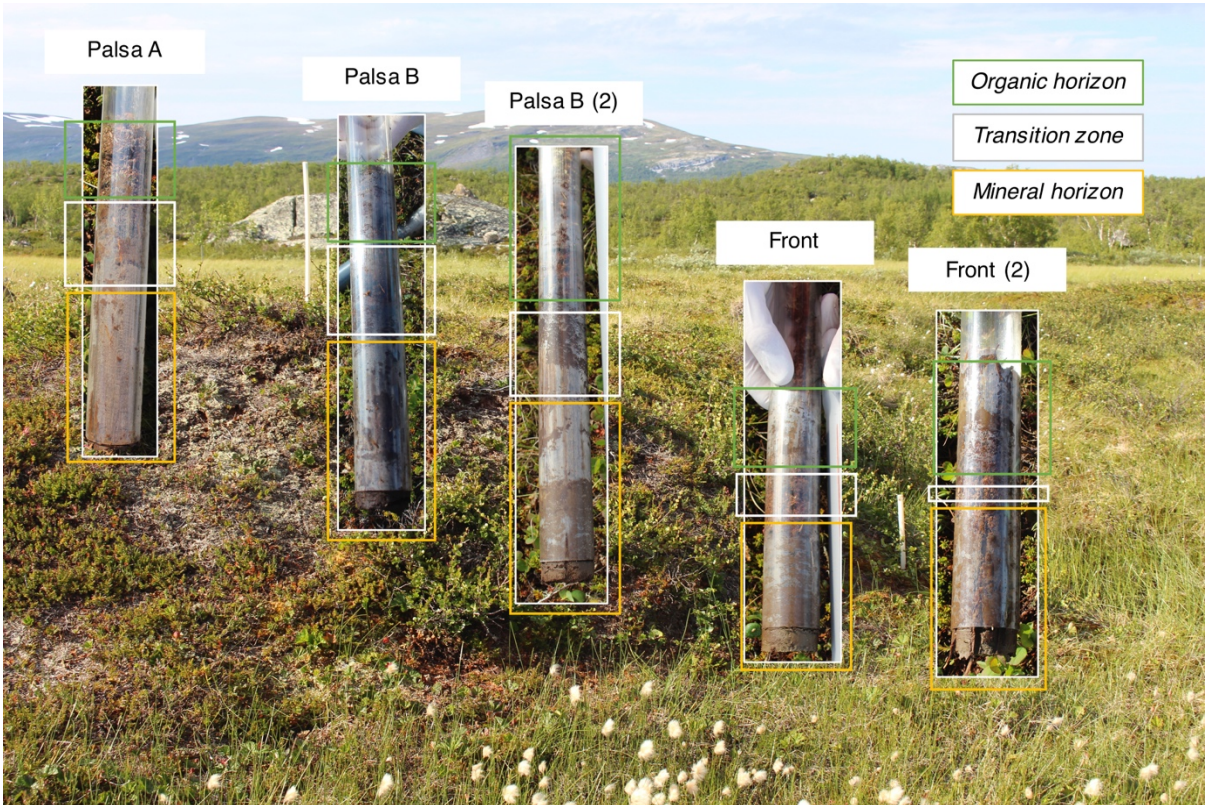

Figure S7. Coring along palsa hillslopes. *Ten soil cores were taken along different palsa hillslopes to capture spatial heterogeneity of iron-carbon associations along the peatland mire. In transect 3 (shown here, see also Figure S1), five cores were taken along a palsa hillslope towards the collapsing front into bog (68°21'27.33"N, 19° 3'1.91"E), immediately frozen in liquid nitrogen and stored at -80°C until analysis of iron-carbon associations and of present and active microbial community.*

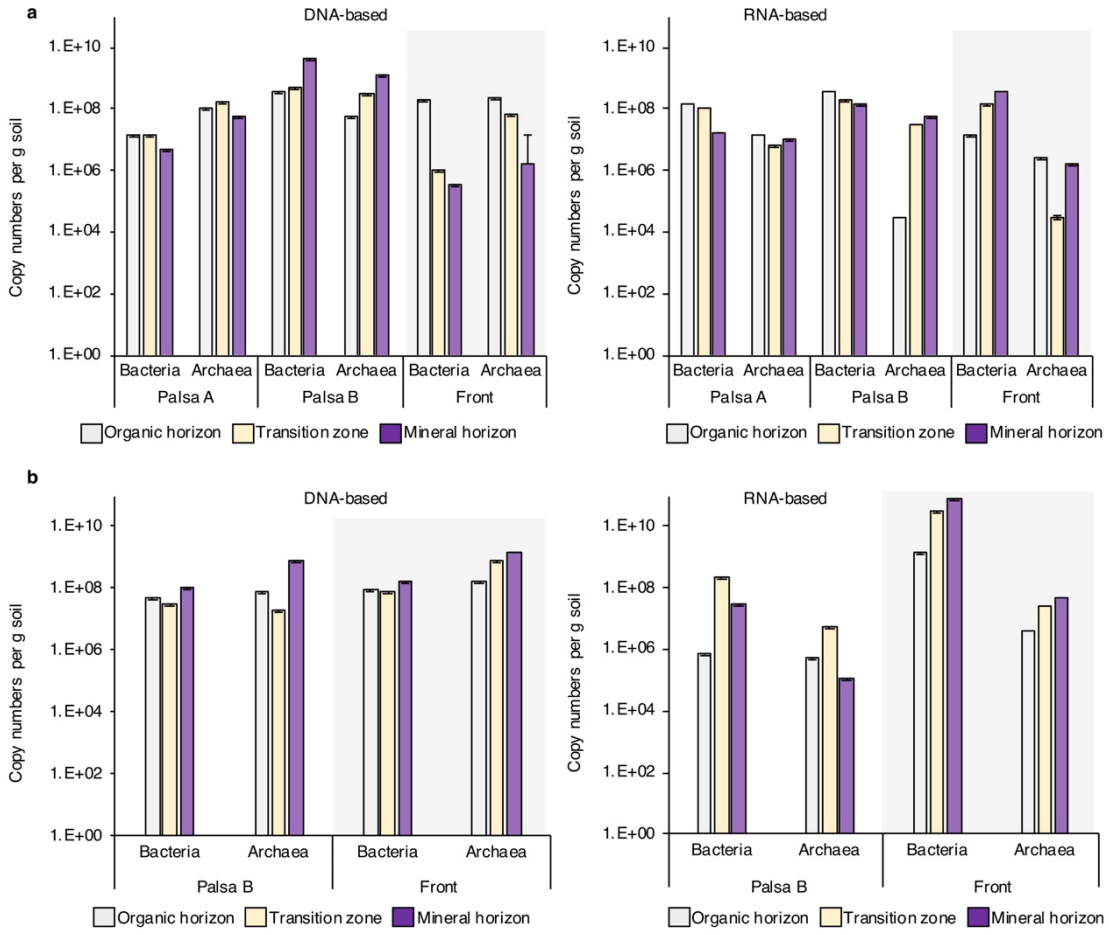

Figure S8. Abundance of bacteria and archaea (copy numbers based on qPCR analysis specific for 16S rRNA genes; DNA-based on the left, RNA-based on the right). *a, and b, show replicate analysis for Palsa A, Palsa B and Front (a), and Palsa A and Front (b).*

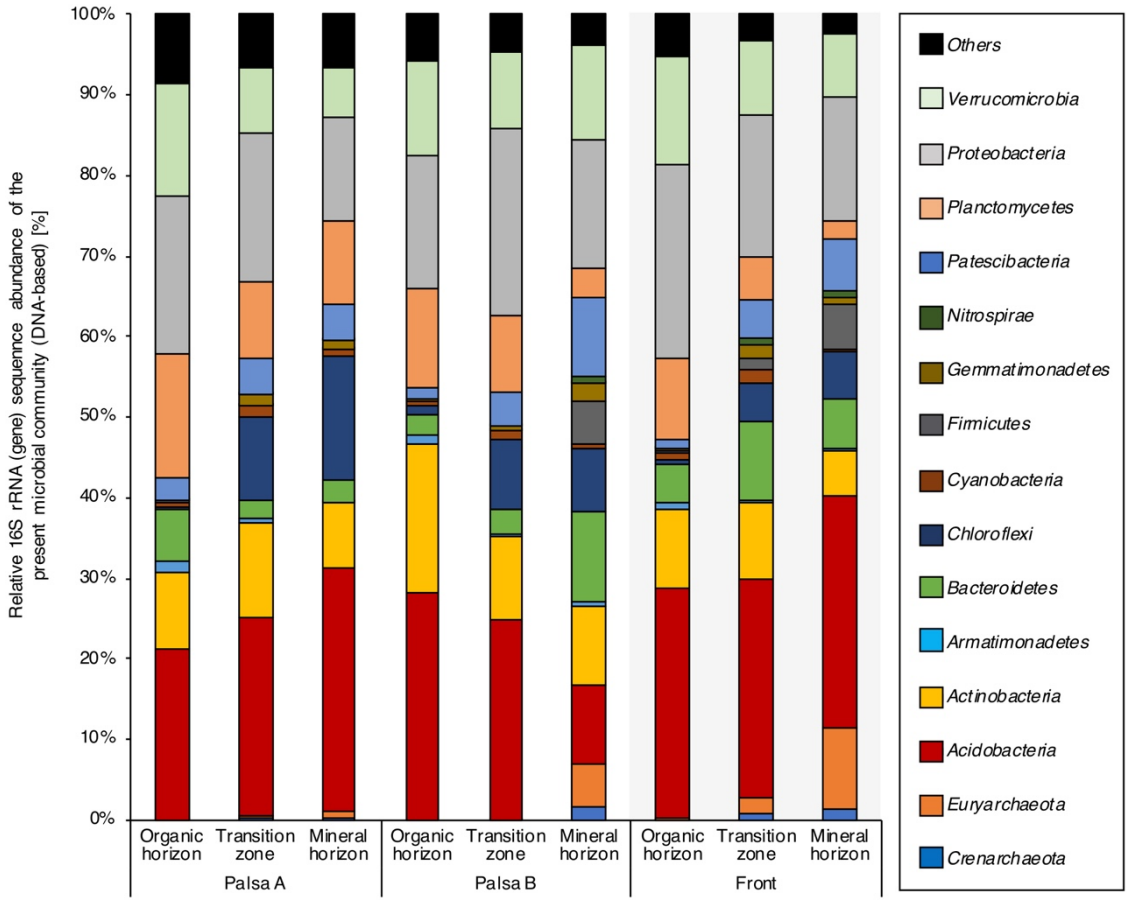

Figure S9. Taxonomic identification of the microbial communities along the palsa hillslope based on 16S rRNA gene amplicon analysis (DNA-based). *Data were averaged among triplicate analysis of each soil horizon (organic horizon, transition zone, mineral horizon).*

Table S1. Overview of iron(II)-oxidizing microorganisms that were cross-checked in the 16S rRNA amplicon gene sequencing results (DNA- and RNA-based) in this study (adapted from Otte et al.[2] and Weber et al.[3], see also Dinh et al.[4] and Berg et al.[5]).

Iron(II)-oxidizing microorganisms (species or strains)
Acidianus brierleyi
Acidiplasma aeolicum; A. cupricumulans
Acidimicrobium ferrooxidans sp. strain DSM 10331
Acidithiobacillus ferrooxidans sp. strain ATCC 23270
Acidovorax sp. strains 2AN, BoFeN1, BrG1; *A. delafieldii*; *A. ebreus* strain TPSY
Alicyclobacillus disulidooxidans; A. tolerans
Aquabacterium sp. strains BrG2, HidR2
Azoarcus sp. strain ToN1
Azospira sp. strain TR1; *A. oryzae*
Bradyrhizobium japonicum sp. strains 22, in8p8, wssI4
Candidatus Brocadia sinica
Candidatus Scalindua sp.
Chlorobium luteolum DSM273; *C. ferrooxidans* sp. strain KoFox
Chromobacterium violaceum sp. strain 2002
Citrobacter freundii sp. strain PXL1
Comamonas sp. strain MPI12
Crenothrix sp. #
Cupriavidus necator sp. strains A5-1, ss1-6-6
Dechlorobacter hydrogenophilus sp. strain LT-1
Dechloromonas sp.; D. agitata sp. strains CKB, is5; *D. aromatica* sp. strains RCB, UWNR4; *D. suillum* sp. strain PS
Dechlorospirillum sp. strain M1
Denitromonas indolicum
Desulfitobacterium frappieri sp. strain G2
Desulfobacterium corrodens (Dinh *et al.*, 2004)
Escherichia coli sp. strain E4
Ferrimicrobium acidiphilum
Ferriphaselus amnicola (Siderooxydans)
Ferrithrix thermotolerans
Ferritrophicum radicicola
Ferroglobus placidus sp. strain AEDII12DO
Ferroplasma acidarmanus sp. strain fer1
Ferrovibrio denitrificans
Gallionella capsiferriformans; G. ferruginea; G. strain ES-2
Geobacter metallireducens sp. strain GS-15
Geothrix spp.
Hoeflea marina; *H. siderophila* sp. strain Hf1
Hyphomicrobium sp.

(Table continues on next page)

Hyphomonas sp.
Klebsiella-like sp. strain FW33AN
Leptospirillum ferrooxidans; L. ferriphilum
Leptothrix cholodnii; L. discophora
Magnetococcus sp. (Berg *et al*., 2016)
Magnetospirillum bellicus sp. strain VDY
Marinobacter aquaeolei sp. strain VT8
Mariprofundus ferrooxidans sp. strains PV-1, RL-1, JV-1, GSBS
Metallosphaera sedula sp. strain J1
Nocardioides sp. strain In31
Paracoccus sp.*; P. denitrificans; P. ferrooxydans* sp. strain BDN-1*; P. pantotrophus; P. versutus*
Parvibaculum sp. strain MBN-A2
Pedomicrobium spp.
Propionivibrio militaris sp. strain MP
Pseudogulbenkiania ferrooxidans sp. strain 2002
Pseudomonas sp. strains LP-1, SZF15; *P. stutzeri*
Ralstonia solanacearum sp. strain in4ss52
Rhodanobacter sp. strain MPN-A3
Rhodobacter sp. strain SW2*; R. ferrooxydans*
Rhodomicrobium vannielii
Rhodopseudomonas palustris strain TIE-1
Rhodovulum sp.*; R. iodosum; R. robiginosum*
Rubrivivax group sp. strains BrG4, BrG5
Siderocapsa sp.
Sideroxydans paludicola; S. lithotrophicus sp. strain ES-1
Sphaerotilus natans sp. strain DSM 6575
Sulfobacillus spp.
Sulfolobus acidocaldarius
Thauera aromatica sp. strain AR-1
Thermomonas sp. strain BrG3
Thiobacillus denitrificans
Thiodictyon sp.
Thiomicrospira denitrificans
Zixibacteria sp. strain RBG-1

Crenothrix is most often associated with methanotrophy but there are also hints for Fe(II) oxidation.

Table S2. Overview of iron(III)-reducing microorganisms that were cross-checked in the 16S rRNA amplicon gene sequencing results in this study (adapted from Otte et al.[2] and Weber et al.[3], see also Berg et al.[5], Li et al.[6], Holmes et al.[7], Finneran et al.[8]).

Iron(III)-reducing microorganisms (species or strains)
Acidithiobacillus ferrooxidans
Aeromonas hydrophila
Albidoferax ferrireducens
Alteromonas hydrophila
Anaeromyxobacter sp.
Bacillus infernus
Clostridium sp.
Deferribacter thermophilus
Desulfobacter propionicus
Desulfobacterium sp.
Desulfobulbus spp.
Desulfococcus spp.
Desulfotalea spp.
Desulfotomaculum sp. (Berg *et al*., 2016)
Desulfovibrio sp. *(*Li *et al., 2016)*
Desulfuromonas spp.
Desulfuromusa spp.
Ferribacterium limneticum
Ferrimonas balearica
Ferroglobus placidus
Geobacter spp.
Geoglobus sp.
Geothrix fermentans
Geovibrio ferrireducens
Malonomonas sp. (Holmes *et al*., 2004)
Myxococcales sp.
Pantoea agglomerans sp. strain Sp1
Pelobacter sp.
Pseudomonas sp.
Pseudorhodoferax (Berg *et al*., 2016)
Pyrobaculum sp.
Rhodobacter sp.
Rhodoferax sp. (Finneran *et al*., 2003)
Shewanella colwelliana
Sinorhodobacter sp.
Sulfurospirillum barnesii
Thermoterrabacterium ferrireducens
Thermotoga maritima
Thermus sp. strain SA01
Thiobacillus ferrooxidans

Table S3. Overview of methanogenic microorganisms that were cross-checked in the 16S rRNA amplicon gene sequencing results in this study (see also Kim&Whitman[9] and Mondav et al.[10]).

Methanogenic microorganisms (genera, species or strains)
Methanobacterium sp.
Methanobrevibacter sp.
Methanocaldococcus sp.
Methanococcus sp.
Methanococcoides sp.
Methanohalophilus sp.
Methanohalobium sp.
Methanolobus sp.
Methanomicrobium sp.
Methanothermobacter sp.
Methanosphaera sp.
Methanothermus sp.
Methanotorris sp.
Methanopyrus sp.
Methanothermococcus sp.
Methanolacinia sp.
Methanoignis sp.
Methanogenium sp.
Methanoplanus sp.
Methanoculleus sp.
Methanofollis sp.
Methanocorpusculum sp.
Methanospirillum sp.
Methanocella sp.
Methanolinea sp.
Methanosphaerula sp.
Methanosarcina sp.
Methanosalsum sp.
Methanosaeta sp.
Methanoregula sp.
Methanothrix sp.
Methermicoccus sp.
Methanomethylovorans sp.
Methanoflorens sp., *M. stordalenmirensis (Mondav et al., 2014)*
Methanomassillicoccaceae sp.
Bathyarchaeia

Table S4. Overview of methanotrophic microorganisms that were cross-checked in the 16S rRNA amplicon gene sequencing results (DNA- and RNA-based) in this study (see also Jiang et al.[11] and Singelton et al.[12]).

Methanotrophic microorganisms (genera, species or strains)
Methylomonas sp.
Methylobacter sp.
Methylobacterium sp.
Methylovirgula sp.
Methylococcus sp.
Methlyosinus sp.
Methylocystis sp.
Methylosphaera sp.
Methylocaldum sp.
Methylothermus sp.
Methylocapsa sp.
Crenotrhix sp., *Crenothrix polyspora*
Clonothrix sp., *Clonothrix fusca*
Methylocella sp., *Methylocella silvestris*
Methylokorus sp.
Acidimethylosilex sp.
Methyloacida sp.
Rhodoblastus sp.
Roseiarcus sp.

Table S5. Absolute values of iron and carbon in locations Palsa A, Palsa B and Front of the cores reported in the main text. *Errors of the dithionite/citrate extractable a, iron (reactive Fe, control corrected) and b, carbon (carbon bound to reactive iron, control corrected) represent a combined standard deviation of sodium chloride bicarbonate extractable a, iron and b, carbon, b, citrate blank and dithionite/citrate extractable a, iron and b, carbon (not control corrected).*

	Palsa A				Palsa A			
	Reactive Fe [mg/g soil]	Error bars	Associated OC [mg/g soil]	Error bars	Leachable Fe [mg/g soil]	Error bars	Leachable OC [mg/g soil]	Error bars
Organic horizon	0.20	0.12	1.42	1.42	0.05	0.07	2.26	0.45
Transition zone	10.04	0.07	83.69	10.04	0.09	0.07	4.06	0.00
Mineral horizon	3.76	0.48	47.21	14.30	0.05	0.03	2.00	0.19
	Palsa B				Palsa B			
	Reactive Fe [mg/g soil]	Error bars	Associated OC [mg/g soil]	Error bars	Leachable Fe [mg/g soil]	Error bars	Leachable OC [mg/g soil]	Error bars
Organic horizon	0.67	0.07	4.80	0.52	0.00	0.00	3.05	0.71
Transition zone	4.61	0.78	76.60	16.89	0.00	0.00	2.76	0.00
Mineral horizon	4.22	0.09	25.08	4.22	0.00	0.00	0.85	0.00
	Front				Front			
	Reactive Fe [mg/g soil]	Error bars	Associated OC [mg/g soil]	Error bars	Leachable Fe [mg/g soil]	Error bars	Leachable OC [mg/g soil]	Error bars
Organic horizon	0.59	0.30	0.00	0.00	0.07	0.10	2.01	1.11
Transition zone	3.22	0.06	40.88	24.76	0.31	0.01	3.67	0.25
Mineral horizon	3.46	1.40	11.60	8.54	0.63	0.59	1.53	0.47

*Reactive Fe = dithionite extractable Fe - salt extractable Fe (leachable OC)

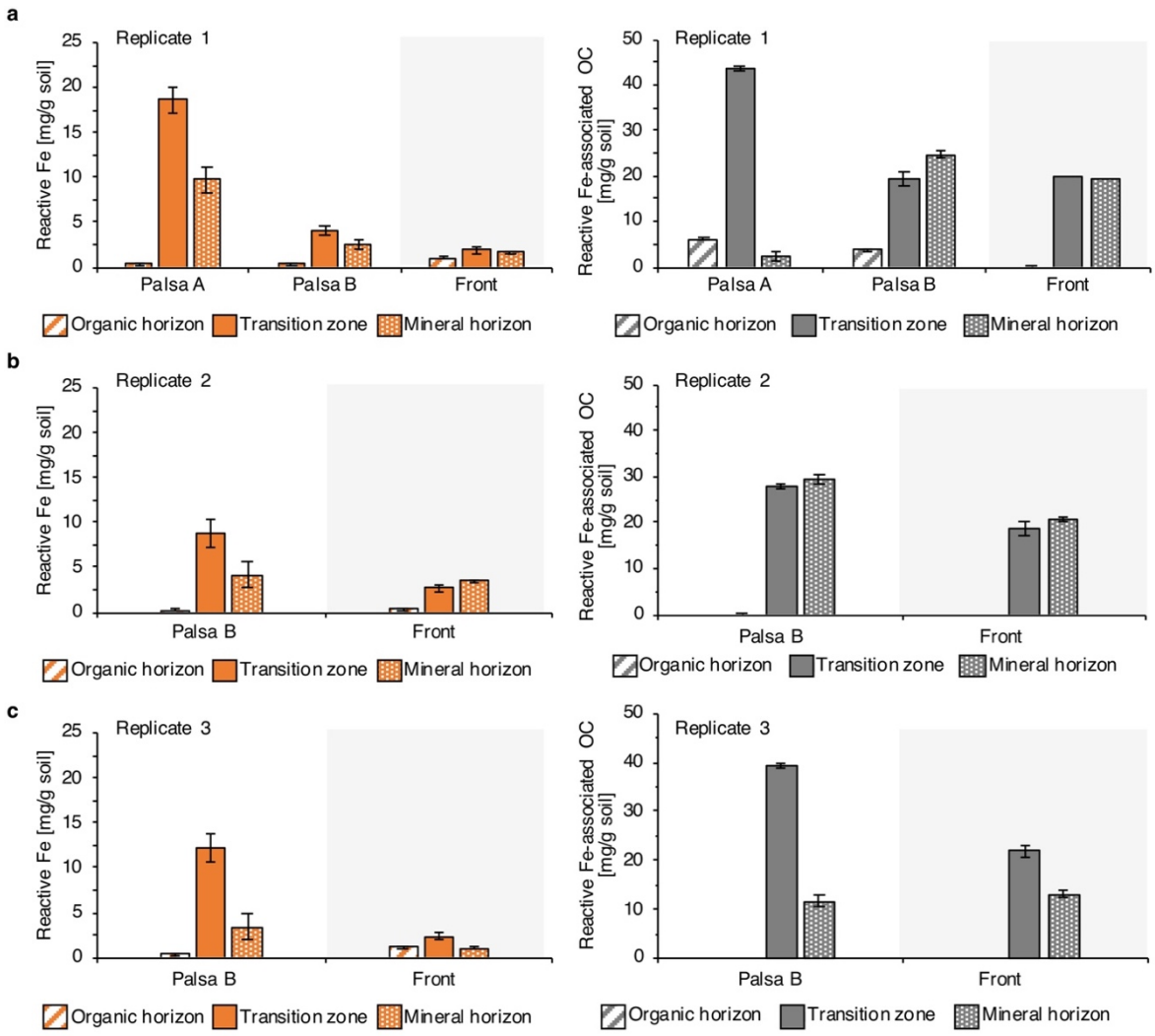

Figure S10. Organic carbon (OC, grey) associated with reactive iron (Fe, orange) along three replicate palsa hillslopes: a, replicate 1 (transect 3), b, replicate 2 (transect 3) and c, replicate 3 (transect 2). *Reactive Fe and associated organic carbon along the palsa hillslope (Palsa A, Palsa B and Front) per each soil horizon (organic horizon, transition zone and mineral horizon) [mg/g] decreases towards the collapsing front. Palsa A shows the highest reactive Fe and associated organic carbon in intact permafrost soils. Along the palsa hillslope towards the collapsing front, reactive Fe and associated OC are lost in the solid phase. Reactive Fe reported values are the average of sodium dithionite citrate duplicate extractions of each soil horizon, control corrected by a sodium chloride bicarbonate extractable Fe (leachable Fe). Associated OC reported values are the average of sodium dithionite citrate extractions of each soil horizon, control corrected by the citrate background and the sodium chloride bicarbonate extractable OC (leachable OC) (see also Material and Methods). Cores were taken in July 2019 (see Figure S1). Error bars of the reactive Fe represent a combined standard deviation of sodium chloride bicarbonate extractable iron and dithionite/citrate*

extractable Fe. Errors of the associated carbon represent a combined standard deviation of citrate blank, sodium chloride bicarbonate extractable OC and dithionite/citrate extractable OC.

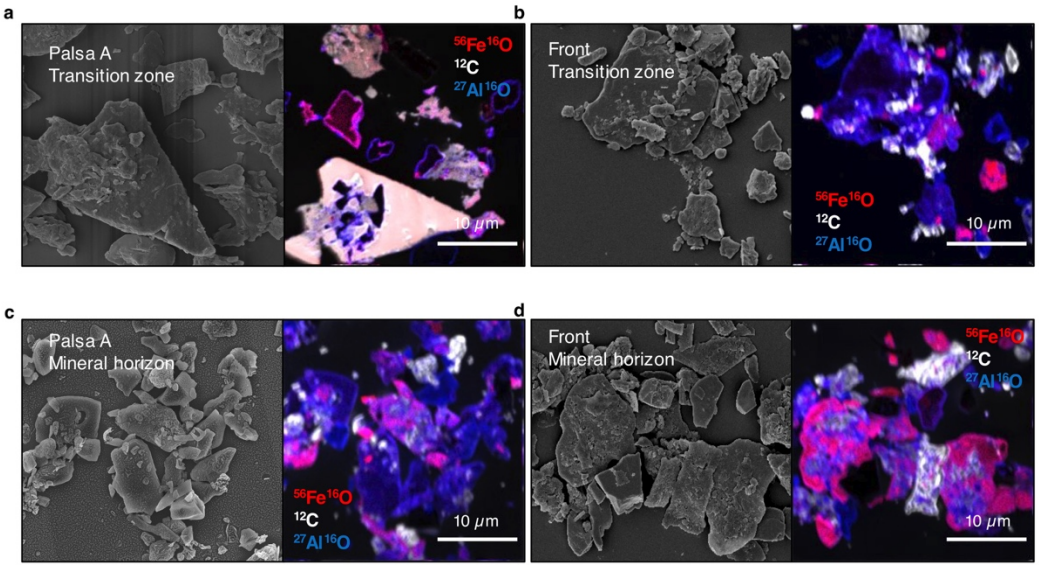

Figure S11. Correlative scanning electron microscopy and nanoscale secondary ion mass spectrometry (nanoSIMS) of fine fraction of palsa soil horizons along the palsa hillslope. *Fine particle analysis of a, Palsa A transition zone; b, Front transition zone; c, Palsa A mineral horizon and d, Front mineral horizon (transect 1, Figure S1). Seven detectors were used during nanoSIMS measurements for $^{12}C^-$, $^{16}O^-$, $^{12}C^{14}N^-$, $^{31}P^-$, $^{32}S^-$, $^{27}Al^{16}O^-$ and $^{56}Fe^{16}O^-$ and $^{27}Al^{16}O$. Here, $^{12}C^-$ (white), $^{56}Fe^{16}O^-$ (red) and $^{27}Al^{16}O^-$ (blue) are overlaid in a single composite image.*

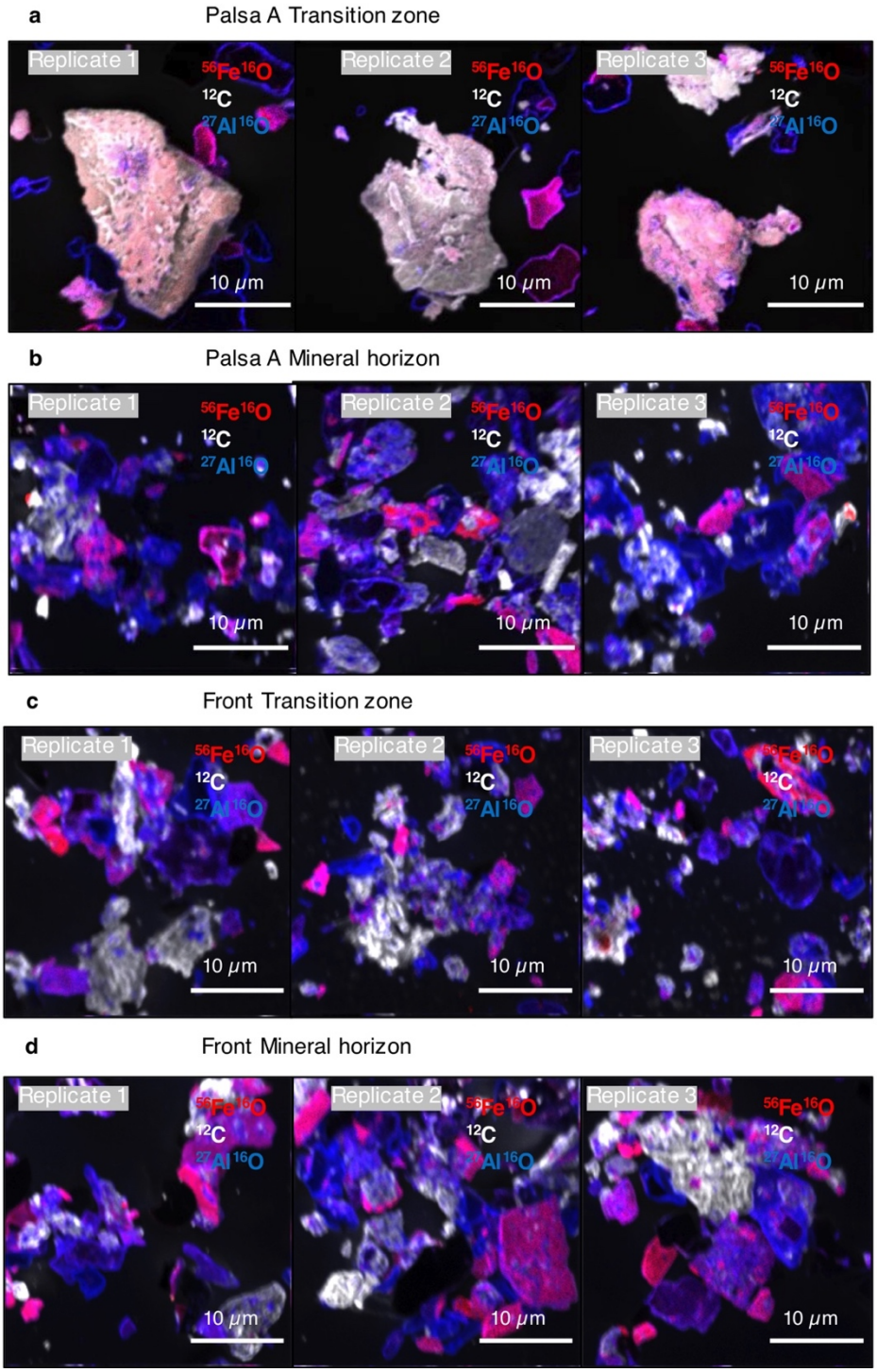

Figure S12. Replicate analysis of nanoscale secondary ion mass spectrometry (nanoSIMS) of fine fraction: a, Palsa A transition zone; b, Palsa A mineral horizon; c, Front transition zone and d, Front mineral horizon (transect 1, Figure S1). *Seven detectors were used during nanoSIMS measurements for for $^{12}C^-$, $^{16}O^-$, $^{12}C^{14}N^-$, $^{31}P^-$, $^{32}S^-$, $^{27}Al^{16}O^-$ and $^{56}Fe^{16}O^-$ and $^{27}Al^{16}O$. Here, $^{12}C^-$ (white), $^{56}Fe^{16}O^-$ (red) and $^{27}Al^{16}O^-$ (blue) are overlaid in a single image. In total, four representative fine particles were analyzed with nanoSIMS.*

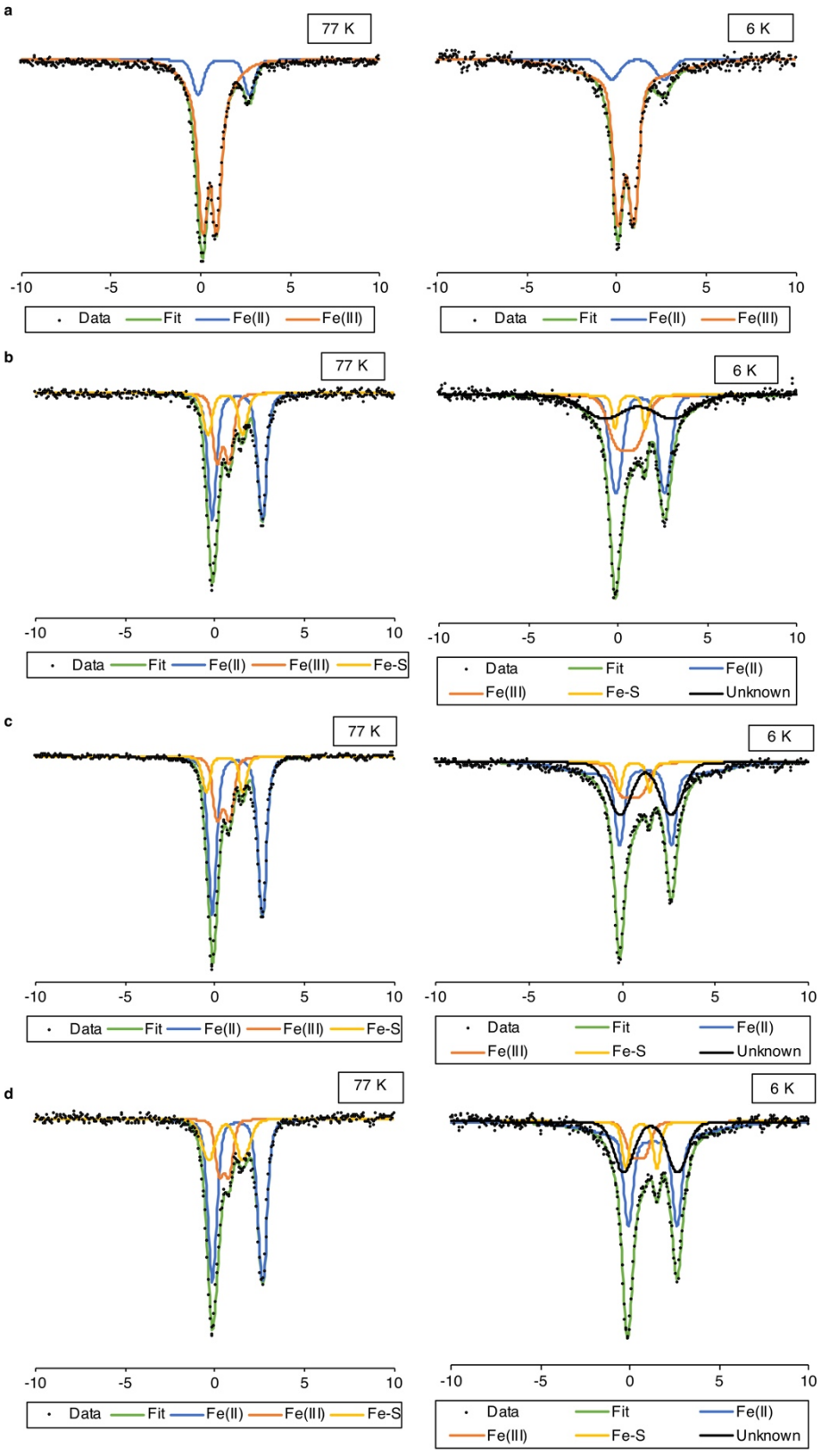

Figure S13. Mössbauer spectroscopy analysis at 77 K and 6 K of the present Fe minerals along the thaw gradient: *a, Palsa A transition zone; b, Palsa A mineral horizon; c, Bog (Bog C[13]) mineral horizon; d, Fen (Fen E[13]) mineral horizon.*

Table S6. Mössbauer spectroscopy parameters (measured at 77 and 6 K) derived from fitting spectra obtained for Palsa A transition zone and mineral horizon, Bog (Bog C[13]) and Fen (Fen E[13]) mineral horizon.

Sample	Components	CS[a] (mm/s)	ΔE$_{Q}$ [b] (mm/s)	σ(Δ) [c] (mm/s)	B$_{hf}$ [d] (T)	RA[e] (%)	± (%)	χ2 [f]
77 K								
Palsa A								
Transition zone	Fe(II)	1.28	2.87	0.45	0.00	15.30	0.10	1.77
	Fe(III)	0.50	1.18	1.01	2.06	84.70	0.10	
Palsa A								
Mineral horizon	Fe(II)	1.24	2.79	0.39	0.00	54.46	0.97	0.88
	Fe(III)	0.46	0.67	0.35	0.26	27.45	0.91	
	Fe-S	0.58	1.96	0.40	0.00	18.09	0.93	
Bog (Bog C, see Patzner *et al*., 2020)								
Mineral horizon	Fe(II)	1.25	2.78	0.37	0.00	62.87	0.38	3.47
	Fe(III)	0.47	0.68	0.37	0.31	24.73	0.34	
	Fe-S	0.54	2.07	0.30	0.00	12.40	0.34	
Fen (Fen E, see Patzner *et al*., 2020)								
Mineral horizon	Fe(II)	1.25	2.79	0.44	0.00	61.30	0.21	0.61
	Fe(III)	0.52	0.54	0.31	0.41	17.30	0.18	
	Fe-S	0.61	1.93	0.67	0.03	21.40	0.22	
6 K								
Palsa A								
Transition zone	Fe(II)	1.17	2.90	0.80	0.00	12.30	0.16	0.85
	Fe(III)	0.52	2.17	2.65	2.26	87.70	0.16	
Palsa A								
Mineral horizon	Fe(II)	1.25	2.73	0.58	0.00	38.10	0.25	0.81
	Fe-S	0.68	1.68	0.19	0.00	6.50	0.16	
	Fe(III)	0.49	1.19	0.79	0.64	26.90	0.27	
	Unknown	1.13	3.87	2.06	0.29	28.50	0.30	
Bog (Bog C, see Patzner *et al*., 2020)								
Mineral horizon	Fe(II)	1.26	4.07	2.55	1.50	42.10	0.77	0.75
	Fe-S	0.66	1.64	0.22	0.00	6.00	0.18	
	Fe(III)	0.48	1.07	0.70	0.60	15.90	0.34	
	Unknown	1.26	2.77	1.13	0.08	36.00	0.76	
Fen (Fen E, see Patzner *et al*., 2020)								
Mineral horizon	Fe(II)	1.28	3.65	2.62	2.03	49.20	0.54	0.54
	Fe-S	0.64	1.74	0.27	0.00	10.70	0.27	
	Fe(III)	0.47	0.76	0.48	0.55	11.50	0.27	
	Unknown	1.16	3.02	0.98	0.02	28.50	0.58	

a CS = center shift
b ΔEQ = quadrupole splitting;
c σ(Δ) = standard deviation of quadrupole splitting component d Bhf = hyperfine magnetic field
e RA = Relative abundance
f χ2 = goodness of fit

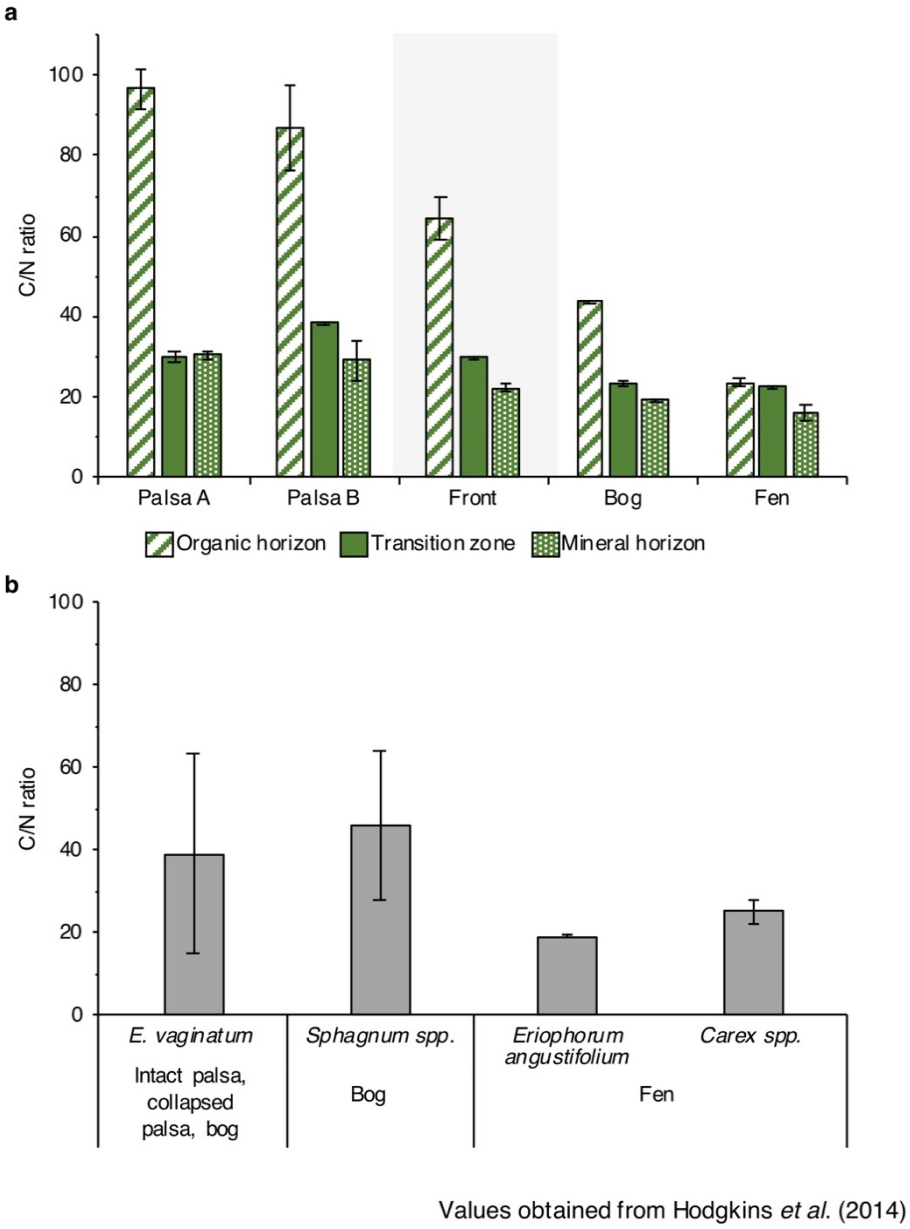

Figure S14. C/N weight ratios of a, soil samples of distinguished soil horizon along palsa hillslope and thaw gradient, in comparison to b, living plant samples of dominant Stordalen species (modified and adapted from Hodgkins et al.[13]). *Reported values represent the average of triplicate analysis of cores Palsa A, Palsa B, Front (transect 1, Figure S1) and Bog C and Fen E, which were previously puplished[13]. Error bars represent the standard deviation of triplicate analysis of cores Palsa A, Palsa B, Front (transect 1, Figure S1), one bog (Bog C) and one fen core (Fen E) (see also Patzner et al.[13]).*

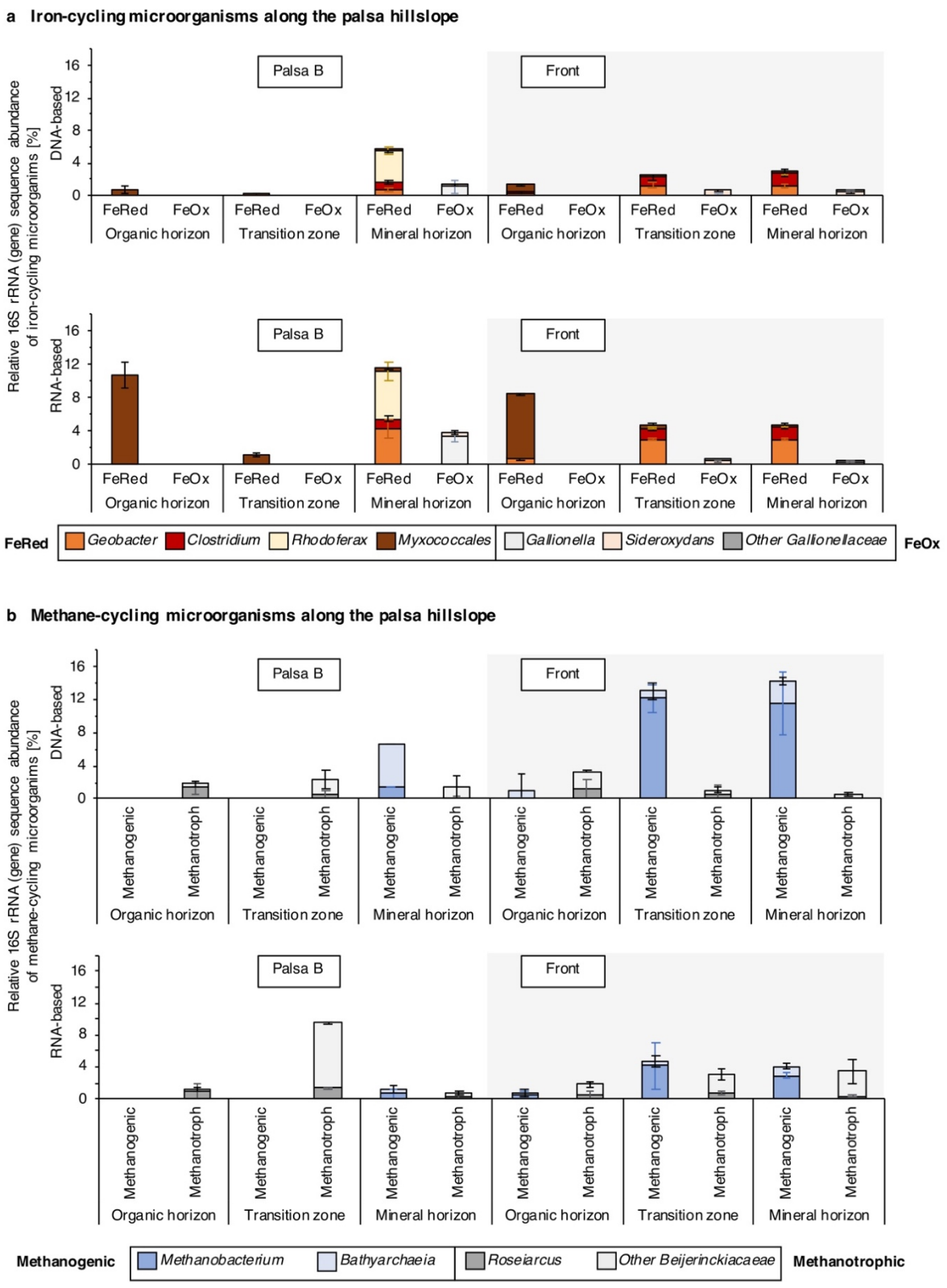

Figure S15. Relative abundance of 16S rRNA (gene) sequence of a, iron- and b, methane cycling microorganisms (DNA- and RNA-based) in replicate cores (Palsa B and Front) along the palsa hillslope (transect 3, Figure 1). *All iron- and methane-cycling taxa below 0.1% relative 16S rRNA gene sequencing abundance are not illustrated in this figure. For*

absolute abundance of bacteria and archaea based on qPCR analysis, specific for 16S rRNA gene (based on DNA) and Fe- and methane-cycling microorganisms, analyzed in these study (adapted from Otte et al.[2] and Weber et al.[3]), see also Figure S8. Reported values and error bars represent the average and standard deviation of triplicate analysis of each soil horizon (organic horizon, transition zone and mineral horizon) along the palsa hillslope.

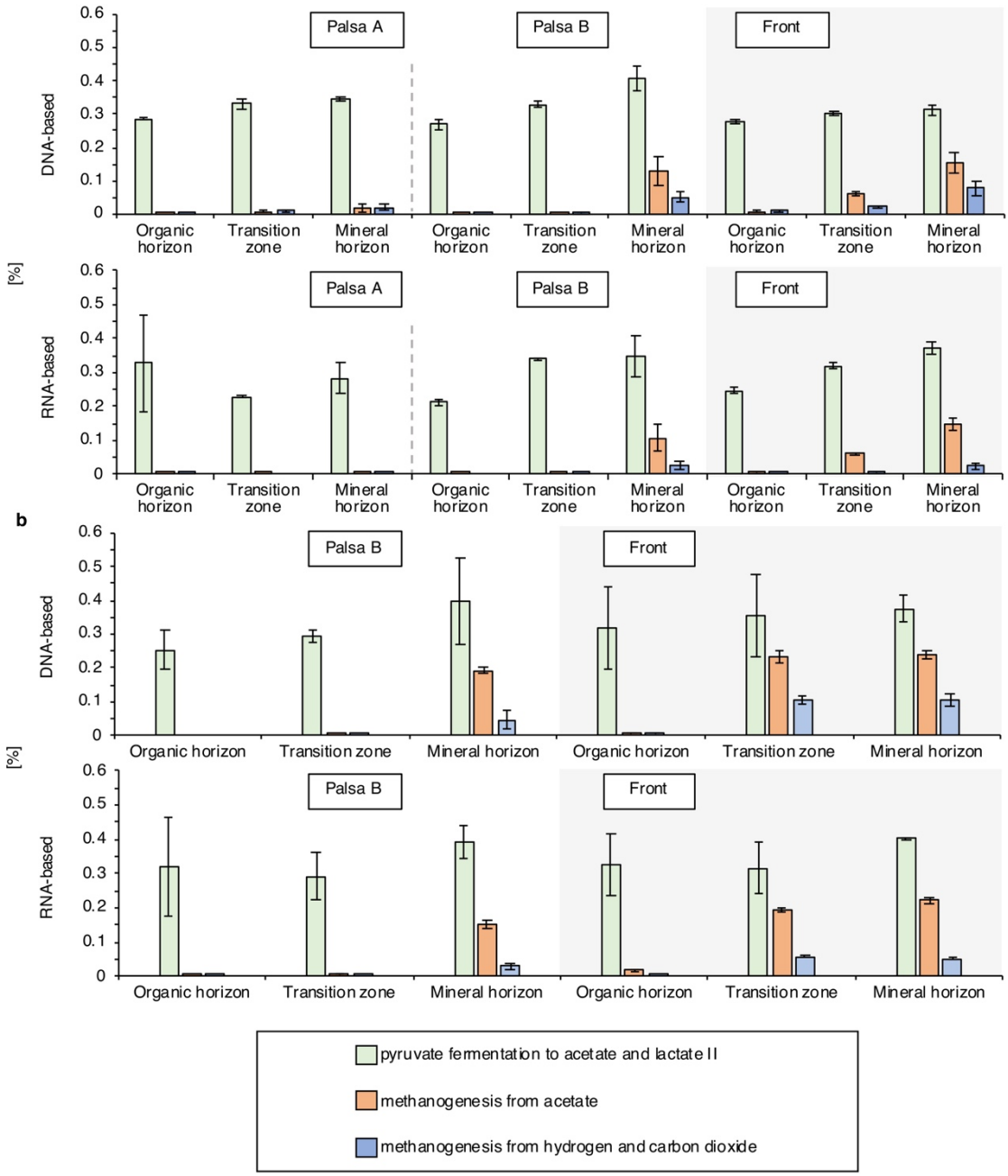

Figure S16. Predicted metabolic pathways of the present (DNA-based) and potentially active (RNA-based) microbial communities along the palsa hillslope in a, cores presented in the main text (transect 3, Figure S1) and b, replicate cores. *Analyses were performed with MetaCyc Metabolic Pathway Database. Reported values and error bars represent the average and standard deviation of triplicate analysis of each soil horizon (organic horizon, transition zone and mineral horizon) along the palsa hillslope.*

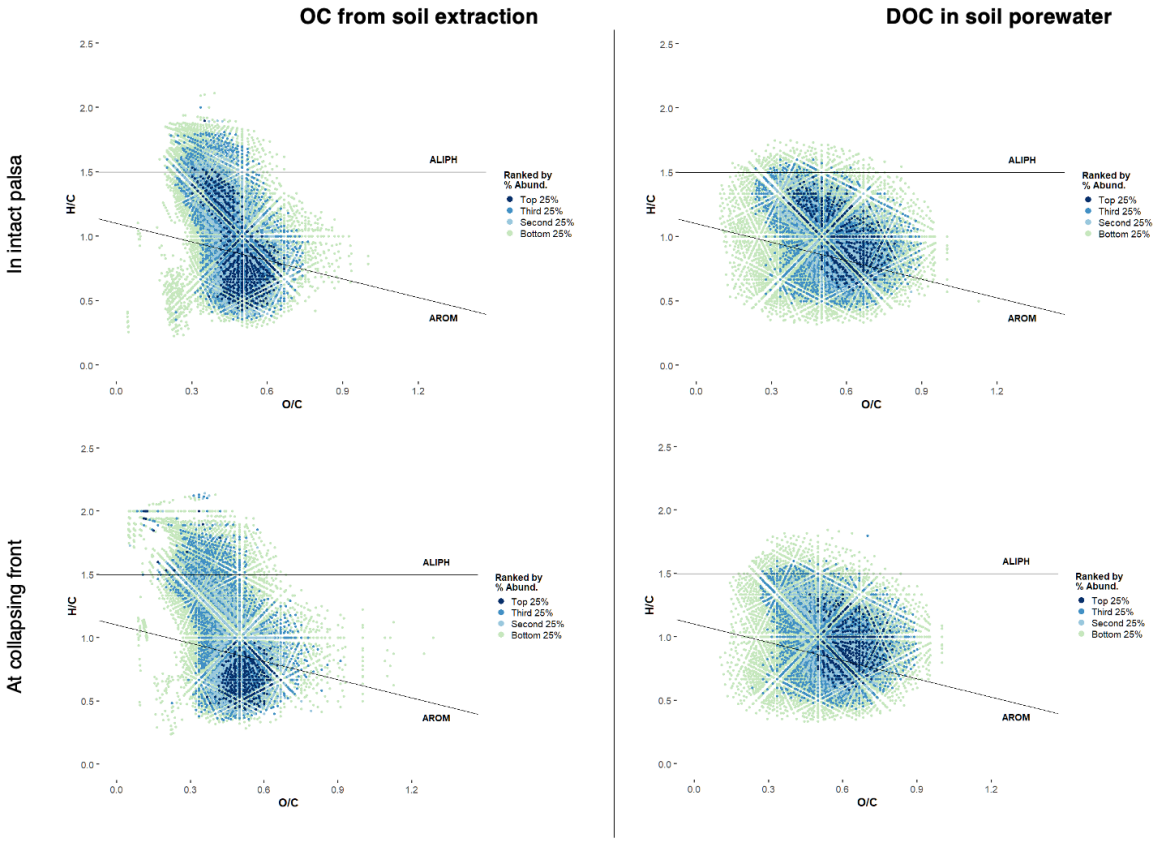

Figure S17. Van Krevelen diagrams for individual samples for solid phase extracted OC (dithionite extractable) from the transition zone of the intact palsa and of the collapsing front (transect 1, Figure S1) and DOC, extracted from 30 cm depth, in intact palsa and at the collapsing front.

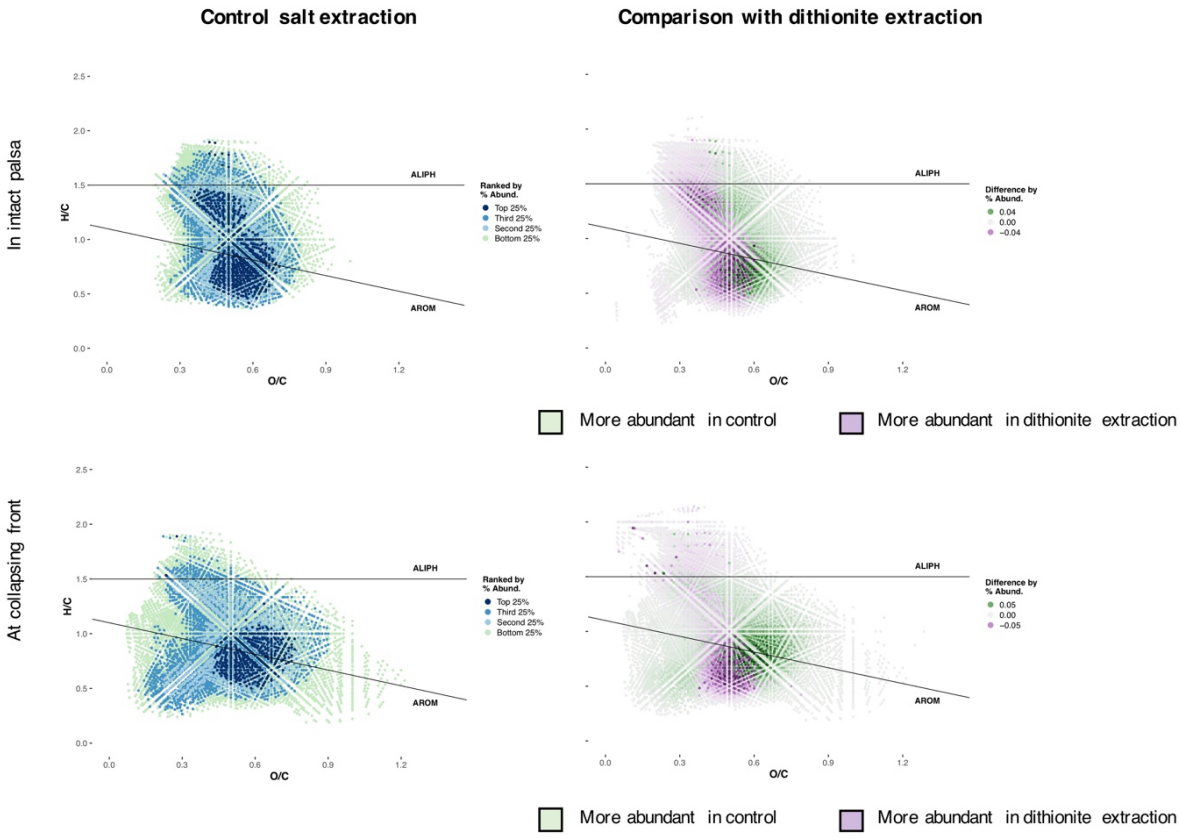

Figure S18. Van Krevelen diagrams of control extractions (sodium chloride bicarbonate with the same ionic strength and pH as the sodium dithionite extraction): left, each individual van Krevelen diagram and right, in direct comparison with the sodium dithionite citrate extractable CHO. *Organic carbon (OC) which is more abundant in control (green) represents OC which is leachable of the soil by the same ionic strength and pH as the sodium dithionite extraction. OC which is more abundant in the sodium dithionite extraction (purple) is only dissolved by reductive dissolution.*

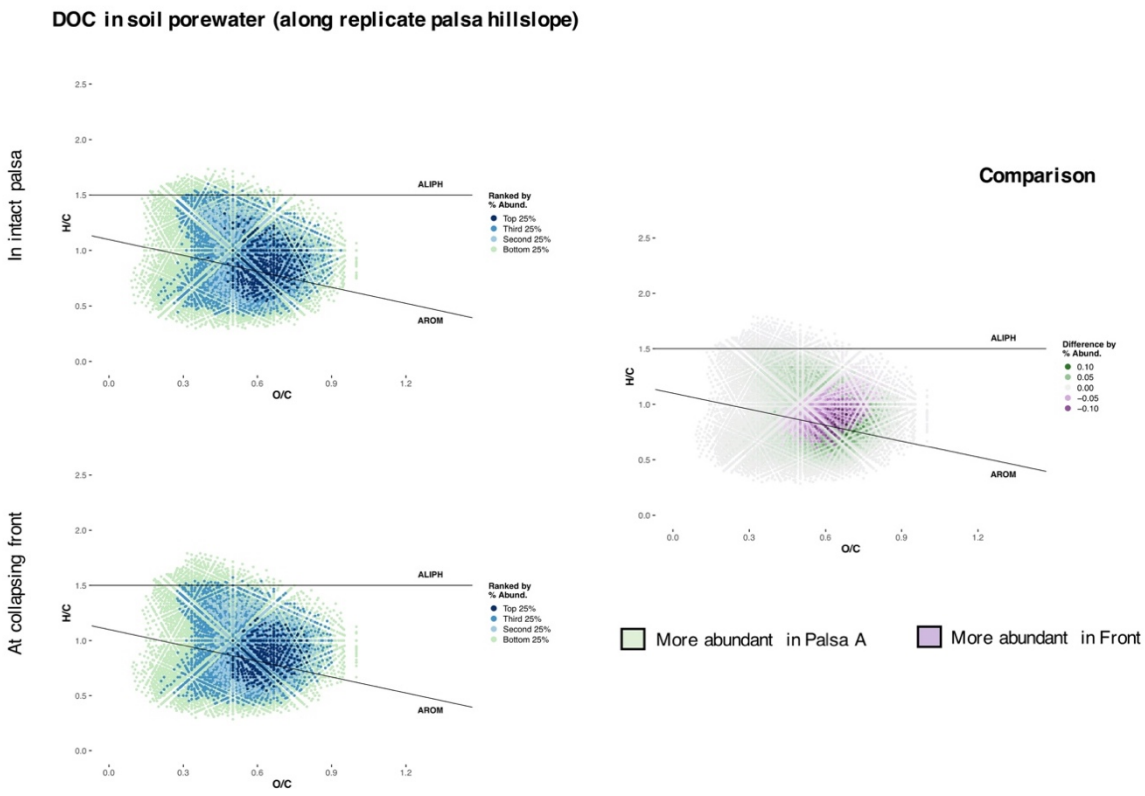

Figure S19. Van Krevelen diagrams for replicate porewater samples (30 cm depth) (left) and in direct comparison to each other (right). *Dissolved OC, which is only found in Palsa A, is enriched in more aliphatic compounds (green). Towards Front and Bog, only more aromatic molecules (purple) remain.*

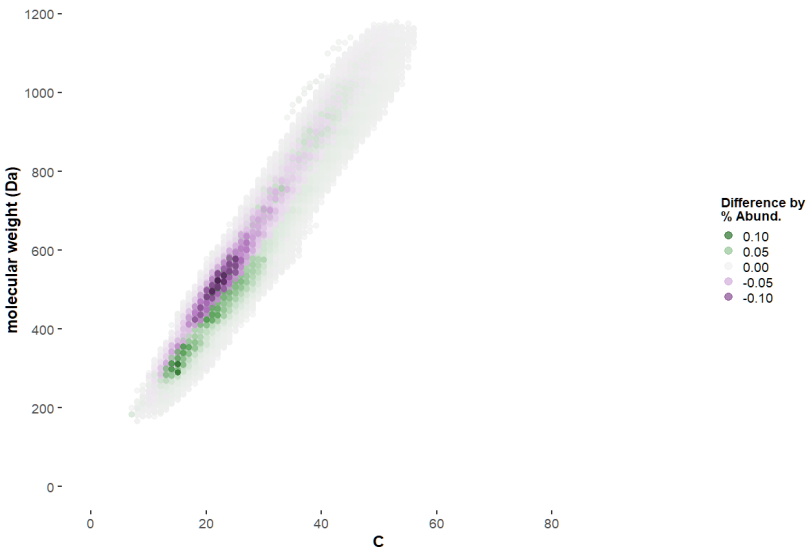

Figure S20. Molecular weight (MW) of dissolved organic carbon compounds in intact palsa versus at the collapsing front. *Lower MW compounds have higher relative abundance in porewater samples from intact palsa at a lower molecular weight for a given carbon number (colored in green). Higher MW compounds have higher relative abundance for a given carbon number at the collapsing front (colored in purple).*

Table S7. Elemental composition percentage and number of FT-ICR-MS assigned formula. *Values are derived from total assigned formula tables. N/A values for CHNOS formula in porewater samples and salt control extractions are due to lack of reliable formula series detected in those samples. A comparison of the soil extractions using salt or dithionite solutions indicates that the extracts are not identical, but provides little to no evidence of CHOS molecular artifacts formed through reactions with dithionite, as reported by* Lv *et al.*[15].

Sample Type	Sample	Extraction	CHO	CHNO	CHOS	CHNOS
			(% abundance / # formula)			
Soil extraction	Palsa A, Transition zone	Dithionite	74.19%/7486	11.21%/2887	13.76%/2018	0.84%/319
		Salt control	58.67%/4952	7.08%/1716	34.25%/6609	N/A
	Front, Transition zone	Dithionite	76.12%/7466	9.25%/2668	14.42%/2881	0.21%/98
		Salt control	76.22%/6536	7.08%/1716	13.79%/2249	N/A
Porewater	Palsa A	N/A	89.79%/9009	7.81%/3374	2.40%/991	N/A
	Front	N/A	87.41%/9072	10.80%/4172	1.79%/984	N/A

References

1 Rinne, J., ICOS Sweden Ecosystem eco time series (ICOS Sweden), Abisko-Stordalen Palsa Bog, 2018-12-31–2019-12-31, https://hdl.handle.net/11676/s5oBzukX_FaXpHU___86QasO) (2021).

2 Otte, J. M. *et al.* The distribution of active iron-cycling bacteria in marine and freshwater sediments is decoupled from geochemical gradients. *Method Enzymol* **20**, 2483-2499 (2018).

3 Weber, K. A., Achenbach, L.A., Coates, J.D. Microorganisms pumping iron: anaerobic microbial iron oxidation and reduction. *Nat. Rev. Microbiol.* **4**, 752-764 (2006).

4 Dinh, H. T., Kuever, J., MussBmann, M., Hassel, A.W. Iron corrosion by novel anaerobic microorganisms. *Nature* **427**, 829 (2004).

5 Berg, J. S., Michellod, D., Pjevac, P., Martinez-Perez, C., Buckner, C.R., Hach, P.F. Instensive cryptic microbial iron cycling in the low iron water column of the meromictic Lake Cadagno. *Method Enzymol* **18**, 5288-5302 (2016).

6 Li, X., Zhang, W., Liu, T., Chen, L., Chen, P., Li, F. Changes in the composition and diversity of microbial communities during anaerobic nitate reduction and Fe(II) oxidation at circumneutral pH in paddy soil. *Soil Biol Biochem* **94**, 70-79 (2016).

7 Holmes, D., Bond, D., O'neil, R., Reimers, C., Tender, L., Lovely, D. Microbial communities associated with electrodes harvesting electricity from a variety of aquatic sediments *Microb Ecol* **48**, 178-190 (2004).

8 Finneran, K. T., Johnsen, C.V., Lovely, D.R. Rhodoferax ferrireducens sp. nov., a psychotolerant, facultatively anaerobic bacterium that oxidizes acetate with the reduction of Fe(III). *Inst J Syst Evol Microbiol* **53**, 669-673 (2003).

9 Kim, W., Whitman, W.B. Methanogens. *Encyclopedia of Food Microbiology (Second Edition), Academic Press, ISBN 9780123847331*, 602-606 (2014).

10 Mondav, R. *et al.* Discovery of a novel methanogen prevalent in thawing permafrost. *Nat Commun* **5**, 3212 (2014).

11 Jiang, H., Chen, J.C., Murrell, P., Jiang, C., Zhang, C., Xing, X.-H., Smith, T.J. . Methanotrophs: Multifunctional bacteria with promising applications in environmental bioengineering. *Comprehensive Biotechnology (Second Edition), Academic Press, ISBN 9780080885049*, 249-262 (2011).

12 Singelton, C. M. *et al.* Methanotrophy across a natural permafrost thaw environment *The ISME Journal* **12**, 2544-2558 (2018).

13 Patzner, M. S. *et al.* Iron mineral dissolution releases iron and associated organic carbon during permafrost thaw. *Nat Commun* **11**, 6329 (2020).

14 Hodgkins, S. B. *et al.* Changes in peat chemistry associated with permafrost thaw increase greenhouse gas production. *Proc. Natl. Acad. Sci. USA* **111**, 5819-5824, (2014).

15 15 Lv, J., Huang, Z., Christie, P., Zhang, S. Reducing reagents induce molecular artifacts in the extraction of soil organic matter. *ACS Earth and Space Chem* **4** (11), 1913-1919 (2020).

Chapter 4 – Personal contribution

The original hypothesis was formulated by myself, Dr. C. Bryce and Prof. Dr. A. Kappler. Together with the support of Dr. C. Bryce and Prof. Dr. A. Kappler, I designed the project, interpreted the data and wrote the manuscript. I, together with Dr. E. Lundin, collected the samples. I gathered the data presented in the main text. Supporting information was collected by N. Kainz, M. Barczok and C. Smith. Dr. E. Herndon and Dr. L. Kinsmann-Costello contributed to the data analysis and interpretation. Dr. S. Fischer and I collected the SEM and EDX analysis. Together with Dr. D. Straub and Jun.-Prof. Dr. S. Kleindienst, I interpreted the microbial community data.

Chapter 4

Seasonal fluctuations of the rusty carbon sink in thawing permafrost peatlands

Monique S. Patzner[1], Nora Kainz[1], Erik Lundin[2], Maximilian Barczok[3], Chelsea Smith[4], Elizabeth Herndon[3,5], Lauren Kinsman-Costello[4], Stefan Fischer[6], Daniel Straub[7,8], Sara Kleindienst[7], Andreas Kappler[1,9] & Casey Bryce[1,10]

[1]Geomicrobiology, Center for Applied Geosciences, University of Tuebingen, Schnarrenbergstrasse 94-96, 72076 Tuebingen, Germany.
[2]Swedish Polar Research Secretariat, Abisko Scientific Research Station, Abisko, Vetenskapens väg 38, 98107 Abisko, Sweden.
[3]Department of Geology, Kent State University, Kent, OH, 44242, US.
[4]Department of Biological Sciences, Kent State University, Kent, OH, 44242, US.
[5]Environmental Sciences Division, Oak Ridge National Laboratory, 1 Bethel Valley Rd, Oak Ridge, TN 37830.
[6]Tuebingen Structural Microscopy Core Facility, Center for Applied Geosciences, University Tuebingen, Schnarrenbergstrasse 94-96, 72076 Tuebingen, Germany
[7]Microbial Ecology, Center for Applied Geosciences, University Tuebingen, Schnarrenbergstrasse 94-96, 72076 Tuebingen, Germany.
[8]Quantitative Biology Center (QBiC), University Tuebingen, Auf der Morgenstelle 10, 72076 Tuebingen, Germany.
[9]Cluster of Excellence: EXC 2124: Controlling Microbes to Fight Infection, Tuebingen, Germany.
[10]School of Earth Sciences, University of Bristol, Bristol, UK.

Manuscript submitted for publication to: *Environmental Science & Technology*

Abstract

In the active layer underlain by intact permafrost and by partially-thawed soils, up to 20% of total organic carbon (OC) is bound to reactive iron (Fe) minerals, protecting the OC from microbial degradation and transformation into greenhouse gases (GHG) such as CO_2 and CH_4. During the summer, shifts in runoff and soil moisture influence redox conditions and therefore the balance of Fe oxidation and reduction. Whether this “rusty carbon sink” is stable or continuously dissolved by Fe(III) reduction and reformed by Fe(II) oxidation during redox shifts remains unknown. We exposed ferrihydrite (FH)-coated sand in the active layer along a permafrost thaw gradient over the summer (June to September) to capture changes in redox conditions and quantify formation and dissolution of reactive Fe(III) (oxyhydr)oxides. We found that Fe(III) minerals formed under the constantly oxic conditions in palsa soils overlying intact permafrost over the full summer season. In contrast, in fully-thawed fen areas, conditions were continuously anoxic and until late summer 50.2% of the original Fe(III) (oxyhydr)oxides were lost via dissolution while 44.7% and 5.0% of the Fe remained as Fe(III) and Fe(II) on the sand, respectively. Periodic redox shifts (from 0 mV to +300 mV) were observed over the summer season in the partially-thawed bog due to changes in active layer depth, runoff and soil moisture. This resulted in dissolution and loss of 47.5% of initial Fe(III) (oxyhydr)oxides and release of associated OC in early summer when conditions are wetter and more reduced, and new formation of Fe(III) minerals (34.7% gain in comparison to initial Fe) in the late summer under more dry and oxic conditions which again sequestered Fe-bound organic carbon. Our data suggests that the so-called rusty carbon sink is seasonally dynamic in partially-thawed permafrost peatland soils, thus can either promote or suppress carbon mineralization and lead to seasonal changes in GHG emissions.

Graphical Abstract*

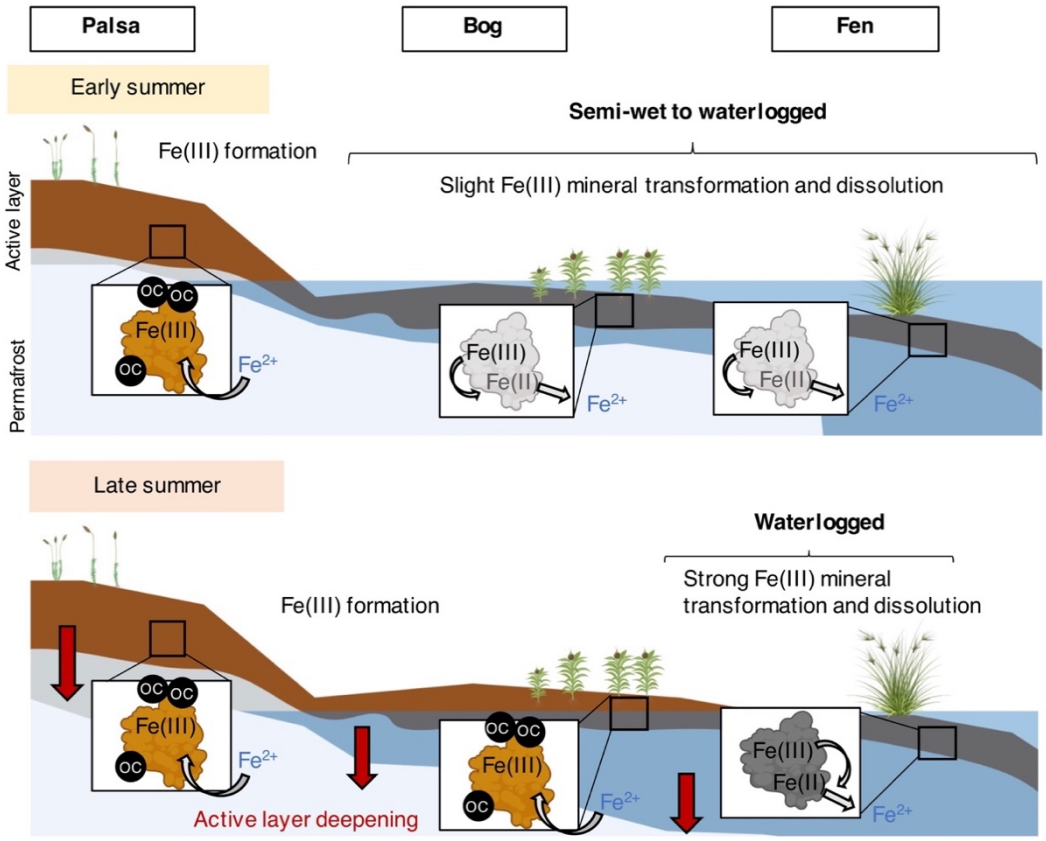

*Graphical abstract is made in ©BioRender- biorender.com.

Introduction

Permafrost peatlands hold enormous amounts of OC, equivalent to over one-third of the carbon currently in the atmosphere (~800 Pg)[1, 2]. By the end of this century, permafrost peatlands are predicted to warm from an annual average air temperature below 2°C to between + 5.6 to + 12.4°C[3], almost twice the rate of the global average[4]. The resultant permafrost thaw leads to soil active layer deepening[5, 6], changes in surface vegetation composition[7, 8], altered carbon accumulation[2, 9] and shifts in microbial communities that degrade or transform OC[10-12]. Ultimately, permafrost peatlands are shifting from a carbon sink to a source of GHG [1, 13, 14]. What controls how fast and to which extent there is a shift from a carbon sink to source of GHG emissions is currently intensively studied.

One parameter relevant for controlling GHG emissions in permafrost environments could be carbon protection by Fe minerals. Fe-OC associations regulate long-term global preservation of natural organic matter in soils and sediments and in the active layer underlain by intact permafrost and in partially-thawed soils[15, 16]. With permafrost thaw, this so-called rusty carbon sink[17] is lost by reductive dissolution promoted by Fe(III)-reducing bacteria under water-logged and O_2 limited conditions[15]. The dissolved OC (DOC) can then be further metabolized and can lead to GHG emissions along the permafrost thaw gradient[18].

However, permafrost peatlands not only experience long-term thaw, but also seasonal changes in freeze-thaw cycles[19], air temperature[20], sunlight[21] and precipitation[20]. With seasonal shifts in runoff and soil moisture[20], soils could drain and (re-)flood[22]. Redox conditions, which are controlled by the availability of electron acceptors such as O_2, fluctuate between oxic (oxygen-rich, drained) and reducing (oxygen-depleted, flooded), where alternative electron acceptors (e.g., Fe(III), NO_3^-, SO_4^{2-}, OC) are converted to reduced species (e.g. Fe(II), NO_2^-/N_2, H_2S, CH_4). Hence, these seasonal redox changes either promote or suppress Fe(III) reduction and Fe(II) oxidation, thus carbon mineralization and ultimately, GHG emissions[23-25]. To date, it remains unknown if the rusty carbon sink in permafrost peatlands is stable or continuously recycled by Fe(III) reduction and Fe(II) oxidation during seasonal redox fluctuations.

To capture the spatial and temporal dynamics of the rusty carbon sink over the thawed summer season from July to September, we exposed sand coated with synthetic Fe(III) oxyhydroxides, here ferrihydrite (FH; simplified formula of $Fe(OH)_3$), in the active layer in three thaw stages at a Swedish peatland (Stordalen mire, Abisko) in early (July) and late summer (August-September). The thaw stages in which the FH-coated sand was exposed were (1)

desiccating palsa underlain by permafrost, (2) partially-thawed bog and (3) fully-thawed fen as previously defined[11, 18, 26, 27]. The objectives of this study were to i) Fe(III) (oxyhydr)oxide formation, dissolution and transformation and ii) to quantify Fe-associated OC along the thaw gradient as redox conditions shift in the thawed summer season.

Material and Methods

Field Site

Stordalen mire in the Abisko region of northern Sweden is a degrading permafrost peatland[28, 29]. Increasing mean annual air temperatures, exceeding the 0°C threshold, led to rapid warming of the Abisko region since the twentieth century[30] causing an active layer deepening and an increase in surface wetness through thawing of permafrost[5]. As previously described[11, 15, 18], the mire consists of three distinct forms of degrading permafrost peatland: (1) palsa (intact permafrost), (2) ombrotrophic peatland or bog (partially-thaw) with *Sphagnum* spp., sedges and shrubs, and (3) minerotrophic peatland or fen (fully-thawed) with sedges, mainly *Eriophorum* spp.[26] (SI, Figure S1).

Exposure Experiment

To capture the spatial and temporal dynamics of the rusty carbon sink over the thawed summer season from July to September, we incubated sand coated with synthetic Fe(III) oxyhydroxides (here FH) in the Stordalen mire peatland. FH-coated sand was exposed for either two weeks in early summer (early July 2019) or two months in late summer (early July to September 2019) in the active layer of palsa, bog and fen along the previously described permafrost thaw gradient[15, 18] (for FH-coated sand synthesis and exposure bag preparation see SI, as well as Figures S1 and S2). For short-term exposure, three bags each were placed for 2 weeks (early summer) at three sites in each of the three thaw stages (9 bags per thaw stage in total; for exact positions see SI, Figure S1). For long-term exposure, three bags each were exposed for 2 months (late summer) at each of the three thaw stage (3 bags per thaw stage in total; SI, Figure S1). The first 10 cm of the soil layer were removed with a coring sleeve and the bags placed into the hole, which was then sealed again with the upper 10 cm soil. The bags were placed at the transition zone, the redox interface between the shallow organic horizon and the deeper mineral horizon (for depth comparison see also Patzner *et al.*[15]). After the corresponding exposure times (two weeks and two months), the FH bags were carefully taken out of the soil, immediately frozen in liquid nitrogen and stored at -80°C until further analysis.

Sequential Fe Extractions

Sequential Fe extractions were used to follow changes in solid-phase Fe redox transformation along the thaw gradient over seasons. Anoxic Na-acetate (1 M, pH 5), followed by 0.5 and 6

M HCl were used to successively dissolve Fe phases with increasing crystallinity[31]. Adsorbed Fe(II)[32, 33] and Fe in amorphous Fe sulfides[34] were extracted by the Na-acetate (referred to adsorbed/amorphous Fe). 0.5 M HCl was chosen to extract poorly crystalline Fe(III) (oxyhydr)oxides and remaining reduced Fe(II) species such as $FeCO_3$[35] or FeS (referred to as poorly crystalline Fe) and 6 M HCl to extract more crystalline, remaining Fe fractions, such as poorly reactive sheet silicate Fe or FeS species[15, 31] (referred to as more crystalline Fe) from the Fe mineral coated sand (for exact extraction procedure see SI).

Selective Fe and OC Extraction

Selective Fe and OC extraction was used to follow changes in solid-phase Fe-OC associations along the thaw gradient over summer. Sodium pyrophosphate (pH 10) was used to determine sodium pyrophosphate extractable Fe, which is defined as colloidal or OM-chelated Fe (referred to Fe associated with OC) and sodium pyrophosphate extractable OC[15, 36]. The source of Fe phases and the associated OM is difficult to specify as sodium pyrophosphate dissolves Fe from organic complexes and promotes peptization and dispersion of Fe oxide colloids[37, 38]. Same amounts of homogenized sand and extract were used as for the sequential Fe extraction, only the incubation time was extended to 16 h, as previously suggested[15, 36].

Geochemical Analyses

The extracts (supernatants) were subsequently analyzed in technical triplicates for Fe (referred to sodium acetate or 0.5 M HCl or 6 M HCl or sodium pyrophosphate extractable Fe) and OC (referred to sodium pyrophosphate extractable OC)[15]. To get the total Fe, the extracts were analyzed using inductively coupled plasma mass spectrometry (ICP-MS). For this, samples were diluted 1:100 and acidified within a final 1% HCl. Within 24 h, Fe (Fe(II) and Fe(tot)) was determined by the spectrophotometric Ferrozine assay[39]. Samples were immediately stabilized upon collection under anoxic conditions in 1 M HCl in 1:10 dilutions for the Ferrozine assay. The obtained Fe(tot) of ICP-MS analysis and by the Ferrozine assay were identical. DOC was quantified in triplicate with a TOC analyzer (High TOC II, Elementar, Elementar Analysensysteme GmbH, Germany). Inorganic carbon was removed by acidifying the samples with 2 M HCl prior analysis.

Total Organic Carbon Analysis

To quantify the total organic carbon (TOC) content of the sands after field exposure, triplicate samples of each bag were dried at 60°C until no further weight loss was observed. The

samples were then ground to fine powders and analyzed by SoilTOC instrument (Elementar Analysensysteme GmbH, Germany).

Scanning Electron Microscopy (SEM) and Energy Dispersive X-Ray Analysis (EDS) was done as described in the SI.

Microbial Community Analysis

Total DNA was extracted as described previously[40]. Briefly, the PowerSoil® RNA and DNA isolation kit was used to extract DNA in triplicates of each exposed ferrihydrite bag with the following modifications: 2 g of sand was used from each bag; Beat-beating was conducted for 10 mins and centrifugation was at maximum speed (7,000g) at 4°C; During extractions, incubation time was extended to 1.5 h at -20°C (for details see SI). Library preparation steps and sequencing were performed by Microsynth AG (Switzerland) as detailed in the SI. Quality control, reconstruction of 16S rRNA gene sequences and taxonomic annotation was performed with nf-core/ampliseq v1.1.2[41, 42] as outlined in the SI.

Isolation of Fe(III)-reducing bacteria was performed with anoxic synthetic fresh water media (as previously described[15]) using a dilution to extinction approach (for further information see SI).

Seasonal Monitoring

To capture seasonal fluctuations in weather and geochemical soil conditions, context data such as precipitation, air temperature, soil moisture and soil temperature were plotted. Precipitation and air temperature were provided by the Abisko Observatory. Soil moisture and soil temperature were provided by Integrated Carbon Observation System (ICOS) Sweden Abisko – Stordalen[43]. Redox potentials in the palsa, bog, and fen were continuously monitored with five redox potential probes (PaleoTerra). Two probes were positioned in both the bog and fen and one was positioned in the palsa. Each redox probe had platinum sensors positioned at 6, 8 and 10 cm depth below the ground surface (for details see SI).

Results and Discussion

Seasonal fluctuations drive redox shifts in thawing permafrost peatlands

Snow melt began in the second half of April in 2019 (air temperatures above 0°C, Figure 1) and lasted around one month. As previously shown, the melt water results in highest annual runoff (up to 75% of the total annual runoff)[20], which was reflected in our own data set by the volumetric soil water content (VSWC). VSWC was highest in the intact palsa (51%) between the end of March and the beginning of April (Figure 1), presumably resulting in increasing runoff into the partially-thawed bog[44]. In early summer, semi-wet bog soils were weakly (+100 to +300 mV[45]) to moderately (-100 to +100 mV[45]) reduced from 6 to 10 cm depth (Figure 1 and SI, Figure S4). From the beginning of the thawed season (soil temperatures above 0°C in May/June), the air temperature increased to a maximum of 18.7°C, accompanied by a soil temperature increase to a maximum of 25.0°C in 2 cm soil depth at the end of July (Figure 1). Increasing evapotranspiration, together with decreasing runoff from intact palsa (VSW of 26%) and increasing active layer depth (30 to 70 cm)[20, 22, 26], led to soil drainage in the partially-thawed bog (Figure 1 and SI, Figure S3). Ultimately, a shift from weakly/moderately reduced to oxic conditions (redox potential above +300 mV) in late summer was observed (Figure 1 and SI, Figure S4).

Through the whole thaw season, the palsa remained relatively dry and oxic (SI, Figure S4), whereas the fen stayed water-logged (VSWC of 40%, Figure 1) and weakly to moderately reduced (SI, Figure S4), confirming previous studies[18, 46]. The annual average air temperature of +0.2°C slightly exceeded the 0°C threshold (above 0°C ice melt and permafrost thaw) supporting the overall warming trend since the early 20th century[30]. The summer of 2019 was dry: only 60 mm rain fell in June and July (Figure 1) compared to the long-term average of 81 mm (1913-2009)[20].

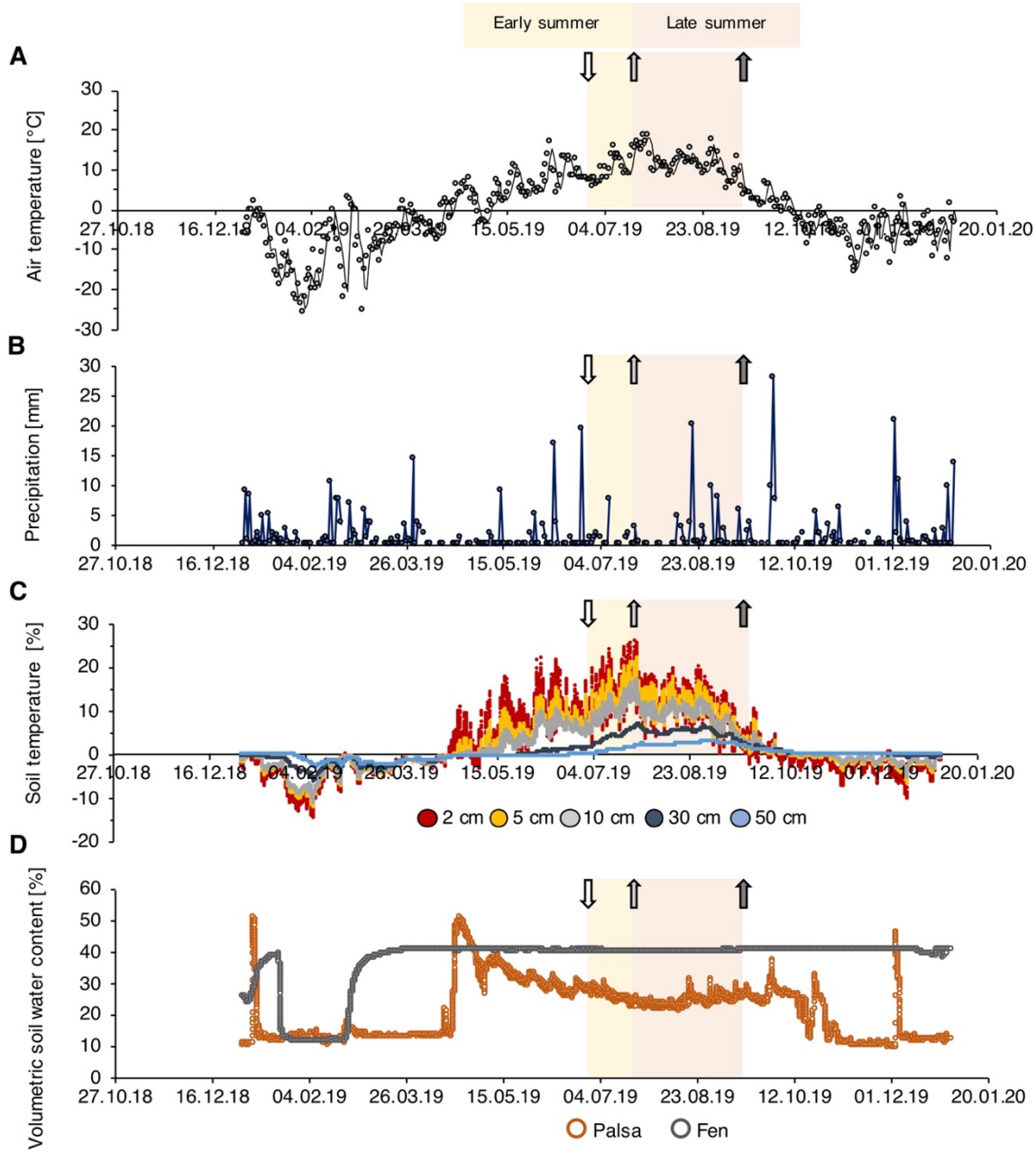

Figure 1. Seasonal fluctuations in weather and soil conditions for Abisko and Stordalen mire in the year 2019. *(A) Air temperature [°C] and (B) precipitation [mm] were monitored by the Abisko Observatory. (C) Average soil temperature at Stordalen mire (average of the three thaw stages) at 2 cm, 5 cm, 10 cm, 30 cm and 50 cm depth and (D) volumetric soil water content [%] in the upper 6 cm from the soil surface in palsa and fen was monitored by Integrated Carbon Observation System (ICOS) Sweden Abisko-Stordalen[43]. For thaw stage specific soil temperatures see SI, Figure S5. Early summer (yellow background) marks the time period that the short-term ferrihydrite bags were exposed for 2 weeks and late summer (red background) the additional time period that the remaining ferrihydrite bags were exposed (in total: 2 months). White arrow marks start of short and long-term exposure. Light grey arrow*

marks end of short-term exposure (exposed in early summer) and dark grey marks the end of the long-term exposure (exposed in early to late summer).

Fe(III) mineral formation and dissolution under changing redox conditions

In the active layer of the palsa underlain by intact permafrost, continuous oxic conditions promoted Fe(II) oxidation to Fe(III) minerals through early to late summer. A 62.1 to 155.3% gain in solid Fe(III) was observed in bags exposed in early to late summer (3.55±1.15 to 5.59±0.46 mg Fe(III) per g sand in comparison to 2.19±0.36 mg per g sand in unexposed FH-coated sand). In the active layer of the partially-thawed bog, weakly to moderately reduced redox conditions in early summer favored Fe(III) (oxyhydr)oxide reduction which is indicated by low Fe(II) per g sand (0.01±0.00 mg Fe(II) per g sand; 1 M Na-acetate extractable Fe, Figure 2) and dissolution leading to a 52.5% loss of Fe (loss of 1.03±0.34 mg Fe(III) (0.5 M HCl extractable Fe) per g sand in comparison to unexposed FH-coated sand, Figure 2). However, a shift to oxic conditions in the active layer of the partially-thawed bog in the late summer, caused by seasonal redox fluctuations, promoted Fe(II) oxidation. Ultimately, this Fe(II) oxidation led to a net 33.3% gain in Fe (compared to the Fe-content in the initial FH-coated sand) in the active layer of the partially-thawed bog in the bags exposed until late summer. The newly formed Fe phase was more crystalline Fe indicated by a gain in 0.73±0.21 mg 6 M HCl extractable Fe per g sand in comparison to unexposed FH-coated sand (2.19±0.36 mg Fe per g sand) (Figure 2).

In the fully-thawed fen, continuous weakly to moderately reducing conditions led to Fe(III) reduction through early to late summer and ultimately to 5.0% Fe(II) formation. 0.11±0.01 mg Fe(II) per g sand were formed during exposure and 50.2% Fe lost in the solid phase (1.09±0.09 mg Fe remaining) in comparison to unexposed FH-coated sand (2.19±0.36 mg Fe per g sand).

The gain of poorly crystalline Fe in bags exposed in the active layer of intact palsa, caused by promotion of Fe(II) oxidation under oxic conditions, supports previous observations showing highest amounts of Fe(III) (oxyhydr)oxides in intact permafrost soils at the redox interface between shallow organic and deeper mineral horizons within the seasonally thawed active layer[15, 47]. Fe(III) formation in bags exposed in the active layer of the partially-thawed bog in late summer could explain the presence of reactive Fe(III) phases in bog soils: Patzner *et al.*[15] found 7.5% reactive Fe (sodium dithionite citrate extractable) of the total Fe (6M HCl extractable) in partially-thawed bog soils. The newly formed, more crystalline Fe(III) phase in bags exposed in the active layer of the partially-thawed bog until late summer could be

explained by exposure to microbially derived Fe(II) which can induce mineral recrystallization and transformation processes in Fe(III) (oxyhydr)oxides towards thermodynamically more stable mineral phases[48]. Along the thaw gradient, aqueous Fe(II) in the porewater increased from 0.02±0.01 mM in the palsa to up to 1.6±0.3 mM in the fully-thawed fen[15] and the pH from 4.1 in the partially-thawed bog to 5.8 in the fully-thawed fen[18]. Fe(II)-catalyzed transformation of FH can result in either goethite (α-FeOOH), lepidocrocite (γ-FeOOH) or magnetite (Fe_3O_4) formation with only minor differences in pH, background ligands, and Fe(II):Fe(III) ratios impacting reaction kinetics and end-phase[48-52]. The presence of DOC in the partially thawed bog[15, 18] could also trigger mineral transformation to less-crystalline FH and lepidocrocite[53]. Exposed FH on the sand grains could also act as a so-called template effect: Chen and Thompson[54] observed goethite formation in various forest soils promoted by a template effect of pre-existing Fe(III) (oxyhydr)oxides. The non-extractable mineral phase (here: quartz) has only a minor effect on oxidation rates[54]. Further studies are needed to identify the newly formed Fe phases by, e.g. Mössbauer spectroscopy or XRD analysis, which for this experimental setup was not possible due to the high background of quartz by the sand grains in comparison to low Fe (wt) %.

Our incubation experiments now provide a mechanistic explanation for the Fe(II) concentrations observed before[15, 55]. Lipson *et al.*[56] estimated that net reduction of Fe(III) (oxyhydr)oxides coupled to oxidation and mineralization of OC contributes to 40-63% of ecosystem respiration depending on organic layer thickness and season. In the FH-exposed bags, Fe(III) reduction was most likely driven by Fe(III)-reducing bacteria such as *Geobacter* sp. We successfully further isolated an Fe(III)-reducing bacteria from the FH-coated sand, bags exposed in the fen that's 16S rRNA gene sequence shared 98% identity to *Geobacter* sp. In addition, *Geobacter* sp. comprised 0.45±0.01% relative abundance in 16S rRNA gene amplicon sequencing of the whole microbial community associated with exposed sand in the fully-thawed fen until late summer (see SI, Figure S6 and S7).

We observed incomplete Fe(III) reduction and dissolution, resulting in 47.5% of the initial Fe(III) remaining in the exposed bags (compared to unexposed FH-coated sand) in the active layer of the partially-thawed bog in early summer and 51.1% in the fully-thawed fen through the whole summer. This incomplete Fe(III) reduction and dissolution could have a number of explanations: (1) The teflon bag itself may slow Fe(III) reduction rates: In teflon packed FH-coated sands, Fe(III) reduction rates were slightly than in unpacked FH-coated sand (SI, Figure S8); (2) Exposed FH-coated sand could have a lower susceptibility to reductive dissolution, as compared to aluminum-silicate-FH coprecipitates[57] which are typically present

in environmental soils; (3) Remaining Fe(III) minerals are less accessible for microbial Fe(III)-reduction due to formation of Fe(II)-surface coatings which lower the reducibility of Fe minerals[58]; or (4) the remaining Fe(III) phase could also be sustained by present Fe(II)-oxidizing bacteria such as *Gallionella* sp. and *Sideroxydans* sp. (SI, Figure S6 and S7), which is most unlikely due to very low dissolved O_2 concentrations (0.15±0.04 μM in partially-thawed bog and 0.02±0.01 μM in fully-thawed fen in early summer, i.e. mid-July[46]). The remaining Fe(III) phase in our exposure experiments might explain the presence of small quantities of reactive Fe(III) phases (2.64±0.03 mg Fe per g soil) at the redox boundary between organic and mineral horizon in the fully-thawed fen, suggesting a minor but persistent Fe fraction remaining in soils even with complete permafrost thaw[15].

Lipson *et al.*[56] observed net oxidation of Fe(II) in the active layer of reduced permafrost soils for which several hypotheses are suggested: (1) Fe(II) oxidation by O_2 or by microaerophilic Fe(II)-oxidizers could be driven by transport of oxygen to deeper layers by plant roots[59], such as *Eriophorum* spp. at Stordalen mire, (2) due to high concentration of dissolved Fe in these soils (1.6±0.3 mM aqueous Fe^{2+} [15]), Fe might circulate throughout the soil profile, becoming oxidized to Fe(III) abiotically by O_2 or by microaerophilic Fe(II)-oxidizers at the surface and diffusing as Fe^{2+} to lower layers, (3) Fe(II) can also be oxidized under anoxic conditions e.g. by microbes coupled to nitrate reduction, abiotically by reactive N-species (e.g. nitrite), perchlorate reduction, by phototrophic Fe(II)-oxidizers or radicals formed by light[60, 61] or/and (4) direct flow of e^- through conductive soil components such as metal (e.g. Fe) ions in the porewater and electric double layer of colloidal surfaces of organic matter and metal ions (highly abundant in peat soils[62]) can couple anoxic processes at depth to oxic processes at the surface[63]. One such conductivity component could even be caused by the presence of *Geobacter* sp. (SI, Figure S6 and S7) which produces conductive biofilms, pilin nanofilaments (known as microbial nanowires) and nanoparticulate Fe (oxyhydr)oxides[64, 65] that form conductive networks over centimeter scale with Fe(III)-reducing microbial cells[66] and humic substances that can shuttle electrons to Fe(III) (oxyhydr)oxides[67].

The exposure experiments reveal the presence of the rusty carbon sink in intact permafrost soils, which is lost with complete permafrost thaw[15]. Our new findings suggest a more dynamic microbial iron cycle in the intermediate, partially-thawed bog, under seasonal fluctuations in the thawed active layer, either promoting or suppressing Fe(II) oxidation and thus Fe(III) mineral formation.

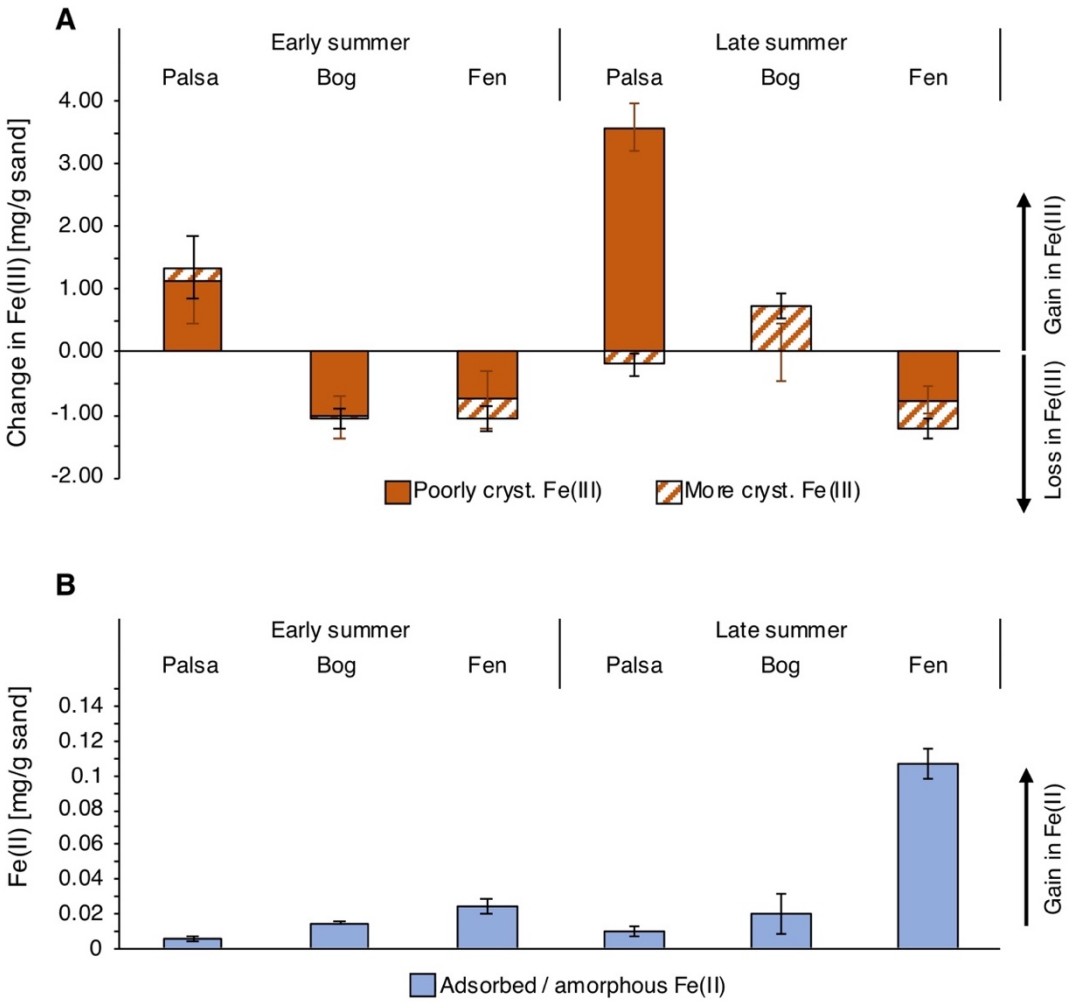

Figure 2. Gain and loss of solid-phase iron (Fe) along a thaw gradient in early (2 weeks exposure) and till late summer (2 months exposure). *(A) Gain and loss in poorly crystalline Fe(III) (1 M HCl extractable) and more crystalline Fe(III) (6 M HCl extractable). Values are normalized to unexposed ferrihydrite (FH)-coated sand (2.19±0.36 mg total Fe per g sand), which was transported to the field but then stored at room temperature until the end of the experiment. Unexposed FH-coated sand included a more crystalline Fe phase (1.01±0.14 mg only 6 M HCl extractable per g sand), probably due to aging over time. Positive values indicate a net gain in Fe and negative values indicate a net loss in Fe in comparison to the unexposed ferrihydrite-coated sand. (B) Adsorbed/amorphous Fe (all Fe(II)) (1 M Na-acetate extractable). No Fe(III) was detected in the 1 M Na-acetate extracts. Reported values for the early summer period are the average and error bars are the combined standard deviation of triplicate analysis, normalized to the unexposed FH-coated sand, of nine homogenized bags, exposed at each thaw stage (palsa, bog and fen). Reported values for the late summer period are the*

average and error bars are the combined standard deviation of triplicate analysis, normalized to the unexposed FH-coated sand, of three homogenized bags, exposed at each thaw stage.

Carbon sequestration by Fe mineral phases under changing redox conditions in thawing permafrost peatlands

In the palsa, no Fe-sequestered carbon (defined by sodium pyrophosphate extractable OC and TOC content) was detected in the bags exposed in the early nor late summer (Figure 3). In early summer, no Fe-OC associations were observed in the bags exposed in the partially-thawed bog and fully-thawed fen areas along the thaw gradient, probably due to the overall loss of Fe caused by mineral dissolution. Carbon sequestered by Fe minerals on the sand grains was only observed in the active layer of the partially-thawed bog and in the fully-thawed fen at the end of the summer (Figure 3).

Previously, it was shown that reactive Fe minerals in intact palsa soils sequester highest organic carbon amounts along a permafrost thaw gradient[15]. Whereas, here, FH exposed in intact palsa soils couldn't sequester any organic carbon. It should be noted that exposed FH-coated sands can only capture the mobile phase of organic carbon (i.e., DOC) in the porewater smaller than 0.55 mm diameter, which is the size of the holes in the teflon bags and thus would include particulate organic carbon and microbes. Dissolved Fe^{2+} migrates upwards to the redox interface, driven by snow melt, permafrost thaw and precipitation, and is oxidized to form Fe(III) (oxyhdyr)oxides[47] at leads to an increase of Fe in bags exposed in intact palsa soils. DOC, however, is more dynamic as it might be metabolized and transformed to CO_2 and CH_4 prior reaching the exposed FH we experimentally incubated in the active layer underlain by intact permafrost. Chen *et al.*[24] found dissolved organic matter (DOM) and soil organic matter (SOM) protection by Fe only under static oxic conditions when Fe^{2+} and DOC were both present. The exclusive presence of Fe^{2+} resulted in production of reactive oxygen species and in an increasing OC mineralization by 8% following oxidation to Fe(III)[24]. Abiotic oxidation of dissolved Fe^{2+} by O_2 produces hydroxyl radicals that are known to degrade organic matter to low molecular weight organic molecules and CO_2[68, 69].

In the active layer of the partially-thawed bog in late summer, 1.23% of the Fe present in the bags was associated with OC (0.04±0.01 mg sodium pyrophosphate extractable Fe per g sand of 2.95±0.57 mg total Fe per g sand) and sequestered highest organic carbon amounts (0.42±0.05 mg sodium pyrophosphate extractable OC per g sand, 34.13% of 1.24±0.01 mg TOC per g sand) along the permafrost thaw gradient over time. This resulted in strong

associations of Fe with carbon (sodium pyrophosphate extractable) (Figure 4, SI Figure S9-S11) with OC/Fe (wt:wt) ratios of 11.7 (SI, Table S1, also for TOC to total Fe ratios and molar ratios). Soil horizons at the redox boundary between organic and mineral horizon in the partially-thawed bog showed similar OC/Fe associations (OC/Fe (wt:wt) ratio of 10.9)[15]. The high OC/Fe (wt:wt) ratios suggest co-precipitation with and/or chelation of metal (Fe) ions by organic compounds which can generate structures above 0.22 OC/Fe (wt:wt) ratios[16, 70-72]. Microscopic images of Fe-OC associations on the sand grains surface could indicate such co-precipitates of OC and Fe (Figure 4; SI Figure S9-S11). In fully-thawed fen, 18.06% of the Fe (0.18±0.07 mg sodium pyrophosphate extractable Fe per g sand of 1.02±0.09 mg total Fe per g sand) was associated with OC (0.37±0.04 mg sodium pyrophosphate extractable OC per g sand, 38.12% of 0.98±0.01 mg TOC per g sand) with OC/Fe (wt:wt) ratios of 2.03 (Figure 3 and 4; SI Figure S9 and S10 and Table S1), still suggesting co-precipitation rather than sorption, in late summer.

Carbon sequestration after Fe(II) oxidation and Fe(III) mineral formation in bags exposed in the active layer of the partially-thawed bog until late summer could explain highest amounts of reactive Fe-bound carbon (sodium dithionite citrate extractable) (39.4% of TOC at the redox boundary between organic and mineral horizon) in soils of the partially-thawed bog along the thaw gradient after palsa collapse[15]. However, our data shows that the rusty carbon sink in the active layer of the partially-thawed bog soils in permafrost peatlands is not stable over the thawed summer, but continuously recycled by Fe(III) reduction and Fe(II) oxidation resulting in a shift from carbon source, shown by the lack of Fe-sequestered OC in early summer, towards a rusty carbon sink, shown by the presence of Fe-sequestered OC in late summer in the partially-thawed bog.

The Fe sequestration of very small quantities of OC (determined by sodium pyrophosphate extracts and TOC analysis shown in Figure 3; in comparison to intact palsa soils with 40.09±3.59 mg sodium pyrophosphate extractable OC per g soil[15]) by remaining Fe(III) oxides, being resistant to mineral reduction and dissolution, are seen in the exposure experiment bags in the fully-thawed fen until late summer. The presence of remaining Fe(III) oxides in the exposed FH bags after occurred mineral reduction and dissolution explains small quantities of 5.97 mg sodium pyrophosphate extractable OC per g soil at the boundary soil layer between organic and mineral horizon in fully-thawed fen soils[15]. The remaining Fe(III) phase (44.7%) in the exposed FH bags could still sequester rather small amounts of carbon from the surrounding porewater (in comparison to intact palsa soils with 40.09±3.59 mg OC per g soil[15]), as was observed in the water column of other fen types[73]. Along the thaw gradient, DOC increases from 19.7±0.8 mg/L in the palsa to 102.1±14.1 mg/L in the fen areas[15]. But it remains

unclear, why, after mineral dissolution occurred, no OC was observed to be associated with the remaining Fe(III) phase in the partially-thawed bog and fully-thawed fen after early summer exposure. Explanations could be differences in the mineralogy of the remaining Fe(III) phase or Fe(II)-OC coatings on the sand grains surface, which is supported by the fact that highest solid Fe(II) was observed in bags in fully-thawed fen after late summer exposure.

TOC analysis revealed the same trend as the sodium pyrophosphate extractable OC along the thaw gradient over the thawed summer season (Figure 3) with even higher amounts of carbon in comparison to Fe-associated OC (sodium pyrophosphate extractable OC) in the partially-thawed bog (Figure 3). One potential explanation could be the microbial biomass increase along the thaw gradient. Biomass increases along the thaw gradient with 2.6 times more microbial cells per gram of soil found in fully-thawed fen relative to palsa and bog[11]. The lower microbial biomass in palsa and bog soils may explain why our DNA extraction was only successful for bags exposed in the fully-thawed fen in late summer (SI, Figures S6 and S7). These higher TOC amounts could thus be a sum of Fe-associated OC and of biomass associated with the sand grains in early summer in the partially-thawed bog and through the whole summer in fully-thawed fen.

Our data indicates different carbon sequestration mechanisms by iron oxides in the active layer over summer along the permafrost thaw gradient and illustrates that soils shift from being a carbon dioxide source (via microbially mediated Fe reductive mineral dissolution coupled to organic carbon mineralization) in early summer to a rusty carbon sink (via formation of iron oxide minerals and sequestration of associated organic carbon either fixed by microbes living on the particle and/or trapped from DOC) in late summer in partially-thawed bog. Thus, the rusty carbon sink strongly depends on seasonal fluctuations in runoff, soil moisture and ultimately, redox conditions.

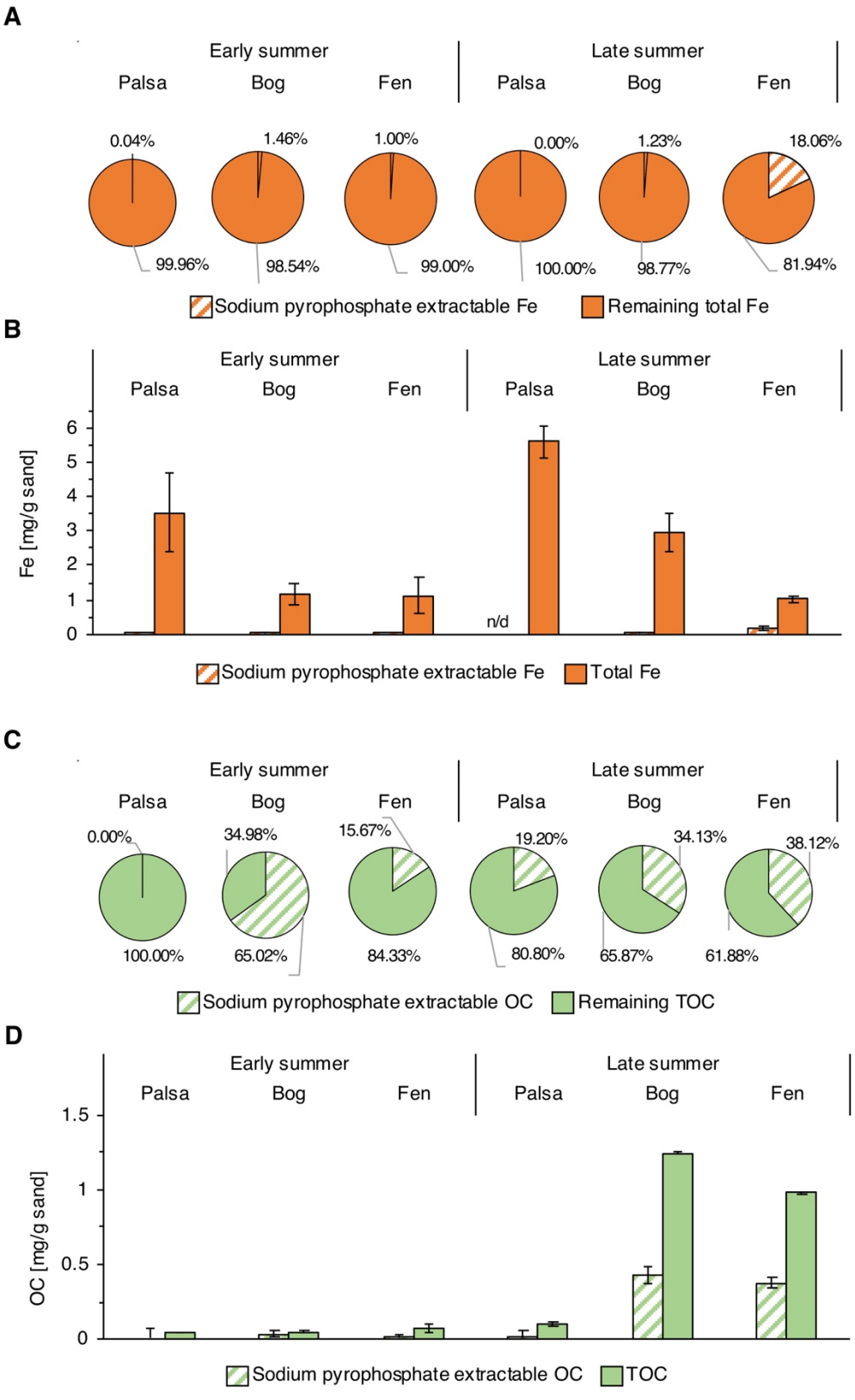

Figure 3. Iron (Fe)-organic carbon (OC) associations on ferrihydrite-coated sand grains incubated along the thaw gradient in early (2 weeks exposure) and until late summer (2 months exposure). *(A) Colloidal/OM-chelated Fe (defined as sodium pyrophosphate*

extractable Fe) (in orange lines) [% of the total Fe content associated with sand (in orange)] along the thaw gradient with time. (B) Absolute amounts of sodium pyrophosphate extractable Fe and total Fe along the thaw gradient with time. (C) Sodium pyrophosphate extractable OC (in green lines) [% of the total OC (TOC) associated with sand (in green)] along the thaw gradient with time. (D) Absolute amounts of sodium pyrophosphate extractable OC and TOC along the thaw gradient with time. Reported values for the early summer period are the average and error bars are the standard deviation of triplicate analysis of nine homogenized bags, which were exposed at each thaw stage (palsa, bog and fen). Reported values for the late summer period are the average and error bars are the standard deviation of triplicate analysis of three homogenized bags, exposed at each thaw stage. n/d = not detected.

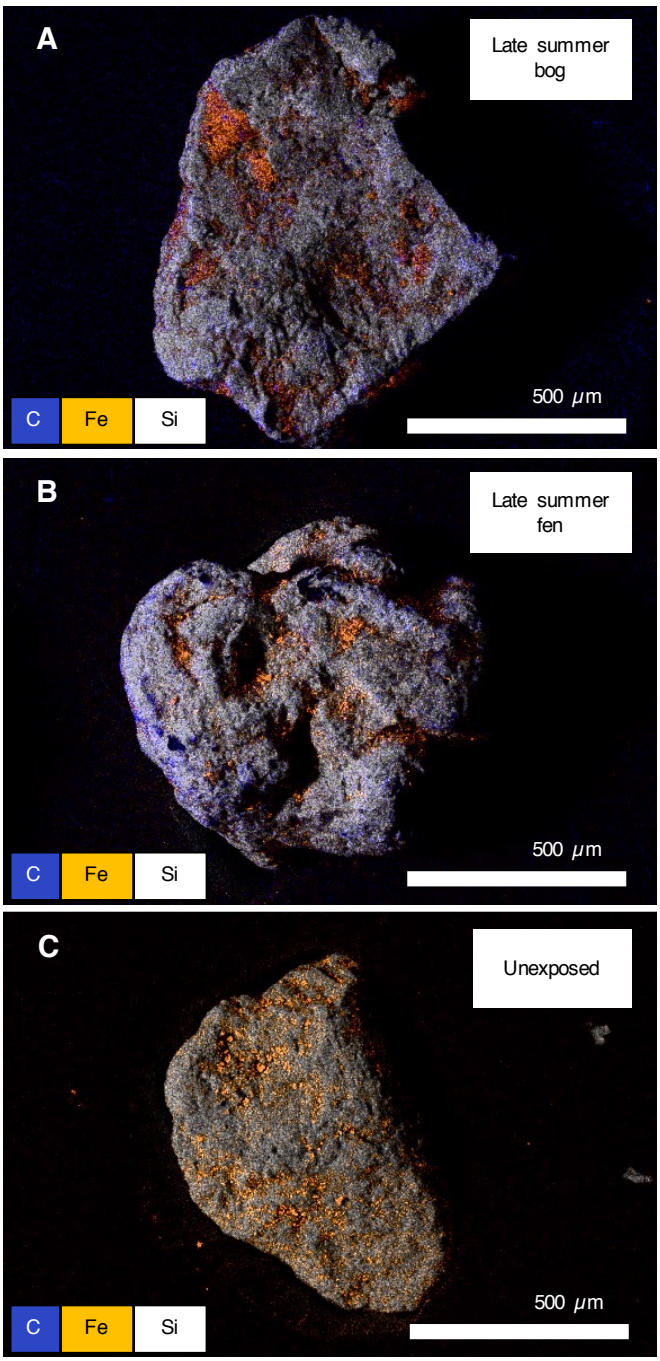

Figure 4. EDS derived chemical distribution maps of iron (Fe)-organic carbon (OC) associations on ferrihydrite (FH)-coated sand grains incubated in the partially-thawed bog (A) and in fully-thawed fen (B) after late summer exposure (for 2 months) in comparison to unexposed FH-coated sand (C). *Results shown are representatives and replicate analysis is reported in the Supporting Information (SI, Figures S10 and S11).*

Environmental Implications

Permafrost environments experience drastic changes caused by global warming[13]. Rising temperatures in the Arctic[74] trigger increasing permafrost temperatures[75] and ultimately an increase in the thickness and variability of the active layer[76]. Multiple evidence exists that the Arctic hydrological cycle is intensifying as a result of warming[77], leading to rise in all fluxes including precipitation, runoff and evapotranspiration[78]. These changes ultimately drive rapid shifts in water levels and redox conditions from flooded and more reduced to drained and oxic permafrost-affected soils[79]. The presented study demonstrates that iron cycling in thawing permafrost peatlands correlates with redox conditions and that shifts in redox potential resulted in either Fe(II) oxidation and Fe(III) mineral formation, sequestering OC, or Fe(III) reduction, resulting in OC release. Iron cycling from Fe(II) to Fe(III) depending on shifts in redox conditions driven by seasonal fluctuations in runoff and soil moisture is in line with previous observations in a drained thaw lake basin on the Arctic coastal plain[56]. The seasonality of the rusty carbon sink in permafrost environments can strongly drive GHG emissions. On the one hand, Fe(III) reduction leads to direct CO_2 emissions since it is coupled to oxidation and mineralization of organic matter[56, 61]. Additionally, the released previously Fe-associated OC becomes more accessible to decomposers. Fe(III) reduction can also inhibit methanogenesis by being more thermodynamically favorable[80]. McCalley *et al.*[10] found seasonal variations in CH_4 fluxes and their ^{13}C content in partially-thawed bog and fully-thawed fen, which could be partly driven by the use of Fe(III) microbial metabolism. On the other hand, stable and newly formed Fe(III) minerals can sequester carbon and protect it from microbial consumption[81, 82], thus suppressing GHG emissions. Future studies should assess the extent of GHG emissions caused by formation, transformation and destruction of Fe(III) minerals under fluctuating redox conditions in thawing permafrost environments. Recently, Coward *et al.*[58] suggested that Fe-OC associations might be protected by surface coatings or by being embedded in a composite aggregate strucutre[83]. Thus, future *in situ* experiments should be conducted with a more complex matrix such as Fe-OC co-precipitates or biogenically derived Fe(III) (oxyhydr)oxides and other important ions in soils (e.g. Al).

Acknowledgements

The authors would like to acknowledge the Abisko Scientific Research Station and ICOS Sweden (Swedish Research Council: 2019-00205) for their support during sampling missions and providing the context data (precipitation, air temperature, soil temperature, soil moisture) (special thanks to Annika Kristoffersson and Jutta Holst). We thank M. Logan (Colorado State University, Fort Collins, Colorado) for assistance in the field, Sören Drabesch (University Tuebingen) for ICP-MS analyzes and H. Joss (University Tuebingen, Germany) for carbon analyzes. The authors acknowledge infrastructural support by the Deutsche Forschungsgemeinschaft (DFG, German Research Foundation) under Germany's Excellence Strategy, cluster of Excellence EXC2124, project ID 390838134. This work was supported by the University of Tuebingen (Programme for the Promotion of Junior Researchers award to Casey Bryce) and by the German Academic Scholarship Foundation (scholarship to Monique S. Patzner). We also thank the German Research Foundation DFG (INST 37/1027-1 FUGG) for financial support provided for the acquisition of the cryogenic focused ion beam scanning electron microscope.

References

1. Schuur, E. A. G.; McGuire, A. D.; Schadel, C.; Grosse, G.; Harden, J. W.; Hayes, D. J.; Hugelius, G.; Koven, C. D.; Kuhry, P.; Lawrence, D. M.; Natali, S. M.; Olefeldt, D.; Romanovsky, V. E.; Schaefer, K.; Turetsky, M. R.; Treat, C. C.; Vonk, J. E. Climate change and the permafrost carbon feedback. *Nature* **2015,** *520*, (7546), 171-179.
2. McGuire, A. D.; Anderson, L. G.; Christensen, T. R.; Dallimore, S.; Guo, L. D.; Hayes, D. J.; Heimann, M.; Lorenson, T. D.; Macdonald, R. W.; Roulet, N. Sensitivity of the carbon cycle in the Arctic to climate change. *Ecol Monogr* **2009,** *79*, (4), 523-555.
3. Christensen, J. H. *et al*. Climate phenomena and their relevance for future regional climate change. In *Climate Change 2013 the Physical Science Basis: Working Group I Contribution to the Fifth Assessment Report of the Intergovernmental Panel on Climate Change*. *Cambridge University Press* **2013**, 1217-1308.
4. IPCC, Climate change 2007: the physical science basis," in Contribution of Working Group I to the Fourth Assessment Report of the Intergovernmental Panel on Climate Change, eds S. Solomon, D. Qin, M. Manning, Z. Chen, M. Marquis, K. B. Averyt, M. Tignor and H. L. Miller (Cambridge, New York, NY: Cambridge University Press) **2007**.
5. Swindles, G. T.; Morris, P. J.; Mullan, D.; Watson, E. J.; Turner, T. E.; Roland, T. P.; Amesbury, M. J.; Kokfelt, U.; Schoning, K.; Pratte, S.; Gallego-Sala, A.; Charman, D. J.; Sanderson, N.; Garneau, M.; Carrivick, J. L.; Woulds, C.; Holden, J.; Parry, L.; Galloway, J. M. The long-term fate of permafrost peatlands under rapid climate warming. *Sci Rep* **2015,** *5*, 17951.
6. Hugelius, G.; Loisel, J.; Chadburn, S.; Jackson, R. B.; Jones, M.; MacDonald, G.; Marushchak, M.; Olefeldt, D.; Packalen, M.; Siewert, M. B.; Treat, C.; Turetsky, M.; Voigt, C.; Yu, Z. C. Large stocks of peatland carbon and nitrogen are vulnerable to permafrost thaw. *P Natl Acad Sci USA* **2020,** *117*, (34), 20438-20446.
7. Malmer, N.; Johansson, T.; Olsrud, M.; Christensen, T. R. Vegetation, climatic changes and net carbon sequestration in a North-Scandinavian subarctic mire over 30 years. *Global Change Biol* **2005,** *11*, (11), 1895-1909.
8. Xiao-Ying, J., Hui-Jun, J., Iwahana, G., Marchenko, S.S., Dong-Liang, L., Xiao-Ying, L., Si-Hai, L. Impacts of climate-induced permafrost degradation on vegetation: A review. *Advances in Climate Change Research* **2020**, *1*, (1), 29-47.
9. Olid, C.; Klaminder, J.; Monteux, S.; Johansson, M.; Dorrepaal, E. Decade of experimental permafrost thaw reduces turnover of young carbon and increases losses of old carbon, without affecting the net carbon balance. *Global Change Biol* **2020,** *26*, (10), 5886-5898.
10. McCalley, C. K.; Woodcroft, B. J.; Hodgkins, S. B.; Wehr, R. A.; Kim, E. H.; Mondav, R.; Crill, P. M.; Chanton, J. P.; Rich, V. I.; Tyson, G. W.; Saleska, S. R. Methane dynamics regulated by microbial community response to permafrost thaw. *Nature* **2014,** *514*, (7523), 478-481.
11. Woodcroft, B. J.; Singelton, C. M; Boyd, J. A.; Evans, P. N.; Emerson, J. B.; Zayed, A. A. F.; Hoelzle, R. D.; Lamberton, T. O.; McCalley, C. K.; Hodgkins, S. B.; Wilson, R. M.; Purvine, S. O.; Nicora, C. D.; Li, C.; Frolking, S.; Chanton, J. P.; Crill, P. M.; Saleska, S. R.; Rich, V. I.;

Tyson, G. W. Genome-centric view of carbon processing in thawing permafrost. *Nature* **2018,** *560*, 49-54.

12. Mackelprang, R.; Waldrop, M. P.; DeAngelis, K. M.; David, M. M.; Chavarria, K. L.; Blazewicz, S. J.; Rubin, E. M.; Jansson, J. K. Metagenomic analysis of a permafrost microbial community reveals a rapid response to thaw. *Nature* **2011,** *480*, (7377), 368-U120.
13. Turetsky, M. R.; Abbott, B.W.; Jones, M.C.; Anthony, K.W.; Olefeldt, D.; Schuur, E.A.G.; Grosse, G.; Kuhry, P.; Hugelius, G.; Koven C.; Lawrence, D.M.; Gibson, C.; Sannel, A.B.K.; McGuire, A.D. Carbon release through abrupt permafrost thaw. *Nat Geosci* **2020,** *13*, 138-143.
14. Lundin, E. J.; Klaminder, J.; Giesler, R.; Persson, A.; Olefeldt, D.; Heliasz, M.; Christensen, T. R.; Karlsson, J. Is the subarctic landscape still a carbon sink? Evidence from a detailed catchment balance. *Geophys Res Lett* **2016,** *43*, (5), 1988-1995.
15. Patzner, M. S.; Mueller, C. W.; Malusova, M.; Baur, M.; Nikeleit, V.; Scholten, T.; Hoeschen, C.; Byrne, J. M.; Borch, T.; Kappler, A.; Bryce C. Iron mineral dissolution releases iron and associated organic carbon during permafrost thaw. *Nat Commun* **2020**, *11,* 6329.
16. Mu, C. C.; Zhang, T. J.; Zhao, Q.; Guo, H.; Zhong, W.; Su, H.; Wu, Q. B. Soil organic carbon stabilization by iron in permafrost regions of the Qinghai-Tibet Plateau. *Geophys Res Lett* **2016,** *43*, (19), 10286-10294.
17. Eglinton, T. I. GEOCHEMISTRY A rusty carbon sink. *Nature* **2012,** *483*, (7388), 165-166.
18. Hodgkins, S. B.; Tfaily, M. M.; McCalley, C. K.; Logan, T. A.; Crill, P. M.; Saleska, S. R.; Rich, V. I.; Chanton, J. P. Changes in peat chemistry associated with permafrost thaw increase greenhouse gas production. *P Natl Acad Sci USA* **2014,** *111*, (16), 5819-5824.
19. Genxu, W.; Hongchang, H.; Taibin, L. The influence of freeze-thaw cycles of active layer on surface runoff in a permafrost watershed. *Journal of Hydrology* **2009,** *375*, (3-4), 438-449.
20. Olefeldt, D.; Roulet, N. T.; Bergeron, O.; Crill, P.; Bäckstrand, K.; Christensen, T. R. Net carbon accumulation of a high-latitude permafrost palsa mire similar to permafrost-free peatlands. . *Geophys Res Lett* **2012,** *39*, (3), L03501.
21. Frolking, S. E.; Bubier, J. L.; Moore, T. R.; Ball, T.; Bellisario, L. M.; Bhardwaj, A.; Carroll, P.; Crill, P. M.; Lafleur, P. M.; McCaughey, J. H.; Roulet, N. T.; Suyker, A. E.; Verma, S. B.; Waddington, J. M.; Whiting, G. J. Relationship between ecosystem productivity and photosynthetically active radiation for northern peatlands. *Global Biogeochem Cy* **1998,** *12*, 115-126.
22. Bäckstrand, K.; Crill, P. M.; Jackowicz-Korczynski, M.; Mastepanov, M.; Christensen, T. R.; Bastviken, D. Annual carbon gas budget for a subarctic peatland, Northern Sweden. . *Biogeosciences* **2010,** *7*, 95-108.
23. LaCroix, R. E.; Tfaily, M. M.; McCreight, M.; Jones, M. E.; Spokas, L.; Keiluweit, M. Shifting mineral and redox controls on carbon cycling in seasonally flooded mineral soils. *Biogeosciences* **2019,** *16*, (13), 2573-2589.
24. Chen, C.; Hall, S. J.; Coward, E.; Thompson, A. Iron-mediated organic matter decomposition in humid soils can counteract protection. *Nat Commun* **2020,** *11*, (1), 2255.

25. Gault, A. G.; Langley, S.; Ibrahim, A.; Renaud, R.; Takahashi, Y.; Boothman, C.; Lloyd, J. R.; Clark, I. D.; Ferris, F. G.; Fortin, D. Seasonal changes in mineralogy, geochemistry and microbial community of bacteriogenic iron oxides (BIOS) deposited in a circumneutral wetland. *Geomicrobiol J* **2012,** *29*, 161-172.
26. Johansson, T.; Malmer, N.; Crill, P. M.; Friborg, T.; Akerman, J. H.; Mastepanov, M.; Christensen, T. R. Decadal vegetation changes in a northern peatland, greenhouse gas fluxes and net radiative forcing. *Global Change Biol* **2006,** *12*, (12), 2352-2369.
27. Lupascu, M.; Wadham, J. L.; Hornibrook, E. R. C.; Pancost, R. D. Temperature Sensitivity of Methane Production in the Permafrost Active Layer at Stordalen, Sweden: a Comparison with Non-permafrost Northern Wetlands. *Arct Antarct Alp Res* **2012,** *44*, (4), 469-482.
28. Malmer, N. B. W. Peat Formation and Mass Balanec in Subarctic Ombrotophic Peatland around Abisko, Northern Scandinavia. . *Ecological Bulletins* **1996,** *45*, 79-92.
29. Kokfelt, U.; Rosen, P.; Schoning, K.; Christensen, T. R.; Forster, J.; Karlsson, J.; Reuss, N.; Rundgren, M.; Callaghan, T. V.; Jonasson, C.; Hammarlund, D. Ecosystem responses to increased precipitation and permafrost decay in subarctic Sweden inferred from peat and lake sediments. *Global Change Biol* **2009,** *15*, (7), 1652-1663.
30. Callaghan, T. V.; Bergholm, F.; Christensen, T. R.; Jonasson, C.; Kokfelt, U.; Johansson, M. A new climate era in the sub-Arctic: Accelerating climate changes and multiple impacts. *Geophys Res Lett* **2010,** *37*, L14705.
31. Lueder, U.; Maisch, M.; Laufer, K.; Jorgensen, B. B.; Kappler, A.; Schmidt, C. Influence of physical pertubation on Fe(II) supply in coastal marine sediments. *Environ Sci Technol* **2020,** *54*, 3209-3218.
32. Roden, E. E.; Zachara, J. M. Microbial reduction of crystalline iron(III) oxides: Influence of oxide surface area and potential for cell growth. *Environ Sci Technol* **1996,** *30*, 1618-1628.
33. Tessier, A.; Campbell, P. G.; Bisson, M. Sequential extraction procedure for the speciation of particulate trace metals. *Anal Chem* **1979** *51*, 844-851.
34. Shannon, R. D.; White, J. R. The selectivity of a squential extraction procedure for the determination of iron oxyhydroxides andiron sulfides in lake sediments. *Biogeochemistry* **1991,** *14*, 193-208.
35. Heron, G.; Crouzet, C.; Bourg, A. C.; Christensen, T. H. Speciation of Fe(II) and Fe(III) in contaminated aquifer sediments using chemical extraction techniques. *Environ Sci Technol* **1994,** *28*, 1698-1705.
36. Coward, E. K.; Thompson, A. T.; Plante, A. F. Iron-mediated mineralogical control of organic matter accumulation in tropical soils. *Geoderma* **2017,** *306*, 206-216.
37. Kaiser, K., Zech, W. Defects in estimation of aluminum in humus complexes of podzolic soils by pyrophosphate extraction. *Soil Science* **1996,** *161*, (7), 452-458.
38. Schuppli, P. A.; Ross, G. J.; McKeague, J. A. The effective removal of suspended materials from pyrophosphate extracts of soils from tropical and temperate regions. *Soil Sci Soc Am J* **1983,** *47*, 1026-1032.
39. Stookey, L. L. Ferrozine - a New Spectrophotometric Reagent for Iron. *Anal Chem* **1970,** *42*, (7), 779-781.
40. Otte, J. M.; Harter, J.; Laufer, K.; Blackwell, N.; Straub, D.; Kappler, A.; Kleindienst, S. The distribution

of active iron-cycling bacteria in marine and freshwater sediments is decoupled from geochemical gradients. *Method Enzymol* **2018,** *20*, (7), 2483-2499.
41. Ewels, P. A.; Peltzer, A.; Fillinger, S.; Patel, H.; Alneberg, J.; Wilm, A.; Garcia, M. U.; Di Tommaso, P.; Nahnsen, S. The nf-core framework for community-curated bioinformatics pipelines. *Nat. Biotechnol.* **2020,** *38*, (3), 276-278.
42. Straub, D.; Blackwell, N.; Langarica-Fuentes, A.; Peltzer, A.; Nahnsen, S.; Kleindienst, S., Interpretations of environmental microbial community studies are biased by the selected 16S rRNA (gene) amplicon sequencing pipeline. *Front Microbiol* **2020,** *11,* 550420.
43. Rinne, J. ICOS Sweden Ecosystem eco time series (ICOS Sweden), Abisko-Stordalen Palsa Bog, 2018-12-31–2019-12-31, https://hdl.handle.net/11676/s5oBzukX_FaXpHU___86QasO) **2021**.
44. Olefeldt, D.; Roulet, N. T. Effects of permafrost and hydrology on the composition and transport of dissolved organic carbon in a subarctic peatland complex. *J Geophys Res-Biogeo* **2012,** *117*, G01005.
45. Reddy, K. R.; DeLaune, R.D. Biogeochemistry of wetlands: Science and applications. *CRC Press, Boca Raton, FL.* **2008**, ISBN 978-1-56670-678-0.
46. Perryman, C. R.; McCalley, C. K.; Malhotra, A.; Florencia Fahnestock, M.; Kashi, N. N.; Bryce, J. G.; Giesler, R.; Varner, R. K. Thaw Transitions and Redox Conditions Drive Methane Oxidation in a Permafrost Peatland. *J Geophys Res-Biogeo* **2020,** *125*, (3), G005526.
47. Herndon, E. M.; Yang, Z. M.; Bargar, J.; Janot, N.; Regier, T.; Graham, D.; Wullschleger, S.; Gu, B. H.; Liang, L. Y. Geochemical drivers of organic matter decomposition in arctic tundra soils. *Biogeochemistry* **2015,** *126*, (3), 397-414.
48. Hansel, C. M.; Benner, S. G.; Fendorf, S. Competing Fe(II)-induced mineralization pathaways of ferrihydrite. *Environ Sci Technol* **2005**, (39), 7147-7153.
49. Jones, A. M.; Collins, R. N.; Waite, T. D. Redox characterization of the Fe(II)-catalyzed transformation of ferrihydrite to goethite. *Geochim Cosmochim Ac* **2017**, (218), 257-272.
50. Pedersen, H. D.; Postma, D.; Jakobsen, R.; Larsen, O. Fast transformation of iron oxhydroxides by catalytic action of aqueous Fe(II). *Geochim Cosmochim Ac* **2005**, (69), 3967-3977.
51. ThomasArrigo, L. K.; Mikutta, C.; Byrne, J.; Kappler, A.; Kretzschmar, R. Iron(II)-catalyzed iron atom exchange and mineralogical changes in iron-rich organic freshwater flocs: An iron isotope tracer study. *Environ Sci Technol* **2017**, (51), 6897-6907.
52. Yang, L.; Steefel, C.; Marcus, M. A.; Bargar, J. R. Kinetics of Fe(II)-catalyzed transformation of 6-line ferrihydrite under anaerobic flow conditions. *Environ Sci Technol* **2010**, (44), 5469-5475.
53. Chen, C., Thompson, A. Ferrous iron oxidation under varying pO2 levels: The effects of Fe(III)/Al(III) oxide minerals and organic matter. *Environ Sci Technol* **2018,** *52*, 597-606.
54. Chen, C., Thompson, A. The influence of native soil organic matter and minerals on ferroux iron oxidation. *Geochim Cosmochim Ac* **2021**, (292), 254-270.
55. Lipson, D. A.; Jha, M.; Raab, T. K.; Oechel, W. C. Reduction of iron (III) and humic substances plays a major role in anaerobic respiration in an Arctic peat soil. *J Geophys Res-Biogeo* **2010,** *115*, G00I06.

56. Lipson, D. A.; Raab, T. K.; Goria, D.; Zlamal, J. The contribution of Fe(III) and humic acid reduction to ecosystem respiration in drained thaw lake basins of the Arcitc Coastal Plain. *Global Biogeochem Cy* **2013,** *27*, 399-409.
57. Masue-Slowey, Y.; Loeppert, R. H.; Fendorf, S. Alteration of ferrihydrite reductive dissolution and transformation by adsorbed As and structural Al: Implications for As retention. *Geochim Cosmochim Ac* **2011,** *75*, (3), 870-886.
58. Coward, E. K.; Thompson, A.; Plante, A. F. Contrasting Fe speciation in two humid forest soils: Insight into organomineral associations in redox-active environments. *Geochim Cosmochim Ac* **2018,** *238*, 68-84.
59. Colmer, T. D. Long-distance transport of gaes in plants: A perspective on internal aeration and radial oxygen loss from roots. *Plant Cell Environ* **2003,** *26*, 17-36.
60. Weber, K. A.; Achenbach, L.A.; Coates, J.D. Microorganisms pumping iron: Anaerobic microbial iron oxdiation and reduction. *Nat Rev Microbiol* **2006,** *4*, 752-764.
61. Kappler, A.; Bryce, C.; Mansor, M.; Lueder, U.; Byrne, J. M.; Swanner, E. An evolving view on biogeochemical cycling of iron. *Nat Rev Microbiol* **2021**.
62. Comas, X.; Slater, L. Low-frequency electrical properties of peat. *Water Resour. Res.* **2004,** *40*, W12414.
63. Nielsen, L. P.; Risgaard-Petersen, N.; Fossing, H.; Christensen, P. B.; and Sayama, M. Electric currents couple spatially separated biogeochemical processes in marine sediment. *Nature* **2010,** *463*, 1071-1074.
64. Malvankar, N. S.; Vargas, M.; Nevin, K. P.; Franks, A. E.; Leang, C.; Kim, B. C.; Inoue, K.; Mester, T.; Covalla, S. F.; Johnson, J. P.; Rotello, V. M.; Tuominen, M. T.; Lovley, D. R. Tunable metallic-like conducitivity in microbial nanowire networks *Nat. Biotechnol.* **2011,** *6*, 573-579.
65. Regberg, A.; Singha, K.; Tien, M.; Picardal, F.; Zheng, Q.; Schieber, J.; Roden, E.; Brantley, S. L. Electrical conductivity as an indicator of iron reduction rates in abiotic and biotic systems. *Water Resour. Res.* **2011,** *47*, W04509.
66. Kato, S.; Nakamura, R.; Kai, F.; Watanbe, K.; Hashimoto, K. Respiratory interactions of soil bacteria with (semi)conductive iron-oxide minerals. *Method Enzymol* **2010,** *12*, 3114-3123.
67. Roden, E. E.; Kappler, A.; Bauer, I.; Jiang, J.; Paul, A.; Stoesser, R.; Konishi, H.; Xu, H. Extracellular electron transfer through microbial reduction of solid-phase humic substances. *Nat Geosci* **2010,** *3*, 417-421.
68. Hall, S. J.; Silver, W. L. Iron oxidation stimulates organic matter decomposition in humid tropical forest soils. *Global Change Biol* **2013,** *19*, (9), 2804-2813.
69. Trusiak, A.; Treibergs, L. A.; Kling, G. W.; Cory, R. M. The role of iron and reactive oxygen species in the production of CO2 in arctic soil waters. *Geochim Cosmochim Ac* **2018,** *224*, 80-95.
70. Wagai, R.; Mayer, L. M. Sorptive stabilization of organic matter in soils by hydrous iron oxides. *Geochim Cosmochim Ac* **2007,** *71*, (1), 25-35.
71. Kaiser, K.; Guggenberger, G. Sorptive stabilization of organic matter by microporous goethite: sorption into small pores vs. surface complexation. *Eur J Soil Sci* **2007,** *58*, (1), 45-59.
72. Herndon, E.; AlBashaireh, A.; Singer, D.; Chowdhury, T. R.; Gu, B. H.; Graham, D. Influence of iron redox cycling on organo-mineral associations in Arctic tundra soil.

Geochim Cosmochim Ac **2017,** *207*, 210-231.
73. Riedel, T.; Zak, D.; Biester, H.; Dittmar, T. Iron traps terrestrially derived dissolved organic matter at redox interfaces. *P Natl Acad Sci USA* **2013,** *110*, (25), 10101-10105.
74. IPCC: Climate Change 2013: The Physical Science Basis. Contribution of Working Group I to the Fifth Assessment Report of the Intergovern- mental Panel on Climate Change [Stocker, T.F.; Qin, D.; Plattner, G.-K.; Tignor, M.; Allen, S.-K.; Boschung, J.; Nauels, A.; Xia, Y.; Bex, V.; Midgley, P. M. (eds.)]. Cambridge University Press, Cambridge, United Kingdom and New York, NY, USA, 2013, 1535.
75. Osterkamp, T. E. Characteristics of the recent warming of permafrost in Alaska. *J Geophys Res-Biogeo* **2007,** *F02S02*.
76. Romanovsky, V. E.; Osterkamp, T.E. Effects of unfrozen water on heat and mass transport processes in the active layer and permafrost. *Permafrost Periglac* **2000,** *11*, (June), 219-239.
77. Rawlins, M. A.; Steele, M.; Holland, M. M.; Adam, J. C.; Cherry, J. E.; Francis, J. A.; Groisman, P. Y.; Hinzman, L. D.; Huntington, T. G.; Kane, D. L.; Kimball, J. S.; Kwok, R.; Lammers, R. B.; Lee, C. M.; Lettenmaier, D. P.; McDonald, K. C.; Podest, E.; Pundsack, J. W.; Rudels, B.; Serreze, M. C.; Shiklomanov, A.; Skagseth, Ø.; Troy, T. J.; Vörösmarty, C. J.; Wensnahan, M.; Wood, E. F.; Woodgate, R.; Yang, D.; Zhang, K.; Zhang, T. Analysis of the Arctic system for freshwater cycle intensification: Observations and expec- tations. *Journal of Climate* **2010,** *23*, 5715-5737.
78. Walvoord, M. A., Kurylyk, B.L., Hydrologic impacts of thawing permafrost - a review. *Vadose Zone Journal* **2016,** *15*, (6), 1-20.
79. Elberling, B.; Christiansen, H. H.; Hansen, B. U., High nitrous oxide production from thawing permafrost (vol 3, pg 332, 2010). *Nat Geosci* **2010,** *3*, (7), 506-506.
80. Van Bodegom, P. M.; Scholten, J. C. M.; Stams, A. J. M. Direct inhibition of methanogenesis by ferric iron. *FEMS Microbiology Ecology* **2004,** *49*, 261-268.
81. Kleber, M.; Eusterhues, K.; Keiluweit, M.; Mikutta, C.; Mikutta, R.; Nico, P. S., Mineral-Organic Associations: Formation, Properties, and Relevance in Soil Environments. *Adv Agron* **2015,** *130*, 1-140.
82. Totsche, K. U.; Amelung, W.; Gerzabek, M. H.; Guggenberger, G.; Klumpp, E.; Knief, C.; Lehndorff, E.; Mikutta, R.; Peth, S.; Prechtel, A.; Ray, N.; Kogel-Knabner, I., Microaggregates in soils. *J Plant Nutr Soil Sc* **2018,** *181*, (1), 104-136.
83. Asano, M.; Wagai, R. Evidence of aggregate hierarchy at micro- to submicron scales in an allophanic Andisol. *Geoderma* **2014,** *216*, 62-74.

Supplementary information for

Seasonal fluctuations of the rusty carbon sink in thawing permafrost peatlands

Monique S. Patzner[1], Nora Kainz[1], Erik Lundin[2], Maximilian Barczok[3], Chelsea Smith[4], Elizabeth Herndon[3,5], Lauren Kinsman-Costello[4], Stefan Fischer[6], Daniel Straub[7,8], Sara Kleindienst[7], Andreas Kappler[1,9] & Casey Bryce[1,10]

[1]Geomicrobiology, Center for Applied Geosciences, University of Tuebingen, Schnarrenbergstrasse 94-96, 72076 Tuebingen, Germany.
[2]Swedish Polar Research Secretariat, Abisko Scientific Research Station, Abisko, Vetenskapens väg 38, 98107 Abisko, Sweden.
[3]Department of Geology, Kent State University, Kent, OH, 44242, US.
[4]Department of Biological Sciences, Kent State University, Kent, OH, 44242, US.
[5]Environmental Sciences Division, Oak Ridge National Laboratory, 1 Bethel Valley Rd, Oak Ridge, TN 37830.
[6]Tuebingen Structural Microscopy Core Facility, Center for Applied Geosciences, University Tuebingen, Schnarrenbergstrasse 94-96, 72076 Tuebingen, Germany
[7]Microbial Ecology, Center for Applied Geosciences, University Tuebingen, Schnarrenbergstrasse 94-96, 72076 Tuebingen, Germany.
[8]Quantitative Biology Center (QBiC), University Tuebingen, Auf der Morgenstelle 10, 72076 Tuebingen, Germany.
[9]Cluster of Excellence: EXC 2124: Controlling Microbes to Fight Infection, Tuebingen, Germany.
[10]School of Earth Sciences, University of Bristol, Bristol, UK.

Manuscript submitted for publication to: *Environmental Science & Technology*

Synthesis of Ferrihydrite-coated Sand

Quartz sand with a grain size of 0.4-0.8 mm (Carl Roth GmbH + Co.KG, Germany) was used. The sand was pre-treated by first autoclaving the sand at 121°C for 20 minutes, followed by 1 M HCl washing (24 h, completely covered) and finally with Aqua Regia for 5 min to further improve Fe coating efficiency by increasing the surface area, as has been done previously[1, 2]. Afterwards the sand was washed with MiliQ water and dried at 60°C.

The Fe(III) oxyhydroxide 2-line ferrihydrite (FH) was synthesized in the presence of the sand by precipitation from a $Fe(NO_3)_3$*$9H_20$ solution by adding 1 M KOH. The $Fe(NO_3)_3$*$9H_20$ solution was added to 500 g of sand and stirred manually by hand as KOH was added dropwise until a pH of 7.3 was reached. The mixture was then left without stirring. After two hours, the pH was readjusted to 7.5 and the mixture left overnight on a rolling shaker (15 rpm), as has been done previously[1]. Finally, the mixture was washed with MiliQ water and dried at 40°C to avoid temperature-induced modifications of the precipitates[1].

In the end, the fresh synthesized ferrihydrite-coated sand yielded an iron content of 2.19±0.35 mg poorly crystalline Fe(III) per g sand, determined by 0.5 M HCl extraction, performed in triplicates, followed by Fe quantification in the extract by Ferrozine assay[3]. Treating the unexposed sand in the same manner as the exposed sand (transport to the field and back, during exposure time stored at room temperature), formed a more crystalline Fe(III) phase (1.01±0.14 mg Fe(III) per g sand), which was only extractable by 6 M HCl, not extractable with 1 M Na-acetate and 0.5 M HCl. As also previously stated[1], the FH coating increased the specific surface area (SSA) from 0.07 m^2 per g of the initial pure sand to 1.49 m^2 per g of the FH-coated sand (21 times higher than for its uncoated precursor).

Exposure Bags

The FH-coated sand was packed in teflon bags (polytetrafluoroethylene (PTFE); or Teflon®) with 0.1 mm thickness and manually pierced with needles of 0.55 mm diameter under sterile conditions in a Biological Safety Cabinet (BSC). The bag was closed with a cable tie at the top and with a long, red plastic line, which was later used to mark the position of the bag at the surface and pull it out after exposure. The teflon along with additional equipment (FH coated sand, cable ties) was autoclaved (121°C, 1 bar pressure, 20 mins) prior to use, brought into the BSC cabinet and exposed to UV-light for 15 minutes. The teflon was chosen based on the following suitable properties: heat (up to 250°C) and cold (till -196°C) resistant; unaffected by most chemicals, especially iron; no adhesive forces and weather resistant[4, 5].

The bags filled with ferrihydrite-coated sand were stored at room temperature in sterile plastic bags and transported to the field under sterile conditions.

Sequential Fe Extraction

0.5 g of homogenized sand of each exposed exposure bag in triplicates was added under anoxic conditions (100% N_2, remaining O_2 <100 ppm) into Eppendorf tubes. As previously described[6], samples were centrifuged (5 min, 12,000 g) and the porewater (supernatant) was removed. 1 mL of anoxic 1 M Na-acetate solution was added to the pellet, mixed and incubated for 24 h in the dark. Then, the sample was centrifuged (5 min, 12,000 g) and the supernatant was collected and stored anoxically in the dark at 4°C until further analysis. To the pellet, 1 mL of anoxic 0.5 M HCl was added, mixed and incubated in the dark under anoxic conditions for 2 h. After centrifugation again, the supernatant was removed and stored anoxically at 4°C until further analysis. To the remaining pellet, 1 mL of anoxic 6 M HCl was added, mixed and incubated for 24 h in the dark as the last extraction step[6]. The supernatant was again stored under anoxic conditions in the dark at 4°C until further analysis.

Scanning Electron Microscopy (SEM) and Energy Dispersive X-Ray Analysis (EDS)

The sand of the control (unexposed FH-coated sand) and the FH bags exposed for two months along the permafrost thaw gradient (thaw stages: palsa, bog and fen) were anoxically dried (24 h, 100% N_2 atmosphere). After reaching constant weight, the dried sand was pressed in an indium band (Plano GmbH, article number: E432), specifically chosen to avoid a carbon background signal in the EDS analysis. The indium band was then glued to the SEM sample stub with conductive silver paint (ACHESON Silver DAG 141; Plano GmbH, article number: G3692). After a brief drying time, the samples were immediately coated with ~8 nm Pt-layer using a BAL-TEC SCD 500 sputter coater, operated in a working distance of 35 mm, for 90 seconds at 0.02 mbar. SEM and EDS analysis were performed at the Center for Applied Geosciences, University Tuebingen, using a Zeiss Crossbeam 550L Cryo-FIB-SEM, equipped with an Oxford EDS detector (UltimMax 100) and AZtecEnergy Advanced software. SEM images were acquired at a working distance of 5mm by use of the Secondary Electrons Secondary Ions (SESI) detector using an acceleration voltage of 30 kV during the EDS analysis session and at 5 kV (for images about surface information) with a 39x, 250x and 650x magnification and a store resolution of 2048 pixel image width. Four replicates per sample were analyzed.

The EDS analysis was performed at a working distance of 5mm, with a probe current of 200pA, 2048 channels, process time 6, Acquisition mode: Live time and Acquisition time of 470 live seconds.

Microbial Community Analysis

After using the PowerSoil® RNA and DNA isolation kit, DNA samples were eluted in 50 μl RNase/DNase-Free water. DNA concentrations were determined using a Qubit® 2.0 Fluorometer with DNA HS kit (Life Technologies, Carlsbad, CA, USA). Quantitative PCR (qPCR) specific for the 16S rRNA (gene) of bacteria and archaea was performed as described previously[7]. Microbial 16S rRNA (genes) were amplified using primers 515F and 806R[8]. Quality and quantity of the purified amplicons were determined using agarose gel electrophoresis and Nanodrop (NanoDrop 1000, Thermo Scientific, Waltham, MA, USA). Subsequent library preparation steps (Nextera, Illumina) and sequencing were performed by Microsynth AG (Switzerland) using the 2 × 250 bp MiSeq Reagent Kit v2 on an Illumina MiSeq sequencing system (Illumina, San Diego, CA, USA). From 113,554 to 151,092 (average 135,126) read pairs were generated per sample. Quality control, reconstruction of 16S rRNA (gene) sequences and taxonomic annotation was performed with nf-core/ampliseq v1.1.2[9, 10] with Nextflow v20.10.0[11] using containerized software with singularity v3.4.2[12]. Primers were trimmed, and untrimmed sequences were discarded (< 13%, on average 9.6%) with Cutadapt v2.6[13]. Adapter and primer-free sequences were imported into QIIME2 version 2019.10.0[14], processed with DADA2 version 1.10.0[15] to eliminate PhiX contamination, trim reads (before the median quality drops below 38, i.e. position 137 in forward reads and 194 in reverse reads), correct errors, merge read pairs, and remove PCR chimeras; ultimately, in total 937 amplicon sequencing variants (ASVs) were obtained across all samples. Alpha rarefaction curves were produced with the QIIME2 diversity alpha-rarefaction plugin, which indicated that the richness of the samples had been fully observed. A Naive Bayes classifier was fitted with 16S rRNA (gene) sequences extracted with the PCR primer sequences from the QIIME compatible, 99%-identity clustered SILVA v132 database[16]. ASVs were classified by taxon using the fitted classifier[17]. 45 ASVs that classified as chloroplasts or mitochondria were removed, totalling to < 0.5% (average 0.36%) relative abundance per sample, and the remaining 892 ASVs had their abundances extracted by feature-table (https://github.com/qiime2/q2-feature-table).

DNA extraction was only successful for the long-term exposed bags in the fully-thawed fen.

To identify the isolated Fe(III)-reducing bacteria, DNA was extracted of the isolated culture (after ten transfers) using the UltraClean® Microbial DNA Isolation Kit (MO BIO Laboratories,

Carlsbad, CA, US). Then, 16S rRNA gene fragments were amplified using the 341F (CCTACGGGAGGCAGCAG) and 907R (CCGTCAATTCCTTTRAGTTT) primer pair and resulting amplicons were sent for Sanger sequencing (Eurofins GATC biotech, Konstanz, Germany). Sequence results (deposited at database) were analyzed using nucleotide Basic Local Alignment Search Tool (BLAST) to identify the closest relative (performed on the 20th of April 2021, algorithm: blastn, standard database: nucleotide collection (nr/nt), accession number: Y19190.1; see also Figure S5).

Redox Potential Analysis

Redox potential at redox potential probes was recorded every 30 seconds by a datalogger (CR1000, Campbell Scientific) and averaged over 10 minutes. For this study, the reported values at each time point represent the average (± standard error) of values recorded at 6, 8, and 10 cm. In the bog and fen, the values across the two probes were averaged. Redox potential was referenced to two Ag^0/AgCl reference electrodes deployed within the bog and fen. Retrieved data were adjusted to the standard hydrogen electrode (SHE) by adding 213 mV to the recorded values as recommended by the provider company (PaleoTerra).

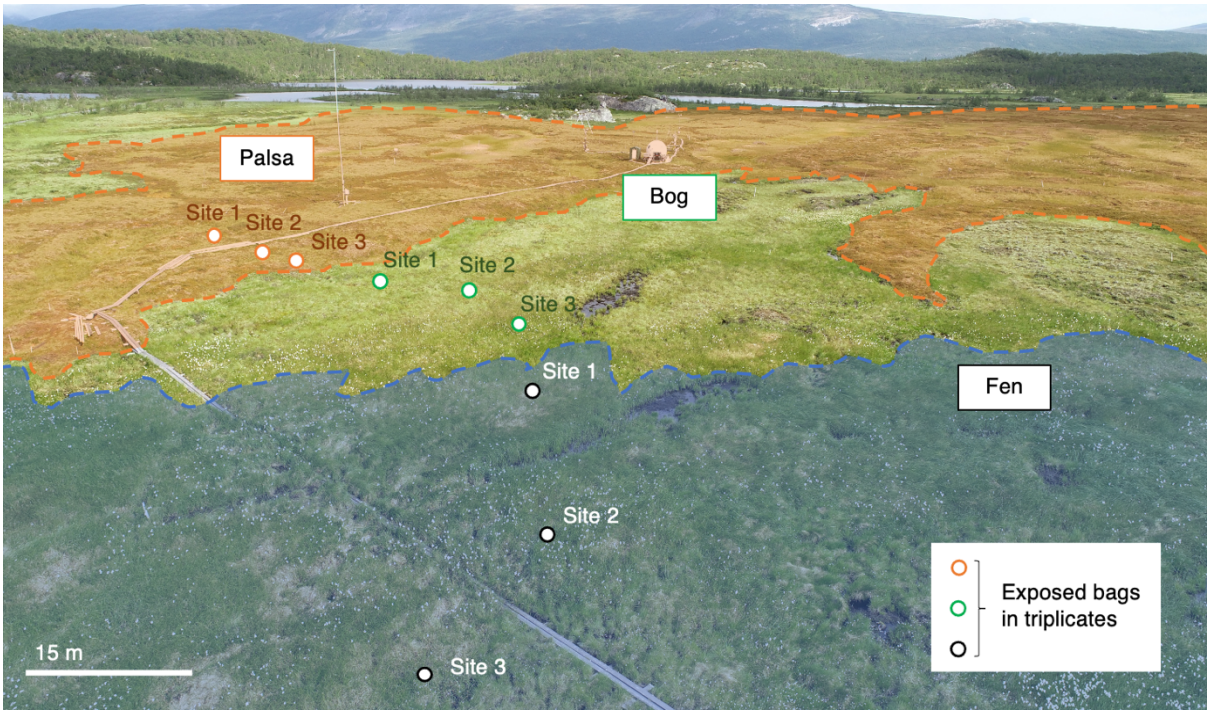

Figure S1. Sites for exposure of the bags with ferrihydrite-coated sand along the thaw gradient from palsa (intact) to bog (partially-thawed) to fen (fully-thawed) at Stordalen mire, Abisko (Sweden). *Orange background marks the palsa, green the bog and blue the fen areas. At each thaw stage (palsa: 68°21'18.91"N, 19° 2'38.02"E to 68°21'18.78"N, 19° 2'39.18"E, bog: 68°21'18.86"N 19° 2'39.94"E to 68°21'18.35"N, 19° 2'40.39"E, fen: 68°21'18.01"N, 19° 2'40.08"E to 68°21'17.38"N, 19° 2'38.99"E), three sites were chosen following the hydrology flow[18]. For the short-term exposure, we exposed 3 replicate bags of ferrihydrite-coated sand for 2 weeks during early summer (9 bags per thaw stage in total). For the longer-term exposure of 2 months, triplicate bags were exposed at the centered positions of each thaw stage to capture conditions characteristic for each thaw stage: palsa site 1, bog site 2 and fen site 2, resulting in three replicate bags per thaw stage.*

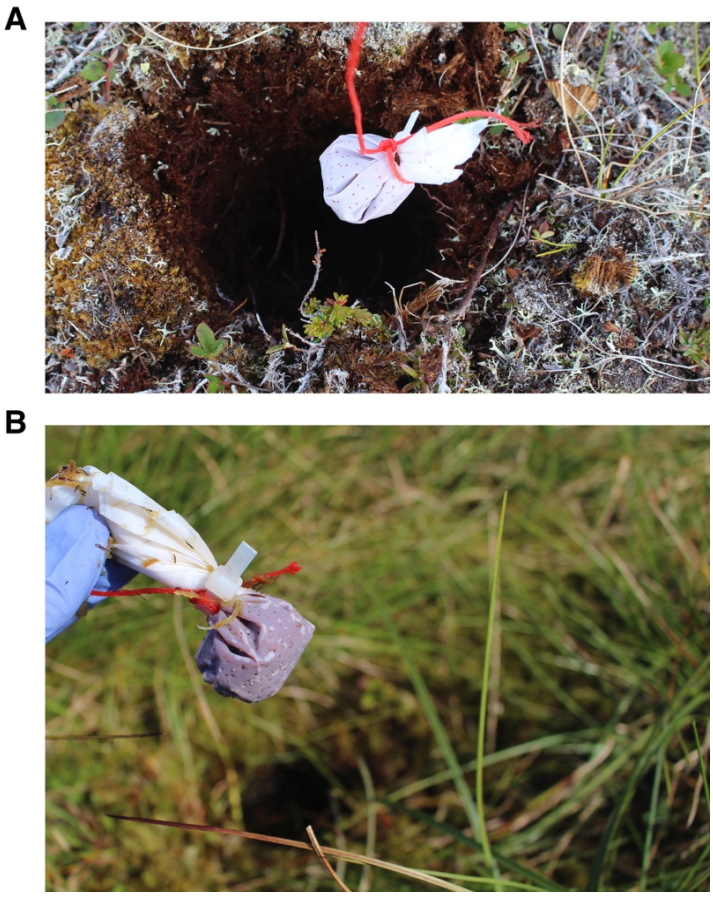

Figure S2. Examples of ferrihydrite-coated sand in teflon bags exposed in intact palsa (A) and fully-thawed fen (B). *Each bag was placed at 10 cm depth and the hole was re-sealed with the soil layer which had been removed.*

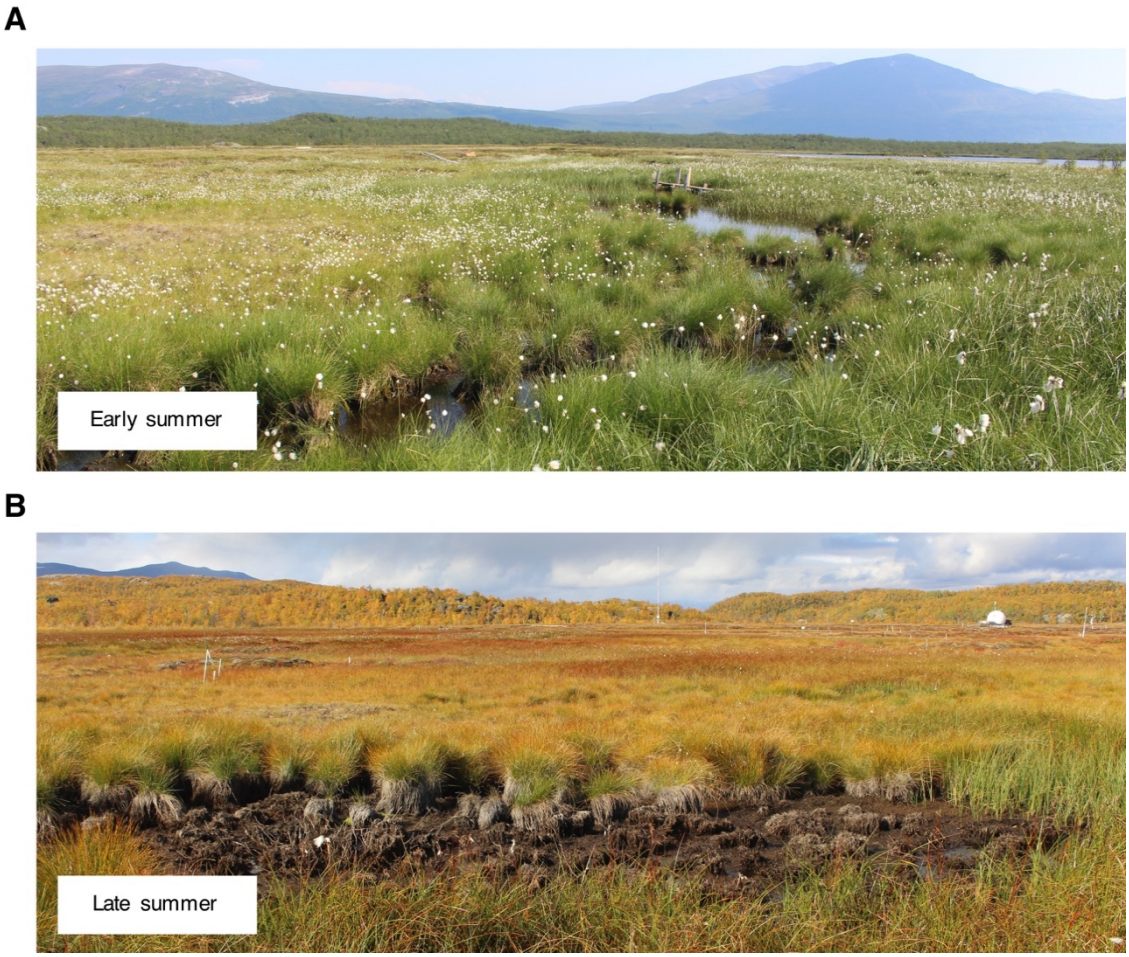

Figure S3. Seasonal changes at Stordalen mire in early summer (A) and late summer (B). *In early summer, the semi-wet bog and waterlogged fen areas were completely water-saturated. During summer, bog areas became drier due to increasing drainage caused by active layer deepening and decreasing volumetric soil water content in the upper 10 cm.*

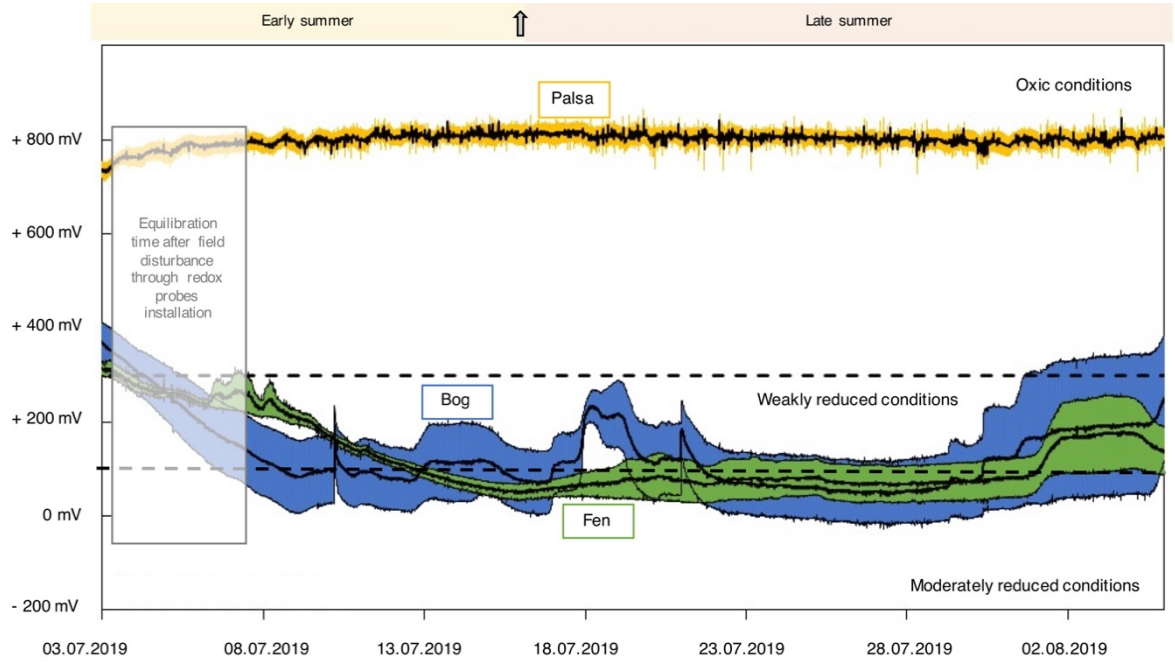

Figure S4. Redox potential along the thaw gradient. Black lines report the average redox potential [mV] and the colored areas represent the standard deviation across the three depths at 6, 8 and 10 cm in each thaw stage. *The redox potential measured in palsa is marked in yellow, in bog in blue and in fen in green. The first 1-2 days represent the equilibrium phase after installing the redox probes in the field. Values above +300 mV are considered as oxic conditions. Values of +300 mV to +100 mV are considered as weakly reduced and values of +100 to -100 mV as moderately reducing conditions[19]. Towards August, the redox potential in bog increases from 0 mV to above +300 mV which marks a potential shift from Fe(III)-reducing to Fe(II)-oxidizing conditions. Unfortunately, the redox probes disconnected from the battery in mid-August and remote data collection ceased.*

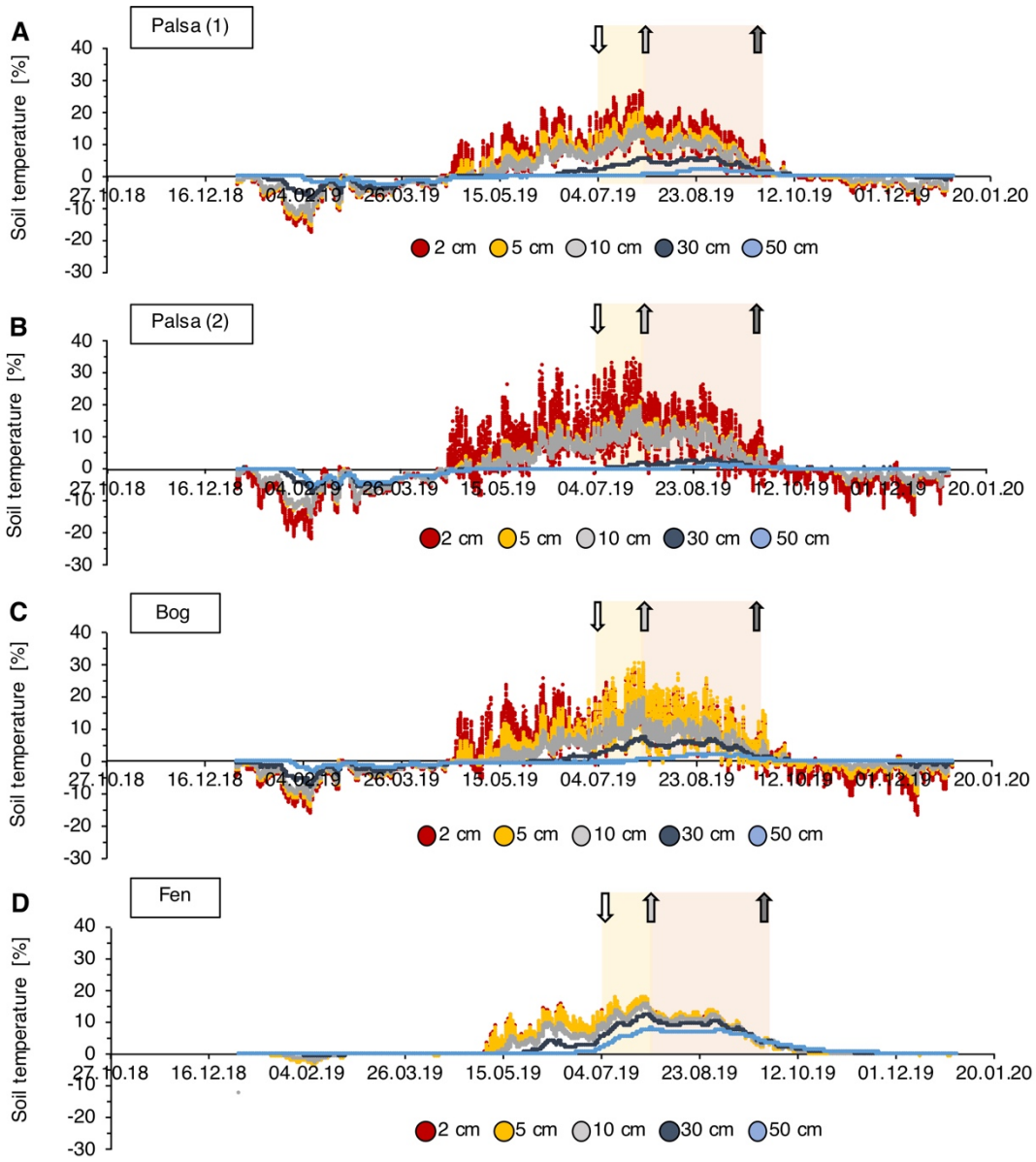

Figure S5. Soil temperatures at each thaw stage at 2 cm, 5 cm, 10 cm, 30 cm and 50 cm soil depth: (A) palsa (replicate 1; 68°21'22.25"N, 19° 2'42.22"E), (B) palsa (replicate 2; 68°21'21.05"N, 19° 2'38.85"E), (C) bog (68°21'20.49"N, 19° 2'45.52"E) and (D) fen (68°21'20.20"N, 19° 2'42.37"E) in the year 2019[20].

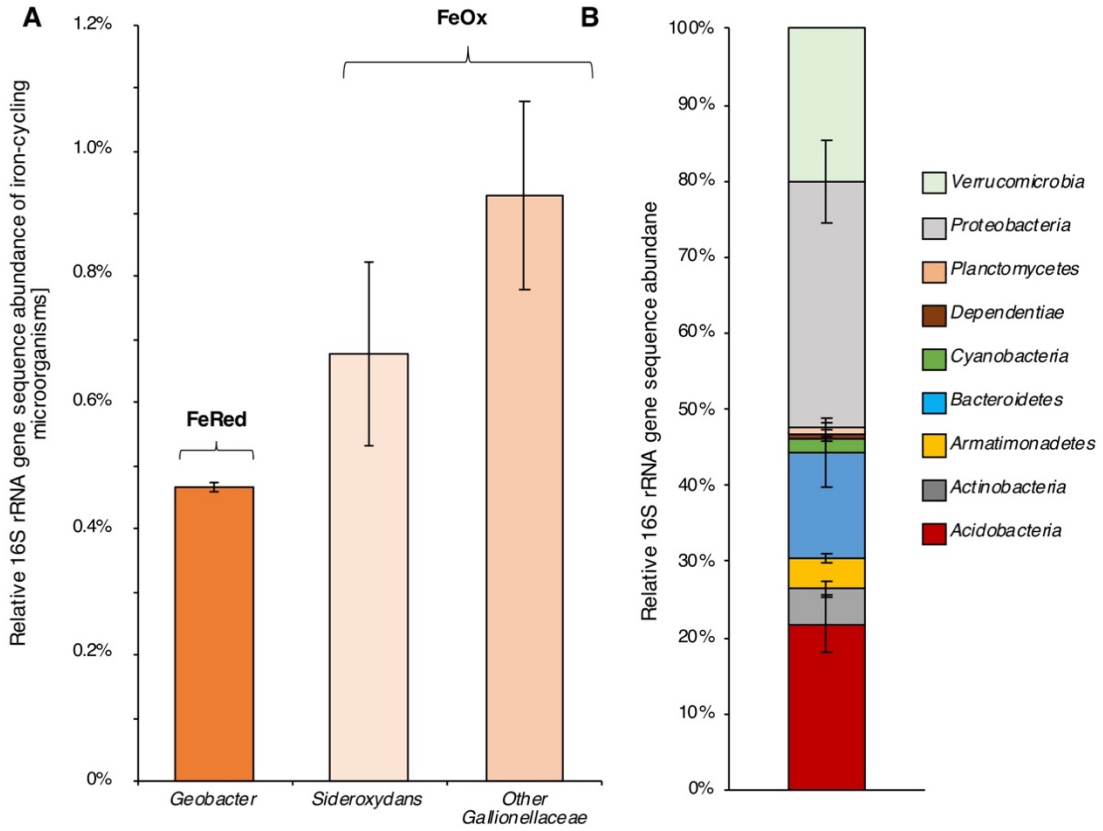

Figure S6. Microbial community of ferrihydrite-coated sand exposed for 2 months in the fully-thawed fen till late summer. *(A) Detected microbial iron-metabolizing key players: Fe(III)-reducing bacteria (FeRed) and Fe(II)-oxidizing bacteria (FeOx). (B) Present microbial community. Values and error bars represent average and standard deviation of triplicate 16S rRNA gene amplicon sequencing abundance analysis of ferrihydrite-coated sand exposed in fully-thawed fen from early to late summer.*

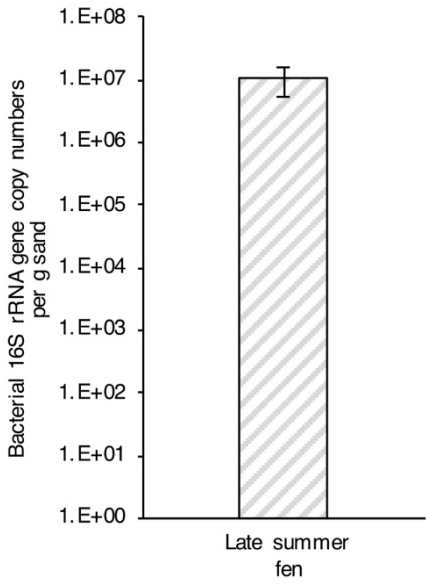

Figure S7. Bacterial 16S rRNA gene copy numbers based on qPCR analysis of the ferrihydrite-coated sand exposed for 2 months in the fully-thawed fen till late summer.

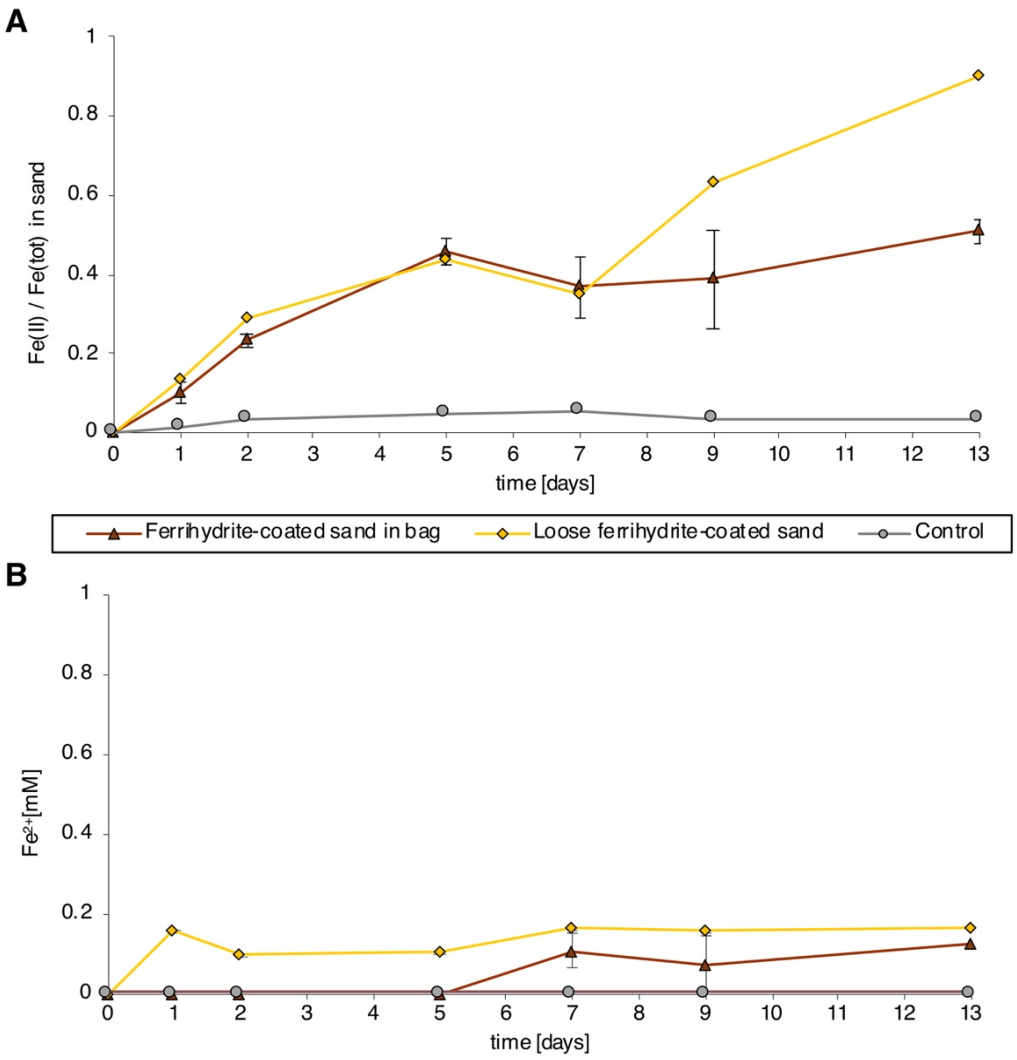

Figure S8. Microbial Fe(III) reduction under lab conditions in loose ferrihydrite-coated sand versus ferrihydrite-coated sand in teflon bags. *(A) Fe(II)/Fe(tot) ratio in sand over 13 days in anoxic fresh water media, containing 5 mM acetate, 2 mM cysteine and inoculated with Geobacter metallidurans (10^8 cells/mL). Reported values represent the average and range of duplicates of each setup. Yellow shows the Fe(II)/Fe(tot) ratio during reduction of loose ferrihydrite-coated sand over time. Brown shows the Fe(II)/Fe(tot) ratio in setups with ferrihydrite-coated sand in teflon bags over time. Control represents data for incubation of loose ferrihydrite-coated sand without Geobacter metallidurans inoculum. An Fe(II)/Fe(tot) ratio of 1 means 100% Fe(II) formation in the sand phase. (B) Only low concentrations of dissolved Fe^{2+} (below 0.2 mM) were present in the liquid phase.*

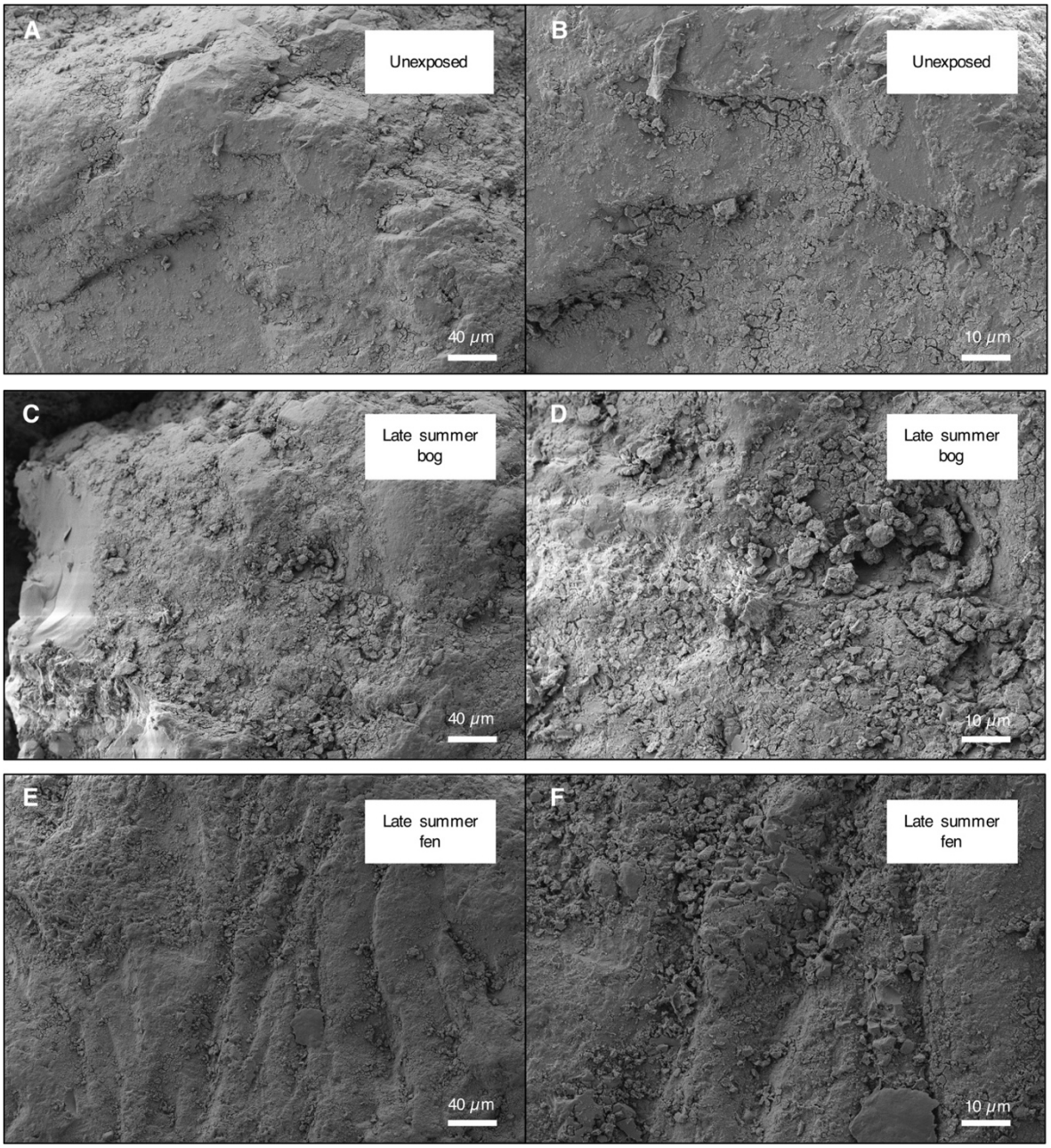

Figure S9. Scanning electron microscopy surface analysis of the ferrihydrite-coated sands before and after exposure. *Unexposed sand shows smooth surfaces and small aggregate formation on the sand grains: (A) overview image and (B) close up image of unexposed sand. Ferrihydrite-coated sand exposed for 2 months till late summer in the partially-thawed bog shows aggregate formation on the surface of the sand grains: (C) overview image and (D) close up image of sand exposed for 2 months till late summer in the partially-thawed bog (replicate analysis to Figure 4 shown in the main text). Ferrihydrite-coated sand exposed for 2 months till late summer in the fully-thawed fen shows aggregate formation on the sand grains surface: (E) overview image and (F) close up image of sand exposed till late summer in the fully-thawed fen.*

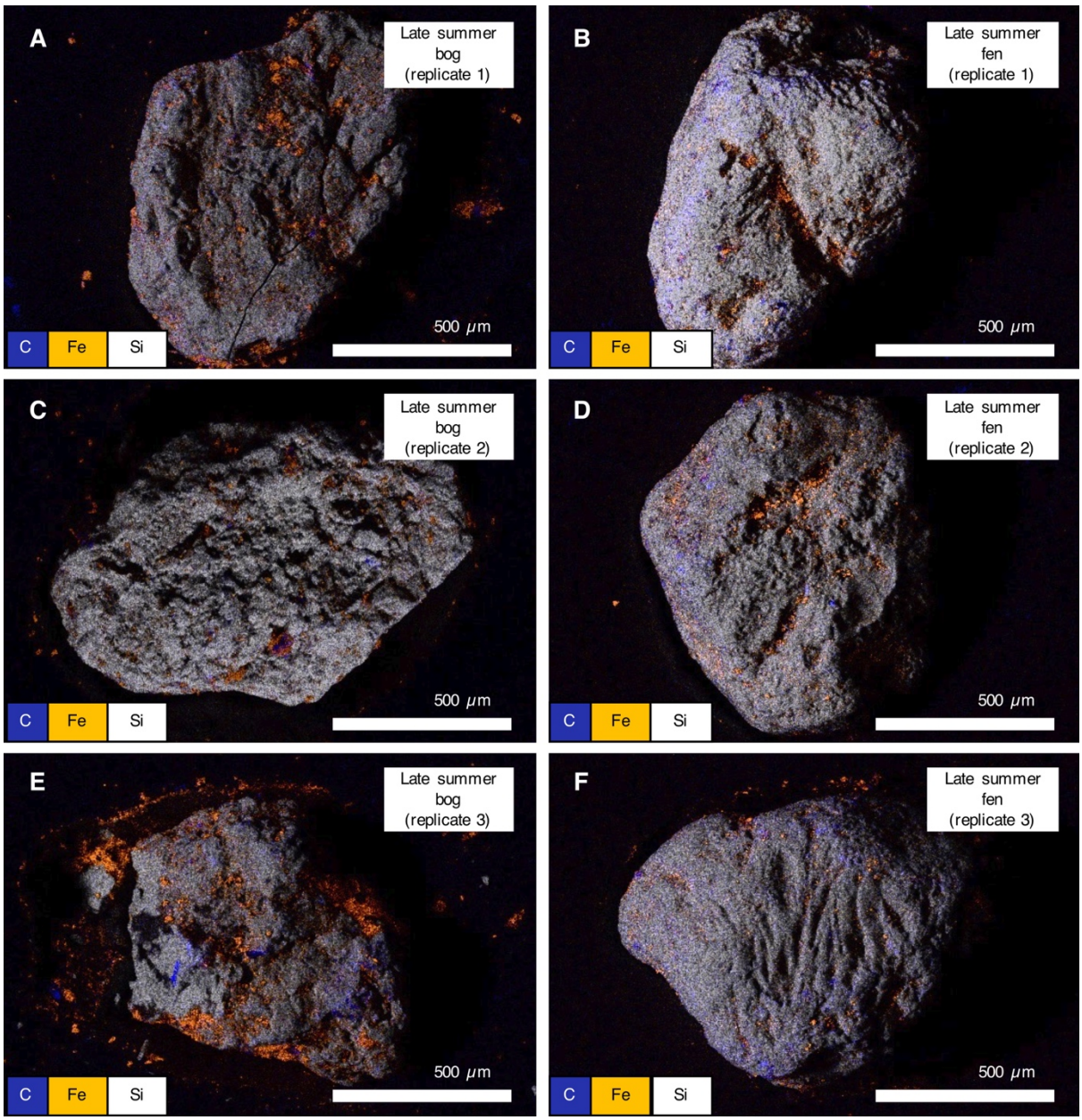

Figure S10. EDS derived chemical distribution maps of the replicate analysis of iron (Fe)-organic carbon (OC) associations at the surface of the ferrihydrite-coated sand grains exposed in partially-thawed bog and fully-thawed fen collected after exposure for 2 months till late summer: (A) and (B) replicate 1, (C) and (D) replicate 2, (E) and (F) replicate 3.

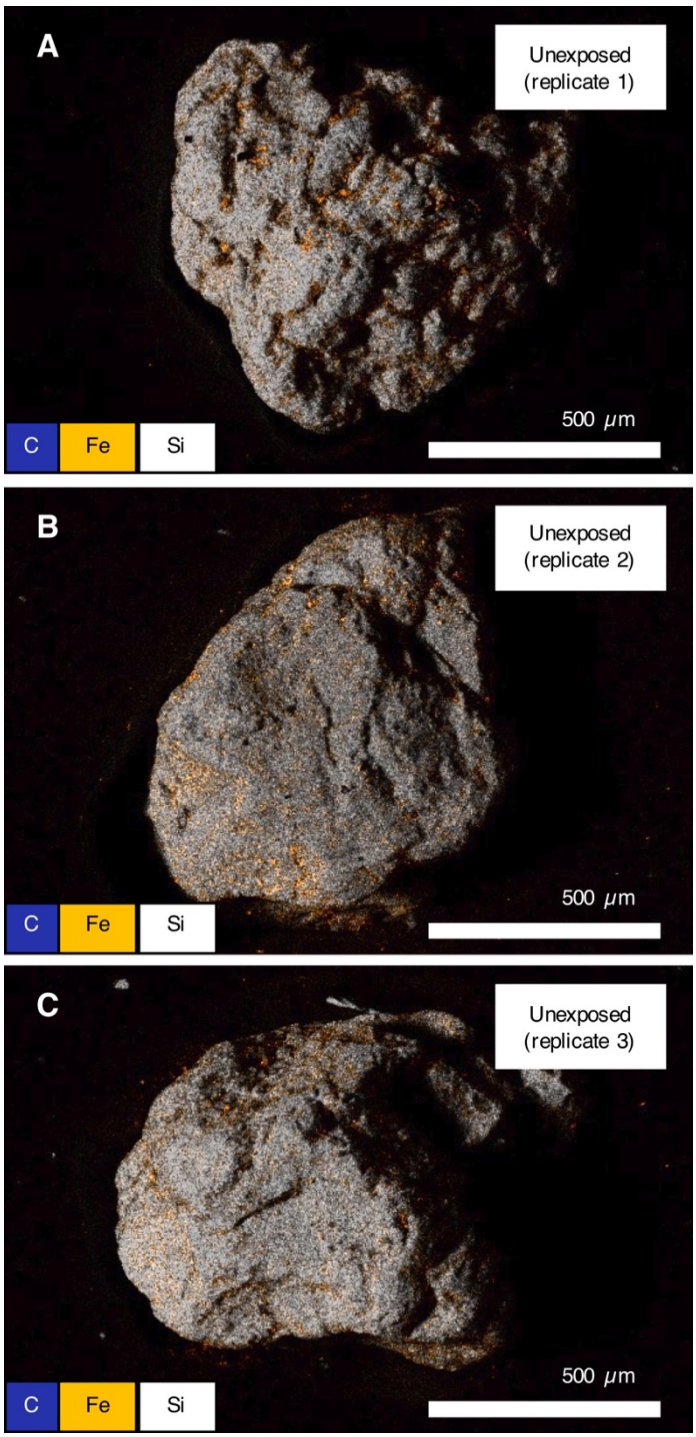

Figure S11. EDS derived chemical distribution maps of iron (Fe) coating on unexposed ferrihydrite-coated sand grains: (A) replicate 1, (B) replicate 2 and (C) replicate 3.

Table S1. Organic carbon (OC) to iron (Fe) ratios in the active layer of the partially thawed bog and in the fully-thawed fen collected after exposure of 2 months till late summer.

		Sodium pyrophosphate extractable OC and Fe	**Total extractable OC and Fe**
		OC/Fe (wt:wt)	TOC/totalFe (wt:wt)
Late summer	Bog	11.70	0.42
	Fen	2.03	0.96
		OC/Fe (molar ratio)	TOC/total Fe (molar ratio)
Late summer	Bog	54.41	1.96
	Fen	9.46	4.47

References

1. Sorwat, J.; Mellage, A.; Kappler, A.; Byrne J. M. Immobilizing magnetite onto quartz sand for chromium remediation. *Journal of Hazardous Materials* **2020,** *400,* 123139.
2. Kango, S.; Kumar, R. Magnetite nanoparticles coated sand for arsenic removal from drinking water. *Environ Earth Sci* **2016,** *75*, (5), 381.
3. Stookey, L. L. Ferrozine - a New Spectrophotometric Reagent for Iron. *Anal Chem* **1970,** *42*, (7), 779-781.
4. Biswas, S.; Vijayan, K. Friction and wear of ptfe - a review. *Wear* **1992,** *158*, 193-211.
5. Buerkle, M.; Asai, Y. Thermal conductance of teflon and polyethylene: insight from an atomistic, single-molecule level. *Sci Rep* **2017,** *7,* 41898 .
6. Lueder, U.; Maisch, M.; Laufer, K.; Jorgensen, B.B.; Kappler, A.: Schmidt, C. Influence of physical pertubation on Fe(II) supply in coastal marine sediments. *Environ Sci Technol* **2020,** *54*, 3209-3218.
7. Otte, J. M.; Harter, J.; Laufer, K.; Blackwell, N.; Straub, D.; Kappler, A.; Kleindienst, S., The distribution of active iron-cycling bacteria in marine and freshwater sediments is decoupled from geochemical gradients. *Method Enzymol* **2018,** *20*, (7), 2483-2499.
8. Caporaso, J. G.; Kuczynski, J.; Stombaugh, J.; Bittinger, K.; Bushman, F. D.; Costello, E. K.; Fierer, N.; Pena, A. G.; Goodrich, J. K.; Gordon, J. I.; Huttley, G. A.; Kelley, S. T.; Knights, D.; Koenig, J. E.; Ley, R. E.; Lozupone, C. A.; McDonald, D.; Muegge, B. D.; Pirrung, M.; Reeder, J.; Sevinsky, J. R.; Tumbaugh, P. J.; Walters, W. A.; Widmann, J.; Yatsunenko, T.; Zaneveld, J.; Knight, R. QIIME allows analysis of high-throughput community sequencing data. *Nat Methods* **2010,** *7*, (5), 335-336.
9. Ewels, P. A.; Peltzer, A.; Fillinger, S.; Patel, H.; Alneberg, J.; Wilm, A.; Garcia, M. U.; Di Tommaso, P.; Nahnsen, S. The nf-core framework for community-curated bioinformatics pipelines. *Nat Biotechnol* **2020,** *38*, (3), 276-278.
10. Straub, D.; Blackwell, N.; Langarica-Fuentes, A.; Peltzer, A.; Nahnsen, S.; Kleindienst, S. Interpretations of environmental microbial community studies are biased by the selected 16S rRNA (gene) amplicon sequencing pipeline. *Front Microbiol* **2020,** *11*, 550420.
11. Di Tommaso, P.; Chatzou, M.; Floden, E. W.; Barja, P. P.; Palumbo, E.; Notredame, C. Nextflow enables reproducible computational workflows. *Nat Biotechnol* **2017,** *35*, (4), 316-319.
12. Kurtzer, G. M.; Sochat, V.; Bauer, M. W. Singularity: Scientific containers for mobility of compute. *PLoS One* **2017,** *12*, (5), e0177459.
13. Martin, M. Cutadapt removes adapter sequences from high-throughput sequencing reads. *EMBnet journal* **2011,** *17*, (1), 3.
14. Bolyen, E.; Rideout, J. R.; Dillon, M. R.; Bokulich, N. A.; Abnet, C. C.; Al-Ghalith, G. A.; Alexander, H.; Alm, E. J.; Arumugam, M.; Asnicar, F.; Bai, Y.; Bisanz, J. E.; Bittinger, K.; Brejnrod, A.; Brislawn, C. J.; Brown, C. T.; Callahan, B. J.; Caraballo-Rodríguez, A. M.; Chase, J.; Cope, E. K.; Da Silva, R.; Diener, C.; Dorrestein, P. C.; Douglas, G. M.; Durall, D. M.; Duvallet, C.; Edwardson, C. F.; Ernst, M.; Estaki, M.; Fouquier, J.; Gauglitz, J. M.; Gibbons, S. M.; Gibson, D. L.; Gonzalez, A.; Gorlick, K.; Guo, J.; Hillmann, B.; Holmes, S.; Holste, H.; Huttenhower, C.; Huttley, G. A.; Janssen, S.; Jarmusch, A. K.;

Jiang, L.; Kaehler, B. D.; Kang, K. B.; Keefe, C. R.; Keim, P.; Kelley, S. T.; Knights, D.; Koester, I.; Kosciolek, T.; Kreps, J.; Langille, M. G. I.; Lee, J.; Ley, R.; Liu, Y. X.; Loftfield, E.; Lozupone, C.; Maher, M.; Marotz, C.; Martin, B. D.; McDonald, D.; McIver, L. J.; Melnik, A. V.; Metcalf, J. L.; Morgan, S. C.; Morton, J. T.; Naimey, A. T.; Navas-Molina, J. A.; Nothias, L. F.; Orchanian, S. B.; Pearson, T.; Peoples, S. L.; Petras, D.; Preuss, M. L.; Pruesse, E.; Rasmussen, L. B.; Rivers, A.; Robeson, M. S., 2nd; Rosenthal, P.; Segata, N.; Shaffer, M.; Shiffer, A.; Sinha, R.; Song, S. J.; Spear, J. R.; Swafford, A. D.; Thompson, L. R.; Torres, P. J.; Trinh, P.; Tripathi, A.; Turnbaugh, P. J.; Ul-Hasan, S.; van der Hooft, J. J. J.; Vargas, F.; Vázquez-Baeza, Y.; Vogtmann, E.; von Hippel, M.; Walters, W.; Wan, Y.; Wang, M.; Warren, J.; Weber, K. C.; Williamson, C. H. D.; Willis, A. D.; Xu, Z. Z.; Zaneveld, J. R.; Zhang, Y.; Zhu, Q.; Knight, R.; Caporaso, J. G. Reproducible, interactive, scalable and extensible microbiome data science using QIIME 2. *Nat Biotechnol* **2019,** *37*, (8), 852-857.

15. Callahan, B. J.; McMurdie, P. J.; Rosen, M. J.; Han, A. W.; Johnson, A. J.; Holmes, S. P. DADA2: High-resolution sample inference from Illumina amplicon data. *Nat Methods* **2016,** *13*, (7), 581-3.
16. Pruesse, E.; Quast, C.; Knittel, K.; Fuchs, B. M.; Ludwig, W.; Peplies, J.; Glockner, F. O. SILVA: a comprehensive online resource for quality checked and aligned ribosomal RNA sequence data compatible with ARB. *Nucleic Acids Res* **2007,** *35*, (21), 7188-96.
17. Bokulich, N. A.; Kaehler, B. D.; Rideout, J. R.; Dillon, M.; Bolyen, E.; Knight, R.; Huttley, G. A.; Gregory Caporaso, J. Optimizing taxonomic classification of marker-gene amplicon sequences with QIIME 2's q2-feature-classifier plugin. *Microbiome* **2018,** *6*, (1), 90.
18. Olefeldt, D.; Roulet, N. T. Effects of permafrost and hydrology on the composition and transport of dissolved organic carbon in a subarctic peatland complex. *J Geophys Res-Biogeo* **2012,** *117,* G01005.
19. Reddy, K. R.; DeLaune, R.D. Biogeochemistry of wetlands: Science and applications. *CRC Press, Boca Raton, FL.* **2008**, ISBN 978-1-56670-678-0.
20. Rinne, J., ICOS Sweden Ecosystem eco time series (ICOS Sweden), Abisko-Stordalen Palsa Bog, 2018-12-31–2019-12-31, https://hdl.handle.net/11676/s5oBzukX_FaXpHU___86QasO) **2021**.

Chapter 5 – Personal contribution

The original hypothesis was formulated by myself, Prof. Dr. C.W. Mueller, Dr. C. Bryce and Prof. Dr. A. Kappler. H. Joss and I designed the project together with Dr. C. Bryce and Prof. Dr. A. Kappler. H. Joss conducted the analyses in the laboratory under my supervision and wrote the original draft of the manuscript with my guidance. Prof. Dr. C.W. Mueller collected and provided the permafrost soil samples and conducted the nanoSIMS analysis. M. Maisch performed the Mössbauer analysis.

Chapter 5

Cryoturbation leads to iron-organic carbon associations along a permafrost soil chronosequence in northern Alaska

Hanna Joss[1], **Monique S. Patzner[1]**, Markus Maisch[1], Carsten W. Mueller[2,3], Andreas Kappler[1,4], Casey Bryce[1,5]

[1]Geomicrobiology, Center for Applied Geoscience, University of Tuebingen, Germany.
[2]Research Department Ecology and Ecosystem Management, Chair of Soil Science, Technical University of Munich, Freising-Weihenstephan, Germany.
[3]Department of Geosciences and Natural Resource Management, University of Copenhagen, Denmark.
[4]Cluster of Excellence: EXC 2124: Controlling Microbes to Fight Infection, Tuebingen, Germany.
[5]School of Earth Sciences, University of Bristol, UK.

Manuscript submitted for publication to: *Geoderma*

Abstract

In permafrost soils, substantial amounts of organic carbon (OC) are potentially protected from microbial degradation and transformation into greenhouse gases by the association with reactive iron (Fe) minerals. One predicted outcome, as permafrost environments respond to climate change, is the drainage of thaw lakes on which soils subsequently develop. However, the role and extent of Fe-OC associations in future OC stabilization during soil development is unknown. To fill this knowledge gap, we have examined Fe-OC associations in organic, cryoturbated and mineral horizons along a chronosequence of drained thaw lake basins in Utqiaġvik, Alaska, covering 5500 years of soil development by combining selective chemical extractions, spectroscopic and nanoscale analyses. We found that in cryoturbated horizons, on average ~17 % of the total OC content is associated with reactive Fe minerals, compared to ~10 % in organic or mineral horizons. As soil development advances, the total stocks of Fe-associated OC more than double within the first 50 years after thaw lake drainage, because of increased storage of Fe-associated OC in cryoturbated horizons (from 8 to 75 % of the total Fe-associated OC stock). Our results suggest that differences in Fe-OC associations between soil horizons lead to differences in stored Fe-associated OC between soils of different age. Spatially-resolved nanoscale secondary ion mass spectrometry (NanoSIMS) analysis showed that OC is primarily associated with Fe(III) (oxyhydr)oxides which were identified by ^{57}Fe Mössbauer spectroscopy analysis as ferrihydrite. High OC:Fe mass ratios (>0.22) determined by chemical extractions indicate that Fe-OC associations are formed via co-precipitation, chelation and aggregation. These results imply that, given the proposed enhanced drainage of thaw lakes under climate change, OC can be increasingly incorporated and stabilized by the association with reactive Fe minerals as a result of soil formation and increased cryoturbation.

Introduction

Increasing soil temperatures induced by climate change are accelerating permafrost thaw. Since permafrost soils store approximately 1035±150 Pg organic carbon (OC) in the upper 3 m (Hugelius et al., 2014), rapid warming could potentially unlock vast amounts of OC and stimulate release of greenhouse gases to the atmosphere. Thermokarst landscapes are assumed to be most vulnerable to abrupt changes in a warming climate (Walter Anthony et al., 2018; Turetsky et al., 2020). They cover around 20 % of the northern permafrost region and are estimated to store around 30 % of the total OC (TOC) present in the upper 3 m of the circumpolar permafrost region (Olefeldt et al., 2016). As in other arctic lowland regions, thermokarst lakes are the dominating landscape feature of northern Alaska and follow a general thaw lake cycle (Grosse, Jones and Arp, 2013; Hinkel et al., 2003). Lakes form by thermokarst processes and drain due to e.g. ice-wedge or coastal erosion. After drainage, terrestrial soils develop in the drained thermokarst lake basins on the remaining sediments and ice-wedge growth continues which potentially reforms lakes. It is assumed that the reformation of thaw lakes will be absent in the future, due to insufficient ice wedge growth (Fuchs et al., 2019) which disrupts the thaw lake cycle and promotes the ongoing soil development on drained thaw lake basins. The soils developing on these thermokarst lake basins are increasingly influenced by cryoturbation which redistributes relatively young OC from the topsoil into deeper soil layers and contributes on average 55% to the soil OC density in the active layer and the near-permafrost surface in permafrost soils from Alaska (Bockheim, 2007).

Previous studies on permafrost soils have intensively focused on the decomposition of the stored OC (Schädel et al., 2016; Estop-Aragones et al., 2020; Hopple et al., 2020), whereas only a few have focused on the stabilization mechanisms of OC which can mitigate the permafrost carbon feedback (Osterkamp and Romanovsky, 1999; Schuur et al., 2015; Mu et al., 2016; Mueller et al., 2017; Mu et al., 2020; Prater et al., 2020; Wang et al., 2020; Patzner et al., 2020). In soils, the fate of OC is determined by an interplay of various physical, chemical and biological components (Lehmann et al., 2020). The accessibility of OC for microorganisms is reduced by physical protection within soil aggregates and by interactions with minerals that stabilize OC via sorption, co-precipitation or aggregation (Kaiser and Guggenberger, 2000; Wagai and Mayer, 2007; Kögel-Knabner et al., 2008; von Lützow et al., 2008; Hemingway et al., 2019).

Reactive iron (Fe) minerals (defined as those reductively dissolvable by sodium dithionite, e.g. Fe(III) (oxyhydr)oxides) are particularly important for the stabilization of OC in various environments (Lalonde, Ouellet and Gélinas, 2012; Zhao et al., 2016; Shields et al., 2016; Coward, Thompson and Plante, 2017), whereas Fe-OC associations in organic rich soils of high latitude regions are less well studied. Recent studies point towards a significant proportion of reactive Fe associated OC in permafrost soils (Herndon et al., 2017; Mu et al., 2016; Mu et al., 2020; Sowers et al., 2020; Patzner et al., 2020). In the permafrost soil chronosequence of drained thaw lake basins in northern Alaska we have studied, Mueller et al.(2015) found the oldest OC fraction directly associated with minerals, especially with Fe (oxyhydr)oxides (Mueller et al., 2017; Mueller, Steffens and Buddenbaum, 2020). This highlights the potential of reactive Fe minerals in the stabilization of OC over thousands of years in thermokarst regions (Kögel-Knabner et al., 2008; Mueller et al., 2015).

Despite the recognized role of reactive Fe minerals in the association with OC in permafrost soils, very little is known about the long-term development of Fe-OC associations especially in thermokarst regions. In order to address this knowledge gap, we quantified Fe-OC associations of soil cores from drained thaw lake basins spanning 5500 years of soil development by using selective chemical extractions. We further identified the reactive Fe minerals involved in the association with OC in different soil horizons and soil development stages along the chronosequence with ^{57}Fe-specific Mössbauer spectroscopy. This was complemented by visually highlighting spatial Fe-OC associations in soil horizons using correlative scanning electron microscopy and nanoscale secondary ion mass spectrometry. This approach allows us to evaluate biogeochemical drivers of Fe-OC associations along the soil profile and during progressive soil development after thaw lake drainage.

Material and Methods

Sampling and soil properties

Permafrost soil cores along a chronosequence of drained thaw lake basins near Utqiaġvik in northern Alaska were collected in April 2010 during the sampling campaign described in Mueller et al. (2015). Based on vegetation succession and ^{14}C data, the soil chronosequence is classified into distinct age classes covering young (0-50 years), medium (50-300 years), old (300-2000 years) and ancient (2000-5500 years) drained basins (Hinkel et al., 2003). Briefly, four soil cores of each age class were collected using an 80-150 cm long corer from the Snow, Ice, Permafrost Research Establishment (SIPRE) with 7.5 cm diameter attached to a Big Beaver earth drill apparatus (Little Beaver, US). Samples were transported within 8 h to a cold room in Utqiaġvik where soil description followed. The frozen cores were cut with a chop saw into corresponding soil horizons and subsamples were oven-dried at 60°C for further analysis. Within our study, two soil cores of each age class were analyzed from locations spanning from 71°12´ to 71°16´ N in latitude and 156°25´ to 156°39´W longitude (Figure SI 1). These soil cores were selected based on the core depth and on soil horizons to capture soil profiles representative for the individual age classes (informed by Mueller et al. (2015)). The selected soil cores along the chronosequence differ in maximum core length (sampled soil depth) ranging from 90 to 126 cm and reach the permafrost layer at around 30 to 50 cm depth (Figure 1). Soil cores of the young age class show little to no cryoturbation and are mainly dominated by one organic horizon followed by mineral horizons. The abundance of soil horizons with indications of cryoturbated soil material increases with the age of the drained thaw lake basins. Buried horizons are combined with, and referred to as, cryoturbated horizons in the following discussion as they both lead to a redistribution of organic material into deeper soil layers.

Selective extractions

Soil horizons of two soil cores representative of each age class were selectively extracted to quantify different Fe mineral phases and the associated OC (Cornell and Giovanoli, 1988; Mehra and Jackson, 1960). To prepare for the chemical extractions, glass vials were washed with 1 M HCl, rinsed with deionized water and sterilized for 4.5 h at 180°C. Oven-dried soil samples (0.15±0.05 g) were weighed into glass vials in duplicates and degassed with N_2 prior to extraction. To target poorly crystalline and crystalline Fe(III) (oxyhydr)oxides (in the following considered as the total extractable Fe), samples were extracted anoxically in the dark over 24 h at 70°C with 3.125 mL of a 6 M HCl solution (Pehkonen, 1995; Foucher et al., 2000; Peltier, Dahl and Gaillard, 2005; Rutledge et al., 2010; Porsch and Kappler, 2011).

In parallel, a dithionite-citrate bicarbonate extraction was carried out to selectively extract reactive Fe minerals (defined here as reductively dissolvable by dithionite-citrate extraction) such as ferrihydrite, goethite, lepidocrocite, akaganeite and hematite nanoparticles (Mehra and Jackson, 1960; Raiswell, Canfield and Berner, 1994; Cornell and Schwertmann, 2003; Coward, Thompson and Plante, 2017). This extraction also allows for the quantification of OC that is mobilized during the reductive dissolution of reactive Fe minerals (in the following referred to as Fe-associated OC) (Lalonde, Ouellet and Gélinas, 2012; Mu et al., 2016; Mu et al., 2020; Patzner et al., 2020). We followed the dithionite-citrate extraction which is performed for 16 h on a rolling shaker under room temperature and anoxically in the dark (Coward, Thompson and Plante, 2017; Wagai and Mayer, 2007; Wagai et al., 2013) and combined different approaches to account for potential difficulties when using this extraction method as previously discussed in detail by Patzner et al. (2020) and shortly discussed in the following. Due to the instability of dithionite in solution (Varadachari, Goswami and Ghosh, 2006), powdered dithionite was added to the sample to reach a final concentration of 0.1 M by adding 3.125 mL of a 0.27 M trisodium citrate, 0.11 M sodium bicarbonate solution (pH 7, N_2:CO_2 (90:10, v:v) headspace). Sodium bicarbonate was used as a buffer (pH 7) to prevent hydrolysis and re-sorption of organic matter under acidic pH. Fisher et al. (2020) showed that under neutral pH, the dithionite-citrate extraction only partially dissolves reactive Fe minerals, thus leading to an underestimation of the amount of reactive Fe minerals in the analyzed soil cores. Trisodium citrate was used as a complexing agent to prevent re-precipitation of the mobilized Fe and sorption of OC (Mehra and Jackson, 1960). A pre-test carried out under the same conditions (pH, ionic strength) showed that without citrate, 43.5±17.6 % less reactive Fe and 37.2±4.4 % less reactive Fe-associated OC was obtained in an organic horizon of a medium aged soil core (Table SI 1). To account for effects of soil drying on reactive Fe minerals and Fe-associated OC, comparable permafrost soil material from a desiccating palsa in northern Sweden (Patzner et al., 2020) was dried under anoxic and oxic conditions at room temperature and 60°C. We obtained similar reactive Fe and Fe-associated OC contents by the dithionite-citrate extraction method for all drying techniques (Table SI 2).

To also account for the OC which is readily desorbed from the sample and not directly associated with reactive Fe minerals, a 1.85 M sodium chloride (NaCl), 0.11 M sodium bicarbonate solution (pH 7, N_2:CO_2 (90:10, v:v) headspace) was performed as control extraction under the same conditions as the dithionite-citrate extraction (Table SI 3) (Lalonde, Ouellet and Gélinas, 2012; Patzner et al., 2020). It has to be noted that the NaCl control extraction was shown to also extract OC that was weakly bound to reactive Fe minerals (Fisher et al., 2020). As the OC quantified by the NaCl control extraction is subtracted from the OC

mobilized by the dithionite-citrate extraction, the amount of Fe-associated OC is likely underestimated.

Geochemical analyses

The supernatant from the selective extractions was obtained by centrifugation (10 min, 13 400 rpm) and subsequently analyzed for total Fe (6 M HCl extractable) and reactive Fe (dithionite-citrate extractable) using the ferrozine assay (Stookey, 1970) following the protocol from Hegler et al. (2008). Briefly, to quantify total Fe, 80 μL of hydroxylamine-HCl were incubated for 30 min with 20 μL of the supernatant which was diluted in 1 M HCl beforehand. The dilution of samples ensured that the initial brownish color of the supernatant, resulting from OC, did not interfere with the spectrophotometric quantification. 100 μL of ferrozine was then added, the solution was mixed and incubated for 5 min to allow for the spectrophotometric quantification at 562 nm. Subsequently, reactive Fe contents were calculated by subtracting the Fe readily mobilized during the NaCl control extraction.

OC in the supernatant of the selective extractions and in the trisodium citrate-bicarbonate solution (citrate background) was analyzed by combustion at 750°C (Elemental analyzer, multi N/C 2100S, Analytik Jena GmbH, Germany). The Fe-associated OC was calculated by subtracting the OC background from the trisodium citrate-bicarbonate solution and the NaCl control extraction. As a consequence of the high OC background imposed by the use of citrate, Fe-associated OC could not be quantified in four soil horizons (young 1: 56-82 and 82-117 cm, ancient 1: 87-116 cm and ancient 2: 34-50 cm), however the amount of Fe-associated OC was typically high and detectable in most samples.

The TOC content of horizons in soil cores from drained thaw lake basins was previously analyzed in the study of Mueller et al. (2015). Briefly, sample material was ground with a ball mill and measured in duplicates via dry combustion (Vario MAX CNS Analyzer, Elementar, Hanau, Germany). The measured carbon contents represent the TOC content due to absence of carbonates.

Stocks of reactive Fe and associated OC (Eq. 1) were calculated based on content, bulk density (BD) and layer thickness of the horizons in each soil core (Table SI 3).

$$Stock\ [kg\ m^{-2}] = content\ [mg\ g^{-1}] * BD\ [g\ cm^{-3}] * layer\ thickness\ [m] \qquad (1)$$

To account for differences along the permafrost soil chronosequence, reactive Fe and associated OC stock of same horizons (organic, cryoturbated or mineral) within one soil core

were summed up and averaged between replicate soil cores of one age class to represent the average total sum present in distinct soil horizons within one age class.

Fe mineralogy and spectroscopic analysis

To identify the mineralogy of the reactive Fe minerals potentially involved in the association with OC, ^{57}Fe-specific Mössbauer spectroscopy was applied. Prior to Mössbauer analysis, dried sample material from organic, cryoturbated and mineral horizons of two endmember soil cores (young, ancient) was mortared and loaded into plexiglass holders (1 cm^2), forming a thin film of sample material. Plexiglass holders were tightly closed with parafilm and transmission spectra were collected at 77 K and 5 K using a constant acceleration drive system (WissEL) in transmission mode with a ^{57}Co/Rh source. All spectra were calibrated against a 7 μm thick α-^{57}Fe foil that was measured at 295 K. Sample analysis was carried out using Recoil (University of Ottawa) and the Voigt Based Fitting (VBF) routine (Rancourt & Ping, 1991). The half width at half maximum was constrained to 0.124 mm s^{-1} during fitting.

For visualizing Fe-OC associations with correlative scanning electron microscopy (SEM) and nanoscale secondary ion mass spectrometry (NanoSIMS) analysis, the deepest horizon of an intact frozen soil core (medium 2, Figure 1) was chemically fixed, dried over an acetone row and subsequently impregnated with Araldite 502 (Araldite kit 502, electron microscope sciences, Hatfield, USA). The impregnated soil core was sectioned and polished (see details in Mueller et al. (2017)). Prior to SEM analysis (Jeol JSM 5900LV, Freising, Germany) in backscatter electron mode and NanoSIMS analysis, the intact cross section was gold-coated by physical vapor deposition under argon atmosphere to circumvent possible charging effects. The NanoSIMS measurements were recorded at the Cameca NanoSIMS 50 L (Gennevilliers, France) of the Lehrstuhl für Bodenkunde, TU München, Germany. Electron multiplier secondary ion collectors were used for $^{12}C^{14}N^-$, $^{27}Al^{16}O^-$ and $^{56}Fe^{16}O^-$. Prior to analysis, impurities and the coating layer were sputtered away by using a high primary beam current and charging during the measurements was compensated by an electron beam generated by the electron flood gun of the NanoSIMS instrument (Mueller et al., 2013). The NanoSIMS data was analyzed using the Look@NanoSIMS plugin for MatLab (Polerecky et al., 2012), images were corrected for detector dead time and drift corrected.

Statistical analysis

An analysis of variance (ANOVA) was applied to identify differences between soil age classes, combined with a post-hoc test to identify age classes that are different from another. Whenever normal distribution or homogeneity of variances was not given, a non-parametric Kruskal Wallis test was performed. For correlation analysis of non-normally distributed data, p-values (p) and correlation coefficients (r) are given for a Spearman (p_s and r_s) correlation. Additionally, linear regressions (R^2) were calculated to identify relationships between reactive Fe and associated OC across age classes.

Results and Discussion

Changes in reactive Fe and associated OC along the soil chronosequence

Greater differences in reactive Fe and associated OC between soil horizons than with depth

Contents of reactive Fe and associated OC did not show a clear trend with depth, but were significantly different between soil horizons across the soil profiles ($p < 0.001$, Kruskall Wallis test) (Figure 2, Figure 3). Reactive Fe contents were highest in organic horizons (10 to 60 mg g^{-1} DW-$soil^{-1}$) with a significantly higher content compared to cryoturbated ($p < 0.001$, 5 to 20 mg g^{-1} DW-$soil^{-1}$) and mineral horizons ($p < 0.001$, 2 to 20 mg g^{-1} DW-$soil^{-1}$) (Figure 2, Figure 3). Cryoturbated horizons incorporate, in comparison to directly over- or underlying mineral horizons, higher amounts of reactive Fe (Figure 2, even though overall differences in reactive Fe between cryoturbated and mineral horizons were not significant.

Horizons with elevated contents of reactive Fe in comparison to over- or underlying horizons were also identified to overlay the permafrost table (Figure 1), subject to annual freeze/thaw cycles that experience fluctuations in redox conditions. At such redox interfaces, Fe(III) (oxyhydr)oxides are assumed to be effectively recycled forming poorly crystalline Fe minerals (Moormann and van Breemen, 1978) which counteracts the crystallization of reactive Fe minerals with time. Even though Chen et al. (2020) postulated the formation of more crystalline Fe minerals under redox fluctuations due to oxygen limitation, the association with high amounts of OC, as found in affected soil horizons, impede the crystallization of reactive Fe minerals (Schwertmann, 1966). Additionally, Fe(II) which is reduced in deeper, anoxic soil layers migrates upwards and subsequently is oxidized by oxygen and precipitates as Fe(III) (oxyhydr)oxides (Liang et al., 1993; Herndon et al., 2015). This likely explains highest contents and percentages (as % of total Fe) of reactive Fe found in organic horizons in our soil cores (~100% reactive Fe of the total Fe, Figure SI 2).

In accordance to other studies from the same region, we also find highest amounts of poorly crystalline Fe minerals (represented here as reactive Fe) in organic horizons (Herndon et al., 2017) and overall higher amounts of reactive Fe compared to other permafrost regions (Mu et al., 2016; Patzner et al., 2020).

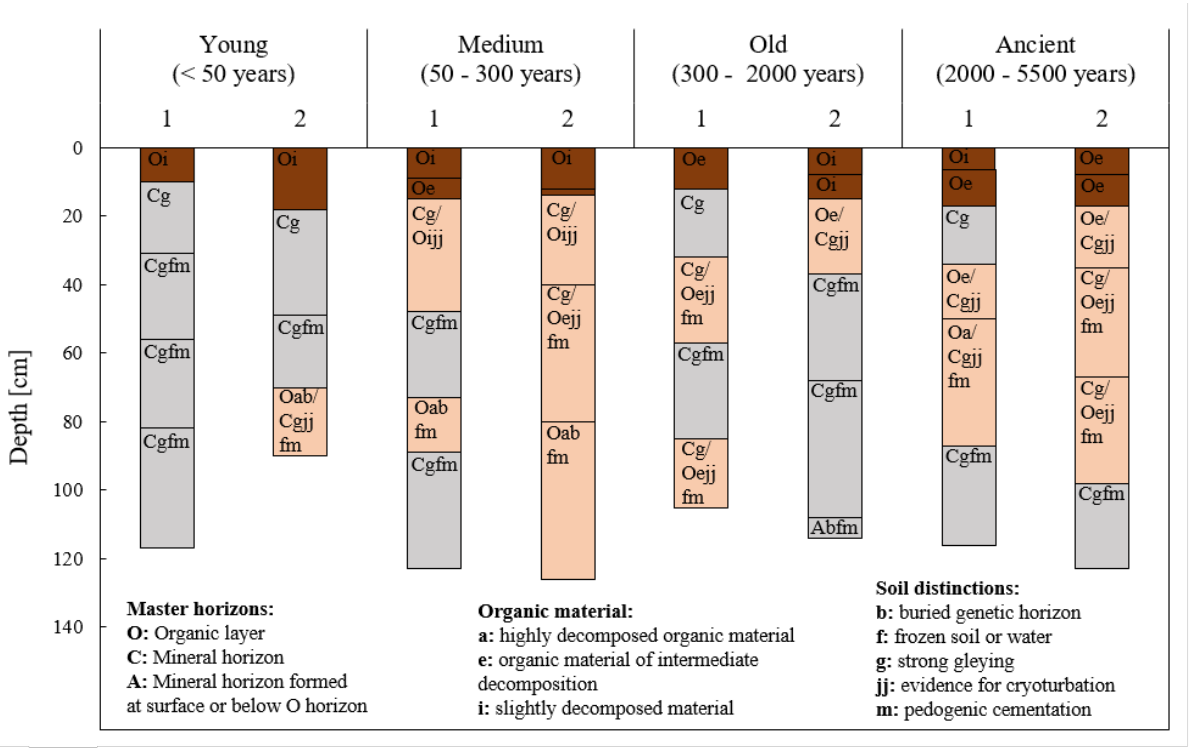

Figure 1. Classification according to Mueller et al. (2015) and description of soil horizons of replicate soil cores of the four different age classes. *Abbreviations assigned to the distinct soil horizons are described below the figure. Colors indicate organic horizons (brown), cryoturbated/buried horizons (beige) and mineral horizons (grey).*

Fe-associated OC contents were also highest in organic horizons (20 to 80 mg g^{-1} DW-$soil^{-1}$) and are significantly different from cryoturbated ($p < 0.001$, 0 to 40 mg g^{-1} DW-$soil^{-1}$) and mineral horizons ($p < 0.001$, 0 to 25 mg g^{-1} DW-$soil^{-1}$) (Figure 2, Figure 3). It has to be noted that TOC contents were also greatest in organic horizons (Figure SI 2). In deeper soil layers, significantly elevated contents of Fe-associated OC were found in cryoturbated horizons in comparison to mineral horizons ($p = 0.025$). This can be explained by the introduction of OC into deeper soil layers by cryoturbation (Figure SI 2).

Cryoturbation redistributes mostly young, undecomposed OC into deeper soil layers (Ping et al., 1998), as was also shown by ^{14}C analysis for the same permafrost soil samples (Mueller et al., 2015). The relocated OC in cryoturbated horizons was furthermore characterized to be more bioavailable compared to over- or underlying mineral horizons as indicated by O-N/alkyl C to alkyl C ratios obtained by NMR spectroscopy (Mueller et al., 2015). Thus, it can be assumed that easily available OC is associated with reactive Fe minerals as the Fe-associated OC constitutes a large proportion of the TOC in cryoturbated horizons. Also, similar amounts of Fe-associated OC are present in other permafrost regions (Mu et al., 2016; Patzner et al.,

2020), whereas Fe-associated OC contents could be underestimated as a result of the NaCl control extraction (Fisher et al., 2020).

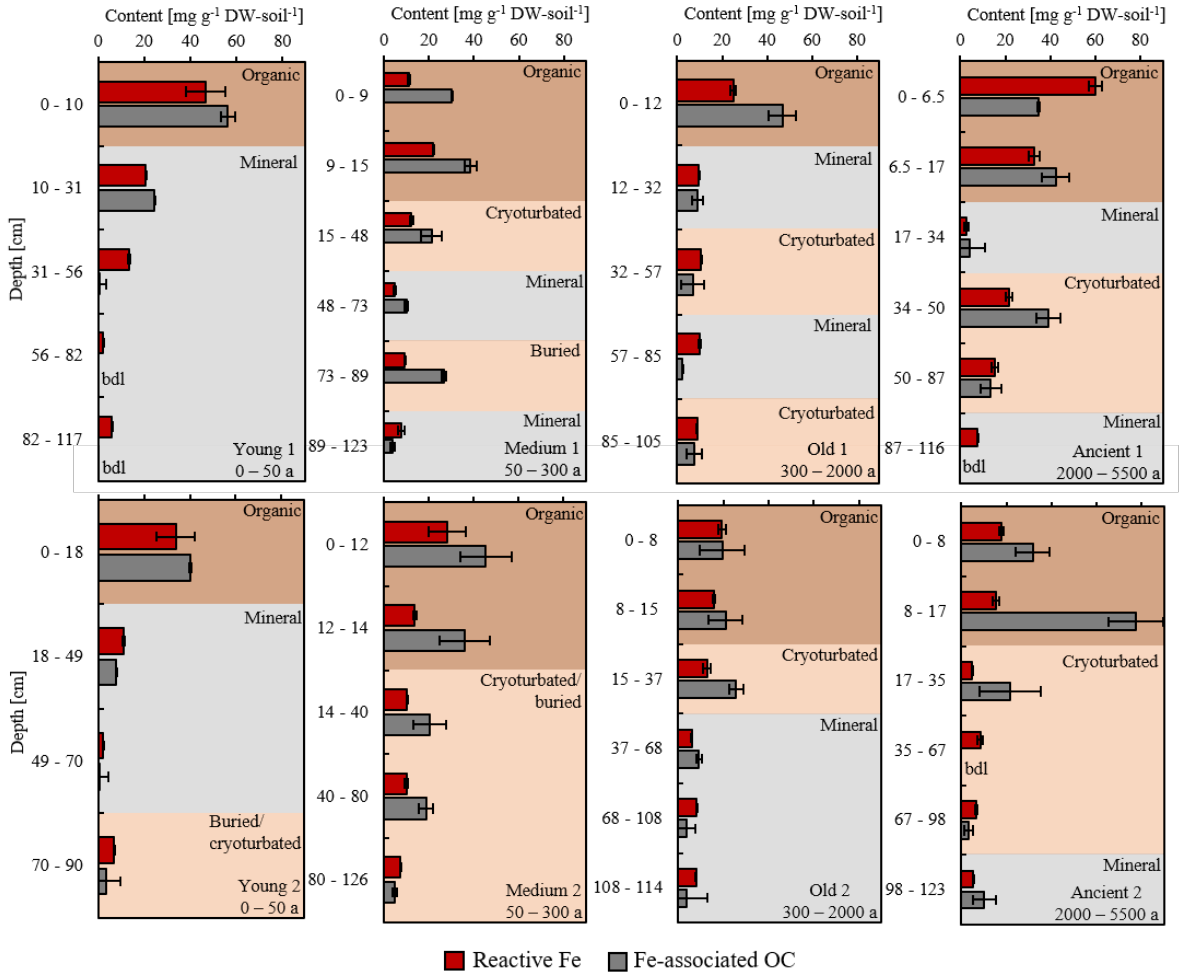

Figure 2. Soil horizons determine the content of reactive Fe (red) and Fe-associated OC (grey) along the soil profile of replicate cores (1, 2) from four age classes (young, medium, old, ancient) of drained thaw lake basins from Alaska. *Reactive Fe is dithionite-citrate extractable Fe corrected by NaCl control extraction and Fe-associated OC is dithionite-citrate extractable OC corrected by NaCl control extraction and citrate background, presented as mg g^{-1}DW-soil^{-1}. Soil horizons are highlighted by color shading (brown: organic, beige: cryoturbated/buried, grey: mineral). Error bars represent a combined standard deviation of duplicate extractions per horizon of replicate soil cores.*

Generally, reactive Fe and Fe-associated OC contents over all soil horizons and age classes correlate significantly (p_s<0.001, r_s=0.76) (Figure 2). By categorizing the percentage of Fe-associated OC into four ranges (0-10, 10-25, 25-50, 50-100 %) (Figure 3), it can be shown that Fe-associated OC constitutes a higher proportion of TOC in cryoturbated horizons

compared to organic and mineral horizons. Cryoturbated horizons show mainly 10-25 % Fe-associated OC, whereas organic horizons have between 0-25 % and mineral horizons have between 0-10 % Fe-associated OC.

The depth distribution demonstrates that the content of reactive Fe and associated OC is controlled by soil horizons rather than by depth or age class and is supported by significant differences found between soil horizons.

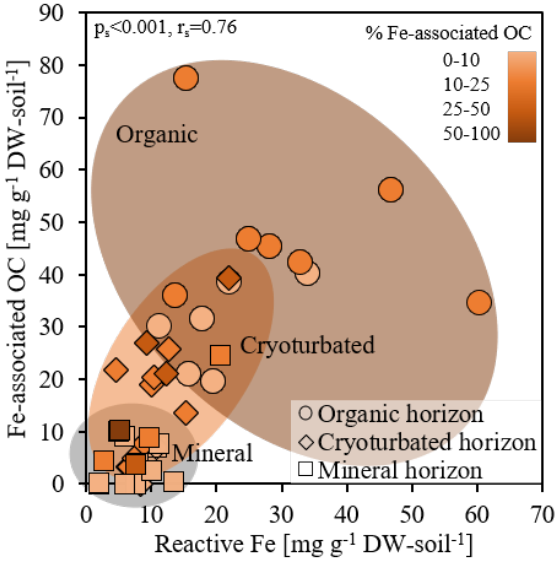

Figure 3. Horizon-dependent correlation of reactive Fe and Fe-associated OC in organic horizons (circle, n = 13), cryoturbated/buried horizons (diamond, n = 14) and mineral horizons (square, n = 16) of replicate cores (1, 2) from four age classes (young, medium, old, ancient) of drained thaw lake basins from Alaska. *Reactive Fe is dithionite-citrate extractable Fe corrected by NaCl control extraction and Fe-associated OC is dithionite-citrate extractable OC corrected by NaCl control extraction and citrate background, presented as mg g^{-1} DW-$soil^{-1}$. Data points represent the average from duplicate extractions filled with a color gradient depending on the amount of Fe-associated OC as percentage of TOC.*

Reactive Fe and Fe-associated OC increasingly distributed in cryoturbated horizons with progressive soil development

In order to follow the Fe-OC associations with progressive soil development, soil horizons of replicate soil cores of four age classes were analyzed, integrated over the soil profile and averaged over the replicate cores. The relationship of reactive Fe and associated OC is increasingly heterogeneous along the soil chronosequence (Figure SI 3). Overall, a maximum of 73.66±5.65 % of the total extractable Fe was quantified as reactive Fe and 13.68±2.31 %

of the TOC was found to be associated with reactive Fe minerals over the soil profiles (Table 1). In comparison to other studies focusing on Fe-OC associations in permafrost soils, we find similar amounts of OC associated with reactive Fe minerals. In permafrost soils from the Qinghai-Tibetan-Plateau, a maximum of 23.09±16.42 % of the TOC is associated with reactive Fe minerals in soil cores of an alpine desert steppe (Mu et al., 2016) and a maximum of 7 % in soils overlying intact permafrost in Sweden when averaged over the soil profile (Patzner et al., 2020).

Across age classes of the permafrost soil chronosequence, reactive Fe contents are relatively constant (Figure 4 a), but significant differences between age classes were found for the content of Fe-associated OC ($p = 0.008$) between the young and the medium ($p = 0.0214$, 66.34±8.75 to 128.12±18.86 mg g^{-1} DW-$soil^{-1}$, Table 1) and the young and ancient age class ($p = 0.0118$, 66.34±8.75 to 139.25±23.54 mg g^{-1} DW-$soil^{-1}$, Table 1) (Figure 4 a). Even though the majority of reactive Fe and associated OC content is contained in organic horizons along the soil chronosequence, cryoturbated horizons incorporate 6 to 8 times more reactive Fe (from ~4 % in young to 24-36 % in older age classes) and 10 to 14 times more associated OC (from ~2 % in young to 26-36 % in older age classes) from the young to the older age classes (medium, old, ancient) (Figure 4 a). Our consistent trend in reactive Fe across soil age classes indicates either a stable pool of reactive Fe minerals over 5500 years of soil development by impeded crystallization and hydrolysis of Fe minerals by association with OC (Schwertmann and Murad, 1988; Cornell and Schwertmann, 2003; Amstaetter, Borch and Kappler, 2012) or likely results from effective recycling of Fe minerals under redox fluctuations as was already observed in the same permafrost region (Herndon et al., 2017).

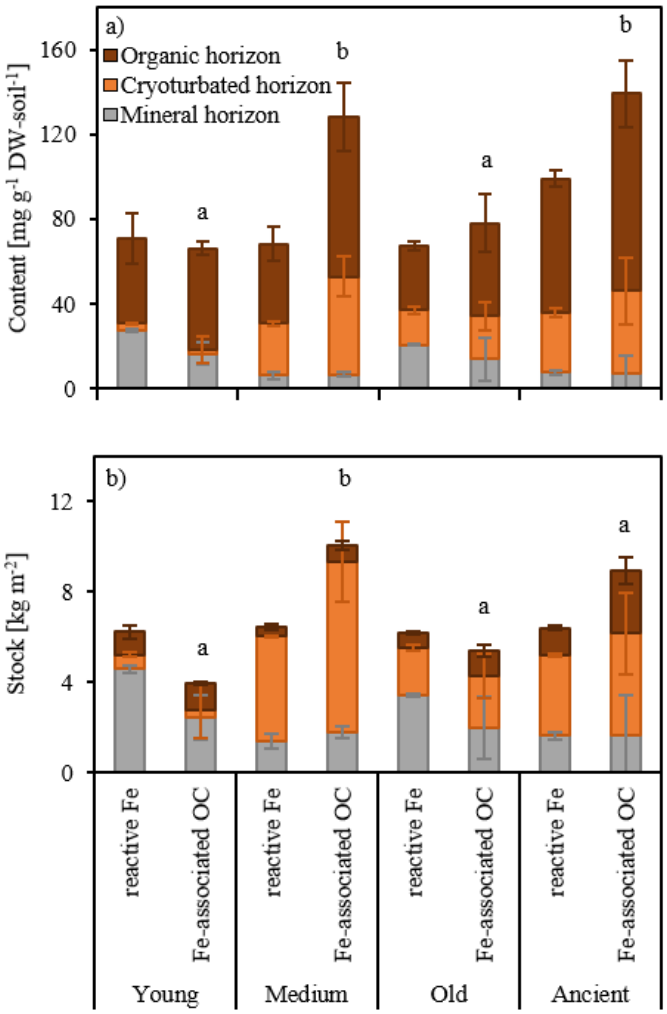

Figure 4. Reactive Fe and associated OC a) content in mg g^{-1} DW-soil^{-1} and b) stock in kg m^{-2} of in distinct soil horizons (organic: brown, cryoturbated/buried: orange, grey: mineral) along the soil chronosequence. *Distribution of reactive Fe and associated OC contents highlight the role of organic horizons, whereas cryoturbated horizons are more important regarding stocks along the soil chronosequence. Reactive Fe is dithionite-citrate extractable Fe corrected by NaCl control extraction and Fe-associated OC is dithionite-citrate extractable OC corrected by NaCl control extraction and citrate background. Error bars represent a combined standard deviation of duplicate extractions per horizon of replicate soil cores. Significant differences between age classes are highlighted with letters a and b.*

Stocks of reactive Fe do not significantly change (6.22±0.33 to 6.40±0.34 kg m^{-2} from young to ancient, Figure 4 b, Table 1), but the distribution of reactive Fe in soil horizons differs along the soil chronosequence. Cryoturbated horizons store 10 % of the total reactive Fe stock in the young age class and 34-72 % in the older age classes (medium, old, ancient). Fe-

associated OC stocks are significantly different between age classes (p = 0.0285) (Figure 4 b, Table 1) and significantly increase from the young (3.95±1.59 kg m^{-2}) to the medium age class (10.04±1.81 kg m^{-2}) (p = 0.0346). Changes in Fe-associated OC are driven by an increased incorporation of OC in cryoturbated horizons as they increase in abundance along the soil chronosequence.

Stocks of Fe-associated OC in cryoturbated horizons concurrently increase from around 8 % in the young age class to 42-75 % Fe-associated OC of the total Fe-associated OC stock in the older age classes (medium, old, ancient) (Figure 4 b). This underlines the shift from mineral horizons contributing most to the Fe-associated OC and reactive Fe stock in young (0-50 years) permafrost soils of drained thaw lake basins to cryoturbated horizons storing most reactive Fe and associated OC with progressive soil development.

Table 1. Overview of content, percentage and stock of reactive Fe and associated OC integrated over the whole soil profile and averaged over two replicate soil cores along the soil chronosequence. *Reactive Fe is dithionite-citrate extractable Fe corrected by NaCl control extraction and Fe-associated OC is dithionite-citrate extractable OC corrected by NaCl control extraction and citrate background.*

		Young	Medium	Old	Ancient
Content					
[mg g^{-1} DW-$soil^{-1}$]	Reactive Fe	71.11 ± 11.92	68.40 ± 8.47	67.18 ± 2.75	99.17 ± 4.71
	Fe-associated OC	66.34 ± 8.75	128.12 ± 18.86	77.99 ± 18.37	139.25 ± 23.54
Percentage					
[%]	Reactive Fe	59.51 ± 11.69	56.55 ± 8.09	59.21 ± 3.80	73.66 ± 5.65
	Fe-associated OC	10.96 ± 1.45	12.77 ± 1.88	8.28 ± 1.95	13.68 ± 2.31
Stock					
[kg m^{-2}]	Reactive Fe	6.22 ± 0.33	6.44 ± 0.39	6.85 ± 0.27	6.40 ± 0.34
	Fe-associated OC	3.95 ± 1.59	10.04 ± 1.81	7.73 ± 1.36	8.92 ± 2.60

The nature of Fe-OC associations

Differences in Fe mineral crystallinity between soil horizons

The crystallinity of Fe minerals can highly impact their capacity to interact with OC (Herndon et al., 2017). We therefore performed ^{57}Fe-specific Mössbauer spectroscopy analysis at 77 K and 5 K to identify and quantify the relative abundances of Fe minerals. Mössbauer transmission spectra of organic horizons of the young and ancient age class showed similar properties for spectra collected at 77 K (Figure SI 5 a, b, Table SI 4). The absence of a magnetic-ordering phase at 77 K and the presence of a sextet in the Mössbauer spectra collected at 5 K suggests the presence of a poorly crystalline Fe(III) mineral phase with

hyperfine field parameters similar to ferrihydrite (Figure SI 5 a, b, Figure SI 6 a, b, Table SI 4). This supports findings from selective extractions in organic horizons where reactive Fe minerals (which would include ferrihydrite) account for almost all of the total extractable Fe pool (Table SI 3). In cryoturbated and mineral horizons, 77 K Mössbauer spectra indicated the presence of an additional ferrous Fe mineral phase in both the young and ancient age class (Figure 5 c, d, e, f) which undergoes magnetic ordering only at 5 K (Figure SI 6 c, d, e, f, Table SI 4). This can be typical for a poorly crystalline Fe(II) mineral phase such as vivianite, siderite or Fe(II)-rich phyllosilicates although a clear identification could not be achieved by Mössbauer spectroscopy only. Phyllosilicates are not targeted by the dithionite-citrate extraction but will dissolve to a small extent in the 6 M HCl extraction. A poorly crystalline Fe(II) mineral such as vivianite would likely dissolve in the dithionite-citrate extraction (Williams, Mayer and Nriagu, 1980). Moreover, the preparation of the sample material under oxic conditions might lead to the abiotic oxidation of such oxygen sensitive ferrous Fe minerals. Taken this into consideration, and the lower abundance of reactive Fe minerals in the total extractable Fe pool compared to organic horizons (Table SI 3), suggests that the observed phase is probably an Fe(II)-bearing phyllosilicate (Raiswell, Canfield and Berner, 1994; Poulton and Canfield, 2005). Overall, Mössbauer spectroscopy enabled the identification of ferrihydrite as the poorly crystalline mineral phase most abundant in organic horizons with lower abundance due to a more pronounced Fe(II) phase in cryoturbated and mineral horizons. Fe minerals of higher crystallinity such as magnetite are typically generated by dissimilatory Fe(III) reduction (Lovley et al., 1987) and present in permafrost soils from northern Alaska (Lipson et al., 2010), but are not involved in Fe-OC associations found in our study. Unlike Sowers et al. (2020) which investigated a Yedoma chronosequence over 36000 years, we did not observe a change in Fe mineral crystallinity with soil development, but rather a change in Fe mineral crystallinity in soil horizons. Cryoturbated and mineral horizons contain similar Fe mineral phases in our study, but differ greatly in their amount of Fe-associated OC. Thus, we conclude that Fe mineral crystallinity does not solely affect the association of OC in permafrost soils of drained thaw lake basins, but is potentially influenced by the type of interaction between OC and reactive Fe minerals.

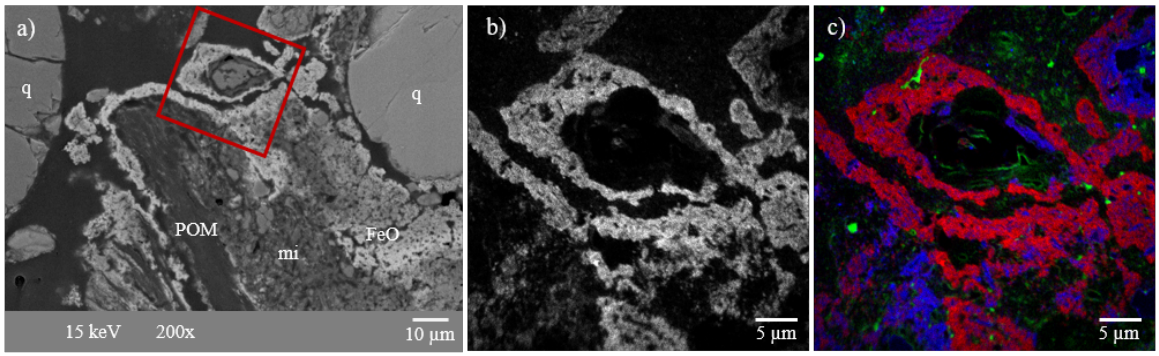

Figure 5. Cross section of an embedded intact soil core derived from the permafrost layer to illustrate the intricate connection of Fe oxides (FeO) with soil organic matter (i.e. particulate organic matter, POM) and the soil matrix (quartz grains, q; clay minerals, mi). *a) Backscattered SEM image showing the incrustation of particulate organic matter and silt and clay minerals (mi) by FeO (brighter zones in backscattered SEM image). The red square indicates the NanoSIMS measurement spot (b, c). b) Microscale distribution of Fe measured as $^{56}Fe^{16}O^-$ by NanoSIMS. c) Composite image of Fe (red, $^{56}Fe^{16}O^-$), organic matter (green, $^{12}C^{14}N^-$) and aluminium (blue, $^{27}Al^{16}O^-$) (detailed description of sample in Mueller et al. (2017)).*

Co-precipitation, chelation and aggregation primarily explain the nature of Fe-OC associations

Fe-associated OC to reactive Fe ratios (OC:Fe) obtained by the dithionite-citrate extraction can indicate the mechanism of Fe-OC interactions. A mass ratio over 0.22 is indicative for Fe-OC associations predominantly formed by co-precipitation or chelation (Wagai and Mayer, 2007). Below an OC:Fe mass ratio of 0.22, OC is mainly assumed to be sorbed onto Fe minerals. In the present study, 86 % of the permafrost samples exceed an OC:Fe mass ratios of 0.22 with significant differences between soil horizons ($p = 0.01$, Kruskall Wallis test) (Figure 6). Organic horizons consistently exceed a OC:Fe mass ratio of 0.22 with ratios between 0.57 and 5.05. They are significantly different from mineral horizons ($p = 0.01$) that show lower OC:Fe mass ratios (0 to 2.02). OC:Fe mass ratios in cryoturbated horizons range between 0 and 4.72. Given the release of OC bound in soil microaggregate structures during dithionite-citrate extraction (Wagai and Mayer, 2007), high OC:Fe mass ratios indicate the contribution of aggregation.

Cryoturbated horizons show a high proportion of particulate organic matter where plant residues can for example promote soil aggregate formation by providing a priming structure for aggregating mineral particles (Mueller et al., 2017; Prater et al., 2020). The intricate

connection of reactive Fe minerals, organic matter and the soil matrix in a cryoturbated horizon (medium 2) is illustrated by using combined SEM and NanoSIMS analysis (Figure 5). The backscattered SEM image showed particulate organic matter (POM) and clay minerals (mi) enclosed by Fe minerals (FeO) in the soil cross section and delimited quartz grains (q) (Figure 5 a). Microscale distributions showed a close spatial association of Fe minerals visualized as $^{56}Fe^{16}O^-$ intertwined with POM as $^{12}C^{14}N^-$ and clay and silt minerals shown as $^{27}Al^{16}O^-$ as detected by NanoSIMS (Figure 5 b, c).

This highlights the role of reactive Fe minerals in retaining OC in soil horizons with emphasis on cryoturbated horizons. Thus, we propose that OC is primarily co-precipitated, chelated or aggregated with reactive Fe minerals.

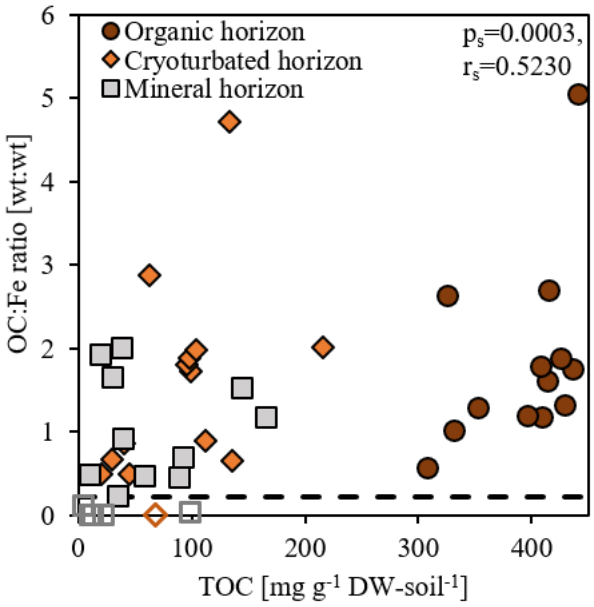

Figure 6. OC:Fe mass ratios in relation to the TOC content in mg g^{-1} DW-soil^{-1} separated into organic horizons (brown circle), cryoturbated/buried horizons (orange diamond) and mineral horizons (grey square) of replicate cores (1, 2) from four age classes (young, medium, old, ancient) of drained thaw lake basins from Alaska. *OC:Fe mass ratios were calculated using reactive Fe and Fe-associated OC contents. Reactive Fe is dithionite-citrate extractable Fe corrected by NaCl control extraction and Fe-associated OC is dithionite-citrate extractable OC corrected by NaCl control extraction and citrate background. The dashed line represents the presumed threshold for sorption of reactive Fe minerals on natural organic matter (Wagai and Mayer, 2007). OC:Fe mass ratios largely exceeding 0.22, indicate co-precipitation or chelation of organic compounds. Samples exceeding this threshold are illustrated as filled symbols, whereas framed symbols are below a ratio of 0.22.*

The type of Fe-OC interactions seems to be governed to a certain extent by the amount of TOC present in soil horizons, as supported by significant correlation between OC:Fe mass ratios and TOC content ($p_s = 0.0003$, $r_s = 0.5230$). Furthermore, the association of OC seems not to be limited by the amount of reactive Fe in our permafrost soil cores, in contrast to Fe-OC associations in forest soils (Zhao et al., 2016). The Fe-associated OC in our study largely exceeds the theoretical maximum of sorbed OC onto Fe (oxyhydr)oxides, calculated as 0.22 times the reactive Fe content (Herndon et al., 2017) (Figure SI 4). High OC:Fe mass ratios in distinct soil horizons can possibly be explained by changes in solubility of redox active metals (Eusterhues, Rumpel and Kögel-Knabner, 2005), as it can also be observed at the redox interface in permafrost affected soils.

Besides the amount of OC, pH also influences the nature of the Fe-OC association (Wagai and Mayer, 2007). On average, higher OC:Fe mass ratios can be found in older age classes where pH is generally lower and TOC is higher compared to the young age class (young = 0.55 ± 0.54, medium = 1.85 ± 0.76, old = 1.03 ± 0.59, ancient = 1.68 ± 1.65) (Kao-Kniffin et al., 2015). In summary, our results show that Fe-OC associations are primarily formed by co-precipitation, chelation and aggregation in drained thaw lake basins of northern Alaska which is in accordance with findings from other permafrost regions (Mu et al., 2020; Patzner et al., 2020). Contrary findings in the same region, where Fe-OC associations are restricted to sorption (Herndon et al., 2017), highlights the heterogeneity of Fe-OC associations and the need for further investigations.

Potential fate of Fe-OC associations under climate change

The molecular diversity was long thought to be the main factor limiting the decomposition of organic matter. Lehmann et al. (2020) recently underlined that spatial and temporal variations in the soil shape the functional complexity and collectively determine OC persistence. As permafrost soils are highly variable ecosystems with annual freeze-thaw cycles, Fe-OC associations are considered to play an important role in retaining OC under a changing climate. Increasing permafrost thaw can result in waterlogged and anoxic conditions under which Fe minerals are dissolved by dissimilatory Fe(III) reducing microorganisms that releases the Fe-associated OC (Patzner et al., 2020). By this, greenhouse gas emissions could be exaggerated by microbial Fe(III) reduction which is directly coupled to OC mineralization leading to CO_2 emissions (Lovley et al., 1987). As well as by the reductive dissolution of reactive Fe minerals mobilizing the previously bound OC which becomes available for microbial respiration. Additionally, Fe(III) reduction can also be coupled to other microbial processes such as anaerobic oxidation of methane which influences greenhouse gas

emissions (van Huissteden et al., 2011) and thus the response of permafrost soils to climate change.

At the Arctic Coastal Plain of northern Alaska, microbial Fe(III) reduction contributes up to 63 % to the total respiration (Lipson et al., 2013) which emphasizes the important role of Fe minerals in the association with OC. Thermokarst regions of the Arctic Coastal Plain in Alaska are assumed to shift from a stable (Hinkel et al., 2007) to a susceptible environment under future climate (Nitze et al., 2020). Due to the lack of ground ice-wedge build-up under future climate scenarios, it is expected that thermokarst lakes will no longer follow the long postulated thermokarst lake cycle where reformation of thermokarst lakes was expected after around 5500 years of drainage (Jorgenson and Shur, 2007; Bouchard et al., 2017; Fuchs et al., 2019). Consequently, OC introduced by cryoturbation can be associated and stabilized by reactive Fe minerals under increasing soil drainage which promotes oxic conditions (Herndon, Kinsman-Costello and Godsey, 2020). This association potentially preserves OC over thousands of years mitigating the rapid loss of respired C as greenhouse gases to the atmosphere.

Acknowledgments

We thank Jenny Kao-Kniffin, James Bockheim and Kenneth Hinkel for the invitation to join the 2010 expedition, the joint work in the field and all logistic assistance. We are grateful for assistance in field work and sampling by Christine Mlot and the Barrow Arctic Science Consortium (BASC). The funding for the sampling campaign was provided by the NSF Postdoctoral Fellowship in Polar Regions Research (#0852036). We thank Marie Greiner and Miroslava Malusova for assistance in the lab, Ellen Röhm for OC measurements and Johannes Lugmeier for NanoSIMS measurements. The authors acknowledge infrastructural support by the Deutsche Forschungsgemeinschaft (DFG, German Research Foundation) under Germany's Excellence Strategy, cluster of Excellence EXC2124, project ID 390838134. We are grateful for the financial support from the German Science Foundation (DFG) in the frame of the "Initiation of International Collaboration" program (MU 3021/2-1), for support from the German Academic Scholarship Foundation (scholarship to MSP) and for support through the "Programme for the Promotion of Junior Researchers" award to CB from the University of Tübingen.

References

Amstaetter K., Borch T. and Kappler A. (2012) Influence of humic acid imposed changes of ferrihydrite aggregation on microbial Fe(III) reduction. *Geochimica et Cosmochimica Acta* 85, 326–341.

Bockheim J. G. (2007) Importance of Cryoturbation in Redistributing Organic Carbon in Permafrost-Affected Soils. *Soil Science Society of America Journal* 71, 1335.

Bouchard F., MacDonald L. A., Turner K. W., Thienpont J. R., Medeiros A. S., Biskaborn B. K., Korosi J., Hall R. I., Pienitz R. and Wolfe B. B. (2017) Paleolimnology of thermokarst lakes: a window into permafrost landscape evolution. *Arctic Science* 3, 91–117.

Chen C., Hall S. J., Coward E. and Thompson A. (2020) Iron-mediated organic matter decomposition in humid soils can counteract protection. *Nature communications* 11, 2255.

Cornell R. M. and Giovanoli R. (1988) Acid dissolution of akaganeite and lepidocrocite: The effect of crystal morphology. *Clays and Clay Minerals* 36, 385–390.

Cornell R. M. and Schwertmann U. (2003) The Iron Oxides.

Coward E. K., Thompson A. T. and Plante A. F. (2017) Iron-mediated mineralogical control of organic matter accumulation in tropical soils. *Geoderma* 306, 206–216.

Estop-Aragones C., Olefeldt D., Abbott B. W., Chanton J. P., Czimczik C. I., Dean J. F., Egan J. E., Gandois L., Garnett M. H., Hartley I. P., Hoyt A., Lupascu M., Natali S. M., O'Donnell J. A., Raymond P. A., Tanentzap A. J., Tank S. E., Schuur E. A. G., Turetsky M. and Anthony K. W. (2020) Assessing the Potential for Mobilization of Old Soil Carbon After Permafrost Thaw: A Synthesis of 14 C Measurements From the Northern Permafrost Region. *Global Biogeochemical Cycles* 34.

Eusterhues K., Rumpel C. and Kögel-Knabner I. (2005) Organo-mineral associations in sandy acid forest soils: importance of specific surface area, iron oxides and micropores. *Eur J Soil Sci* 56, 753-763.

Fisher B. J., Moore O. W., Faust J. C., Peacock C. L. and März C. (2020) Experimental evaluation of the extractability of iron bound organic carbon in sediments as a function of carboxyl content. *Chemical Geology* 556, 119853.

Foucher D., Niessen S., Fisher J.-C., Kwokal Ž. and Mikac N. (2000) The use of hydrochloric acid for determining solid-phase association of mercury in anoxic sediments. *ESF Conference*.

Fuchs M., Lenz J., Jock S., Nitze I., Jones B. M., Strauss J., Günther F. and Grosse G. (2019) Organic Carbon and Nitrogen Stocks Along a Thermokarst Lake Sequence in Arctic Alaska. *J. Geophys. Res. Biogeosci.* 124, 1230–1247.

Grosse G., Jones B. and Arp C. (2013) *Thermokarst Lakes, Drainage, and Drained Basins*.

Grosse G., Schirrmeister L. and Malthus T. J. (2006) Application of Landsat-7 satellite data and a DEM for the quantification of thermokarst-affected terrain types in the periglacial Lena-Anabar coastal lowland. *Polar Research* 25, 51–67.

Hegler F., Posth N. R., Jiang J. and Kappler A. (2008) Physiology of phototrophic iron(II)-oxidizing bacteria: implications for modern and ancient environments. *FEMS microbiology ecology* 66, 250–260.

Hemingway J. D., Rothman D. H., Grant K. E., Rosengard S. Z., Eglinton T. I., Derry L. A. and Galy V. V. (2019) Mineral protection regulates long-term global preservation of natural organic carbon. *Nature* 570, 228–231.

Herndon E. M., AlBashaireh A., Singer D., Roy Chowdhury T., Gu B. and Graham D. (2017) Influence of iron redox cycling on organo-mineral associations in Arctic tundra soil. *Geochimica et Cosmochimica Acta* 207, 210–231.

Herndon E. M., Kinsman-Costello L. and Godsey S. (2020) Biogeochemical Cycling of Redox-Sensitive Elements in Permafrost-Affected Ecosystems. In *Biogeochemical cycles* (eds. K. Dontsova, Z. Balogh-Brunstad and G. Le Roux). American Geophysical Union; Wiley. Washington, Hoboken, pp. 245–265.

Herndon E. M., Yang Z., Bargar J., Janot N., Regier T. Z., Graham D. E., Wullschleger S. D., Gu B. and Liang L. (2015) Geochemical drivers of organic matter decomposition in arctic tundra soils. *Biogeochemistry* 126, 397–414.

Hinkel K. M., Eisner W. R., Bockheim J. G., Nelson F. E., Peterson K. M. and Dai X. (2003) Spatial Extent, Age, and Carbon Stocks in Drained Thaw Lake Basins on the Barrow Peninsula, Alaska. *Arctic, Antarctic, and Alpine Research* 35, 291–300.

Hinkel K. M., Jones B. M., Eisner W. R., Cuomo C. J., Beck R. A. and Frohn R. (2007) Methods to assess natural and anthropogenic thaw lake drainage on the western Arctic coastal plain of northern Alaska. *J. Geophys. Res.* 112.

Hopple A. M., Wilson R. M., Kolton M., Zalman C. A., Chanton J. P., Kostka J., Hanson P. J., Keller J. K. and Bridgham S. D. (2020) Massive peatland carbon banks vulnerable to rising temperatures. *Nat Commun* 11, 2373.

Hugelius G., Strauss J., Zubrzycki S., Harden J. W., Schuur E. A. G., Ping C.-L., Schirrmeister L., Grosse G., Michaelson G. J., Koven C. D., O&apos, Donnell J. A., Elberling B., Mishra U., Camill P., Yu Z., Palmtag J. and Kuhry P. (2014) Estimated stocks of circumpolar permafrost carbon with quantified uncertainty ranges and identified data gaps. *Biogeosciences* 11, 6573–6593.

Jorgenson M. T. and Shur Y. (2007) Evolution of lakes and basins in northern Alaska and discussion of the thaw lake cycle. *J. Geophys. Res.* 112.

Kaiser K. and Guggenberger G. (2000) The role of DOM sorption to mineral surfaces in the preservation of organic matter in soils. *Organic Geochemistry*, 711–725.

Kao-Kniffin J., Woodcroft B. J., Carver S. M., Bockheim J. G., Handelsman J., Tyson G. W., Hinkel K. M. and Mueller C. W. (2015) Archaeal and bacterial communities across a chronosequence of drained lake basins in Arctic Alaska. *Scientific reports* 5, 18165.

Kögel-Knabner I., Guggenberger G., Kleber M., Kandeler E., Kalbitz K., Scheu S., Eusterhues K. and Leinweber P. (2008) Organo-mineral associations in temperate soils: Integrating biology, mineralogy, and organic matter chemistry. *J. Plant Nutr. Soil Sci.* 171, 61–82.

Lalonde K., Ouellet A. and Gélinas Y. (2012) The Rusty Sink: Iron and the preservation of organic matter in sediments 483, 198–200.

Lehmann J., Hansel C. M., Kaiser C., Kleber M., Maher K., Manzoni S., Nunan N., Reichstein M., Schimel J. P., Torn M. S., Wieder W. R. and Kögel-Knabner I. (2020) Persistence of soil organic carbon caused by functional complexity. *Nat. Geosci.* 13, 529–534.

Liang L., McCarthy J. F., Jolley L. W., McNabb A. and Mehlhorn T. L. (1993) Iron dynamics: Transformation of Fe(II)/Fe(III) during injection of natural organic matter in a sandy aquifer. *Geochimica et Cosmochimica Acta*, 1987–1999.

Lipson D. A., Jha M., Raab T. K. and Oechel W. C. (2010) Reduction of iron (III) and humic substances plays a major role in anaerobic respiration in an Arctic peat soil. *J. Geophys. Res.* 115.

Lipson D. A., Raab T. K., Goria D. and Zlamal J. (2013) The contribution of Fe(III) and humic acid reduction to ecosystem respiration in drained thaw lake basins of the Arctic Coastal Plain. *Global Biogeochem. Cycles* 27, 399–409.

Lovley D. R., Stolz J. F., Nord G. L. and Phillips E. J. P. (1987) Anaerobic production of magnetite by a dissimilatory iron-reducing microorganism. *Nature* 330, 252–254.

Mehra O. P. and Jackson M. L. (1960) Iron Oxide Removal from Soils and Clays by a Dithionite-Citrate System Buffered with Sodium Bicarbonate. *Clays and Clay Minerals* 7, 317–327.

Moormann F. R. and van Breemen N. (1978) *Rice: soil, water, land.* Int. Rice Res. Inst.

Mu C., Zhang F., Mu M., Chen X., Li Z. and Zhang T. (2020) Organic carbon stabilized by iron during slump deformation on the Qinghai-Tibetan Plateau. *CATENA* 187, 104282.

Mu C. C., Zhang T. J., Zhao Q., Guo H., Zhong W., Su H. and Wu Q. B. (2016) Soil organic carbon stabilization by iron in permafrost regions of the Qinghai-Tibet Plateau. *Geophys. Res. Lett.* 43, 10,286-10,294.

Mueller C. W., Hoeschen C., Steffens M., Buddenbaum H., Hinkel K., Bockheim J. G. and Kao-Kniffin J. (2017) Microscale soil structures foster organic matter stabilization in permafrost soils. *Geoderma* 293, 44–53.

Mueller C. W., Rethemeyer J., Kao-Kniffin J., Löppmann S., Hinkel K. M. and Bockheim J. G. (2015) Large amounts of labile organic carbon in permafrost soils of northern Alaska. *Global change biology* 21, 2804–2817.

Mueller C. W., Weber P. K., Kilburn M. R., Hoeschen C., Kleber M. and Pett-Ridge J. (2013) Advances in the Analysis of Biogeochemical Interfaces. *Advances in Agronomy* 121, 1–46.

Nitze I., Cooley S. W., Duguay C. R., Jones B. M. and Grosse G. (2020) The catastrophic thermokarst lake drainage events of 2018 in northwestern Alaska: fast-forward into the future. *The Cryosphere* 14, 4279–4297.

Olefeldt D., Goswami S., Grosse G., Hayes D., Hugelius G., Kuhry P., McGuire A. D., Romanovsky V. E., Sannel A. B. K., Schuur E. A. G. and Turetsky M. R. (2016) Circumpolar distribution and carbon storage of thermokarst landscapes. *Nat Commun* 7, 13043.

Osterkamp T. E. and Romanovsky V. E. (1999) Evidence for warming and thawing of discontinuous permafrost in Alaska. *Permafrost Periglac. Process.* 10, 17–37.

Patzner M. S., Mueller C. W., Malusova M., Baur M., Nikeleit V., Scholten T., Hoeschen C., Byrne J. M., Borch T., Kappler A. and Bryce C. (2020) Iron mineral dissolution releases iron and associated organic carbon during permafrost thaw. *Nat Commun* 11, 6329.

Pehkonen S. (1995) Determination of the oxidation states of iron in natural waters. A review. *Analyst* 120, 2655.

Peltier E., Dahl A. L. and Gaillard J.-F. (2005) Metal speciation in anoxic sediments: when sulfides can be construed as oxides. *Environmental science & technology* 39, 311–316.

Ping C. L., Bockheim J. G., Kimble J. M., Michaelson G. J. and Walker D. A. (1998) Characteristics of cryogenic soils along a latitudinal transect in arctic Alaska. *J. Geophys. Res.* 103, 28917–28928.

Polerecky L., Adam B., Milucka J., Musat N., Vagner T. and Kuypers M. M. M. (2012) Look@NanoSIMS--a tool for the analysis of nanoSIMS data in environmental microbiology. *Environmental microbiology* 14, 1009–1023.

Porsch K. and Kappler A. (2011) FeII oxidation by molecular O2 during HCl extraction. *Environ. Chem.* 8, 190.

Poulton S. W. and Canfield D. E. (2005) Development of a sequential extraction procedure for iron: implications for iron partitioning in continentally derived particulates. *Chemical Geology* 214, 209–221.

Prater I., Zubrzycki S., Buegger F., Zoor-Füllgraff L. C., Angst G., Dannenmann M. and Mueller C. W. (2020) *From fibrous plant residues to mineral-associated organic carbon - the fate of organic matter in Arctic permafrost soils*.

Raiswell R., Canfield D. E. and Berner R. A. (1994) A comparison of iron extraction methods for the determination of degree of pyritisation and the recognition of iron-limited pyrite formation. *Chemical Geology* 111, 101–110.

Rutledge S., Campbell D. I., Baldocchi D. and Schipper L. A. (2010) Photodegradation leads to increased carbon dioxide losses from terrestrial organic matter. *Global Change Biol* 16, 3065-3074.

Schädel C., Bader M. K.-F., Schuur E. A. G., Biasi C., Bracho R., Čapek P., Baets S. de, Diáková K., Ernakovich J., Estop-Aragones C., Graham D. E., Hartley I. P., Iversen C. M., Kane E., Knoblauch C., Lupascu M., Martikainen P. J., Natali S. M., Norby R. J., O'Donnell J. A., Chowdhury T. R., Šantrůčková H., Shaver G., Sloan V. L., Treat C. C., Turetsky M. R., Waldrop M. P. and Wickland K. P. (2016) Potential carbon emissions dominated by carbon dioxide from thawed permafrost soils. *Nat. Clim. Chang.* 6, 950–953.

Schuur E. A. G., McGuire A. D., Schädel C., Grosse G., Harden J. W., Hayes D. J., Hugelius G., Koven C. D., Kuhry P., Lawrence D. M., Natali S. M., Olefeldt D., Romanovsky V. E., Schaefer K., Turetsky M. R., Treat C. C. and Vonk J. E. (2015) Climate change and the permafrost carbon feedback. *Nature* 520, 171–179.

Schwertmann U. (1966) Inhibitory Effect of Soil Organic Matter on the Crystallization of Amorphous Ferric Hydroxide. *Nature* 212, 645–646.

Schwertmann U. and Murad E. (1988) The nature of an iron oxide - organic iron association in a peaty environment. *Clay Minerals* 23, 291–299.

Shields M. R., Bianchi T. S., Gélinas Y., Allison M. A. and Twilley R. R. (2016) Enhanced terrestrial carbon preservation promoted by reactive iron in deltaic sediments. *Geophys. Res. Lett.* 43, 1149–1157.

Sowers T. D., Wani R. P., Coward E. K., Fischel M. H. H., Betts A. R., Douglas T. A., Duckworth O. W. and Sparks D. L. (2020) Spatially Resolved Organomineral Interactions across a Permafrost Chronosequence. *Environmental science & technology* 54, 2951–2960.

Stookey L. L. (1970) Ferrozine---a new spectrophotometric reagent for iron. *Anal. Chem.* 42, 779–781.

Turetsky M. R., Abbott B. W., Jones M. C., Anthony K. W., Olefeldt D., Schuur E. A. G., Grosse G., Kuhry P., Hugelius G., Koven C., Lawrence D. M., Gibson C., Sannel A. B. K. and McGuire A. D. (2020) Carbon release through abrupt permafrost thaw. *Nat. Geosci.* 13, 138–143.

van Huissteden J., Berrittella C., Parmentier F. J. W., Mi Y., Maximov T. C. and Dolman A. J. (2011) Methane emissions from permafrost thaw lakes limited by lake drainage. *Nat. Clim. Chang.* 1, 119–123.

Varadachari C., Goswami G. and Ghosh K. (2006) Dissolution of Iron Oxides. *Clay Research*, 1–19.

von Lützow M., Kögel-Knabner I., Ludwig B., Matzner E., Flessa H., Ekschmitt K., Guggenberger G., Marschner B. and Kalbitz K. (2008) Stabilization

mechanisms of organic matter in four temperate soils: Development and application of a conceptual model. *J. Plant Nutr. Soil Sci.* 171, 111–124.

Wagai R. and Mayer L. M. (2007) Sorptive stabilization of organic matter in soils by hydrous iron oxides. *Geochimica et Cosmochimica Acta* 71, 25–35.

Wagai R., Mayer L. M., Kitayama K. and Shirato Y. (2013) Association of organic matter with iron and aluminum across a range of soils determined via selective dissolution techniques coupled with dissolved nitrogen analysis. *Biogeochemistry* 112, 95–109.

Walter Anthony K., Schneider von Deimling T., Nitze I., Frolking S., Emond A., Daanen R., Anthony P., Lindgren P., Jones B. and Grosse G. (2018) 21st-century modeled permafrost carbon emissions accelerated by abrupt thaw beneath lakes. *Nat Commun* 9, 3262.

Wang Y., Xu Y., Wei D., Shi L., Jia Z. and Yang Y. (2020) Different chemical composition and storage mechanism of soil organic matter between active and permafrost layers on the Qinghai–Tibetan Plateau. *J Soils Sediments* 20, 653–664.

Williams J. D. H., Mayer T. and Nriagu J. O. (1980) Extractability of Phosphorus from Phosphate Minerals Common in Soils and Sediments. *Soil Science Society of America Journal* 44, 462–465.

Zhao Q., Poulson S. R., Obrist D., Sumaila S., Dynes J. J., McBeth J. M. and Yang Y. (2016) Iron-bound organic carbon in forest soils: quantification and characterization. *Biogeosciences* 13, 4777–4788.

Supplementary information for

Cryoturbation leads to iron-organic carbon associations along a permafrost soil chronosequence in northern Alaska

Hanna Joss[1], **Monique S. Patzner[1]**, Markus Maisch[1], Carsten W. Mueller[2,3], Andreas Kappler[1,4], Casey Bryce[1,5]

[1]Geomicrobiology, Center for Applied Geoscience, University of Tuebingen, Germany.
[2]Research Department Ecology and Ecosystem Management, Chair of Soil Science, Technical University of Munich, Freising-Weihenstephan, Germany.
[3]Department of Geosciences and Natural Resource Management, University of Copenhagen, Denmark.
[4]Cluster of Excellence: EXC 2124: Controlling Microbes to Fight Infection, Tuebingen, Germany.
[5]School of Earth Sciences, University of Bristol, UK.

Manuscript submitted for publication to: *Geoderma*

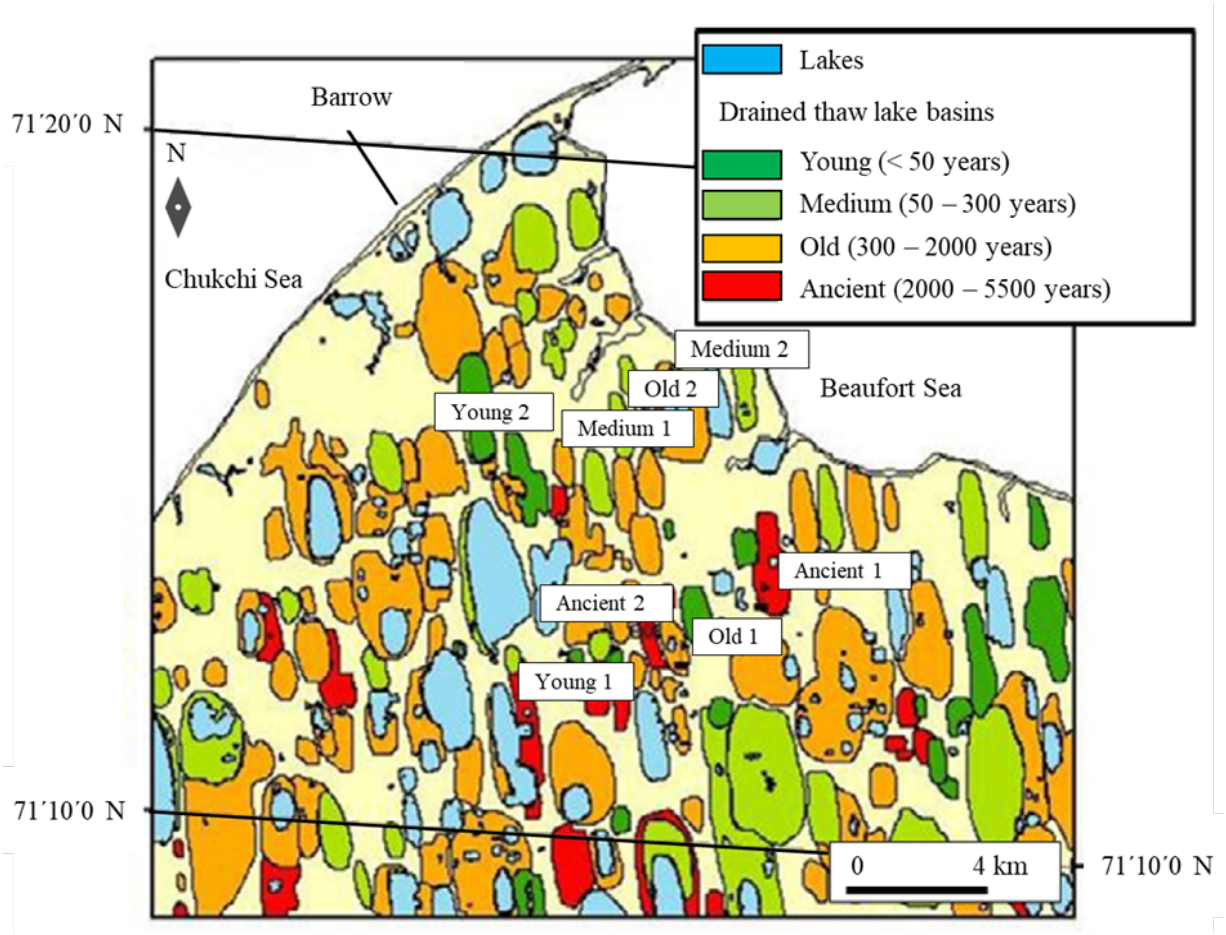

Figure SI 1. Map of the area around Barrow, Alaska. *Drained thaw lake basins are colored based on their age. Sampling sites are indicated within the map (modified from Mueller et al. (2015)).*

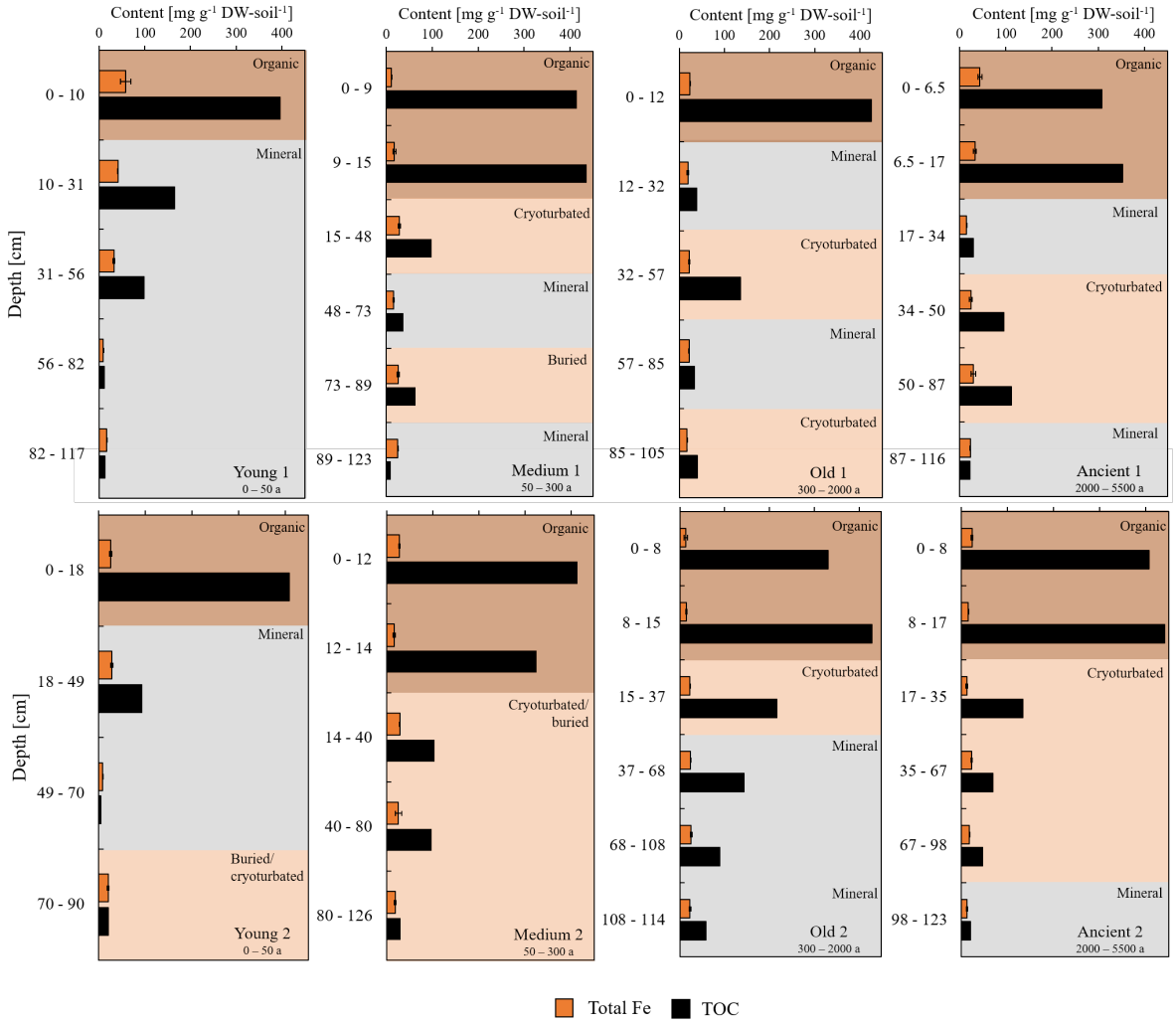

Figure SI 2. Content of total Fe (orange, 6 M HCl extractable) and TOC (black) in mg g^{-1} DW-soil^{-1} along the soil profile of replicate cores (1, 2) from four age classes (young, medium, old, ancient) of drained thaw lake basins from Alaska. *Soil horizons are highlighted by color shading (brown: organic, beige: cryoturbated/buried, grey: mineral). Error bars of total Fe represent standard deviation from duplicate extractions per each soil horizon. TOC data was obtained by Mueller et al. (2015).*

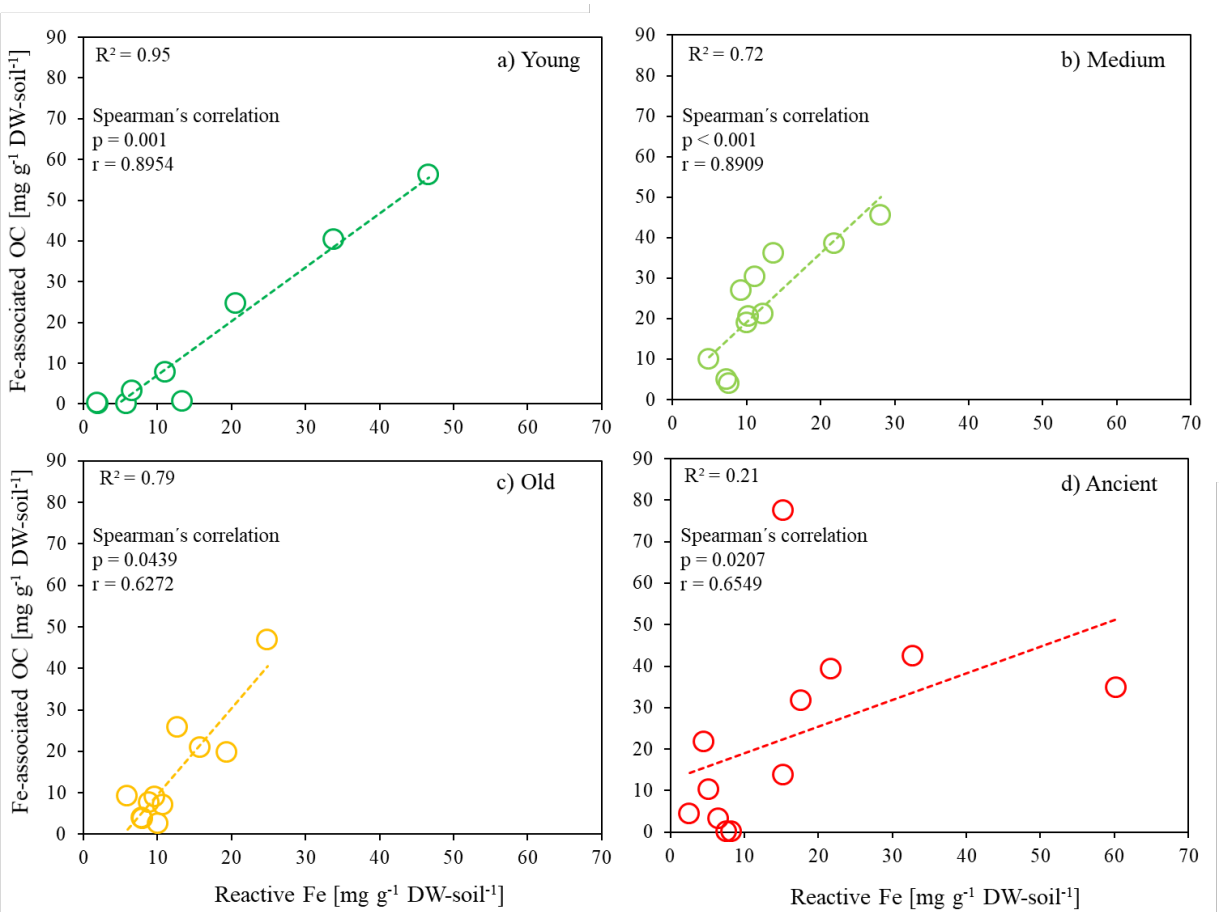

Figure SI 3. Age dependent correlation of reactive Fe and Fe-associated OC of soil profiles of replicate cores (1, 2) from four age classes (young, medium, old, ancient) of drained thaw lake basins from Alaska. (n = 43). Divided into (a) young (dark green, n = 9), (b) medium (light green, n = 11), (c) old (yellow, n = 11) and (d) ancient (red, n = 12) illustrating increasing heterogeneity with age. *Reactive Fe is dithionite-citrate extractable Fe corrected by NaCl control extraction and Fe-associated OC is dithionite-citrate extractable OC corrected by NaCl control extraction and citrate background, presented as mg g^{-1} DW-$soil^{-1}$. Data points represent average from duplicate extraction with linear trendlines highlighted in respective colors. R squared of linear regression and Spearman correlation coefficients are given within the figure.*

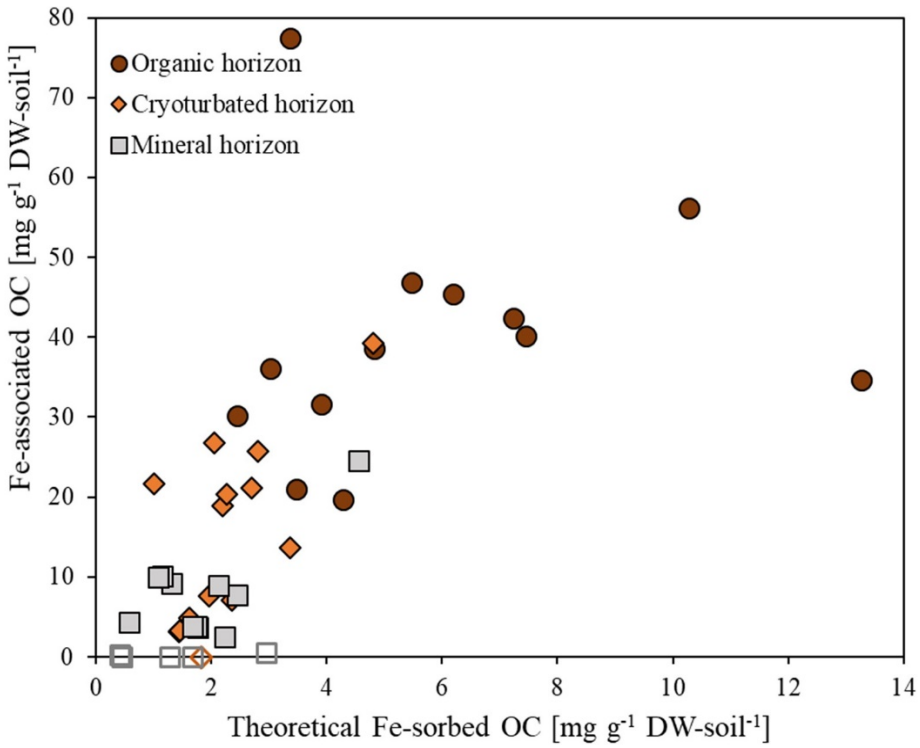

Figure SI 4. Content of Fe-associated OC against theoretical maximum adsorption of OC to iron oxide surfaces, calculated as 0.22 times the reactive Fe content based on Wagai and Mayer (2007) following Herndon et al. (2017). *Reactive Fe is dithionite-citrate extractable Fe corrected by NaCl control extraction and Fe-associated OC is dithionite-citrate extractable OC corrected by NaCl control extraction and citrate background, presented as mg g^{-1} DW-$soil^{-1}$. Filled symbols represent samples with OC:Fe mass ratios >0.22 and framed symbols are below a ratio of 0.22.*

Table SI 1. Pre-test for dithionite-citrate extraction to investigate the need of citrate as metal ion complexing agent. *Without citrate, less reactive Fe and associated OC were obtained, thus verifying the need of citrate despite the high OC background.*

Treatment	Reactive Fe	Fe-associated OC
	[mg g^{-1} DW-$soil^{-1}$]	
Sodium dithionite + NaCl/bicarbonate solution	6.66 ± 1.68	1045.48 ± 85.77
Sodium dithionite + citrate/bicarbonate solution	15.29 ± 4.85	2638.76 ± 243.05

Table SI 2. Effect of sample drying on reactive Fe and Fe-associated OC content in permafrost soil samples from a palsa transition zone collected in Abisko, Sweden (data comparable to Patzner et al. (2020)). *Reactive Fe is dithionite-citrate extractable Fe corrected by NaCl control extraction and Fe-associated OC is dithionite-citrate extractable OC corrected by NaCl control extraction and citrate background, presented as mg g^{-1} DW-$soil^{-1}$.*

Treatment	Reactive Fe	Fe-associated OC
	[mg g^{-1} DW-$soil^{-1}$]*	
anoxic		
60°C dried	7.38 ± 0.25	86.64 ± 15.03
air dried	7.13 ± 0.09	94.75 ± 29.46
oxic		
60°C dried	6.84 ± 0.12	82.81 ± 7.31
air dried	6.41 ± 0.19	87.58 ± 5.33

*not NaCl control corrected

Table SI 3. Summary table of bulk density, content, stock and percentage of total Fe (6 M HCl extractable), reactive Fe and Fe-associated OC (dithionite-citrate extractable), control Fe and OC (NaCl extraction), TOC content and OC:Fe mass ratio of all soil horizons from replicate soil cores (1, 2) along a soil chronosequence of drained thaw lake basins from Alaska. *Reactive Fe is dithionite-citrate extractable Fe corrected by NaCl control extraction and Fe-associated OC is dithionite-citrate extractable OC corrected by NaCl control extraction and citrate background. Colors indicate organic horizons (brown), cryoturbated/buried horizons (light orange) and mineral horizons (grey).*

	Bulk density	Reactive Fe (control corrected)	Reactive Fe stock (control corrected)	Relative amount reactive Fe	Fe-associated OC (control corrected)	Fe-associated OC (control corrected)	Relative amount Fe-associated OC	OC:Fe	Total Fe	Control Fe	*TOC	Control OC
	g cm^{-3}	mg g^{-1}	kg m^{-2}	% of tot. Fe	mg g^{-1}	kg m^{-2}	% of TOC		mg g^{-1}	mg g^{-1}	mg g^{-1}	mg g^{-1}
Young 1 (0-50 a)												
0-10 cm	0.29	46.68 ± 8.40	1.34 ± 0.24	80.60 ± 21.69	56.19 ± 3.04	1.62 ± 0.09	14.19 ± 0.77	1.20	57.91 ± 11.58	0.10 ± 0.03	395.98	22.45 ± 2.75
10-31 cm	0.57	20.66 ± 0.30	2.48 ± 0.04	49.60 ± 0.91	24.54 ± 0.32	2.94 ± 0.04	14.80 ± 0.19	1.19	41.66 ± 0.47	0.09 ± 0.00	165.85	6.47 ± 0.24
31-56 cm	0.39	13.43 ± 0.42	1.30 ± 0.04	41.18 ± 2.46	0.50 ± 3.00	0.05 ± 0.29	0.50 ± 3.02	0.04	32.61 ± 1.67	0.02 ± 0.00	99.05	2.21 ± 0.01
56-82 cm	1.26	2.05 ± 0.23	0.67 ± 0.07	22.77 ± 2.58	bdl ± bdl	bdl ± bdl	bdl ± bdl	bdl	9.02 ± 0.22	0.00 ± 0.00	11.06	0.78 ± 0.11
82-117 cm	0.79	5.84 ± 0.04	1.62 ± 0.01	35.70 ± 0.25	bdl ± bdl	bdl ± bdl	bdl ± bdl	bdl	16.37 ± 0.06	0.00 ± 0.00	13.07	0.61 ± 0.01
Total		**88.67 ± 8.42**	**7.42 ± 0.26**	**56.27 ± 6.79**	**81.23 ± 4.28**	**4.61 ± 0.31**	**11.86 ± 0.67**		**157.56 ± 11.71**	**0.21 ± 0.03**	**685.01**	**32.53 ± 2.76**
Young 2 (0-50 a)												
0-18cm	0.11	33.90 ± 8.42	0.64 ± 0.16	134.64 ± 35.84	40.21 ± 0.67	0.77 ± 0.01	9.84 ± 0.16	1.19	25.18 ± 2.40	0.07 ± 0.01	408.71	14.67 ± 0.29
18-49cm	0.77	11.15 ± 0.48	2.65 ± 0.12	39.63 ± 3.48	7.76 ± 0.28	1.85 ± 0.07	8.45 ± 0.30	0.70	28.13 ± 2.14	0.05 ± 0.01	91.93	4.67 ± 0.12
49-70cm	1.06	1.91 ± 0.08	0.43 ± 0.02	24.46 ± 1.01	0.21 ± 4.26	0.05 ± 0.95	4.77 ± 97.28	0.11	7.81 ± 0.03	bdl ± bdl	4.38	0.94 ± 0.02
70-90cm	0.98	6.61 ± 0.07	1.30 ± 0.01	32.53 ± 2.58	3.26 ± 6.29	0.64 ± 1.24	15.72 ± 30.35	0.49	20.31 ± 1.60	bdl ± bdl	20.73	1.41 ± 0.10
Total		**53.56 ± 8.44**	**5.02 ± 0.20**	**65.78 ± 10.76**	**51.44 ± 7.63**	**3.30 ± 1.56**	**9.78 ± 1.45**		**81.42 ± 3.59**	**0.12 ± 0.02**	**525.76**	**21.69 ± 0.33**
Medium 1 (50-300 a)												
0-9 cm	0.06	11.16 ± 0.34	0.06 ± 0.00	98.32 ± 4.33	30.24 ± 0.37	0.17 ± 0.00	7.28 ± 0.09	2.71	11.35 ± 0.36	0.06 ± 0.02	415.30	17.85 ± 0.37
9-15 cm	0.13	21.89 ± 0.16	0.17 ± 0.00	123.61 ± 20.44	38.55 ± 2.61	0.31 ± 0.02	8.84 ± 0.60	1.76	17.71 ± 2.92	0.17 ± 0.03	436.30	15.50 ± 1.98
15-48 cm	0.58	12.25 ± 0.62	2.33 ± 0.12	42.90 ± 3.80	21.10 ± 4.72	4.02 ± 0.90	28.48 ± 6.37	1.72	28.57 ± 2.08	0.10 ± 0.01	74.10	6.01 ± 0.75
48-73 cm	1.15	4.92 ± 0.56	1.42 ± 0.16	30.75 ± 4.69	9.93 ± 0.59	2.86 ± 0.17	26.20 ± 1.55	2.02	15.99 ± 1.63	0.01 ± 0.01	37.90	1.33 ± 0.09
73-89 cm	0.36	9.31 ± 0.16	0.54 ± 0.01	35.78 ± 2.92	26.84 ± 0.97	1.56 ± 0.06	42.41 ± 1.54	2.88	26.03 ± 2.08	0.04 ± 0.04	63.30	3.12 ± 0.24
89-123 cm	0.53	7.63 ± 1.44	1.37 ± 0.26	30.94 ± 5.87	3.81 ± 1.19	0.68 ± 0.21	39.31 ± 12.26	0.50	24.67 ± 0.43	0.00 ± 0.00	9.70	0.69 ± 0.16
Total		**67.18 ± 1.72**	**5.90 ± 0.33**	**54.03 ± 2.35**	**130.48 ± 5.65**	**9.61 ± 0.94**	**12.59 ± 0.55**		**124.33 ± 4.49**	**0.38 ± 0.06**	**1036.60**	**44.48 ± 2.17**
Medium 2 (50-300 a)												
0-12cm	0.13	28.18 ± 8.23	0.45 ± 0.13	100.10 ± 29.42	45.44 ± 11.51	0.73 ± 0.18	10.99 ± 2.78	1.61	28.15 ± 0.94	0.10 ± 0.03	413.52	0.85 ± 0.13
12-14cm	0.27	13.71 ± 0.69	0.07 ± 0.00	82.49 ± 13.46	36.13 ± 11.16	0.20 ± 0.06	11.12 ± 3.44	2.64	16.62 ± 2.58	0.12 ± 0.00	324.82	0.74 ± 0.12
14-40cm	0.66	10.34 ± 0.21	1.78 ± 0.04	36.23 ± 0.79	20.40 ± 7.40	3.51 ± 1.27	19.71 ± 7.15	1.97	28.53 ± 0.20	0.11 ± 0.00	103.54	0.27 ± 0.01
40-80cm	0.60	10.02 ± 0.72	2.40 ± 0.17	38.91 ± 10.52	18.86 ± 3.23	4.51 ± 0.77	19.26 ± 3.30	1.88	25.76 ± 6.72	0.06 ± 0.00	97.93	0.24 ± 0.01
80-126cm	0.67	7.38 ± 0.08	2.27 ± 0.03	39.81 ± 3.19	4.92 ± 1.15	1.51 ± 0.35	16.24 ± 3.79	0.67	18.54 ± 1.47	bdl ± bdl	30.32	0.06 ± 0.01
Total		**69.63 ± 8.29**	**6.97 ± 0.22**	**59.10 ± 7.97**	**125.75 ± 17.99**	**10.46 ± 1.54**	**12.96 ± 1.85**		**117.61 ± 7.41**	**0.40 ± 0.03**	**970.13**	**2.16 ± 0.17**

	Bulk density	Reactive Fe (control corrected)	Reactive Fe stock (control corrected)	Relative amount reactive Fe	Fe-associated OC (control corrected)	Fe-associated OC (control corrected)	Relative amount Fe-associated OC	OC:Fe	Total Fe	Control Fe	*TOC	Control OC
	g cm^{-3}	mg g^{-1}	kg m^{-2}	% of tot. Fe	mg g^{-1}	kg m^{-2}	% of TOC		mg g^{-1}	mg g^{-1}	mg g^{-1}	mg g^{-1}
Old 1 (300-2000 a)												
0-12 cm	0.33	24.87 ± 1.21	0.98 ± 0.05	106.43 ± 5.22	46.82 ± 6.01	1.85 ± 0.24	11.01 ± 1.41	1.88	23.37 ± 0.14	0.41 ± 0.00	425.40	13.14 ± 0.53
12-32 cm	1.14	9.65 ± 0.16	2.20 ± 0.04	49.24 ± 5.28	8.94 ± 2.43	2.04 ± 0.55	23.03 ± 6.25	0.93	19.59 ± 2.07	0.30 ± 0.15	38.80	1.76 ± 0.31
32-57 cm	0.50	10.75 ± 0.04	1.36 ± 0.01	48.39 ± 1.69	7.04 ± 5.17	0.89 ± 0.65	5.19 ± 3.81	0.66	22.21 ± 0.77	0.21 ± 0.00	135.60	3.10 ± 0.42
57-85 cm	0.61	10.13 ± 0.45	1.72 ± 0.08	46.34 ± 2.40	2.46 ± 0.24	0.42 ± 0.04	7.18 ± 0.69	0.24	21.86 ± 0.57	0.18 ± 0.02	34.20	1.93 ± 0.17
85-105 cm	0.99	8.96 ± 0.26	1.77 ± 0.05	51.05 ± 1.53	7.68 ± 3.35	1.52 ± 0.66	18.91 ± 8.25	0.86	17.56 ± 0.13	0.18 ± 0.00	40.60	1.67 ± 0.01
Total		**64.36 ± 1.33**	**8.03 ± 0.11**	**61.54 ± 1.85**	**72.94 ± 8.94**	**6.71 ± 1.11**	**10.81 ± 1.33**		**104.58 ± 2.29**	**1.28 ± 0.15**	**674.60**	**21.61 ± 0.76**
Old 2 (300-2000 a)												
0-8 cm	0.13	19.45 ± 1.65	0.20 ± 0.02	144.36 ± 44.21	19.69 ± 9.89	0.20 ± 0.10	5.95 ± 2.99	1.01	13.47 ± 3.96	0.10 ± 0.02	331.00	14.68 ± 2.20
8-15 cm	0.11	15.77 ± 0.53	0.12 ± 0.00	105.11 ± 8.18	20.95 ± 7.38	0.16 ± 0.06	4.88 ± 1.72	1.33	15.01 ± 1.05	0.22 ± 0.00	429.15	13.57 ± 0.73
15-37 cm	0.39	12.78 ± 1.65	1.08 ± 0.14	56.85 ± 7.50	25.75 ± 3.09	2.18 ± 0.26	11.91 ± 1.43	2.02	22.48 ± 0.63	0.12 ± 0.05	216.24	10.01 ± 2.75
37-68 cm	0.08	5.99 ± 0.17	0.15 ± 0.00	25.67 ± 0.73	9.16 ± 1.19	0.23 ± 0.03	6.37 ± 0.83	1.53	23.33 ± 0.02	0.05 ± 0.00	143.88	4.84 ± 0.07
68-108 cm	0.65	8.04 ± 0.09	2.10 ± 0.02	32.13 ± 2.58	3.65 ± 3.78	0.95 ± 0.99	4.08 ± 4.23	0.45	25.03 ± 1.99	0.06 ± 0.01	89.34	4.17 ± 0.40
108-114 cm	1.45	7.97 ± 0.13	0.69 ± 0.01	34.64 ± 3.40	3.84 ± 8.93	0.33 ± 0.78	6.55 ± 15.25	0.48	23.02 ± 2.23	bdl ± bdl	58.57	2.25 ± 0.08
Total		**70.00 ± 2.41**	**4.34 ± 0.14**	**57.22 ± 3.10**	**83.04 ± 16.04**	**4.05 ± 1.29**	**6.55 ± 1.26**		**122.33 ± 5.11**	**0.55 ± 0.05**	**1268.18**	**49.53 ± 3.61**
Ancient 1 (2000-5500 a)												
0-7 cm	0.17	60.26 ± 2.94	0.74 ± 0.04	136.85 ± 13.80	34.65 ± 0.41	0.42 ± 0.00	11.26 ± 0.13	0.57	44.03 ± 3.88	0.04 ± 0.01	307.70	22.70 ± 0.07
7-17 cm	0.14	32.88 ± 2.26	0.45 ± 0.03	99.65 ± 11.03	42.38 ± 6.24	0.58 ± 0.08	12.02 ± 1.77	1.29	33.00 ± 2.86	0.31 ± 0.02	352.50	20.02 ± 0.49
17-34 cm	1.12	2.63 ± 0.93	0.50 ± 0.18	17.15 ± 6.04	4.36 ± 6.56	0.83 ± 1.25	14.74 ± 22.16	1.66	15.36 ± 0.04	0.02 ± 0.00	29.60	3.81 ± 0.17
34-50 cm	0.60	21.82 ± 1.42	2.08 ± 0.14	89.94 ± 13.31	39.24 ± 5.29	3.75 ± 0.51	41.13 ± 5.55	1.80	24.26 ± 3.23	0.11 ± 0.08	95.40	8.81 ± 2.73
50-87 cm	0.45	15.33 ± 1.24	2.53 ± 0.21	51.54 ± 9.18	13.62 ± 4.67	2.25 ± 0.77	12.09 ± 4.15	0.89	29.75 ± 4.72	0.02 ± 0.00	112.60	5.72 ± 0.09
87-116 cm	0.66	7.62 ± 0.09	1.45 ± 0.02	32.88 ± 0.53	bdl ± bdl	bdl ± bdl	bdl ± bdl	bdl	23.19 ± 0.25	0.00 ± 0.01	22.90	3.04 ± 0.41
Total		**140.55 ± 4.26**	**7.76 ± 0.31**	**82.88 ± 4.44**	**134.25 ± 11.49**	**7.83 ± 1.55**	**14.58 ± 3.72**		**169.59 ± 7.48**	**0.50 ± 0.08**	**920.70**	**64.11 ± 2.82**
Ancient 2 (2000-5500 a)												
0-7 cm	0.35	17.72 ± 0.86	0.50 ± 0.02	77.12 ± 6.70	31.68 ± 7.70	0.90 ± 0.22	7.77 ± 1.89	1.79	22.97 ± 1.66	0.07 ± 0.00	407.85	12.09 ± 0.90
7-17 cm	0.52	15.33 ± 1.42	0.72 ± 0.07	105.89 ± 9.94	77.50 ± 12.02	3.63 ± 0.56	17.57 ± 2.72	5.05	14.48 ± 0.20	0.14 ± 0.01	441.09	16.77 ± 0.18
17-34 cm	0.61	4.59 ± 0.15	0.51 ± 0.02	38.98 ± 6.10	21.70 ± 13.77	2.39 ± 1.52	16.28 ± 10.33	4.72	11.78 ± 1.81	0.03 ± 0.00	133.30	5.45 ± 0.49
34-50 cm	0.32	8.33 ± 1.06	0.85 ± 0.11	38.59 ± 5.43	bdl ± bdl	bdl ± bdl	bdl ± bdl	bdl	21.59 ± 1.28	0.03 ± 0.02	67.93	3.49 ± 0.21
50-87 cm	0.57	6.56 ± 0.34	1.16 ± 0.06	38.51 ± 2.45	3.20 ± 1.86	0.57 ± 0.33	7.02 ± 4.07	0.49	17.04 ± 0.64	bdl ± bdl	45.60	3.47 ± 0.06
87-116 cm	0.99	5.25 ± 0.03	1.30 ± 0.01	44.40 ± 4.62	10.16 ± 5.01	2.53 ± 1.25	51.01 ± 25.17	1.94	11.83 ± 1.23	bdl ± bdl	19.92	2.99 ± 0.06
Total		**57.79 ± 2.01**	**5.04 ± 0.14**	**57.97 ± 2.70**	**144.25 ± 20.54**	**10.01 ± 2.08**	**12.93 ± 1.91**		**99.69 ± 3.10**	**0.27 ± 0.02**	**1115.70**	**44.26 ± 1.07**

*TOC: data obtained by Mueller et al. (2015)

bdl: beow detection limit, indicates horizons where Fe-associated OC was lower than combined citrate background and control OC

Table SI 4. Mössbauer spectra hyperfine parameters for organic, cryoturbated and mineral horizons of young and ancient soil cores along a permafrost soil chronosequence of drained thaw lake basins from Alaska.

Sample	Temperature	Phase	CS	i E_Q	Í	B_{hf}	Pop (±)	p2	Fe mineral phase
	K		mm s^{-1}	mm s^{-1}	mm s^{-1}	T	%		
Young 1 - organic	77	Db1	0.42	0.73			100 (0.32)	0.57	Fe(III), Fh
	5	Sxt	0.44		-0.02	45.5	88 (0.31)	0.6	Fe(III), Fh
		Db	0.54	0.84			11 (0.57)		œ
Young 2 - cryoturbated	77	Db1	0.47	0.68			58.1 (0.27)	0.69	Fe(III), Fh
		Db2	1.24	2.88			41.9 (0.27)		Fe(II)
	5	Sxt1	0.45		-0.05	47.4	26.0 (0.26)	1.01	Fe(III), Fh
		Sxt2	0.93		0.38	7.75	74.0 (0.41)		œ
Young 1 - mineral	77	Db1	0.47	0.69			57.9 (0.29)	0.62	Fe(III), Fh
		Db2	1.24	2.86			42.1 (0.20)		Fe(II)
	5	Sxt1	0.42		-0.08	48.7	28.3 (0.49)	0.77	Fe(III), Fh
		Sxt2	0.92		0.43	7.55	71.7 (0.49)		œ
Ancient 1 - organic	77	Db1	0.49	0.77			100 (0.14)	0.59	Fe(III), Fh
	5	Sxt	0.47		-0.05	47.8	69.4 (0.48)	0.66	Fe(III), Fh
		Db	0.48	0.53			30.6 (0.42)		œ
Ancient 1 - cryoturbated	77	Db1	0.43	0.75			54.3 (0.42)	0.59	Fe(III), Fh
		Db2	1.2	2.71			45.7 (0.40)		Fe(II)
	5	Sxt1	0.43		-0.06	47.46	33.3 (0.49)	0.67	Fe(III), Fh
		Sxt2	0.87		0.44	7.84	66.6 (0.55)		œ
Ancient 1 - mineral	77	Db1	0.49	0.71			42.9 (0.34)	0.67	Fe(III), Fh
		Db2	1.21	2.7			57.1 (0.19)		Fe(II)
	5	Sxt1	0.45		-0.05	47.35	28.4 (0.31)	1.15	Fe(III), Fh
		Sxt2	0.91		0.39	7.72	71.6 (0.21)		œ

Db: doublet, Sxt: sextet, CS: center shift, i EQ: quadrupole splitting, Í: quadrupole shift, B_{hf}: hyperfine field, Pop: relative abundance, p2: goodness of fit, Fe mineral phase - Fe(II): ferrous Fe, Fe(III): ferric Fe, Fh: ferrihydrite, œ: unknown

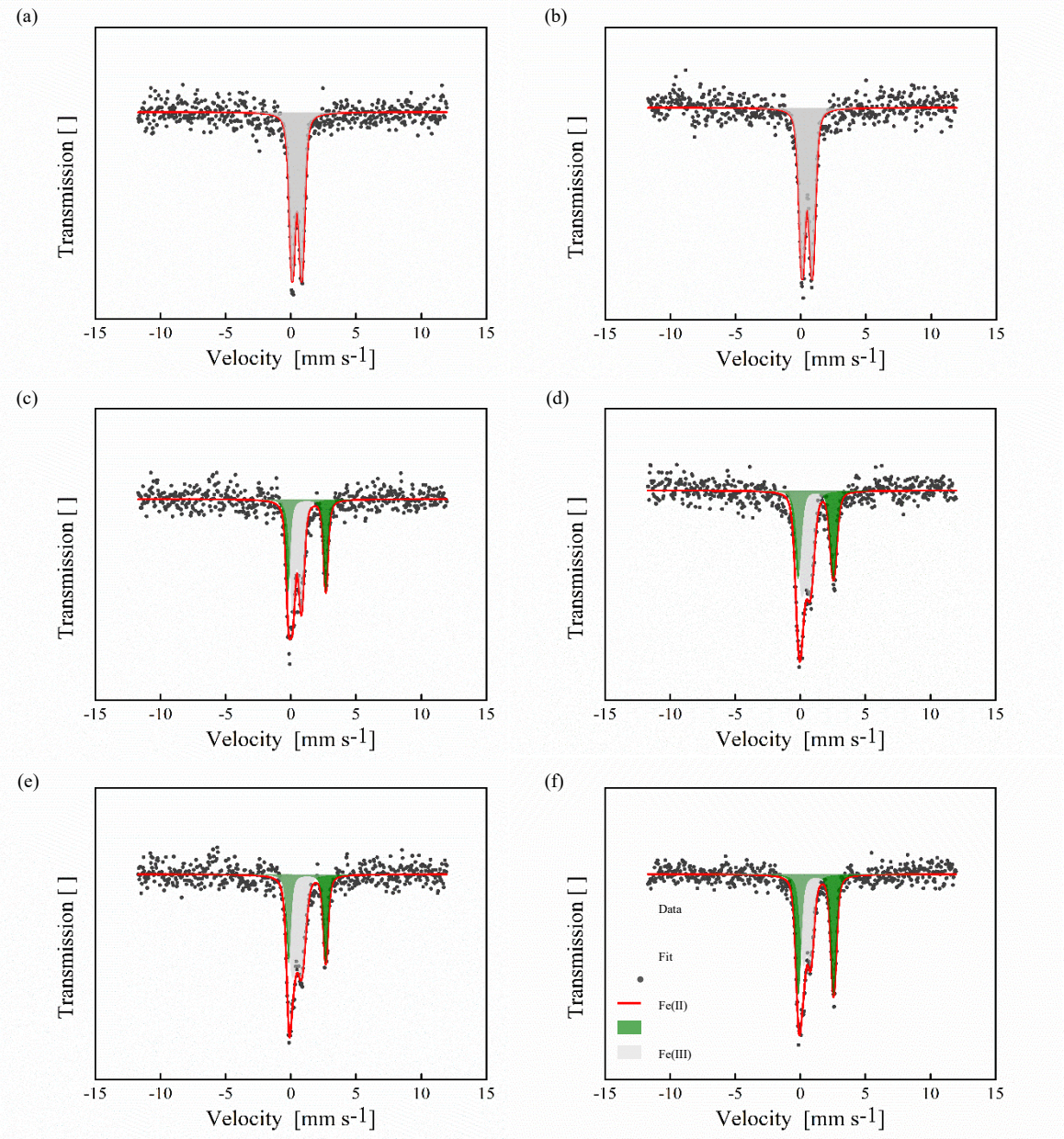

Figure SI 5. Mössbauer transmission spectra collected at 77 K for (a) Young 1 – organic, (b) Ancient 1 – organic, (c) Young 2 – cryoturbated, (d) Ancient 1 – cryoturbated, (e) Young 1 – mineral and (f) Ancient 1 – mineral horizons of young and ancient soil cores along a permafrost soil chronosequence in northern Alaska.

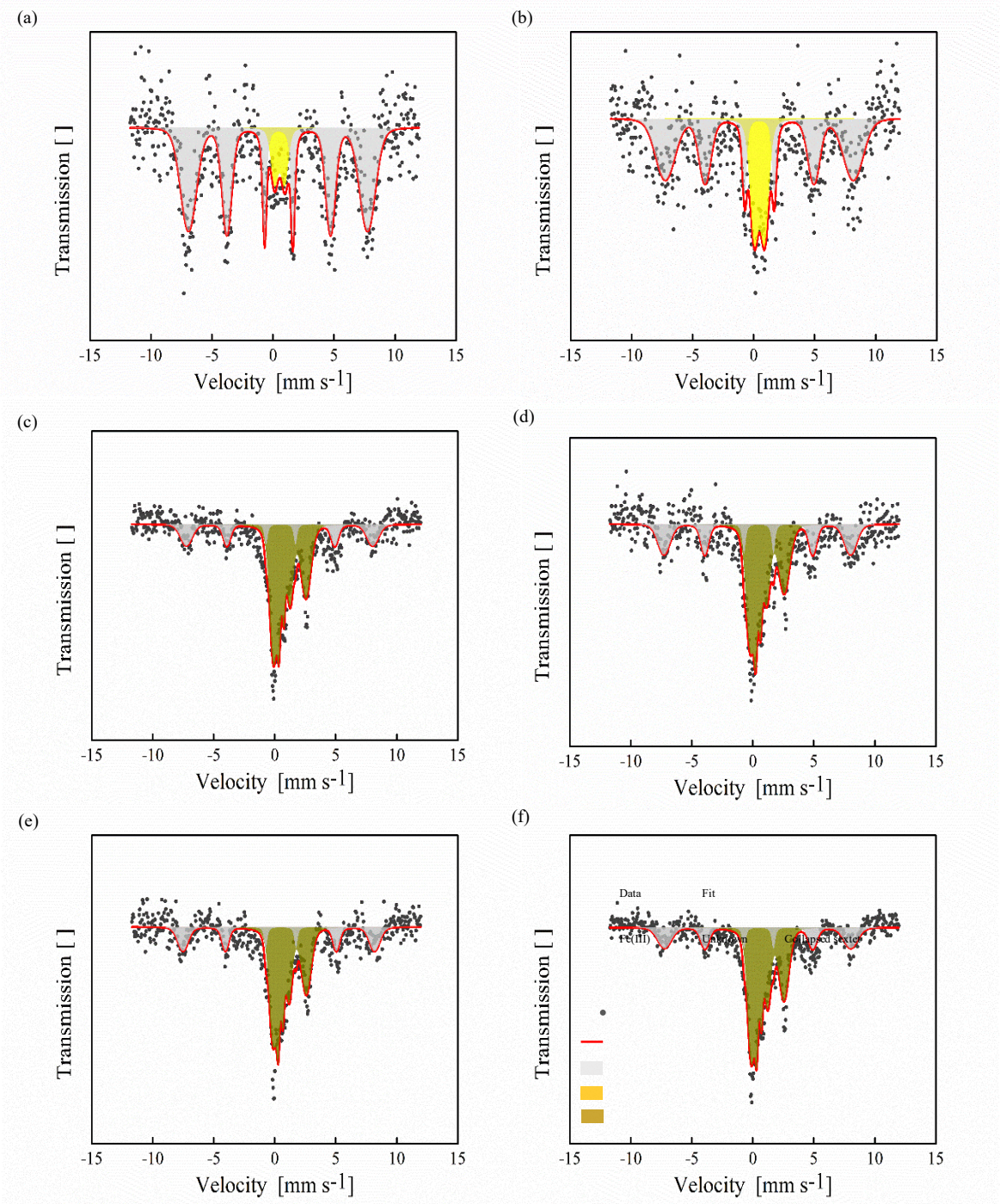

Figure SI 6. Mössbauer transmission spectra collected at 5 K for (a) Young 1 – organic, (b) Ancient 1 – organic, (c) Young 2 – cryoturbated, (d) Ancient 1 – cryoturbated, (e) Young 1 – mineral and (f) Ancient 1 – mineral horizons of young and ancient soil cores along a permafrost soil chronosequence in northern Alaska.

References

Herndon E. M., AlBashaireh A., Singer D., Roy Chowdhury T., Gu B. and Graham D. (2017) Influence of iron redox cycling on organo-mineral associations in Arctic tundra soil. *Geochimica et Cosmochimica Acta* **207**, 210–231.

Mueller C. W., Rethemeyer J., Kao-Kniffin J., Löppmann S., Hinkel K. M. and Bockheim J. G. (2015) Large amounts of labile organic carbon in permafrost soils of northern Alaska. *Global change biology* **21**, 2804–2817.

Patzner M. S., Mueller C. W., Malusova M., Baur M., Nikeleit V., Scholten T., Hoeschen C., Byrne J. M., Borch T., Kappler A. and Bryce C. (2020) Iron mineral dissolution releases iron and associated organic carbon during permafrost thaw. *Nat Commun* **11**, 6329.

Wagai R. and Mayer L. M. (2007) Sorptive stabilization of organic matter in soils by hydrous iron oxides. *Geochimica et Cosmochimica Acta* **71**, 25–35.

General conclusions and outlook

Minerals, specifically poorly crystalline minerals (e.g. iron(III) (oxyhydr)oxides), are widely assumed to protect organic matter (OM) from degradation in the environment, thus promoting the persistence of OM in soils and sediments. At the mineral-organic interface a broad set of interactions occur, with minerals adsorbing OM to their surfaces[1] and/or acting as catalysts for organic reactions[2,3]. Minerals can serve as redox partners for OM through direct electron transfer[4] or by generating reactive oxygen species[5], which then oxidize the associated organic compounds[6]. Furthermore, the compartmentalization of soil and sediments by minerals creates unique microsites that host diverse microbial communities. This multiplicity of interactions, as previously stated by Kleber *et al.*[7], suggests that the general assumption that the mineral matrix provides a protective function for OM is 'overly simplistic'. Kleber *et al.*[7] stated that future work must recognize adsorption as a condition for further reactions, an intermediate stage, and not as a final destination for organic adsorbates. Further, Kleber *et al.*[7] emphasized that future work should consider the spatial and functional complexity, including redox fluctuations, that is characteristic of the environment where mineral-OM interactions are observed. The need to move away from traditional batch experiments, conducted with phases dispersed in a slurry, is clearly stated[7]. Instead, the focus should be set on experimental approaches preserving the 3D microstructure of natural mineral-OM interfaces[7].

Our research on the microbial iron (Fe) cycle in thawing permafrost peatlands reveals that the rusty carbon sink is not a permanent state, in fact, is highly dynamic and strongly depends on spatial, but also temporal fluctuating redox conditions. This PhD focused mainly on *in situ* quantification and characterization of reactive iron-organic carbon (OC) associations and of microbial key players in iron- and methane-cycling along a thaw gradient at Stordalen mire. The findings of this research stress the need of interdisciplinary approaches combining lab based-experiments, including slurry batch experiments to gain basic mechanistic understanding and ultimately experiments with preserved, intact 3D microstructure of Fe-OC associations with field work and *in situ* measurements at various permafrost sites. Only the combination of lab-based and *in situ* will help to answer the fundamental questions in science by being able to upscale microscale processes to its global impact via model predictions. Only by these interdisciplinary approaches, we are able to face and find solutions for environmental problems, such as the climate crisis.

General conclusions and outlook

In the following, the findings of this PhD work are discussed and the base for potential future experiments and approaches is aligned.

The rusty carbon sink in thawing permafrost environments

The rusty carbon sink was described already in numerous permafrost environments[8-10] with the potential to preserve 19.5±12.3% of total soil OC (TSOC) pool[10]. This PhD work describes for the first time what happens to this rusty carbon sink during and after complete permafrost thaw. It clearly shows that the rusty carbon sink is destabilized by global warming and can not preserve OC with permafrost thaw.

In the active layer of the palsa, underlain by intact permafrost, we found up to 20% of TSOC bound to reactive Fe (Figure 1). Along palsa hillslopes into the semi-wet, partially-thawed bog, Fe mineral dissolution in the active layer leads to a release of Fe and Fe-bound OC into the surrounding porewater (Figure 1). Here, in the active layer of the partially-thawed bog the rusty carbon sink appears to be very dynamic due to seasonal redox fluctuations. In early summer, directly after snow melt, the soils are water-logged, and oxygen (O_2) limited. Remaining reactive iron phases, after palsa collapse, are dissolved and Fe and associated OC are released. Whereas, in late summer, due to increasing active layer depth and decreasing runoff, the conditions become more dry and less reduced, leading to Fe(II) oxidation and reactive Fe mineral formation with the potential to sequester OC. In the completely thawed fen, constant water-logging and O_2 limitation lead to permanent reduced conditions favoring microbial iron(III) reduction resulting in mineral dissolution and aqueous Fe^{2+} and dissolved OC (DOC) mobilization (Figure 1).

Still some open questions remain (see also Figure 1):

(1) How much OC is bound to reactive Fe in deeper soil layers?

The presented work focused on the active layer along the permafrost thaw gradient at Stordalen mire, Abisko (Sweden), ignoring deeper, still frozen soil mineral layers. Our results along a chronosequence of drained thaw lake basins showed that deeper cryoturbated horizons have the highest potential to sequester OC being bound to reactive Fe (chapter 5).

(2) How much OC is bound to (Fe in) clays along the permafrost thaw gradient?

Along the permafrost thaw gradient, Fe in clays is increasing significantly in the transition zone and mineral horizon from palsa to fen. During EXAFS analysis, the best fits were obtained with natural nontronite and ferrosmectite (chapter 2). As previously stated, the interactions of hydrous Fe oxides and phyllosilicate clays can modify DOC sorption and desorption by affecting the surface charges of the minerals[11].

(3) *How much OC is bound to reactive Fe in the porewater and surface water bodies in form of colloids?*

The release of aqueous Fe^{2+} and DOC during permafrost thaw results in colloidal formation of freshly formed Fe-OC associations at the oxic to anoxic interface in surface water in fen[12]. First results reveal that the iron is mainly reactive Fe and binds a substantial amount of OC (unpublished data).

(4) *How much OC is bound to reactive Fe in soils affected by birch forest expansion into the wetland?*

At the subarctic permafrost peatland, Stordalen mire, birch trees (*Betula pubescence* ssp. *czerepanovii*) are expanding into the wetland as a response to permafrost thawing[13]. An increase of birch forest cover from 8.7 to 22.9% was recorded between 1997-2010[13,14]. Preliminary results showed an increase in reactive Fe-OC associations along a wetland to birch forest transect (unpublished data).

To answer these questions, field sampling of soil (including deeper layers and permafrost ice), as well as surface and porewater filtered through different sizes (not only 0.22 μm as done in this study) to capture Fe-OC associations in different fractions should be conducted. Additionally, similar as described in chapter 4, *in situ* sorption experiments should be conducted with biogenically formed reactive Fe minerals, co-precipitates with OC and (reactive Fe in) clays pre- or un-sorbed with OC, also exposed in deeper soil layers and not only during summer, but complete seasons, to better understand the dynamics of the rusty carbon sink.

In the lab, focus could be set on the evaluation of the dithionite citrate approach to quantify reactive Fe and associated OC (Figure 1). Known issues with this extraction are mentioned in chapter 2. The following question remains:

(1) *Is the dithionite citrate approach over- or underestimating the reactive Fe-associated OC?*

Fisher *et al.*[15] showed evidence for partial dissolution of the Fe phases and associated OC by the dithionite citrate approach, indicating that carbon sequestration by Fe minerals is likely to be more significant than currently estimated. The dithionite citrate approach could be evaluated under e.g. different extraction pHs (buffered and un-

buffered) and different sampling preparation methods (freeze-dried vs. drying at room temperature).

Additionally, different extractions should be performed to target higher crystalline Fe phases (stronger than 6M HCl, as this was the strongest extraction performed in this thesis) and (Fe in) clays and its associated OC.

Ultimately, these future experiments are essential to further understand the dynamics of the rusty carbon sink with progressive climate change.

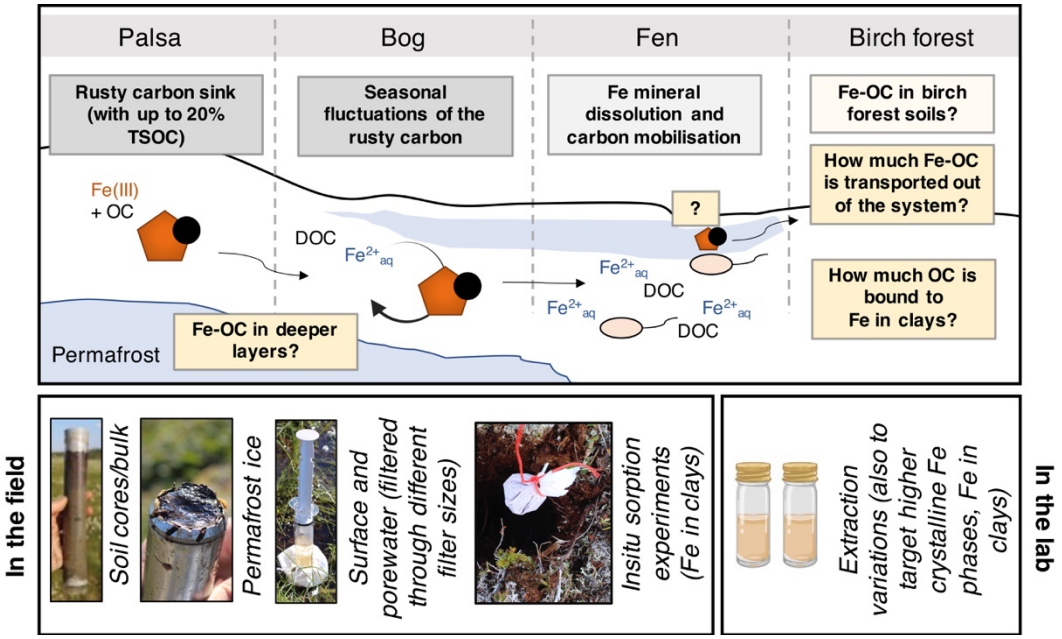

Figure 1. Knowns and unknowns about the rusty carbon sink along a permafrost thaw gradient. *Grey and schematic illustrates findings of this PhD work, whereas yellow shows the remaining unknowns concerning the dynamics of the rusty carbon sink from palsa to bog to fen to birch forest. Field work should be combining sampling with in situ sorption experiments. In the lab, further extractions could be conducted to evaluate the dithionite citrate approach and to target (Fe in) clays and its associated OC. Lab equipment (extraction vials) is made by ©BioRender - biorender.com.*

Organic carbon associated with iron minerals in permafrost peatlands

Extensive carbon characterization has been performed on DOC in permafrost environments[13,16,17]. To date, it remains challenging to characterize mineral-associated OC in environmental systems without effecting its initial soil matrix and/or OC composition by the experimental setup. In this thesis, we were able to quantify and to identify the reactive Fe-associated OC along a thawing permafrost gradient.

In the active layer of the palsa, underlain by intact permafrost, the reactive Fe-bound OC is comprised of loosely bound aliphatic and strongly bound aromatic species (Figure 2). Reductive dissolution of Fe(III) minerals by Fe(III)-reducing microorganisms along the palsa hillslope leads to the release of Fe and the loosely bound aliphatic compounds, resulting in the highest pulse of aqueous Fe^{2+} (153.24 ± 40.14 mg Fe/L) and DOC (535.75 ± 131.45 mg C/L) along the whole thaw gradient. The increasing bioavailability of DOC (vs. previously mineral associated) leads to its further decomposition, an increasing nominal oxidation state of carbon (NOSC) and a peak in bioavailable acetate (61.7 ± 42.6 mg C/L). The strongly bound aromatics were retained by remaining reactive Fe species along the thaw gradient. In the fen porewater, fatty acids like acetate, lactate, butyrate, and propionate were detected (Figure 2).

The following questions remain (see also Figure 2):

(1) *How bioavailable is the reactive Fe-bound OC in intact palsa soils for the microbial community (e.g. specifically for Fe(III)-reducers, for fermenters, etc.)?*
Relative to aromatic, aliphatic compounds are expected to be more bioavailable to microorganisms[16,18,19].

(2) *What type of OC is bound to reactive Fe phases in deeper, still frozen permafrost layers, which is potentially released during permafrost thaw into the surrounding porewater? How bioavailable is it?*

(3) *What type of OC is bound to reactive Fe phases as colloids in surface and porewater? How accessible is it for microbes?*
Riedel *et al.*[12] hypothesized that vascular plant-derived aromatic and pyrogenic compounds are preferentially retained by iron colloids, whereas the majority of carboxyl-rich aliphatic acids would remain dissolved in the surrounding porewater.

(4) *Are Fe-OC colloids transported out of this system (here described thaw gradient) into rivers and lakes and fertilizing these nearby environments or metabolized and OC emitted as greenhouse gases (GHG) before?*
The peatland Stordalen mire could be a significant source of bioavailable iron and associated OC to surrounding lakes and rivers, as has been shown for other permafrost environments[20].

To answer these questions, field sampling of soil (including deeper layers and permafrost ice), as well as surface and porewater should be conducted to characterize the fate of OC associated to reactive Fe in different environmental compartments. As described previously (Figure 1), the same sorption experiments as described above would be used to characterize bound or released (in comparison to initially pre-sorbed) OC.

In the lab, additional experiments could be conducted to further characterize the reactive Fe-associated OC. Sorption and co-precipitation experiments with poorly crystalline Fe (e.g. synthetic or biogenically formed ferrihydrite) or Fe in clays and *in situ* DOC in bog and fen pore- and surface water could be conducted to determine which fraction of the present OC is preferentially sorbed to/co-precipitated with iron and which fraction remains in solution. Bioavailability experiments would help to determine the accessibility of OC to be metabolized by certain microorganisms (isolated Fe(III)-reducers/fermenters/methanogens etc. from Stordalen mire).

Furthermore, different analytics could be used to identify and quantify the OC in these experimental setups such as nuclear magnetic resonance spectroscopy (NMR) and high resolution mass spectrometry (FT-ICR-MS) or focused ion beam scanning electron microscopy (FIB-SEM), scanning transmission X-ray microscopy (STXM), nanoscale secondary ion mass spectrometry (nanoSIMS), high resolution transmission electron microscopy (HR-TEM) and single particle inductively coupled plasma mass spectrometry (spICP-MS). Because each analysis has its limitations (for FT-ICR-MS, e.g the recovery of OC after solid phase extraction (SPE)-column treatment and different ionization techniques), a combination of different analytics is required to get a most representative characterization of reactive Fe-associated OC.

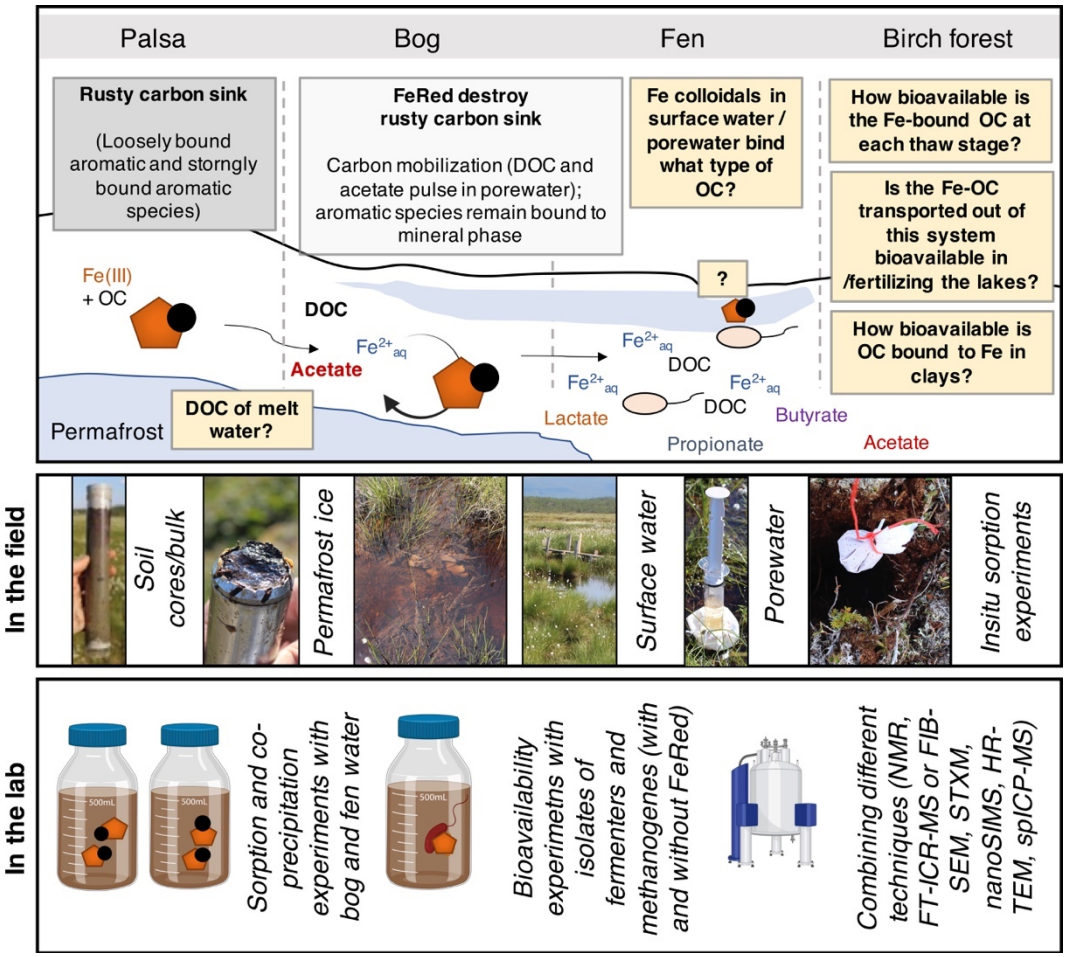

Figure 2. Knowns and unknowns of the fate of OC associated to reactive Fe along the permafrost thaw gradient. *Grey and schematic illustrates findings of this PhD work, whereas yellow shows the remaining unknowns concerning identity of OC associated to reactive Fe from palsa to bog to fen to birch forest. Field work should combine sampling with in situ sorption experiments. In the lab, additional experiments need to be conducted to further determine the identity of reactive Fe-associated OC and its bioavailability along the permafrost thaw gradient. Lab equipment (bottles, instrument) is made by ©BioRender - biorender.com.*

The microbial iron cycle in thawing permafrost peatlands

Classical iron-cycling bacteria such as Fe(III)-reducers (e.g. *Rhodoferax ferrireducens*) and Fe(II)-oxidizers (e.g. *Gallionella ferruginea*) were already found in permafrost environments[21,22]. However, detailed understanding of the microbial iron cycle and its impact on carbon mobilization and greenhouse gas emissions along a permafrost thaw gradient was so far lacking. We described the microbial iron cycle for the first time during palsa collapse and with complete permafrost thaw.

Along the palsa hillslope, we found abundant and active Fe(II)-oxidizing microorganisms such as *Gallionella* sp. and *Sideroxydans* sp. which can not sustain or reform the rusty carbon sink during collapse. During palsa collapse, Fe(III)-reducing microorganisms such as *Geobacter* sp. and *Clostridium* sp. significantly increase in abundance and activity, reduce present reactive Fe oxides coupled to OC oxidation and release previously associated OC, CO_2 and aqueous Fe^{2+}. The increase in Fe(III)-reducing bacteria is accompanied by an increase in abundance and activity of methanogenic microorganisms, mainly *Methanobacterium* sp., and methanotrophic microorganisms, such as *Roseiarcus* sp. and other *Beijerinckiacaeae.* The presence of only hydrogenotrophic methanogens could be explained by the higher thermodynamical favorability of Fe(III) reduction coupled to acetate oxidation as compared to acetoclastic methanogenesis. Along the thaw gradient, Fe(III)-reducing bacteria are increasing from 2.4 x 10^3 cells per g soil to 3.1 x 10^5 cells per g soil in the transition zone (interface between organic and mineral horizon) from palsa, where highest reactive Fe oxide and associated OC amounts can be found, to fen.

To date, a lot of questions remain (see also Figure 3):

(1) *What microbial iron key players are abundant and active in deeper, still frozen soil layers?*
Vigneron *et al.*[23] found contrasting winter versus summer microbial communities in a permafrost thaw lake and that *Gallionella* sp. was only present under frozen conditions.

(2) *How are Fe(II)-oxidizers (microaerophilic, phototrophic and nitrate reducing) distributed along the thaw gradient?*
To date, we were only able to determine an increase for Fe(III)-reducers based on most probable numbers (see chapter 2). The same approach for microaerophilic Fe(II)-

oxidizers (using oxygen and iron gradients in headspace vials[24], gradient tubes[25] and zero valent iron plates[26]) didn't work yet (unpublished data).

(3) *What kind of iron-cycling microorganisms can be found in the porewater and surface waters?*

Emerson *et al.*[21] described microbial iron mats in surface water bodies at the North Slope of Alaska near Toolik Field Station and found sheath-forming *Leptothrix ochracea.* To our best knowledge, no one described the microbial iron community in porewater along a permafrost thaw gradient yet (as e.g. done by Glodowska *et al.*[27] in an arsenic contaminated groundwater aquifer).

(4) *What kind of iron-cycling microorganisms can be found in the soils from fen to birch forest?*

First results indicate an increase of *Gallionella* sp. (up to 24% absolute abundance of 16S rRNA bacteria) towards the expanding birch forest (unpublished data).

(5) *How are iron-cycling and methane-cycling microorganisms interlinked along the whole permafrost thaw gradient?*

In chapter 3, we only focused on the palsa to bog permafrost collapse.

To answer these questions, field sampling of soil (including deeper layers and permafrost ice), as well as surface and porewater should be conducted to identify microbial iron- and methane-cycling key players. As described previously (Figure 1 and Figure 2), the same sorption experiments could be used as isolation strategy (as performed in chapter 2) for Fe(II)-oxidizers.

In the lab, the microbial community analysis, specifically the iron- and methane-cycler, along the thaw gradient in soil, in porewater and in surface water could be identified as described in chapter 2 by 16S rRNA Amplicon (gene) sequencing. Quantification and isolation of Fe(II)-oxidizers could be performed by implementing a new enrichment/isolation technique (e.g. different gradient of iron and oxygen in agar plates). Isolation efforts for iron- and methane-cycling microorganisms should be made using synthetic bog and fen water with additives (such as fatty acids and trace elements) closest to environmental conditions in liquid media, but also soil matrix additives, see e.g. soil substrate membrane system described by Svenning *et al.*[28]. To better understand the link between iron- and methane-cycling, batch experiments could be conducted, similar as performed previously[27], to rule out or identify certain microbial pathways, such as e.g. methane oxidation coupled to iron(III) reduction at this permafrost peatland.

Furthermore, available microbial genome and metagenome data, as for example provided by Woodcroft *et al.*[29], should be further analyzed for iron-cycling microorganisms by using FeGenie for identification of iron genes and iron gene neighborhoods[30].

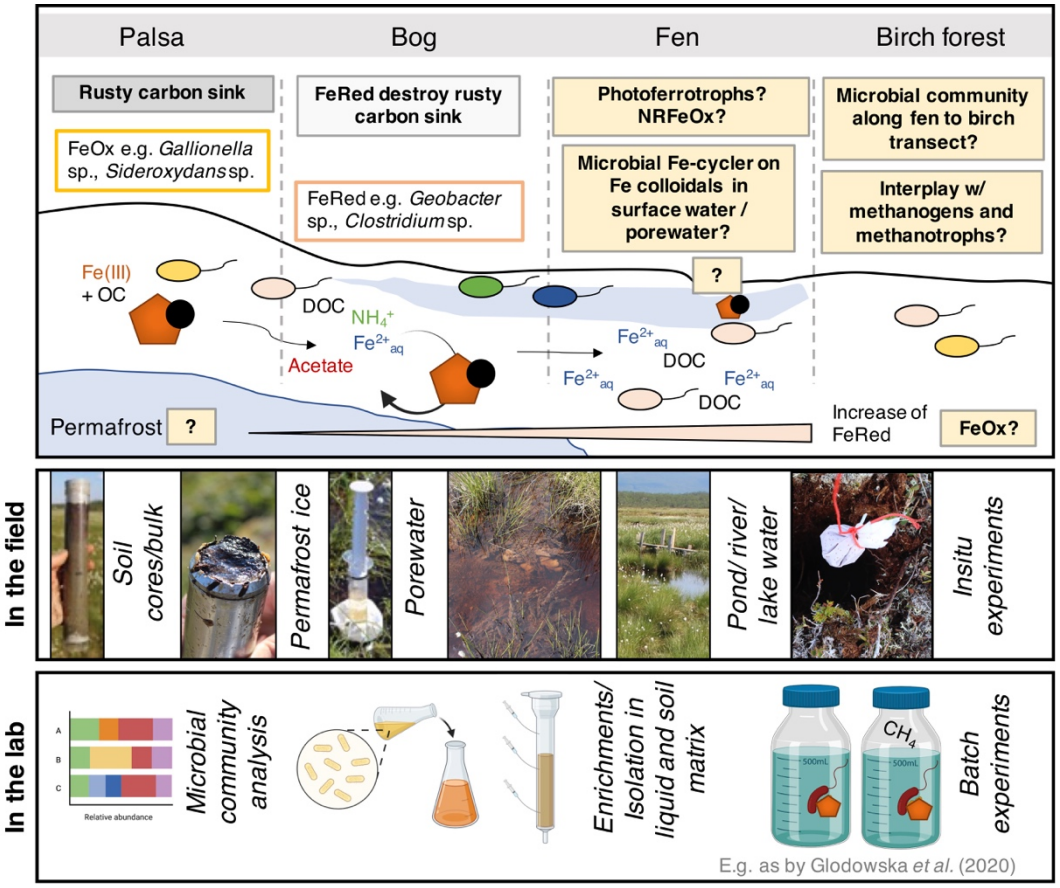

Figure 3. Knowns and unknowns of the fate of the microbial iron cycle along the permafrost thaw gradient. *Grey and schematic illustrates findings of this PhD work, whereas yellow shows the remaining unknowns concerning the microbial iron cycling from palsa to bog to fen to birch forest. Field work should be combining sampling with in situ isolation experiments. In the lab, further experiments, combined with certain bioinformatic tools such as FeGenie, need to be conducted to further determine the microbial iron community along the permafrost thaw gradient, also in already exciting microbial community data sets. Lab equipment (graph, bottles, columns) is made by ©BioRender - biorender.com.*

The loss of the rusty carbon sink and its impact on carbon mobilization and greenhouse gas emissions

The rusty carbon sink was found in different intact permafrost enviornments[8-10,31], but so far, the dynamics of the rusty carbon sink with permafrost thaw and its impact on carbon mobilization and greenhouse gas emissions were not described. Only Lipson *et al.*[32] suggested that net reduction of Fe oxides could potentially contribute to an estimated 40-63% to ecosystem respiration at sites depending on the thickness of the organic layer. We now described the OC mobilization following iron(III) reduction, correlating with methane and carbon dioxide emissions, along a permafrost thaw gradient.

In the active layer of the palsa, underlain by intact permafrost, up to 20% of total OC is bound to reactive Fe. These Fe-OC associations form a rusty carbon sink as long as the permafrost is still intact. As soon as the palsas begin to thaw and start to collapse, conditions become favorable for Fe(III)-reducing bacteria which effectively reduce the reactive Fe oxides and release associated OC and aqueous Fe^{2+}. In the active layer of the semi-wet, partially-thawed bog, the rusty carbon sink can be seasonally (re-)formed and reduced, potentially shifting from a carbon sink to a carbon source, including an increase in dissolved OC and GHG emissions such as CO_2 and CH_4. In the active layer of the fully-thawed fen, only minor quantities of reactive Fe oxides were detected, with no measurable associated OC.

Along the permafrost thaw gradient, increasing CH_4 and CO_2 production potentials, higher relative CH_4/CO_2 ratios, and a shift in CH_4 production pathway from CO_2 reduction to acetate cleavage were observed[17,33,34].

The following open research questions remain (see also Figure 4):

(1) *How much percent of the previously associated OC ends up as dissolved OC and how much percent of the previously associated OC is directly emitted as CO_2 during Fe(III) reduction coupled to carbon oxidation?*

(2) *How much percent of the DOC pulse at the collapsing front is generated by the release of previously iron associated OC and how much percent is coming from other processes during palsa collapse?*

(3) *How much is the seasonal fluctuation of the rusty carbon sink contributing to seasonal GHG emissions (in percent of total GHG emissions)?*

(4) How much percent of the DOC is (re-)trapped by Fe colloids in the surface and porewater?

(5) Is the birch forest expansion favoring a (re-)formation of the rusty carbon sink and if so, how much percent of OC is bound again in these future forest soils?

To answer these questions, field sampling of gases, soil (bulk and cores) and water (surface and porewater) would be required for future microcosm and preserved 3D microstructure experiments (Figure 4). *In situ* experiments should be conducted. It could include the injections of aqueous Fe^{2+} or the exposure of reactive Fe oxides (e.g. ferrihydrite), as already done in laboratory experiments[22], under the gas chambers vs. controls with no iron amendments at the different thaw stages. Additionally, closed columns with ^{57}Fe labeled reactive Fe oxides and sorbed ^{13}C organic matter (^{13}C OM similar produced as has been done in Chen *et al.*[35]) could be exposed in the field. These columns would remain open at the vertical sidewalls with membranes so that a flow through of porewater of a certain size (e.g. smaller than 0.45 μm) would be ensured. Over the experimental run, porewater and gas samples of the column would be taken to determine iron and carbon mobilization, as well as GHG emissions. At the end of the experiment, the microbial community and secondary Fe mineral transformation and associated OC would be determined in the solid phase of the columns (Figure 4).

In the lab, microcosms and preserved 3D microstructure experiments (e.g. column experiments) could be conducted under various environmental conditions including freeze-thaw cycles[36], dark-light shifts[37] and redox fluctuations (oxic vs anoxic)[35] to determine different rates of iron(III) reduction, aqueous Fe^{2+} and carbon mobilization, as well as GHG emissions. To get a better understanding of occurring metabolic pathways, the microbial community would be 16S rRNA Amplicon (gene) sequenced at the beginning, in the middle and at the end of each experimental run and specifically checked for iron- and methane-cycling microorganisms (Figure 4).

Ultimately, the rates of iron(III) reduction, of aqueous Fe^{2+} and carbon mobilization, as well as its resulting GHG production, would be incorporated in existing climate models to better estimate the impact of the loss of the rusty carbon sink on GHG emissions and thus to better predict future GHG emissions of these permafrost environments (Figure 4).

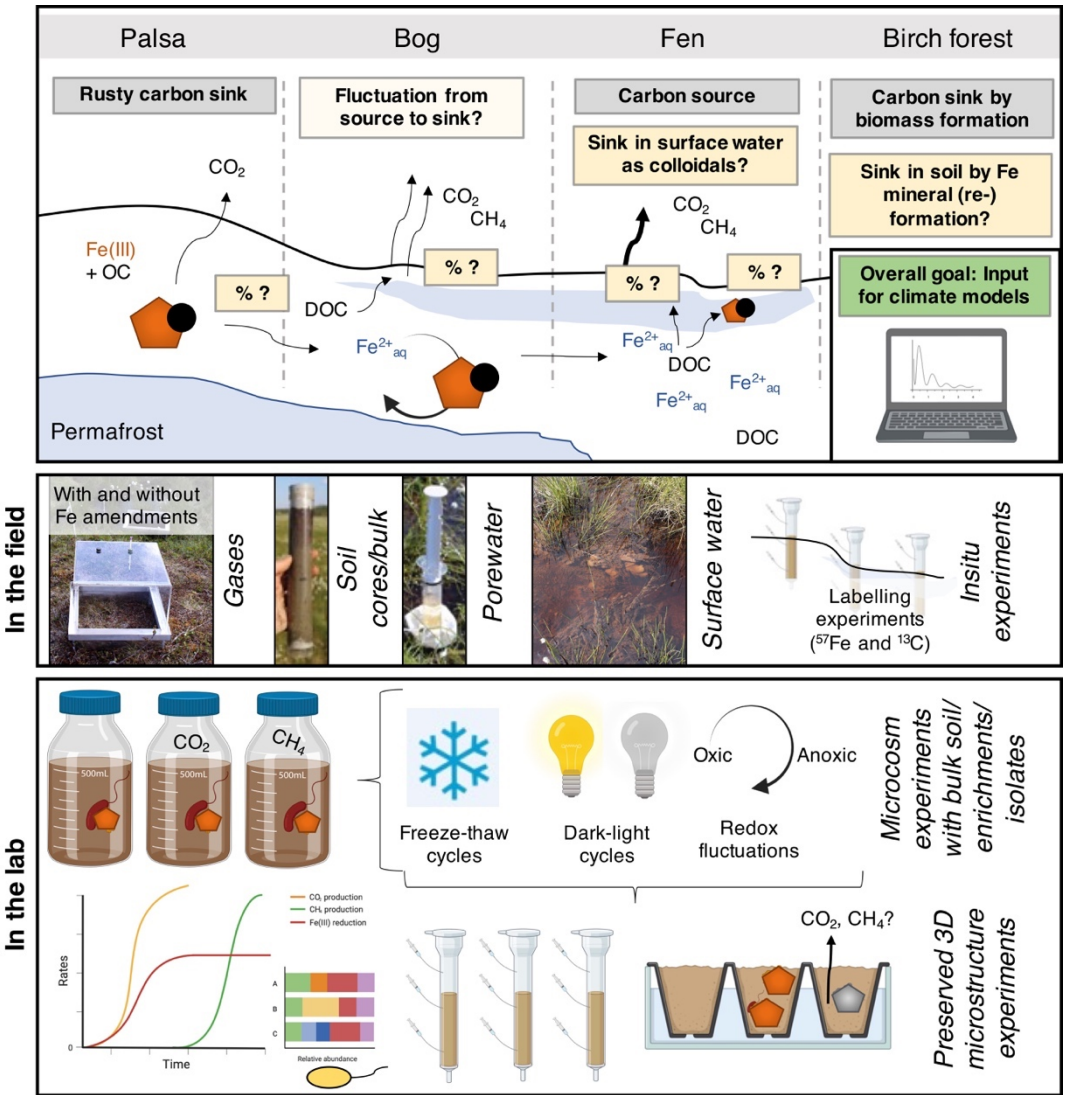

Figure 4. Knowns and unknowns of the loss of the rusty carbon sink on carbon mobilization and greenhouse gas emissions. *Grey and schematic illustrates findings of this PhD work, whereas yellow shows the remaining unknowns concerning the loss of the rusty carbon sink on carbon mobilization and greenhouse gas emissions from palsa to bog to fen to birch forest. Field work should be combining sampling with in situ isolation experiments. In the lab, further experiments need to be conducted to determine rates of Fe(III) reduction, aqueous Fe^{2+} and carbon mobilization and greenhouse gas emissions under various environmental conditions. Lab equipment (bottles, symbols, graphs, columns, plant vessels) is made by ©BioRender - biorender.com.*

Mobilization of mineral-associated organic nitrogen with permafrost thaw

Following CO_2 and CH_4, nitrous oxide (N_2O) is the third most potent GHG, contributing 6% to global warming[38]. Soils are sources of N_2O, so far with highest terrestrial emissions from agricultural and tropical soils[39,40]. Recent measurements of N_2O emitted from permafrost-affected soils showed that also permafrost peatlands are an important and so far, mainly overlooked N_2O source, corresponding to 4% of the global warming potential of Arctic methane emissions at present[41]. Beside increasing awareness of the importance of the nitrogen cycle in permafrost environments[41-43], knowledge gaps remain concerning mineral-associated (organic) nitrogen (ON) in intact permafrost soils and its dynamics with permafrost thaw. Recent studies on New Zealand glacial-affected soils showed that ON stocks were positively correlated to stocks of crystalline Fe oxides[43] which microorganisms were still able to metabolize[45,46]. To our best knowledge, no one ever quantified and identified (reactive Fe) mineral-associated ON along a permafrost thaw gradient.

Findings of this PhD work suggest that also the ON associated with reactive Fe is mobilized during palsa collapse and along the permafrost thaw gradient, contributing to a huge pulse of ammonium at the collapsing front (3.40±1.50 mg/L) (chapter 3, figure 5).
In the active layer of the palsa, underlain by intact permafrost, we found nitrogen-fixing microorganisms such as *Bradyrhizobium* spp. More aliphatic ON (based on FT-ICR-MS analysis) is associated to reactive Fe and released by Fe(III) reduction, driven by Fe(III)-reducing bacteria such as *Geobacter* sp., ultimately contributing to an ammonium pulse in the surrounding porewater. Present and active *Nitrospira* spp. can oxidize ammonia all the way to nitrate. Present and active *Pseudomonas* spp. can further reduce nitrate to dinitrogen (N_2). The presence of *Methylomirabilis* spp. suggests methane oxidation coupled to nitrite reduction. Present and active Deltaproteobacteria have the potential to form N_2O out of nitrate[47]. Present and active *Anaeromyxobacter* spp. partially form produced N_2O to N_2 (unpublished data).

Questions remain, such as (Figure 5):

(1) How much N_2O is emitted along the permafrost thaw gradient and under increasing birch forest expansion?

(2) How much ON is associated with reactive Fe along the permafrost thaw gradient?

(3) How much of the associated ON is directly metabolized during Fe(III) reduction and how much is mobilized into the surrounding porewater?

(4) What role play nitrate-reducing Fe(II)-oxidizers or Methylomirabilis spp. in N_2O emissions along the permafrost thaw gradient?

To answer these questions, field sampling of N_2O emissions, soil (bulk and cores) and water (surface and porewater) would be required for future batch, microcosm, and preserved 3D microstructure experiments (Figure 4). *In situ* flooding experiments could be conducted to better predict the response of the iron cycle and its impact on N_2O emissions under changing redox conditions with progressive permafrost thaw.

In the lab, additional parameters could be examined such as freeze-thaw cycles, dark and light in preserved 3D microstructure experiments. By using diffuse reflectance spectroscopy as a high throughput method[48] particulate and mineral-associated ON could be determined in the solid and liquid phase along the permafrost thaw gradient. Batch and microcosm experiments would help to further determine the mobilization of ON following Fe(III) reduction. Isolation of NRFeOx or *Methylomirabilis* spp. could bring light into their role within the iron and methane cycle linked to the nitrogen cycle and thus N_2O emissions.

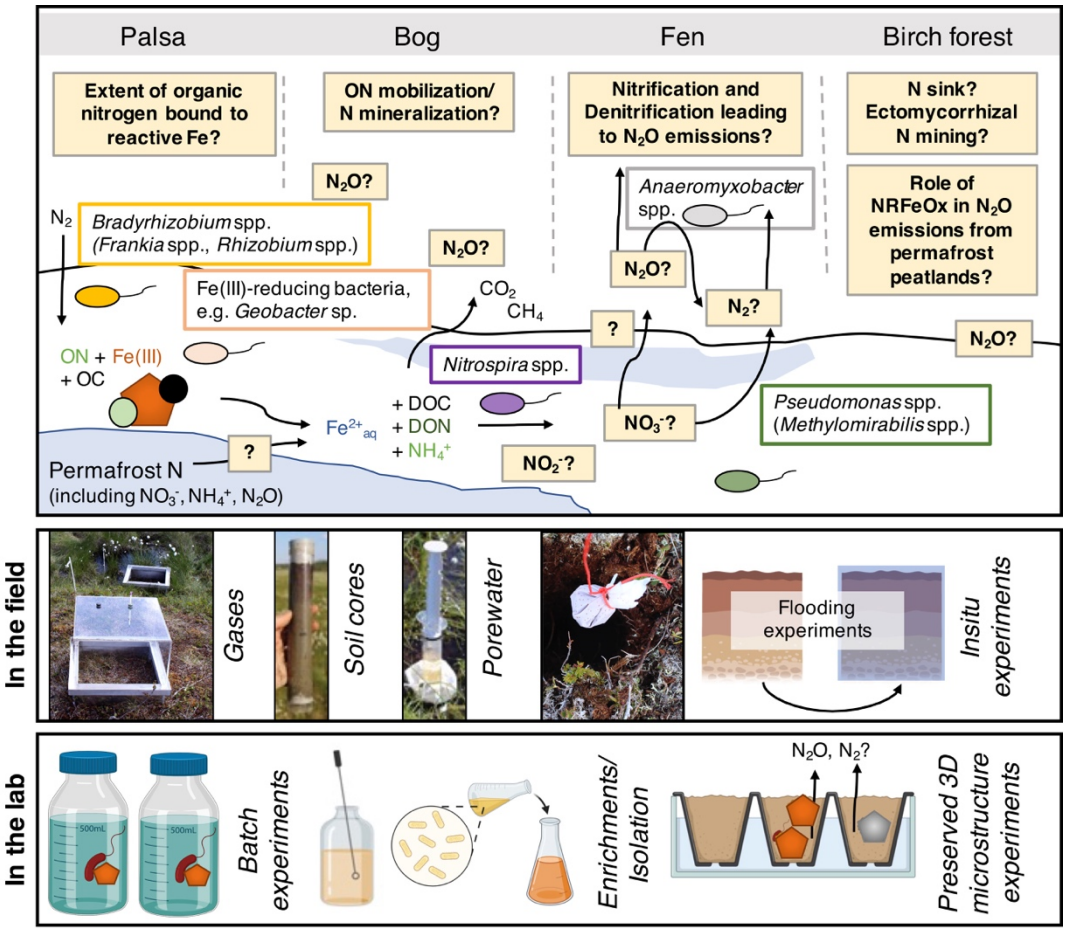

Figure 5. Knowns and unknowns of the mobilization of mineral-associated organic nitrogen along the permafrost thaw gradient. *Schematic illustrates findings of this PhD work, whereas yellow boxes show the remaining unknowns concerning mobilization of mineral-associated organic nitrogen and its impact on N_2O emissions from palsa to bog to fen to birch forest. Future field work could be combining sampling with in situ experiments. In the lab, further experiments need to be conducted to determine the extent of mineral-associated ON, rates of ON mobilization following mineral dissolution by Fe(III) reduction, the role of e.g. NRFeOX or Methylomirabilis spp. and the role of iron minerals in N_2O emissions of permafrost-affected soils. Lab equipment (bottles, plant vessels) is made by ©BioRender - biorender.com.*

The overlooked rhizosphere

Permafrost environments are inhabited by various plants with their roots growing in the seasonal thawed soils[13,49,50]. Along the thaw gradient, vegetation is changing from dry palsas with shrubs and lichens to *Sphagnum* spp. wet bog soils followed by evolution of tall graminoid species as thaw-subsidence increases, resulting in fen areas dominated by *Eriophorum vaginatum* and expanding birch trees *(Betula pubescence* ssp. *czerepanovii)*[13,14,50] (see also Figure 6). Roots have the potential to influence multiple biogeochemical and physical soil processes by physical impact of growing roots (e.g. air trapping in root-adjacent air pockets) and by its interplay with abiotic and microbial processes[51]. For example, radial O_2 loss (ROL) from roots into flooded soils can potentially result in formation of iron mineral coatings around roots, so called iron plaques. These iron plaques could potentially (re-)form a new rusty carbon sink and host a continuum of ecological niches for microbial communities capable of tremendously affecting the cycling of GHG emissions.

The rhizosphere in the active layer was not focus of this PhD work, but, due to its potential impact on iron and carbon cycling, needs to be addressed in future research.

The following questions remain unaddressed (see also Figure 6):

(1) *What role does the root-soil system play for production, consumption, transport, and release of GHGs along the permafrost thaw gradient?*

(2) *What role do different root-exudates play in microbially mediated GHG emissions along the permafrost thaw gradient?*

(3) *Is there Fe plaque formation induced by ROL around plants growing in bog, fen and birch forests and does it act as a rusty carbon sink to stabilize OC, preventing it from microbial decomposition to GHG?*

In the field, gas samples could be taken at various vegetation types at Stordalen mire to provide basic field data and support lab incubation experiments. To link 3D soil structure and plant-microbe-soil carbon transfer in the rhizosphere stable isotope labeling at field scale could be combined with high resolution imaging, as done by Vidal *et al.*[52] with a wheat rhizosphere. Rhizosphere windows could be placed into different plant habitats to visualize root architectural systems and brought back to the lab.

Here, gas movement form below- to aboveground could be tracked visually with pixel analysis with temporally resolved images taken through the rhizosphere windows and used to identify GHG-producing and -consuming hotspots along the roots[53]. Iron reduction experiments with iron plaque on roots being exposed to previously isolated *Geobacter* sp. would further help to determine the impact of the rhizosphere on the extent of iron and carbon mobilization and GHG emissions.

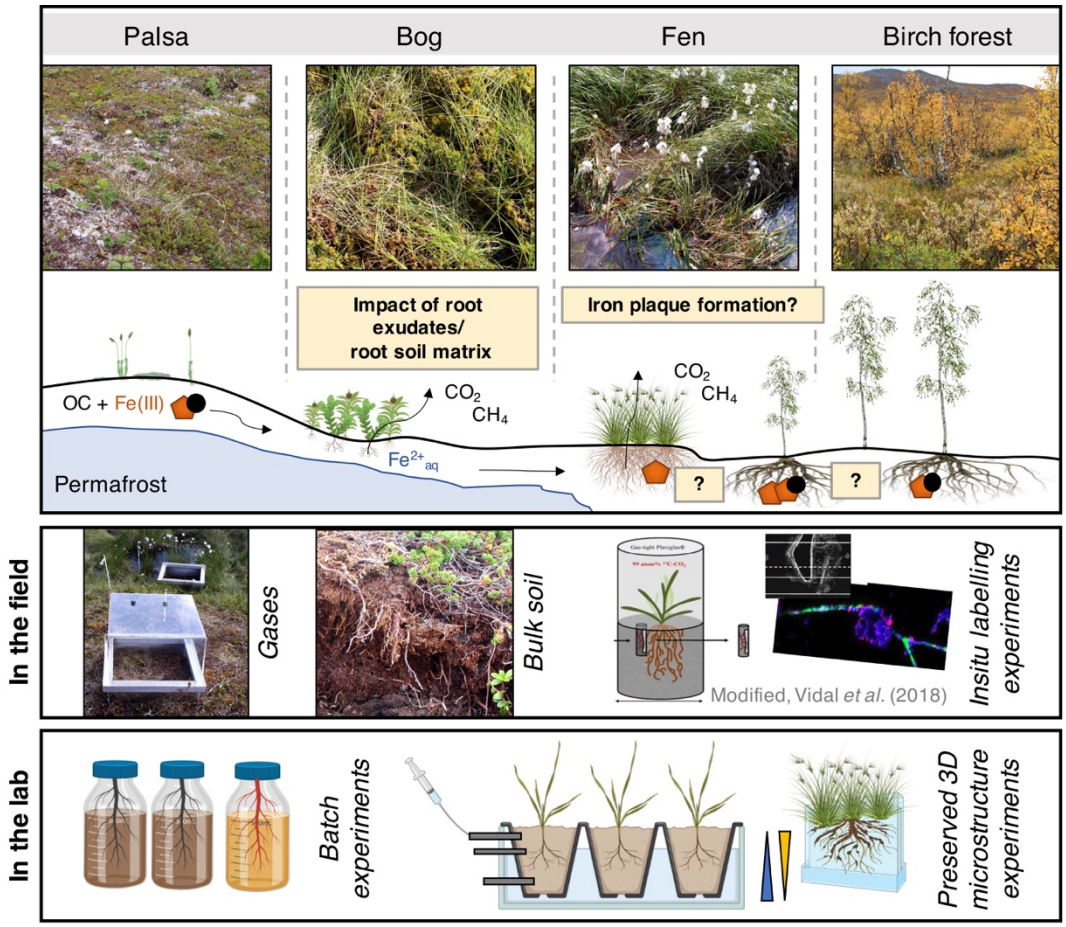

Figure 6. Unknowns of the impact of the rhizosphere on iron- and carbon-cycling along the permafrost thaw gradient. *Yellow shows unknowns concerning the impact of the rhizosphere on iron- and carbon-cycling from palsa to bog to fen to birch forest. Field work should be combining sampling with in situ isolation experiments. In the lab, further experiments need to be conducted to also consider the impact of the rhizosphere in future climate predictions. Plants and lab equipment (bottles, plant vessels) is made by ©BioRender - biorender.com.*

References

1 Sollins, P., Swanston, C. & Kramer, M. Introduction: Stabilization and Destabilization of Soil Organic Matter: A New Focus. *Biogeochemistry* **85**, 1-7 (2007).

2 McBride, M. B. Adsorption and Oxidation of Phenolic Compounds by Iron and Manganese Oxides. *Soil Sci Soc Am J* **51**, 1466-1472 (1987).

3 Sheng, F. *et al.* Rapid Hydrolysis of Penicillin Antibiotics Mediated by Adsorbed Zinc on Goethite Surfaces. *Environ Sci Technol* **53**, 10705-10713 (2019).

4 Newman, D. K. Microbiology. How bacteria respire minerals. *Science* **292**, 1312-1313 (2001).

5 Fridovich, I. Oxygen toxicity: a radical explanation. *J Exp Biol* **201**, 1203-1209 (1998).

6 Waggoner, D., Wozniak, A., Cory, R. & Hatcher, P. The role of reactive oxygen species in the degradation of lignin derived dissolved organic matter. *Geochim Cosmochim Ac* **208**, 171-184 (2017).

7 Kleber, M. *et al.* Dynamic interactions at the mineral–organic matter interface. *Nat Rev Earth & Environ* (2021).

8 Herndon, E. *et al.* Influence of iron redox cycling on organo-mineral associations in Arctic tundra soil. *Geochim Cosmochim Ac* **207**, 210-231 (2017).

9 Sowers, T. D., R. W., Coward, E. K., Fischel, M. H.H., Betts, A. R., Douglas, T. A., Duckworth, O. W., Sparks, D. L. Spatially-resolved organomineral interactions across a permafrost chronosequence. *Environ Sci Technol* **54**, 2951-2960 (2020).

10 Mu, C. C. *et al.* Soil organic carbon stabilization by iron in permafrost regions of the Qinghai-Tibet Plateau. *Geophys Res Lett* **43**, 10286-10294 (2016).

11 Saidy, A. R., Smernik, R. J., Baldock, J. A., Kaiser, K. & Sanderman, J. The sorption of organic carbon onto differing clay minerals in the presence and absence of hydrous iron oxide. *Geoderma* **209-210**, 15-21 (2013).

12 Riedel, T., Zak, D., Biester, H. & Dittmar, T. Iron traps terrestrially derived dissolved organic matter at redox interfaces. *P Natl Acad Sci USA* **110**, 10101-10105 (2013).

13 Callaghan, T. V. *et al.* A new climate era in the sub-Arctic: Accelerating climate changes and multiple impacts. *Geophys Res Lett* **37**, 14705 (2010).

14 Olsson, P. O., Heliasz, M., Jin, H. & Eklundh, L. Mapping the reduction in gross primary productivity in subarctic birch forests due to insect outbreaks. *Biogeosciences* **14**, 1703-1719 (2017).

15 Fisher, B. J., Moore, O. W., Faust, J. C., Peacock, C. L. & März, C. Experimental evaluation of the extractability of iron bound organic carbon in sediments as a function of carboxyl content. *Chem Geol* **556**, 119853 (2020).

16 Mann, P. J., Davydova, A., Zimov, N., Spencer, R. G. M., Davydov, S., Bulygina, E., Zimov, S., Holmes, R. M. . Controls on the composition and lability of dissolved organic matter in Siberia's Kolyma River basin. *J Geophys Res* **117** (2012).

17 Hodgkins, S. B. *et al.* Changes in peat chemistry associated with permafrost thaw increase greenhouse gas production. *P Natl Acad Sci USA* **111**, 5819-5824 (2014).

18 Abbott, B. W., Larouche, J.R., Jones, J.B., Bowden, W.B., Balser, A.W. Elevated dissolved organic carbon biodegradability from thawing and collapsing permafrost. *J Geophys Res* **119**, 2049-2063 (2014).

19 Ward, P. C., Cory, R.M. . Chemical composition of dissolved organic matter draining permafrost soils. *Geochim Cosmochim Ac* **167**, 63-67 (2015).

20 Pokrovsky, O. S., Manasypov, R. M., Loiko, S. V., Shirokova, L. S. Organic and organo-mineral colloids in discontinuous permafrost zone. *Geochim Cosmochim Ac,* 188, 1-20 (2016).

21 Emerson, D., Scott, J. J., Benes, J., Bowden, W. B. Microbial iron oxidation in the Arctic tundra and its implications for biogeochemical cycling. *Appl and Environ Microbiol* **81**, 8066-8075 (2015).

22 Lipson, D. A., Jha, M., Raab, T. K. & Oechel, W. C. Reduction of iron (III) and humic substances plays a major role in anaerobic respiration in an Arctic peat soil. *J Geophys Res-Biogeo* **115**, G00i06 (2010).

23 Vigneron, A. *et al.* Contrasting Winter Versus Summer Microbial Communities and Metabolic Functions in a Permafrost Thaw Lake. *Front Microbiol* **10**, 1656 (2019).

24 Maisch, M., Lueder, U., Laufer, K., Scholze, C., Kappler, A., Schmidt, C. Contribution of microaerophilic iron(II)-oxidizers to iron(III) mineral formation. *Environ Science & Technol* **53** (14), 8197-8204 (2019).

25 Emerson, D. & Moyer, C. Isolation and characterization of novel iron-oxidizing bacteria that grow at circumneutral pH. *Appl Environ Microbiol* **63** (12), 4784-4792 (1997).

26 Laufer, K., Nordhoff, M., Røy, H., Schmidt, C., Behrens, S., Jørgensen, B. B., Kappler A. Coexistence of microaerophilic, nitrate-reducing, and phototrophic Fe(II) oxidizers and Fe(III) reducers in coastal marine sediment. *Appl Environ Microbiol* 82, 1433–1447 (2016).

27 Glodowska, M., Stopelli, E., Schneider, M., Rathi, B., Straub, D., Lightfoot, A., Kipfer, R., Berg, M., Jetten, M., Kleindienst, S., Kappler, A. Arsenic mobilization by anaerobic iron-dependent methane oxidation. *Commun. Earth Environ.* **1**, 7 (2020).

28 Svenning, M. M., Wartiainen, I., Hestnes, A. G. & Binnerup, S. J. Isolation of methane oxidising bacteria from soil by use of a soil substrate membrane system. *FEMS Microbiol Ecol* **44**, 347-354 (2003).

29 Woodcroft, B. J. *et al.* Genome-centric view of carbon processing in thawing permafrost. *Nature* **560**, 49-54 (2018).

30 Garber, A. I. *et al.* FeGenie: A Comprehensive Tool for the Identification of Iron Genes and Iron Gene Neighborhoods in Genome and Metagenome Assemblies. *Front Microbiol* **11** (2020).

31 Gentsch, N. *et al.* Properties and bioavailability of particulate and mineral-associated organic matter in Arctic permafrost soils, Lower Kolyma Region, Russia. *Eur J Soil Sci* **66**, 722-734 (2015).

32 Lipson, D. A., Raab, T.K., Goria, D., Zlamal, J. . The contribution of Fe(III) and humic acid reduction to ecosystem respiration in drained thaw lake basins of the Arcitc Coastal Plain. *Global Biogeochem Cy* **27**, 399-409 (2013).

33 Bäckstrand, K., Crill, P.M., Jackowicz-Korczynski, Mastepanov, M., Christensen, T.R., Bastviken, D. Annual carbon gas budget for a subarctic peatland, Northern Sweden. *Biogeosciences* **7**, 95-108 (2010).

34 Lupascu, M., Wadham, J. L., Hornibrook, E. R. C. & Pancost, R. D. Temperature Sensitivity of Methane Production in the Permafrost Active Layer at Stordalen, Sweden: a Comparison with Non-permafrost Northern Wetlands. *Arct Antarct Alp Res* **44**, 469-482 (2012).

35 Chen, C., Hall, S. J., Coward, E. & Thompson, A. Iron-mediated

organic matter decomposition in humid soils can counteract protection. *Nat Commun* **11**, 2255 (2020).

36 Payandi-Rolland, D., Shirokova, L. S., Labonne, F., Bénézeth, P. & Pokrovsky, O. S. Impact of freeze-thaw cycles on organic carbon and metals in waters of permafrost peatlands. *Chemosphere* **279**, 130510 (2021).

37 Ward, C. P., Nalven, S. G., Crump, B. C., Kling, G. W. & Cory, R. M. Photochemical alteration of organic carbon draining permafrost soils shifts microbial metabolic pathways and stimulates respiration. *Nat Commun* **8**, 772 (2017).

38 IPCC. Climate change 2007: the physical science basis," in Contribution of Working Group I to the Fourth Assessment Report of the Intergovernmental Panel on Climate Change, eds S. Solomon, D. Qin, M. Manning, Z. Chen, M. Marquis, K. B. Averyt, M. Tignor and H. L. Miller (Cambridge, New York, NY: Cambridge University Press). (2007).

39 Kroeze, C., Mosier, A. & Bouwman, L. Closing the global N2O budget: A retrospective analysis 150P 1994. *Global Biogeochem Cy* **13**, 1-8 (1999).

40 Werner, C., Butterbach-Bahl, K., Haas, E., Hickler, T., Kiese, R. A global inventory of N20 emissions from tropical rainforest soils using a detailed biogeochemical model. *Global Biogeochem Cy* **21** (2007).

41 Repo, M. E. *et al.* Large N2O emissions from cryoturbated peat soil in tundra. *Nat Geosci* **2**, 189-192 (2009).

42 Kou, D. *et al.* Progressive nitrogen limitation across the Tibetan alpine permafrost region. *Nat Commun* **11**, 3331 (2020).

43 Voigt, C. *et al.* Nitrous oxide emissions from permafrost-affected soils. *Nat Rev Earth & Environ* **1**, 420-434 (2020).

44 Turner, S. *et al.* Mineralogical impact on long-term patterns of soil nitrogen and phosphorus enzyme activities. *Soil Biology and Biochemistry* **68**, 31-43 (2014).

45 Dippold, M., Biryukov, M. & Kuzyakov, Y. Sorption affects amino acid pathways in soil: Implications from position-specific labeling of alanine. *Soil Biology and Biochemistry* **72**, 180-192 (2014).

46 Turner, S. *et al.* Microbial utilization of mineral-associated nitrogen in soils. *Soil Biol Biochem* **104**, 185-196 (2017).

47 Kuypers, M. M. M., Marchant, H. K., Kartal, B. The microbial nitrogen-cycling network. *Nat Rev Microbiol* **16**, 263-276 (2018).

48 Ramírez, P. B., Calderón, F. J., Haddix, M., Lugato, E., Cotrufo, M. F. Using Diffuse Reflectance Spectroscopy as a High Throughput Method for Quantifying Soil C and N and Their Distribution in Particulate and Mineral-Associated Organic Matter Fractions. *Front in Environl Science* **9** (2021).

49 Raynolds, M. K. *et al.* A raster version of the Circumpolar Arctic Vegetation Map (CAVM). *Remote Sensing of Environment* **232**, 111297 (2019).

50 Johansson, T. *et al.* Decadal vegetation changes in a northern peatland, greenhouse gas fluxes and net radiative forcing. *Global Change Biol* **12**, 2352-2369 (2006).

51 Saleem, M., Law, A. D., Sahib, M. R., Pervaiz, Z. H. & Zhang, Q. Impact of root system architecture on rhizosphere and root microbiome. *Rhizosphere* **6**, 47-51 (2018).

52. Vidal, A. *et al.* Linking 3D Soil Structure and Plant-Microbe-Soil Carbon Transfer in the Rhizosphere. *Front in Environ Science* **6** (2018).

53. Maisch, M., Lueder, U., Kappler, A., Schmidt, C. From Plant to Paddy—How Rice Root Iron Plaque Can

Affect the Paddy Field Iron Cycling.
Soil Syst **4**, 28 (2020).

Statement of personal contribution

The work described in this PhD Thesis was funded by grants from the University Tuebingen (Program for the Promotion of Junior Researchers) to Dr. Casey Bryce and supported by the German Academic Scholarship Foundation (my personal scholarship during my entire studies).

The conceptual background to this project was designed by Prof. Dr. Andreas Kappler and Dr. C. Bryce. Prof. Dr. A. Kappler was the first supervisor throughout the project and Dr. Casey Bryce the second supervisor. Unless otherwise stated, the experiments were either conceptualized by me or together with Dr. C. Bryce and/or Prof. Dr. A. Kappler. The experiments were carried out by me. The discussion and analysis of the obtained results, as well as writing all manuscripts were completed with Dr. C. Bryce and Prof. Dr. A. Kappler; for chapter 2 also in cooperation with Prof. Dr. Thomas Borch, Prof. Dr. Carsten W. Mueller, Miroslava, Malusova, Moritz Baur, Verena Nikeleit, Prof. Dr. Thomas Scholten, Dr. Carmen Hoeschen and Dr. James M. Byrne; for chapter 3 also in cooperation with Prof. Dr. Thomas Borch, Merritt Logan, Dr. Amy McKenna, Dr. Robert Young, Dr. Zhe Zhou, Hanna Joss, Prof. Dr. C. W. Mueller, Dr. C. Hoeschen, Prof. Dr. T. Scholten, Dr. Daniel Straub and Jun.-Prof. Dr. Sara Kleindienst; for chapter 3 also in cooperation with Nora Kainz, Dr. Erik Lundin, Maximilian Barczok, Chelsea Smith, Dr. Elisabeth Herndon, Dr. Lauren Kinsmann-Costello, Dr. Stefan Fischer, Dr. D. Straub and Jun.-Prof. Dr. S. Kleindienst. In detail, the contributions of the named people including myself, as well as other people are as stated below:

Field work: Several people were involved in the field work during sampling campaigns at Stordalen mire, Abisko (Sweden). In July 2017, Dr. C. Bryce leaded the first permafrost field campaign to Abisko and got support by M. Malusova and Johannes Schorr. In July 2018, Dr. C. Bryce helped me sampling during field campaign. In June/July 2019, M. Logan, M. Barczok and C. Smith joined me for a two-week field campaign. M. Logan helped me sampling and collecting various soil and water samples. Together with M. Barczok and C. Smith, redox probes were installed along the permafrost thaw gradient. Dr. C. Bryce, Dr. E. Herndon and Dr. L. Kinsmann-Costello joined the final week. Dr. C. Bryce helped collecting gas samples of the gas chambers, which we obtained from Prof. Dr. Mette Svenning. In September 2019, H. Joss and Sara Anthony joined me during field campaign and helped me collecting soil, gas and water samples of the different thaw stages. In August 2020, Dr. E. Lundin collected the ferrihydrite bags exposed for 1 year along the mire and helped us out in the middle of a

pandemic, which made it impossible for us to go ourselves to Abisko. All these field campaigns were supported by the Abisko Research station, in particular by Jennie Wikström, Dr. Erik Lundin, Niklas Rakos, Annika Kristoffersson and Alexander Meire.

Chapter 2: The original hypothesis was formulated by myself, Dr. C. Bryce and Prof. Dr. A. Kappler. Together with Dr. C. Bryce and Prof. Dr. A. Kappler, I designed the project, interpreted the data and wrote the manuscript. Dr. C. Bryce, M. Malusova and I collected the samples. I gathered the data presented in the main text. Supporting information from the 2017 campaign was collected by V. Nikeleit, M. Malusova, M. Baur and Dr. C. Bryce. Prof. Dr. T. Borch conducted the synchrotron analysis and contributed to the data analysis and interpretation. I collected, analyzed and interpreted the nanoSIMS data together with Dr. C. Hoeschen and Prof. Dr. C. W. Mueller. Dr. J. M. Byrne and I conducted the SEM analyses. Prof. Dr. T. Scholten contributed to project design and data interpretation. Further, Dr. Hannah Miller helped with EXAFS analysis. Dr. Emiliano conducted the ICP-MS measurements.

Chapter 3: The original hypothesis was formulated by myself, Dr. C. Bryce and Prof. Dr. A. Kappler. Together with the support of Dr. C. Bryce and Prof. Dr. A. Kappler, I designed the project, interpreted the data and wrote the manuscript. Dr. C. Bryce, M. Logan and I collected the samples. I conducted the experiments and gathered the data presented in the main text. M. Logan and Dr. A. McKenna conducted the FT-ICR-MS measurements and contributed to the data interpretation. Prof. Dr. T. Borch and Dr. R. Young contributed to the data analysis and interpretation. Dr. Z. Zhou performed the Mössbauer spectroscopy and helped interpreting the results. H. Joss helped collecting the porewater samples and with data interpretation. With the help of Dr. C. Hoeschen and Prof. Dr. C.W. Mueller, I collected, analyzed and interpreted nanoSIMS data. Dr. D. Straub helped processing the Amplicon sequencing samples and, together with Prof. Dr. S. Kleindienst, with interpretation of the microbial community results. Prof. Dr. T. Scholten contributed to project design and data interpretation.

Chapter 4: The original hypothesis was formulated by myself, Dr. C. Bryce and Prof. Dr. A. Kappler. Together with the support of Dr. C. Bryce and Prof. Dr. A. Kappler, I designed the project, interpreted the data and wrote the manuscript. I, together with Dr. E. Lundin, collected the samples. I gathered the data presented in the main text. Supporting information was collected by N. Kainz, M. Barczok and C. Smith. Dr. E. Herndon and Dr. L. Kinsmann-Costello contributed to the data analysis and interpretation. Dr. S. Fischer and I collected the SEM and

EDX analysis. Together with Dr. D. Straub and Jun.-Prof. Dr. S. Kleindienst, I interpreted the microbial community data.

Chapter 5: The original hypothesis was formulated by myself, Prof. Dr. C.W. Mueller, Dr. C. Bryce and Prof. Dr. A. Kappler. H. Joss and I designed the project together with Dr. C. Bryce and Prof. Dr. A. Kappler. H. Joss conducted analyses in the laboratory with my supervision and wrote the original draft of the manuscript with my guidance. Prof. Dr. C.W. Mueller collected and provided the permafrost soil samples and conducted the nanoSIMS analysis. Markus Maisch performed the Mössbauer analysis.

I state hereby that I have not plagiarized or copied any of the text. Chapters 2-5 have been or will be submitted to different scientific journals, so that they might be published in a slightly modified version elsewhere in the future.

Curriculum Vitae

Personal data

Name	Monique Sézanne Patzner
Date and place of birth	July 17th 1991 Konstanz, Germany
Citizenship	German

Academic Education

Ph.D. in Environmental Science (04/2021)

Scholarship of the German Academic Scholarship Foundation

Thesis title: *Microbial iron cycling in permafrost peatlands affected by global warming – impact on carbon mobilization and greenhouse gas emissions*

Geomicrobiology Dep., Center for Applied Geoscience, U. of Tuebingen
Supervisors: Prof. Dr. Andreas Kappler, Prof. Dr. Thomas Borch & Dr. Casey Bryce

---

M.Sc. Geoecology (2015 – 2018)

Scholarship of the German Academic Scholarship Foundation

Thesis title: *Microbial arsenic mobilization in groundwater aquifers of the Red River Delta, Vietnam – A microcosm based approach*

Geomicrobiology Dep., Center for Applied Geoscience, U. of Tuebingen
Supervisors: Prof. Dr. Andreas Kappler & Dr. Michael Berg (Eawag, Zuerich)

B.Sc. Geoecology (2012 – 2015)

Scholarship of the German Academic Scholarship Foundation

Thesis title: *The role of Mn(II)-oxidizing bacteria in household sand filters, Vietnam – Mn(IV) oxide layer, an indicator for total iron and arsenic removal?*

Geomicrobiology Dep., Center for Applied Geoscience, U. of Tuebingen
Supervisors: Prof. Dr. Andreas Kappler & Dr. Stefan Hug (Eawag, Zuerich)

Publications

Barczok, M.R., Smith, C.E., Kinsman-Costello, L., Singer, D.M., **Patzner, M.S**., Bryce, C., Kappler, A., Herndon, E.M. (2021). Impact of increasing permafrost thaw and surface ponding on iron speciation and phosphorous bioavailability in Abisko, Sweden, in prep.

Logan, M., **Patzner, M. S**., Kappler, A., Bryce, C., Borch, T. (2021). Mineral-associated organic nitrogen released during permafrost thaw, in prep.

Patzner, M.S., Kainz, N., Lundin, E., Barczok, M., Smith, C. E., Herndon, E. M., Kinsmann-Costello, L., Fischer, S., Straub, D., Kleindienst, S., Kappler, A., Bryce, C. (2021). Seasonal fluctuations of the rusty carbon sink in thawing permafrost peatlands, submitted.

Patzner, M. S., Logan, M., Joss, H., Mueller, C. W., Hoeschen, C., Scholten, T., Kleindienst, S., Borch, T., Kappler, A., Bryce, C. (2020). Microbial iron(III) reduction during palsa collapse promotes greenhouse gas emissions before complete permafrost thaw, submitted.

Joss, H**., Patzner, M. S.**, Mueller, C. W., Kappler, A., Bryce, C. (2020) Vertical and temporal dynamics of iron-organic carbon associations along a permafrost soil chronosequence, submitted.

Patzner, M. S., Mueller, C. W., Malusova, M., Nikeleit, V., Scholten, T., Hoeschen, C., Byrne, J. M., Borch, T., Kappler, A., Bryce, C. (2020) Iron mineral dissolution releases iron and associated organic carbon during permafrost thaw, *Nature Communications 11*, 6329.

Stopelli, E., Vu Thi, D., Tran Thi, M., Pham Thi, T., Viet Pham Hung, V., Lightfoot, A., Kipfer, R., Schneider, M., Eiche, E., Kontny, A., Neumann, T., Glodowska, M., **Patzner, M.**, Kappler, A., Kleindienst, S., Rathi, B., Cirpka, O., Bostick, B., Prommer, H., Winkel, L., Berg, M. (2020) Spatial and temporal evolution of groundwater arsenic contamination in the Red River delta, Vietnam: interplay of mobilisation and retardation processes, *Science of the Total Environment*, in press.

Glodowska, M., Stopelli, E., Schneider, M., Lightfoot, A., Rathi, B., Straub, D., **Patzner, M.**, Berg, M., Duyen, V.T., Kleindienst, S., Kappler, A. (2019) Role of in-situ natural organic matter in mobilizing As during microbial reduction of Fe(III)-mineral-bearing aquifer sediments from Hanoi (Vietnam), *Environmental Science and Technology* 54, 4149 – 4159.

Conference Contributions (*Presenting Author)

European Geoscience Union online sharing (04/2020)
Oral online presentation: *Organic carbon sorbed to reactive iron minerals released during permafrost collapse*

Goldschmidt Conference, Barcelona, Spain (08/2019)
Oral presentation: *Dynamics of the rusty carbon sink along a thaw gradient in permafrost peatlands*

Abisko Research station, Abisko, Sweden (06/2019)
Oral presentation: *Microbial iron cycle in permafrost peatlands – impact on the carbon cycle and greenhouse gas emissions*

Colorado State University, Fort Collins, United States (06/2018)

Oral presentation: *The microbial iron cycle in permafrost peatlands*

Chair of Soil Science, Technical University Munich, Freising, Germany (05/2018)
Oral presentation: *Fe-C associations in permafrost peatlands*

Goldschmidt Conference, Boston, United States (08/2018)
Oral presentation: *Microbial arsenic mobilization in groundwater aquifers of the Red River Delta, Vietnam*
Poster presentation: *Microbial iron cycling during permafrost thaw*

Conference Contributions (*Co-author)

American Chemical Society online sharing (04/2021)
Oral online presentation: Ultrahigh resolution mass spectrometry analysis of organic nitrogen released upon permafrost thaw
Logan, M.N., **Patzner, M.S.,** Bryce, C., Kappler, A., Borch, T.

Goldschmidt Conference, Lyon, France (07/2021)
Oral presentation: Microbial iron cycling during permafrost thaw
Bryce, C., **Patzner, M.S.,** Mueller, C.W., Logan, M., Eberle, A., Straub, D., Kleindienst, S., Hoeschen, C., Smith, C., Barczok, Kinsman-Costello, L., Herndon, E. M., Borch, T., Robert, Y., M., Kappler, A.

Goldschmidt Conference, Lyon, France (07/2021)
Oral presentation: Composition and reactivity of Fe-C aggregates along a permafrost thaw gradient
Chauhan, A., **Patzner, M.S.,** Mansor, M., Joshi, P., ThomasArrigo, L.K., Bryce, C., Kretzschmar, R., Kappler, A.

Goldschmidt Conference, Lyon, France (07/2021)
Oral presentation: Role of iron minerals for the fate of soil organic carbon during permafrost thaw
Voggenreiter, E., **Patzner, M.S.,** Joshi, P., Borch, T., Bryce, C., Kappler, A.

Goldschmidt Conference, Lyon, France (07/2021)
Poster presentation: Improving determination of iron-associated organic carbon in organic-rich soils
Eberle, A., Byrne J., **Patzner, M.S.,** Kappler, A., Gallego-Sala, A., Pancost, R., Bryce C.

Goldschmidt Conference, Lyon, France (07/2021)
Oral presentation: Impact of increasing permafrost thaw and surface ponding on iron speciation and phosphorous bioavailability in Abisko, Sweden
Barczok, M.R., Smith, C.E., Kinsman-Costello, L., Singer, D.M., **Patzner, M.S**., Bryce, C., Kappler, A., Herndon, E.M.

Professional Development Activities

Analyses at Chair of Soil Science, Technical U, Munich,
Freising, Germany (9/2018, 11/2019 and 02/2020)
Focus: Training and own nanoSIMS analyses of fine organic-rich Fe-mineral particles along a thaw gradient

Summer soil school at Colorado State University, Fort Collins, United States (06/2018)
Focus: Gain an integrated perspective on soil ecology and biogeochemistry to address critical questions using up-to date field and laboratory analytical techniques and models

Research stay at CSU, Fort Collins, United States (06/2018)
(Colorado State University)
Focus: Oral presentation of PhD project, training in FT-ICR-MS (fourier-transform ion cyclotron resonance mass spectrometry) analyses of organic carbon- and nitrogen-rich samples

Research stay at Eawag, Zuerich, Switzerland (03/2015 – 05/2015)
(Swiss Federal Institute of Aquatic Science and Technology)
Focus: Column experiments (1) to model SONO filters used in Bangladesh for arsenic removal and (2) to determine the role of Mn(II)-oxidizing bacteria in household sand filters used in Vietnam for arsenic removal

Research stay at CETASD, Hanoi, Vietnam (08/2014 – 11/2014)
(Center for Environmental Technology and Sustainable Development)
Focus: Research on (1) evironmental contamination and human exposure of polychlorinated biphenyls (PCBs) in Hanoi, Ho Chi Minh City and Bien Hoa, Vietnam, (2) household sand filters to remove arsenic from contaminated groundwater, (3) monitoring arsenic contamination in regions of Hanoi and (4) survey on general consciousness of the arsenic problem

Scientific research, Geomicrobiology, Tuebingen, Germany (04/2014 – 08/2014)
Focus: Column experiments to determine arsenic, iron and manganese removal in drinking water filters used in Vietnam and Bangladesh.

Student assistant, Geomicrobiology, Tuebingen, Germany (2012 – 2013)

Teaching & Mentoring experience

Co-supervision of PhD student (Ankita Chauhan) (02/2020 – 04/2021)
Geomicrobiology Dep. U. of Tuebingen
Thesis: *Comparison and structure of iron-binding antimicrobial compound Pulcherrimin in comparison to other environmentally relevant Fe-organic complexes*

Co-supervision of Bachelor student (Anastasia Rodana) (11/2019 – 05/2021)
Geomicrobiology Dep., U. of Tuebingen
Experiments: Freeze-thaw cycles of arctic thaw ponds removing reactive Fe and associated OC
Thesis: *Wetland formation and birch forest expansion serving as a potential carbon sink – iron organic matter associations in microoxic (root) soil environments*

Co-supervision of Master student (Hanna Joß) (09/2019 – 06/2020)
Geomicrobiology Dep., U. of Tuebingen

Thesis: *Vertical and temporal dynamics of iron-organic carbon associations across permafrost sites*

Co-supervision of research assistant (Sara Anthony) (09/2019 – 04/2020)
Geomicrobiology Dep., U. of Tuebingen
Research: *The microbial iron cycle and its impact on greenhouse gas emissions*

Co-supervision of Bachelor student (Nora Kainz) (01/2019 – 05/2019)
Geomicrobiology Dep., U. of Tuebingen
Thesis: *Mineral-filled bags for the study of microbial transformations during permafrost thaw*

Co-supervision of Master student (Johannes Schorr) (04/2018 – 05/2018)
Geomicrobiology Dep., U. of Tuebingen
Scientific practice: *Extraction method development to identify different Fe phases and associated organic carbon in permafrost soils*

Co-supervision of Master student (Moritz Baur) (09/2018 – 04/2019)
Geomicrobiology Dep., U. of Tuebingen
Thesis: *Iron-metabolizing bacteria in permafrost soils*

Co-supervision of Bachelor student (Miroslava Malusova) (11/2017 – 04/2018)
Geomicrobiology Dep., U. of Tuebingen
Thesis: *Potential for microbial iron cycling in a subarctic permafrost peatland*

Co-supervision of Bachelor student (Alena Hayer) (04/2017 – 08/2017)
Geomicrobiology Dep., U. of Tuebingen
Thesis: *Microbial influence on the extent of arsenic and iron mobilization changing redox conditions in a groundwater aquifer in Vietnam*

Geomicrobiology Lab course, Geomicrobiology Dep., U. of Tuebingen (2018 – 2019)
Focus: (1) Teaching basic cultivation methods and analytical skills in geomicrobiology fo Master students from different fields and (2) Leading and supervising short research projects with specific research questions in geomicrobiology.

Assistance in field excursion 'Geomicrobiology and biogeochemistry of high alpine Fe-rich cold-water springs' (2017)
Geomicrobiology Dep., U. of Tuebingen

Tutor Geomicrobiology lecture, Geomicrobiology Dep., U. of Tuebingen. (2013)
Geomicrobiology Dep., U. of Tuebingen

Public Outreach Activities

Stordalen mire, Abisko, Sweden (09/2019)
Oral presentation: *The microbial iron cycle, visible in the field*

Tourist Information Center, Abisko National Park, Abisko, Sweden (06/2019)
Oral presentation (public talk): *Why should we care about microbes in permafrost soils?*

Child University, Geomicrobiology Dep. U. of Tuebingen (2018 – 2020)

Participation in documentary 'The Silent Death' (ZDF, Second German Television), Bangladesh and Vietnam (02/2016)
Focus: Arsenic contamination of groundwater aquifers in Southeast Asia

Field Campaign Experience

Field campaign Permafrost project, Stordalen mire, Abisko, Sweden (09/2019)
Focus: To observe seasonal changes in iron and carbon cycling along the thaw gradient, to study wetland formations and birch forest expansion into the peat mire
Tasks: Porewater and gas sampling, active layer coring

Field campaign Permafrost project, Stordalen mire, Abisko, Sweden (06/2019 – 07/2019)
Focus: To understand and predict the release of previously Fe-associated OC during permafrost collapse to the surrounding porewater and its impact on potential greenhouse gas emissions such as CO_2, CH_4 and N_20
Tasks: Porewater sampling along a palsa hillslope and along a thaw gradient, active layer coring and gas measurements (gas chambers and eosense gas instruments)

Field campaign Permafrost project, Stordalen mire, Abisko, Sweden (07/2018)
Focus: To characterize the different iron phases along a thaw gradient
Tasks: Active layer coring and surface water sampling

Field campaign AdvectAs project, Van Phuc, Hanoi, Vietnam (10/2017)
(AdvectAs = Retardation and mobilization of **As** at redox fronts under **advec**tive flow conditions)
Focus: To understand and predict the large-scale and long-term mobility of As under enhanced hydraulic forcing by systematic characterization of Fe-dominated redox transition zones
Tasks: Rotary/piston coring and surface/aquifer water sampling

Field campaign Arsenic project, Kushtia, Bangladesh and Hanoi, Vietnam (02/2016)
Focus: Sampling of drinking water filters to find visible, low cost indicator for efficient arsenic removal
Tasks: Drinking water (aquifer and sand filtered) and filter material sampling

Professional Memberships

2018 – present	European Association for Geoscience

Language Skills

German:	Fluent	**French:**	Basic
English:	Fluent	**Spanish:**	Basic

Appendix

Public outreach

Permafrostboden – die schmelzende Zeitbombe?

Permafrost – a Thawing Time Bomb?

Tauen Permafrostböden auf, können gewaltige Mengen an Kohlenstoff entweichen. Tübinger Geomikrobiologen erforschen die Bedingungen, unter denen Kohlenstoff zu Klimagas umgewandelt wird.

// When permafrost thaws, vast amounts of carbon are eventually released into the atmosphere. Tübingen Geomicrobiologists are exploring the conditions under which carbon is converted into greenhouse gas.

TEXT Alisa Koch

> *deutsch*

//_____ Das Klimapotenzial des Permafrost ist gewaltig. Rund ein Viertel der Böden auf der Nordhalbkugel sind dauerhaft und bis zu viele hundert Meter tief gefroren – und schließen etwa doppelt so viel Kohlenstoff ein wie derzeit in der Atmosphäre vorhanden. Dieser stammt aus Pflanzen, die einst dort wuchsen und Kohlendioxid aus der Luft sammelten. Ihre Überreste wurden im Dauerfrost konserviert – solch riesige Tiefkühltruhen kommen unter anderem in Alaska, Schweden und Tibet vor. Hier gehen Professor Andreas Kappler und seine Mitarbeiterinnen Monique Patzner und Hanna Joß den Prozessen im Permafrost auf den Grund.

Der Klimawandel lässt die oberen Bodenschichten im Sommer mittlerweile weiter auftauen. Für die Erde ist diese Entwicklung bedrohlich, denn so könnten riesige Mengen an Klimagasen freigesetzt werden und in die Atmosphäre gelangen. „Die existierenden Klimamodelle versuchen, Auswirkungen des Klimawandels vorherzusagen. Der Permafrostboden ist dabei ein großes Fragezeichen. Man weiß nicht, welche Mengen an Methan und CO_2 künftig freigesetzt werden. Wir wollen dazu beitragen, die Modelle zu verfeinern", erklärt Patzner. Hierzu nimmt das Team zur Analyse Bodenproben sowie Wasser- und Gasproben.

Es gibt unterschiedliche Arten von Permafrostböden, in Schweden liegt ein sumpfiges Torfmoor vor. Die Tübinger haben hier erstmals Eisenminerale nachgewiesen, an denen sich Kohlenstoff bindet – eine gute Nachricht für das Klima: Bleibt der Kohlenstoff dort gebunden, gelangt er nicht als Klimagas in die Atmosphäre. Die Klimaforscher fanden diese Minerale auch in Alaska und Tibet. In manchen Abschnitten sind bis zu zwanzig Prozent des Gesamtkohlenstoffs im Permafrost an sie gebunden. Doch wie stabil sind sie und unter welchen Bedingungen lösen sie sich auf?

„Es ist praktisch, dass wir in Schweden die drei Stadien von Permafrostboden vorfinden: den intakten Boden, das Zwischenstadium – wenn der Boden kollabiert ist – und das reine Feuchtgebiet", sagt Patzner. In diesen Stadien hat das Team Proben entnommen. So ließ sich feststellen, dass sich die Eisenminerale im Zwischenstadium auflösen, wenn das Moor unter Wasser steht und wenig Sauerstoff vorhanden ist. Die Folge: Der daran gebundene Kohlenstoff wird freigesetzt.

Derzeit forschen die Tübinger Geowissenschaftler an der Frage, was für eine Art Kohlenstoff hier vorliegt. Ist er bioverfügbar? Das bedeutet, dass Mikroorganismen den Kohlenstoff aufnehmen und verarbeiten können – nur dann wären Bakterien in der Lage, ihn zu „verfuttern" und in Klimagase umzuwandeln. Für das Klima wäre es von Vorteil, wenn der Kohlenstoff nicht bioverfügbar wäre und über Wasserläufe und Flüsse in andere Gebiete transportiert würde, um sich dort möglicherweise wieder an Minerale zu binden. „Das Zusammenspiel der Prozesse im Permafrostboden ist komplex", sagt Andreas Kappler. „Auch für uns bleibt spannend, wie es am Ende ausgeht." _____//

CH_4

> english

Man weiß nicht, welche Mengen an Methan und CO2 künftig freigesetzt werden. Wir wollen dazu beitragen, die Modelle zu verfeinern.

It is currently unknown how high methane and CO2 emissions will be in the future. We want to help refine the models.

//_____ The potential impact of permafrost thawing on the climate is enormous. Around a quarter of the ground in the northern hemisphere is permanently frozen up to many hundred meters depth and contains about twice as much carbon as is currently present in the atmosphere. This carbon originates from plants that once grew in the soil and carbon dioxide from the air. Plant remains are preserved in the frozen permafrost that can be found in countries like Alaska, Sweden and Tibet. Professor Andreas Kappler and team members Monique Patzner and Hanna Joß are investigating the processes that take place in the permafrost.

Increasing temperatures are thawing more of the top layers of the ground than ever before in summer. This is a threat to the planet, as it could release vast amounts of greenhouse gases such as methane and carbon dioxide into the atmosphere. "Scientists are trying to use existing climate models to predict the impact of climate change. However, permafrost is an unknown and unpredictable factor in the equation. It is currently unknown how high methane and CO2 emissions will be in the future. We want to help refine the models", explains Patzner. To gather the data required to improve existing models, the team is analyzing soil, water and gas samples.

There are different types of permafrost; in Sweden samples are being taken from a permafrost peatland. Here, scientists have discovered iron minerals to which carbon binds – which is good news for the climate. If the carbon remains bound to the minerals, it is protected from degradation and will not enter the atmosphere as greenhouse gases. The team has also discovered iron minerals in Alaska and Tibet. In some areas, up to twenty percent of the total carbon in the permafrost is bound to the iron minerals. But how stable are they and under what conditions will they dissolve?

"It is helpful for us that there are three stages of permafrost at our field site in Sweden: the intact soil, the intermediate stage – when the soil has collapsed – and the pure wetland", says Patzner. The team has gathered samples from each thaw stage. They found that the iron minerals dissolve in the intermediate stage when the bog is flooded by water and little oxygen is present. This causes the carbon initially bound to iron minerals to be released.

The Tübingen geoscientists are now targeting the question of what kind of carbon is available here and whether it is bioavailable. This means whether microorganisms can take up and process the carbon – only then would bacteria be able to convert it into greenhouse gases. It would be beneficial for the climate if the carbon would not be bioavailable and thus transported via watercourses to other areas in order to potentially bind to minerals again. "Processes that occur in the permafrost are particularly complex", says Kappler. "We are also kept fascinated by not knowing how the story ends." _____//

01 Professor Andreas Kappler
Photo: Wolfgang Gerber

02 Monique Patzner
Photo: Wolfgang Gerber

CH_4

EBERHARD KARLS
UNIVERSITÄT
TÜBINGEN

Public Relations Department

Dr. Karl Guido Rijkhoek
Director

Janna Eberhardt
Research reporter

Phone +49 7071 29-76788
+49 7071 29-77853
Fax +49 7071 29-5566
karl.rijkhoek[at]uni-tuebingen.de
janna.eberhardt[at]uni-tuebingen.de

www.uni-tuebingen.de/aktuell

Press Release

Bacteria release climate-damaging carbon from thawing permafrost

Researchers from the Universities of Tübingen and Bristol show that iron minerals fail to trap the organic carbon; vast source of CO_2 and methane not included in global warming forecasts

Tübingen, 10.12.2020

Around a quarter of the ground in the northern hemisphere is permanently frozen. These areas are estimated to contain about twice as much carbon as the world's current atmosphere. However, these permafrost soils are increasingly thawing out as the Earth becomes warmer. A University of Tübingen research team led by Professor Andreas Kappler, and Monique Patzner of the Center for Applied Geoscience, and Dr. Casey Bryce – now at the University of Bristol – has investigated the way this development affects the microorganisms in the soil. The results of their study have been published in *Nature Communications.*

The team worked on the assumption that thawing increases the availability of organic carbon for microorganisms to process, in turn releasing vast amounts of carbon dioxide and methane. These gases accelerate the greenhouse effect, leading to further permafrost thawing in a vicious cycle.

Rising temperatures lead to collapse of intact permafrost soils, resulting in landslides and the widespread formation of wetlands. In this latest study, the team investigated what happens to the carbon trapped in the soil when the permafrost thaws out. "The organic material naturally present in the samples accumulated as peat over thousands of years. With permafrost thaw, microbes become active and are able to decompose the

peat," says Kappler. "We also know that iron minerals preserve organic carbon from biodegradation in various environments – and thus they could be a carbon sink even after the permafrost has thawed." The reactive iron is present as a kind of rust and might be expected to trap the organic material in what the scientists call a "rusty carbon sink."

Investigations in Sweden

The team investigated the storage potential of the rusty carbon sink at a permafrost peatland at Stordalen mire, Abisko, Sweden. There, samples of the soil porewater and drill cores were taken of the active layer along a permafrost thaw gradient. The research team examined how much organic material was bound to reactive iron minerals, how stable these Fe-C-associations are with permafrost thaw, and whether the microorganisms present could use the material as a source of food and energy. The team also carried out experiments in the laboratory in Tübingen.

The team found that microorganisms are apparently able to use the iron as a food source, thereby releasing the bound organic carbon into the water in the soil. "That means the rusty carbon sink cannot prevent the organic carbon from escaping from the thawing permafrost," says Andreas Kappler. "Based on data available from elsewhere in the northern hemisphere, we expect that our findings are applicable for permafrost environments worldwide," says Casey Bryce, who headed the study.

The lead author of the publication, Monique Patzner, summarizes: "The rusty carbon sink is only found in intact permafrost soils; this sink is lost during permafrost thaw." Now the researchers are seeking to find out how this facilitates greenhouse gas emissions and thus global warming. "It appears that the previously iron-bound carbon is highly bioavailable and therefore, bacteria could immediately metabolize it into greenhouse gas emissions," says Patzner. "This is a process which is currently absent from climate-change prediction models and must be factored in."

The location from which the samples were taken: the peatland Stordalen mire, Abisko, Sweden. Photo: Monique Patzner

Permafrost areas thaw out and become marshland. Photo: Monique Patzner

The researchers found some remaining frozen layers in this sample of active soil. Photo: Monique Patzner

Drill core of the active layer of the peatland. Photo: Monique Patzner

Along the thaw gradient, surface water is a rusty red, caused by microbes releasing iron and carbon compounds. Photo: Monique Patzner

Publication:
Monique S. Patzner, Carsten W. Mueller, Miroslava Malusova, Moritz Baur, Verena Nikeleit, Thomas Scholten, Carmen Hoeschen, James M. Byrne, Thomas Borch, Andreas Kappler & Casey Bryce: Iron mineral dissolution releases iron and associated organic carbon during permafrost thaw. *Nature Communications*, https://doi.org/10.1038/s41467-020-20102-6

Contact:
University of Tübingen
Faculty of Science
Center for Applied Geoscience – Geomicrobiology

Professor Dr. Andreas Kappler
Phone +49 7071 29-74992
andreas.kappler[at]uni-tuebingen.de

Monique Patzner
Phone +49 7071 29-74715
monique-sezanne.patzner[at]student.uni-tuebingen.de

Dr. Casey Bryce
casey.bryce[at]bristol.ac.uk

Acknowledgements

In the first place, I would like to thank Prof. Dr. Andreas Kappler for his encouraging spirit which enabled me to develop as a young research scientist, broaden my horizon and work on environmental relevant projects. I will never forget how it was, sitting in his “Christmas lecture” where he always offers the students to attend a lab tour through the geomicrobiology lab – me, still studying law, sitting between the students and fascinated by the world of microbes. Joining this lab tour, changed my perspective and the direction I wanted to aim for my future studies. This is how it all started – studying geoecology and starting in the Geomicrobiology labs Tuebingen from my first term on. Thanks for giving me all the freedom to work independently in the lab from the beginning on, being able to develop own ideas and receive suitable feedback when needed! All the time we spent in Vietnam, in Bangladesh and later in Sweden was a time, I will never forget in my life. What a privilege to be part of such a group! I am very happy that he was my mentor during all these years, grateful for his trust into my scientific development! I am extremely happy that he took a Sabbatical and came back from Caltech with the first ideas and fundament for future work on iron cycling in permafrost environments.

Furthermore, I would especially like to acknowledge Dr. Casey Bryce, who took the lead of the permafrost subgroup as a young research group leader in Prof. Dr. Andreas Kappler’s group. Sampling permafrost soil during a heat wave in Sweden, meanwhile we have been covered with mosquitos and others were running around unprotected, without mosquito nets, in bikinis, will always stay unforgettable. I am very happy for this amazing teamwork, together learning the first steps in permafrost science and co-supervising so many students which were interested in the thawing permafrost environment and its climate impact. I am very grateful for her trust into my scientific skills, always supporting my independency in the lab and in the field.

Thanks to Prof. Dr. Britta Planer-Friedrich for accepting to be my external examiner and to be one member of my PhD committee! Goldschmidt in Barcelona and our discussions about freeze-thaw cycles in thawing peatlands will stay in very good memory! Thanks for your inspiration as a leading female scientist.

All this work would have not been possible by the tremendous support of the Abisko Research station. Special thanks go to Dr. Erik Lundin, Jennie Wikström, Niklas Rakos, Annika Kristoffersson, Alexander Meire and Jutta Holst. Tack för ditt arbete! Jag kommer aldrig att glömma min tid i Abisko! Jag är tillbaka och tar en kaffe med er under fika!

Acknowledgements

I would like to acknowledge Prof. Dr. Thomas Borch, who accepted to co-supervise my project, made me part of his working group in Fort Collins and even enlarged the permafrost team by an additional talented PhD student. I am very thankful for his invitation to the Colorado State University in Fort Collins, where I could meet his heartwarming and hospitable research group members. I appreciated all the productive team meetings we had about characterizing mobilized previously mineral-associated organic carbon and its direct impact on greenhouse gas emissions.

Additionally, I want to thank Prof. Dr. Carsten W. Mueller, showing me the nanoscale soil world. I appreciated his input and motivation for science a lot – Jed ved, at han ikke vil have, at jeg forlader videnskaben (selv ikke I et par år). I am very thankful for all my stays in Freising - the warm welcome by the whole working group, especially by Dr. Carmen Hoeschen, Steffen Schweizer, Gertraud Harrington and Johann Lugmeier. Special thanks go to Johann Lugmeier for all his support during nanoSIMS analysis, for all the interesting political discussions we had and all the Asian food we enjoyed in our short lunch breaks.

Further, I want to thank Prof. Dr. Thomas Scholten for his advice during my whole time as a PhD candidate, his very helpful feedback, and insights into soil science, also at the Tibetan plateau. It was fun joining his group seminars, learning from his PhD student Zuonan Cao. Special thanks to Zuonan Cao for sampling Tibetan permafrost soil and brining it all the way to Tuebingen. Also, a big thanks to Steffen Seitz for showing me our local peatlands in Schönbuch forest and helping me out with TOC analysis, being able to finish revisions in time.

I am also very grateful for Dr. Elisabeth Herndon's support and interest during my studies. I will never forget then she first came to my permafrost poster at Goldschmidt 2018 in Boston, discussing with me the key open questions concerning the iron and carbon cycle in permafrost environments. Thanks also to Dr. Lauren Kinsman-Costello, Max Barczok and Chelsea Smith.

Special thanks also to Prof. Dr. Mette Svenning for her support during my studies and her inspiration! It was such a pleasure to visit you in Tromsø – your labs are amazing!

Furthermore, it would not have been possible to realize my doctoral thesis without the financial support! I therefore would like to thank my scholarship foundation – the German Academic Scholarship Foundation – which made all my scientific work during my entire academic career, to this point, possible at all.

Acknowledgements

A huge thanks goes to all my further collaborators and countless colleagues which, most important, also many of them I can call my friends:

All this work would have never been achieved in three years without the amazing support of our extremely well organized and talented technicians – Ellen Röhm, Lars Grimm (Auf nach Albanien mit dem Bus, Lars! ☺), Franziska Schädler and Bernice Nisch. Also a big thanks to the administration, especially to Elisabetha Kraft and Marion Schäffling (thanks for handling all my Swedish bills :D).

Thanks to Alena Hayer, my first Bachelor student already during my own Master Thesis, who from then on stayed in contact with me over all these years!

Special thanks to the increasing Permafrost team (so called “Permafrosties”) - the once which started all this Miroslava Malusova, Johannes Schorr, Moritz Baur and Verena Nikeleit (Thanks for all the ice-creams we had during our 10 min-glovebox breaks in the middle of our MPN setups in the summer!) and all the following once Nora Kainz, Sara Anthony, Hanna Joß, Anastasia Rodana, Ankita Chauhan, Eva Voggenreiter, Katrin Wunsch and Anne Eberle. Especially the autumn field campaign with Sara and Hanna (Danke für Alles!) and an amazing Aurora will stay unforgettable! Thank you all for making this whole work more colorful with all your creativity and additional ideas. Looking forward to all your future work and findings!

A big thanks goes to Merritt Logan who jumped right into the toughest field campaign, two weeks straight without any single break – taking samples before 6 am, being the first once sampling anoxic porewater at the station, taking bunch of soil samples liquid nitrogen frozen and discussing redox processes over and over again. Thanks for one of the best field campaigns and great team work! +1

A big thanks to Elif Köksoy (teşekkürler abla!) and Ulf Lüder who supported me from the beginning on, helped me taggling all my occurring issues and all day-and-night-discussions we had in the coffee kitchen, in the botanical garden, or later, during the pandemic, in phone calls or via zoom. Thanks for always believing in me, encouraging me and supporting me on my final steps - finishing my PhD and accepting a permanent position at the same time. Thanks for your incredible friendship!

I want to thank all former and current Geomicrobiology group members for making my time in this working group – through all the years, starting from 2011 on – unforgettable! You all

created a perfect working environment, a place where I loved to go to – with all the lunch breaks and discussions we had, the after-work beers, BBQ sessions, summer and Christmas events, lab retreats and running sessions, but also holding everything to together in a pandemic, even with an institute move. Many thanks to all of you including Caroline Schmidt, Annette Piepenbrock, Marie Mühe, Manuel Schad, Katja Laufer, Katja Nitzsche, Julia Otte, Sergey Abramov, Yuge Bai, Stefanie Becker, Sören Drabesch, Jianrong Huang, Yu-Ming Huang, Natalia Jakus, Anh Van Le, Markus Maisch, Lea Sauter, Christopher Schwerdhelm and countless others!

I thank my family for their support and trust into the path I chose. Thanks to my dad and mum who always believed in me, always understood my current situation, who taught me that a positive perspective is the key to survive darker times, that seeing good in other people and social engagement is more important than anything else! Thanks to my brother who is the strongest person I know and who always encouraged me to reach high! I especially thank my beloved boyfriend, Jannik Lehnholz, who gave me the strongest support and motivation throughout very intense years, who always made me smile, laugh, enjoy outdoor and living! Thanks to all Patzners, Joosens, Wetzels and Lehnholzens! I also want to thank Timm Bayer here, who I consider as part of my family!

Last but not least, a big thanks to all my other incredible friends such as Lea Stegmaier, Katja Pelaic, Linda Becker, Katharina Reiter, Annamaria Achtzehn, Manuel Fritsch, Nikolaj Marggrander, Katharina Mayer, Katrin & Hansi Nill and others.

I know that this acknowledgement is very long, but I am deeply thankful for all the support I experienced, all the friendship and love! The relationship with your surroundings is the highest good and I am a very lucky person having all of you at my side! “The strength of the team is each individual member. The strength of each member is the team.” (Phil Jackson)